



**HAL**  
open science

# Tailoring the interfacial properties of magnetic multilayers for the observation of skyrmions at room temperature

Constance Moreau-Luchaire

► **To cite this version:**

Constance Moreau-Luchaire. Tailoring the interfacial properties of magnetic multilayers for the observation of skyrmions at room temperature. Condensed Matter [cond-mat]. Université Paris Saclay (COmUE), 2016. English. NNT: 2016SACLS584 . tel-01757282

**HAL Id: tel-01757282**

**<https://theses.hal.science/tel-01757282>**

Submitted on 3 Apr 2018

**HAL** is a multi-disciplinary open access archive for the deposit and dissemination of scientific research documents, whether they are published or not. The documents may come from teaching and research institutions in France or abroad, or from public or private research centers.

L'archive ouverte pluridisciplinaire **HAL**, est destinée au dépôt et à la diffusion de documents scientifiques de niveau recherche, publiés ou non, émanant des établissements d'enseignement et de recherche français ou étrangers, des laboratoires publics ou privés.

NNT : 2016SACLS584

THÈSE DE DOCTORAT  
DE L'UNIVERSITÉ PARIS-SACLAY  
PRÉPARÉE À L'UNIVERSITÉ PARIS-SUD

École doctorale n°564  
École Doctorale Physique en Île de France  
Spécialité de doctorat : Physique

par

**MME CONSTANCE MOREAU-LUCHAIRE**

*Tailoring the interfacial properties of magnetic multilayers for the  
observation of skyrmions at room temperature*

Thèse présentée et soutenue à l'Auditorium TRT, Palaiseau, le 21 décembre 2016.

Composition du Jury :

|                                                                                          |                    |
|------------------------------------------------------------------------------------------|--------------------|
| <b>M. PHILIPPE LECOEUR</b><br>Professeur, C2N, Orsay, France                             | PRÉSIDENT DU JURY  |
| <b>M. DEL ATKINSON</b><br>Professeur, DURHAM UNIVERSITY, Durham, UK                      | RAPPORTEUR         |
| <b>Mme. STEFANIA PIZZINI</b><br>Directrice de Recherche, INSTITUT NÉEL, Grenoble, France | RAPPORTEUR         |
| <b>M. CHRISTOFOROS MOUTAFIS</b><br>Docteur, UNIVERSITY OF MANCHESTER, Manchester, UK     | EXAMINATEUR        |
| <b>M. THOMAS HAUET</b><br>Enseignant-Chercheur, INSTITUT JEAN LAMOUR, Nancy, France      | EXAMINATEUR        |
| <b>M. VINCENT CROS</b><br>Directeur de recherche, UMΦ, CNRS-THALES, Palaiseau, France    | DIRECTEUR DE THÈSE |



# Contents

|                                                                         |           |
|-------------------------------------------------------------------------|-----------|
| <b>Introduction</b>                                                     | <b>7</b>  |
| <b>1 Overview of micromagnetic energies and domain walls</b>            | <b>10</b> |
| 1.1 Overview of micromagnetic energies                                  | 10        |
| 1.1.1 Exchange                                                          | 11        |
| 1.1.1.1 Exchange energy                                                 | 11        |
| 1.1.1.2 Isotropic exchange                                              | 12        |
| 1.1.1.3 Antisymmetric exchange: Dzyaloshinskii-Moriya Interaction (DMI) | 12        |
| 1.1.2 The Spin-Orbit Interaction (SOI)                                  | 15        |
| 1.1.3 External field energy - Zeeman Energy                             | 16        |
| 1.1.3.1 Stray-field energy                                              | 16        |
| 1.1.4 Anisotropy energy                                                 | 17        |
| 1.1.4.1 Magnetocrystalline anisotropy                                   | 17        |
| 1.1.4.2 Surface/interface anisotropy                                    | 17        |
| 1.1.4.3 Influence of the structure on the magnetic anisotropy           | 18        |
| 1.2 A type of solitons : Domain walls                                   | 18        |
| 1.2.1 Introduction                                                      | 18        |
| 1.2.2 Domain walls in thin films with perpendicular anisotropy          | 19        |
| 1.2.3 Domain wall dynamics                                              | 20        |
| 1.2.3.1 Dynamics with applied magnetic field                            | 21        |
| 1.2.3.2 Current induced domain wall motion                              | 22        |
| 1.2.3.3 DMI estimation                                                  | 25        |
| <b>2 Topological properties and dynamics of magnetic skyrmions</b>      | <b>27</b> |
| 2.1 Topological properties and skyrmion spin texture                    | 27        |
| 2.1.1 Skyrmion spin texture                                             | 27        |
| 2.1.2 Topological properties                                            | 28        |
| 2.2 Observation of skyrmions in magnetic materials                      | 31        |
| 2.2.1 Skyrmions in non-centrosymmetric magnets                          | 32        |
| 2.2.2 Skyrmions at interfaces                                           | 41        |
| 2.2.2.1 Introduction                                                    | 41        |
| 2.2.2.2 Observation of skyrmions in multilayers system                  | 43        |

|          |                                                                                                                                                                     |           |
|----------|---------------------------------------------------------------------------------------------------------------------------------------------------------------------|-----------|
| 2.3      | Topological phenomena related to skyrmions: Topological Hall Effect . . .                                                                                           | 46        |
| 2.4      | Dynamics of skyrmions . . . . .                                                                                                                                     | 48        |
| 2.5      | Conclusions and motivations . . . . .                                                                                                                               | 49        |
| <b>3</b> | <b>Selection of materials and experimental techniques</b>                                                                                                           | <b>51</b> |
| 3.1      | Materials and growth methods . . . . .                                                                                                                              | 51        |
| 3.1.1    | Choice of materials . . . . .                                                                                                                                       | 52        |
| 3.1.1.1  | Introduction . . . . .                                                                                                                                              | 52        |
| 3.1.1.2  | <i>ab initio</i> predictions . . . . .                                                                                                                              | 52        |
| 3.1.1.3  | Fe-based samples and Co-based samples . . . . .                                                                                                                     | 55        |
| 3.1.2    | Magnetron sputtering deposition . . . . .                                                                                                                           | 55        |
| 3.1.2.1  | Description . . . . .                                                                                                                                               | 55        |
| 3.1.2.2  | Principle . . . . .                                                                                                                                                 | 55        |
| 3.2      | Preparation and characterization and physical analysis techniques . . . .                                                                                           | 56        |
| 3.2.1    | X-ray reflectivity: characterization of the interfaces . . . . .                                                                                                    | 56        |
| 3.2.1.1  | Principle . . . . .                                                                                                                                                 | 56        |
| 3.2.1.2  | Information provided by an X-ray Reflectivity measurement: thickness and roughness . . . . .                                                                        | 56        |
| 3.2.2    | Magnetometry characterizations: AGFM and SQUID . . . . .                                                                                                            | 57        |
| 3.2.2.1  | AGFM . . . . .                                                                                                                                                      | 57        |
| 3.2.2.2  | SQUID . . . . .                                                                                                                                                     | 59        |
| 3.2.3    | Demagnetization . . . . .                                                                                                                                           | 60        |
| 3.2.4    | Electron Energy-Loss Spectroscopy (EELS) . . . . .                                                                                                                  | 61        |
| 3.2.5    | Lorentz Transmission Electron Microscopy (LTEM) . . . . .                                                                                                           | 62        |
| 3.3      | Magnetic Imaging . . . . .                                                                                                                                          | 64        |
| 3.3.1    | Synchrotron techniques . . . . .                                                                                                                                    | 64        |
| 3.3.1.1  | In absorption: XAS and XMCD . . . . .                                                                                                                               | 64        |
| 3.3.1.2  | In transmission: STXM . . . . .                                                                                                                                     | 66        |
| 3.3.2    | Laboratory technique: MFM . . . . .                                                                                                                                 | 68        |
| 3.3.2.1  | Introduction . . . . .                                                                                                                                              | 68        |
| 3.3.2.2  | Basic of magnetic contrast formation . . . . .                                                                                                                      | 70        |
| 3.3.2.3  | Imaging procedures . . . . .                                                                                                                                        | 71        |
| 3.3.2.4  | Magnetic field . . . . .                                                                                                                                            | 72        |
| 3.3.2.5  | Lift Height . . . . .                                                                                                                                               | 72        |
| 3.3.2.6  | Choice of tips and spatial resolution . . . . .                                                                                                                     | 74        |
| <b>4</b> | <b>Observation of isolated skyrmions at room temperature in ultrathin multilayers</b>                                                                               | <b>75</b> |
| 4.1      | Observation by STXM . . . . .                                                                                                                                       | 76        |
| 4.1.1    | Observation of Pt <sub>10</sub>  Co <sub>0.6</sub>  Pt <sub>1</sub> {Co <sub>0.6</sub>  Pt <sub>1</sub> } <sub>10</sub>  Pt <sub>3</sub> . . . . .                  | 76        |
| 4.1.1.1  | Sample's characterization . . . . .                                                                                                                                 | 76        |
| 4.1.1.2  | Observation in plain films . . . . .                                                                                                                                | 76        |
| 4.1.2    | Observation of Pt <sub>10</sub>  Co <sub>0.6</sub>  Pt <sub>1</sub> {Ir <sub>1</sub>  Co <sub>0.6</sub>  Pt <sub>1</sub> } <sub>10</sub>  Pt <sub>3</sub> . . . . . | 77        |
| 4.1.2.1  | Characterization of the sample . . . . .                                                                                                                            | 77        |

|          |                                                                                    |            |
|----------|------------------------------------------------------------------------------------|------------|
| 4.1.2.2  | Plain films . . . . .                                                              | 82         |
| 4.1.2.3  | Nanostructures . . . . .                                                           | 87         |
| 4.1.3    | Discussion . . . . .                                                               | 91         |
| 4.1.3.1  | Determination of the chirality of the domain walls . . . . .                       | 91         |
| 4.1.3.2  | Conclusions . . . . .                                                              | 94         |
| 4.2      | Observation by Magnetic Force Microscopy . . . . .                                 | 94         |
| 4.2.1    | Observation at remanence after demagnetization . . . . .                           | 95         |
| 4.2.2    | Observation under out-of-plane magnetic field of {Ir Co Pt} sample . . . . .       | 96         |
| 4.3      | Comparison with other experiments . . . . .                                        | 96         |
| 4.4      | Perspective: Moving small skyrmions in nanotracks . . . . .                        | 101        |
| <b>5</b> | <b>Quantitative estimation of the interfacial chiral interaction</b>               | <b>105</b> |
| 5.1      | Principles . . . . .                                                               | 105        |
| 5.1.1    | Introduction . . . . .                                                             | 105        |
| 5.1.2    | Determination of $D$ using mean domain periodicity after demagnetization . . . . . | 106        |
| 5.1.3    | Determination of $D$ using the evolution of skyrmion size with field . . . . .     | 106        |
| 5.2      | DMI amplitude estimated with mean domain width . . . . .                           | 107        |
| 5.3      | Estimation with the evolution of skyrmions with out-of-plane field . . . . .       | 109        |
| 5.3.1    | Plain films . . . . .                                                              | 109        |
| 5.3.1.1  | With STXM experiments . . . . .                                                    | 109        |
| 5.3.1.2  | With MFM experiments . . . . .                                                     | 111        |
| 5.3.2    | DMI estimation in nanostructures . . . . .                                         | 113        |
| 5.3.3    | Influence of the proximity effect . . . . .                                        | 114        |
| 5.3.3.1  | Proximity induced magnetism in paramagnetic metals . . . . .                       | 114        |
| 5.3.3.2  | Induced proximity effect in Ir Co Pt multilayers . . . . .                         | 117        |
| 5.4      | Conclusions . . . . .                                                              | 121        |
| <b>6</b> | <b>Tuning magnetic interactions and skyrmions properties</b>                       | <b>122</b> |
| 6.1      | List of samples and protocol . . . . .                                             | 122        |
| 6.1.1    | List of the samples and motivation . . . . .                                       | 122        |
| 6.1.2    | Protocol . . . . .                                                                 | 123        |
| 6.1.3    | Characterization . . . . .                                                         | 124        |
| 6.1.3.1  | Magnetic characterization . . . . .                                                | 124        |
| 6.1.3.2  | X-Ray Reflectivity . . . . .                                                       | 128        |
| 6.2      | Observations by MFM and DMI estimation . . . . .                                   | 129        |
| 6.2.1    | {Ir Co Pt} samples . . . . .                                                       | 129        |
| 6.2.2    | Changing Ir by W or AlOx . . . . .                                                 | 138        |
| 6.3      | Conclusions and discussion . . . . .                                               | 140        |
| 6.3.1    | DMI . . . . .                                                                      | 140        |
| 6.3.2    | Skyrmion density vs. $K_{\text{eff}}$ . . . . .                                    | 142        |
| 6.3.3    | Conclusion . . . . .                                                               | 142        |
|          | <b>Conclusion</b>                                                                  | <b>145</b> |

---

|                                                                  |            |
|------------------------------------------------------------------|------------|
| <b>A Annex : Complementary micromagnetic simulations study</b>   | <b>150</b> |
| A.1 Mecanism of injection . . . . .                              | 150        |
| A.2 Roles of defects . . . . .                                   | 152        |
| A.2.1 DMI defects . . . . .                                      | 152        |
| A.2.2 Anisotropy defects . . . . .                               | 153        |
| A.3 Skyrmions modes . . . . .                                    | 154        |
| A.3.1 Simulation model and method . . . . .                      | 154        |
| A.3.2 Dynamic response to driving perpendicular fields . . . . . | 155        |
| <b>Résumé</b>                                                    | <b>165</b> |



# Introduction

In recent years, electronic devices such as CPU and memory got faster and smaller. However, the speed improvement seems not that obvious compared to 10 years ago. The silicon-based electronic devices have almost reached their physical limit. The scale of these devices is a problem when the size is down to sub-10 nm, due to a quantum effect that is hard to control. Finding new pathway to build next generation devices becomes a necessity. There are some candidates for next generation devices such as magnetic-tunneling junctions, domain wall race-track memories, carbon nanotubes-based computing units or the quantum computing. So let's try to find a new candidate technology to get over the current bottleneck in electronic devices.

In parallel, the concept of topology has attracted tremendous interest in Condensed Matter Science. New quantum properties are using the concept of topology and the guidance of theory. The famous example for different topologies is the donut and a sphere, two objects that cannot be transformed continuously into each other. In chemistry, topology is known in the context of the handedness of chiral molecules. The phenomenon of chirality was recently found also in condensed matter systems, in magnetic materials with non-centrosymmetric structures and at the surface of topological insulators. Skyrmions are topologically non-trivial magnetic configurations, in real space, magnetic screw-like nanostructures. In analogy to the real-space example of a donut and a Möbius strip, two different topological quantum states cannot be transformed into each other and will coexist.

In this thesis, we investigate a very promising candidate for next generation devices : isolated magnetic skyrmions in ultrathin ferromagnet-based multilayers with preferred out-of-plane alignment of the magnetic moments. Historically, ferromagnetic domains are the most important medium for digital data storage, and magnetic bubbles (with winding number 0) played in the 1960s - 1970s a major role in the research on the statics and dynamics of ferromagnetic domains and in the development of novel devices. On the application side, bubbles were most successfully used in solid state storage devices, in which the information (the bubbles) is shifted within the material instead of the read or write head moving to the position of the information bit. Unfortunately, bubbles memories have shown their limits: their size ( $\sim 1\mu\text{m}$  diameter, and the way to move them (by rotating field) that is unsuitable for application devices. Nowadays, we are

still using rotating magnetic hard disks, and the search for novel concepts for magnetic solid-state devices is more vivid than ever. One concept facing particular interest in this context is the racetrack memory, a magnetic wire in which domain walls are displaced by spin currents. One major challenge in the realization of such a racetrack memory device is the large current density that is required to move straight domain walls. Recently, it was found that chiral skyrmions can be moved with current densities that are roughly one million times smaller than that for straight walls. To promote their application in actual devices, it is important to study their nucleation, stabilization and propagation in technologically relevant system and at room temperature.

At the beginning of my PhD, the main goal was to observe at room temperature stabilized isolated magnetic skyrmions. This goal was achieved by the observation by a synchrotron technique of isolated skyrmions in  $\{\text{Ir|Co|Pt}\}$  samples. After what, we have developed two new approaches to estimate the average DMI strength in samples. Moreover, we have grown several samples with different parameters to change the interfaces at play and thereby try to tune properties of the magnetic skyrmions observable in those samples (such as their size, density and stability under magnetic field) and enhance the interaction that helps stabilize the skyrmions, the so-called Dzyaloshinskii-Moriya Interaction (DMI). Finally, we have designed devices to start the study of the motion of small isolated skyrmions in racetracks.

This thesis is structured as follows.

- Chapter 1 In Chapter 1 we recall the main micromagnetic energies involved in the samples studied during this work, including the Dzyaloshinskii-Moriya interaction (DMI) that helps the stabilization of skyrmions in our case. We also overview the topic of Domain Walls (DWs), other candidates to next generation devices, because of its large amount of similarities with skyrmions.
- Chapter 2 In this Chapter, we are explaining the concept of topology (in particular of skyrmions in magnetism), followed by a review of the history of the observation of magnetic skyrmions in different types of structures, including in the interfaces structures such as in ultra-thin multilayers as the ones we have studied.
- Chapter 3 The conception of these ultrathin multilayers systems is presented in Chapter 3, where growth details, methods of characterizations and methods of observations are presented.
- Chapter 4 This technical report is followed by the observation at room temperature of isolated magnetic skyrmions, which was our first main goal. These observations have been made with a synchrotron technique (STXM) and a laboratory technique (MFM), and a comparison between the two techniques has been made. We also compare the magnetic behavior of two different samples:  $\{\text{Co|Pt}\}$  and  $\{\text{Ir|Co|Pt}\}$  multilayers to show the effect of different DMI amplitudes. We also show some preliminary results on the motion of isolated magnetic skyrmions in racetracks.

Chapter 5 After the achievement of this first goal, we have developed two independent techniques to estimate the DMI strength in our systems. We present here these techniques and apply them to the observations made by STXM and MFM. We conclude on the possibility to estimate the DMI amplitude with STXM or MFM techniques, and on the large value found for {Ir|Co|Pt} sample. We also present some quantitative analysis of the motion of isolated skyrmions in racetracks presented in the previous chapter.

Chapter 6 Finally, we have performed in Chapter 6 a systematic study by MFM of different samples, varying several parameters. We show that we are able to tune properties of skyrmions (such as their size, density and stability under applied out-of-plane magnetic field) and enhance the DMI amplitude.

# Chapter 1

## Overview of micromagnetic energies and domain walls

### Contents

---

|                                                                          |           |
|--------------------------------------------------------------------------|-----------|
| <b>1.1 Overview of micromagnetic energies . . . . .</b>                  | <b>10</b> |
| 1.1.1 Exchange . . . . .                                                 | 11        |
| 1.1.2 The Spin-Orbit Interaction (SOI) . . . . .                         | 15        |
| 1.1.3 External field energy - Zeeman Energy . . . . .                    | 16        |
| 1.1.4 Anisotropy energy . . . . .                                        | 17        |
| <b>1.2 A type of solitons : Domain walls . . . . .</b>                   | <b>18</b> |
| 1.2.1 Introduction . . . . .                                             | 18        |
| 1.2.2 Domain walls in thin films with perpendicular anisotropy . . . . . | 19        |
| 1.2.3 Domain wall dynamics . . . . .                                     | 20        |

---

This chapter is meant to introduce the basic knowledge to understand the context and results of this thesis. First, I will make an overview of all the micromagnetic energies involved in the samples studied. In the second part, I will focus on the notion of domain wall and its dynamic in presence of a magnetic field and an electrical current. This second part is important to understand the background questions when studying skyrmions, as we will see it in the next chapter.

### 1.1 Overview of micromagnetic energies

Ultrathin multilayers composed of a ferromagnet sandwiched by two heavy metals are at the core of this work. In those kind of trilayers, the Hamiltonian presents different terms.

### 1.1.1 Exchange

A ferromagnet has a spontaneous magnetization even in the absence of an applied field. All the magnetic moments lie along a single unique direction (in fact in many ferromagnetic samples this is not true throughout the sample because of domains. In each domain there is a uniform magnetization, but the magnetization of each domain points in a different direction from its neighbors. See next section for more on magnetic domains). This effect is generally due to exchange interactions which are described hereafter.

#### 1.1.1.1 Exchange energy

Similarly to spin, the exchange interaction is a purely quantum phenomenon, which has no analogy in the classical world. It arises from the Coulomb interaction and is characterized by an electrostatic potential integral. It competes with the spin-orbit interaction, which couples the spin and orbital momenta of the electron. In this context, these interactions are often respectively referred to as non-relativistic and relativistic. The magnetic moments and the spontaneous magnetization are realized by the exchange interaction between electrons. There are two main types of exchange. First, atomic moment are determined by intra-atomic exchange between orbitals. Second, there is an interatomic exchange between neighboring magnetic atoms. The most general expression for the two-site exchange energy is:

$$E_{ex} = \frac{1}{2} \sum_{i \neq j} \mathbf{S}_i^+ \hat{\mathbf{A}}_{ij} \mathbf{S}_j, \quad (1.1)$$

where  $\hat{\mathbf{A}}_{ij} = \{A_{ij}^{\alpha\beta}\}$  with  $\alpha\beta = x, y, z$  are generalized exchange tensors. They can be decomposed into three terms:

$$\hat{\mathbf{A}}_{ij} = J_{ij} \hat{\mathbf{I}} + \hat{\mathbf{A}}_{ij}^s + \hat{\mathbf{A}}_{ij}^a, \quad (1.2)$$

where  $J_{ij}$  is an isotropic part of the exchange tensor,

$$J_{ij} = \frac{1}{3} \text{Tr}(\hat{\mathbf{A}}_{ij}), \quad (1.3)$$

and  $\hat{\mathbf{I}}$  is a unit vector. The traceless symmetric anisotropic exchange matrix is defined by:

$$\hat{\mathbf{A}}_{ij}^s = \frac{1}{2} (\hat{\mathbf{A}}_{ij} + \hat{\mathbf{A}}_{ij}^+), \quad (1.4)$$

and the antisymmetric exchange matrix  $\hat{\mathbf{A}}_{ij}^a$  is given by:

$$\hat{\mathbf{A}}_{ij}^a = \frac{1}{2} (\hat{\mathbf{A}}_{ij} - \hat{\mathbf{A}}_{ij}^+). \quad (1.5)$$

The coupling constant (exchange integral)  $J$  is the largest exchange parameter and can attain values of about 0.01 – 0.1 eV. Therefore, the magnetic state of the system

is generally determined mainly by isotropic exchange (but not necessarily all the time, as we are going to see for example in the skyrmion lattices). The anisotropic part of exchange interaction plays an important role in the magnetic ordering of the system, especially in the case  $S = 1/2$  and where the single-ion anisotropy Hamiltonian (crystal field) vanishes.

### 1.1.1.2 Isotropic exchange

The isotropic exchange interaction was first introduced by Heisenberg in 1928 [1] to interpret the origin of the enormously large molecular field acting in ferromagnets. If two atoms  $i$  and  $j$  have spin angular momentum  $S_i$  and  $S_j$ , respectively, then the exchange interaction between them is given by:

$$E_{ex}^{ij} = -J_{ij} \mathbf{S}_i \cdot \mathbf{S}_j, \quad (1.6)$$

where  $J_{ij}$  is an exchange integral. If  $J_{ij}$  is negative, the lowest energy state results from antiparallel spins. A positive value is therefore needed to get a ferromagnetic state. Spins in the same neighborhood can tilt of a small angle. Hence, the last equation can be approximated as:

$$E_{ex}^{ij} = -\frac{1}{4} J_{ij} S^2 ((\mathbf{r}_{ij} \cdot \nabla) \theta_i)^2, \quad (1.7)$$

where  $\mathbf{r}_{ij}$  determines the deviation of the position of the  $j$  spin from the  $i$  spin. When going from the discrete model to the continuum limit, the exchange energy is described by:

$$E_{ex}^i = \int A \left( \frac{\partial m_i}{\partial x_j} \right)^2 dV, \quad (1.8)$$

where  $A = 2J^2 n/a$  is the exchange stiffness constant with unit cell size  $a$  and number of atoms in a unit cell  $n$ . At zero temperature, the exchange stiffness is related to Curie temperature by  $A(0) \approx kT_c/a$ . The order of magnitude of  $A$  is about  $10^{-12} - 10^{-11}$  J/m. In Equation (1.8)  $m = M/M_s$  is the reduced magnetization and  $M_s$  is the saturation magnetization (it is one material property which characterizes a ferromagnetic material). The exchange energy is isotropic because it is independent of the direction of the change relative to the magnetization direction.

### 1.1.1.3 Antisymmetric exchange: Dzyaloshinskii-Moriya Interaction (DMI)

For quite a long time, metallic magnetic materials were described only by the isotropic exchange interaction described above. But, in some cases as we are going to see, an antisymmetric exchange term can be large enough to modify the spin texture.

The antisymmetric part of the exchange interaction can be written as follow:

$$E_{ex}^a = -\frac{1}{2} \sum_{i \neq j} \mathbf{S}_i \hat{\mathbf{A}}_{ij}^a \mathbf{S}_j = -\frac{1}{2} \sum_{i \neq j} \mathbf{D}_{ij} \cdot (\mathbf{S}_i \times \mathbf{S}_j), \quad (1.9)$$

where

$$D_{ij}^x = \frac{A_{ij}^{yz} - A_{ij}^{zy}}{2}, \quad D_{ij}^y = \frac{A_{ij}^{zx} - A_{ij}^{xz}}{2}, \quad D_{ij}^z = \frac{A_{ij}^{xy} - A_{ij}^{yx}}{2}. \quad (1.10)$$

The fact that the exchange interaction might also contain an antisymmetric term was first proposed by Dzyaloshinskii [2] in 1958 and Moriya [3] in 1960. Dzyaloshinskii predicted purely by symmetry considerations, that the combination of spin-orbit coupling and break of the inversion symmetry lead to antisymmetric exchange interaction. Moriya found a microscopic mechanism that gives rise to such a term in systems with spin-orbit couplings. Thereby, the interaction is called Dzyaloshinskii-Moriya Interaction (DM interaction or DMI). The DM interaction favors the tilting of neighboring spins and hereby favors non collinear magnetic textures. And even more, it also forces a sense of tilting: a chirality, defined by the DMI sign.

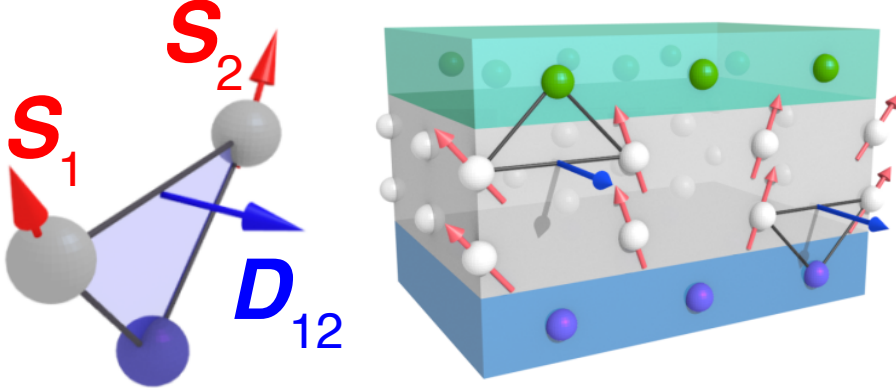


Figure 1.1: Dzyaloshinskii-Moriya Interaction for a single trilayer composed of a magnetic layer (grey) and two heavy metals (blue, green) in the Fert-Lévy picture. *Adapted from [4, 5]*

DMI emerges in systems with strong Spin-Orbit Coupling and lacking inversion of symmetry. MnSi (manganese silicide) is an example of a compound lacking inversion symmetry. Moreover, MnSi has a strong spin-orbit coupling. This is due to several microscopic processes. Inversion symmetry can be broken in different directions leading to a different induced DMI. In the following work, we focus on multilayered systems where the broken symmetry is at the interface of two layers: one ferromagnet and one layer with large spin-orbit coupling (see next paragraph for further details). In Figure 1.1(left), we can see that there is a DMI emerging from the interplay of two atomic spins with a neighboring atom having a large spin-orbit coupling. The resulting DM-vector is in the plane of the interface, pointing outwards from the plane of the spins. Starting with a ferromagnetic state where all the spins are aligned:  $\mathbf{S}_1 \parallel \mathbf{S}_2$ , we then assume a strong spin-orbit coupling that induces a DMI. For a multilayer system (Figure 1.1(right)), the resulting magnetic structure depends on the sign of  $D$ , which defines the chirality, which

depends on the way the symmetry is broken at the interface. Thereby, different helicities can be obtained for different DMI. If  $\mathbf{r}_{12}$  is the vector joining the two spins  $\mathbf{S}_1$  and  $\mathbf{S}_2$ , then the energy of the system is minimized if either  $\mathbf{r}_{12}$  is parallel or perpendicular to  $\mathbf{D}_{12}$ . In the latter case, the DMI tilts  $\mathbf{S}_1$  around  $\mathbf{D}_{12}$  with respect of  $\mathbf{S}_2$ . This rotation eventually results in the configuration showed in Figure 1.1.

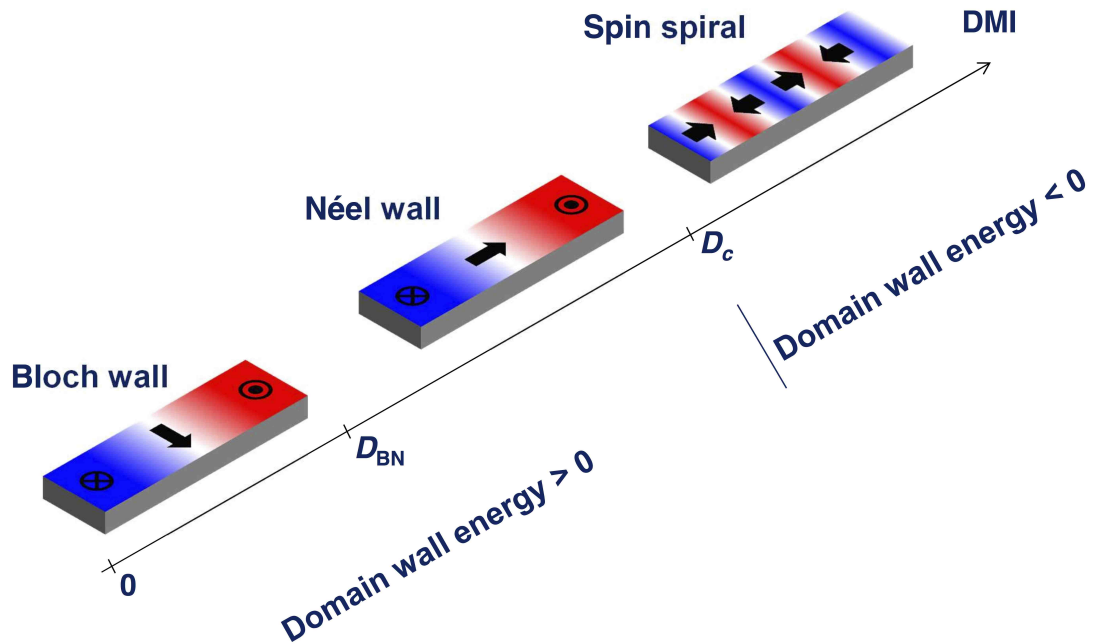


Figure 1.2: Change of domain wall chirality depending on the value of the DMI amplitude in the system (*Courtesy of N. Reyren*).

The inversion asymmetry at an interface can modify the crystal field such that with an appreciable spin-orbit interaction the DMI can have significant effects. This is manifested in perpendicularly magnetized Pt|Co multilayers [6, 7], where the interfacial DMI constitutes an effective in-plane magnetic field which stabilises the Néel domain wall configuration which otherwise would be energetically unfavourable [8] (Figure 1.2). This in-plane field exists only inside the domain wall and acts along the length of the wall. This also induces a specific chirality to the Néel wall which is dependent on the sign of  $D_{ij}$  [8, 6]. Indeed, as seen in Figure 1.2, there is a transition between Bloch and chiral Néel domain wall for low DMI. Above a threshold value  $D_c$ , it is more energetically favorable to tilt the spin so we can expect spiral state or skyrmion lattices. As explained in the following chapter (especially Chapter 5), typical value for  $D$  is very few  $\text{mJ}/\text{m}^3$ .

### 1.1.2 The Spin-Orbit Interaction (SOI)

The *intrinsic* spin-orbit interaction (SOI) between an electron and its atom nucleus arises as follows. We consider a *semi-classical* picture of an electron orbiting around an atom (at a velocity  $|\mathbf{v}|$ ), in the nucleus rest frame. If instead the atom is considered in an inertial frame, comoving with the electron, the nucleus thus appears to be orbiting the electron. The electron experiences a magnetic induction  $\mathbf{B}$  in its rest frame which arises from the Lorentz transformation of the static local electrical field (in the framework of Einstein's special relativity). The resulting magnetic field (magnetic induction) is given by:

$$\mathbf{B} = \frac{1}{c^2} \mathbf{E} \times \mathbf{v}, \quad (1.11)$$

with  $c$  the speed of light in vacuum, and where:

$$\mathbf{E} = -\nabla V(r) = -\frac{\mathbf{r}}{r} \frac{dV(r)}{dr}, \quad (1.12)$$

is the local electric field at the electron due to the nucleus, and  $V(r)$  is the corresponding electron-ion potential in spherical symmetry. This magnetic field interacts with the total spin magnetic moment of the electron to give the following additional spin-orbit (SO) term in the Hamiltonian:

$$\hat{H}_{SO} = -\frac{1}{2} \boldsymbol{\mu} \cdot \mathbf{B}, \quad (1.13)$$

where the factor of  $\frac{1}{2}$  is the relativistic Thomas-Wigner factor. It can be shown that the last equation can be written as:

$$\hat{H}_{SO} = \frac{Ze^2}{2m_e^2 c^2 r^3} \mathbf{L} \cdot \mathbf{S}, \quad (1.14)$$

where the orbital momentum is given by  $\mathbf{L} = \mathbf{r} \times \mathbf{p}$ ,  $m_e$  is the electron's mass,  $Z$  is the atomic number of the nucleus and  $r$  is the radius of the electron orbital. The expectation value  $\langle r^{-3} \rangle$  scales as  $Z^3$ , hence the SOI scales with  $Z^4$  [9], which explains why the SOI is strong in heavy elements such as Pt, W, Ta and Ir. However, it is important to note that orbital hybridisation also plays a significant role when considering complete crystals rather than single atoms.

Equation (1.14) reveals the coupling between spin ( $\mathbf{S}$ ) and orbital ( $\mathbf{L}$ ) angular momentum. The form of  $\hat{H}_{SO}$  given by the equation requires to obtain an (approximated) expression for the electron-ion potential  $V(r)$  and to calculate the  $\hat{\mathbf{S}} \cdot \hat{\mathbf{L}}$  coupling term, a solvable problem only for the case of the hydrogen atom. Instead, in solid-state physics, it is convenient to consider the Hamiltonian arising from the SOI, which can take either of the following forms:

$$\hat{H}_{SO} \propto (\nabla V \times \hat{\mathbf{p}}) \cdot \hat{\boldsymbol{\sigma}}, \quad (1.15)$$

$$\hat{H}_{SO} \propto (\mathbf{E} \times \hat{\mathbf{k}}) \cdot \hat{\boldsymbol{\sigma}}, \quad (1.16)$$

where  $\hat{\mathbf{p}} = \hbar\hat{\mathbf{k}} \equiv -i\hbar\nabla$  is the linear momentum operator and  $\hat{\sigma}$  are the Pauli matrices, such that  $\hat{\mathbf{S}} = \frac{\hbar}{2}\hat{\sigma}$ .

Thus, the SOI couples the electron spin degree of freedom  $\sigma$  to its momentum  $\mathbf{k}$ . Seen from the perspective of the electron spin in a *semi-classical* picture, the spin-orbit coupling gives rise to spin precession, while momentum scattering makes the precession to fluctuate randomly both in magnitude and in orientation.

### 1.1.3 External field energy - Zeeman Energy

The magnetic field energy can be separated in two distinct parts: the *external field energy* and the *stray field energy*. The first part is due to the interaction between the magnetization vector field and an external field  $\mathbf{H}_{ex}$ . It can be written as followed:

$$E_H = -J_s \int \mathbf{H}_{ex} \cdot \mathbf{m} dV. \quad (1.17)$$

For a uniform external field, this energy only depends on the average magnetization and not on the particular domain structure or the sample shape.

#### 1.1.3.1 Stray-field energy

This magnetic field energy is connected with the magnetic field generated by the magnetic body itself. It arises because each magnetic moment in a ferromagnetic sample represents a magnetic dipole and therefore contributes to the total magnetic field inside the sample. Starting from general Maxwell's equation  $div\mathbf{B} = 0$  and materials equations for magnetized bodies  $\mathbf{B} = \mu_0(\mathbf{H} + \mathbf{M})$  the stray field (or demagnetization field)  $H_m$  is defined as the field generated by the divergence of the magnetization  $\mathbf{M}$ :

$$div\mathbf{H}_m = -div\mathbf{M}. \quad (1.18)$$

The sinks and sources of the magnetization act like positive and negative "*magnetic charges*" for the stray field. The  $\mathbf{H}$  field can be calculated with electrostatic techniques. The only difference with an  $\mathbf{E}$  field is that magnetic charges can never appear isolated but are always balanced by opposite charges. The energy connected to the stray field is defined as followed:

$$E_m = \frac{\mu_0}{2} \int \mathbf{H}_m \cdot \mathbf{M} dV. \quad (1.19)$$

A general solution of the stray field problem can be given by potential theory. The reduced volume charge density  $\lambda_v$  and the surface charge density  $\sigma_s$  are defined in terms of the reduced magnetization  $\mathbf{m}(\mathbf{r})$ :

$$\lambda_v = -div\mathbf{m}, \quad \sigma_s = \mathbf{m} \cdot \mathbf{n} \quad (1.20)$$

where  $\mathbf{n}$  is the unit vector normal to the surface and pointing outward.

### 1.1.4 Anisotropy energy

The energy of a ferromagnet depends on the direction of the magnetization relative to the structural axes of the material. This phenomenon relies on the spin-orbit coupling and is described by the anisotropy energy. A distinction is made between anisotropies related to the crystal structure and anisotropies due to deviations from the case of a perfect crystal lattice.

#### 1.1.4.1 Magnetocrystalline anisotropy

The magnetocrystalline anisotropy arises as a result of coupling between the spin and orbital motion of electrons in the crystal lattice. This gives rise to stable directions of the spontaneous magnetization, or easy axes, along which the magnetization preferably aligns. Because of its origin, the magnetocrystalline anisotropy is strongly related to the lattice symmetry. The simplest case of magnetocrystalline anisotropy is uniaxial anisotropy. This type of anisotropy is manifested, e.g., in hexagonal, tetragonal, and rhombohedral structures. The anisotropy energy in those cases has the form (up to fourth-order terms):

$$E_K = K_{u_1} \sin^2 \theta + K_{u_2} \sin^4 \theta, \quad (1.21)$$

where  $\theta$  is the angle between anisotropy axis and magnetization direction. A large positive  $K_{u_1}$  describes an easy axis, whereas a large negative  $K_{u_1}$  describes an easy plane-type of anisotropy.

#### 1.1.4.2 Surface/interface anisotropy

At interfaces the broken symmetry can create specific anisotropies, as suggested by Néel [10]. It is called surface anisotropy and is described by additional phenomenological parameter. The surface anisotropy can favor an easy magnetization direction either parallel or perpendicular to the surface plane. The simplest phenomenological approach is based on the concept of the effective magnetic anisotropy energy which could be separated in a volume and surface terms and approximately conform with the experimental relation:

$$K_{\text{eff}} = K_v + \frac{K_s}{t} \quad (1.22)$$

where  $t$  is the thickness of a layer,  $K_v$  is an energy density per volume and  $K_s$  is an energy density per surface. From (1.22) we define a critical film thickness  $t_{cr} = K_s/K_v$  where transition from in-plane to out-of-plane magnetization occurs. Such behavior is general for all magnetic multilayer compositions, e.g., Co/Pt, Co/Cu, Fe/Au. As far as Co/Pt interface is concerned, in our growth experiment, the transition between in plane and out-of-plane anisotropy occurs for Co thicknesses of 1 nm and higher.

### 1.1.4.3 Influence of the structure on the magnetic anisotropy

In the discussion of the experimental results, it should be realized that the structure of the magnetic layers is extremely important for the actually observed magnetic anisotropies [11]. The importance of the topology of the interfaces and of the crystallographic structure of the magnetic layers was already mentioned. The structural properties are strongly determined by the complex interplay between the employed growth technique, the preparation conditions, the elements which are grown, their thicknesses and lattice mismatch, the symmetry, etc. In practice, layers do not have ideal flat interfaces because films cannot be grown perfectly. Roughness and/or interdiffusion will be present and will modify the magnetic properties.

The effect of roughness on the dipolar anisotropy has been studied theoretically by Bruno [12]. A rough surface can be characterized by the roughness, which is the mean square deviation from the ideally flat surface, and the correlation length, which is the average lateral size of flat areas on the surface (terraces). Roughness creates in-plane demagnetizing fields at the edges of terraces, thereby reducing the shape anisotropy. The anisotropy contribution resulting from the roughness will, therefore, always be positive (favouring PMA) [13, 14].

As mentioned, interdiffusion might occur during the deposition of the layers. It is clear that diffuse interfaces introduce randomness in the magnetic pair bonds according to Néel's model, which obviously reduces the interface anisotropy [15].

## 1.2 A type of solitons : Domain walls

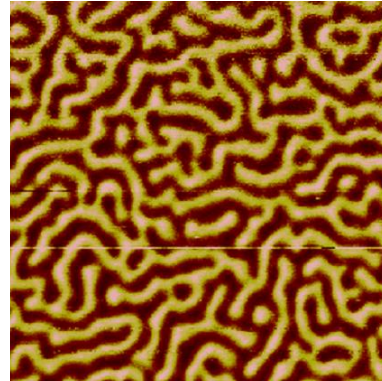
### 1.2.1 Introduction

In this section, we will introduce the notion of a domain wall and its dynamics driven by a magnetic field or an electrical current. During my PhD, we have focused on materials with perpendicular anisotropy and therefore I will describe here only domain walls with such anisotropy, even though a certain number of studies have been performed in planar anisotropy, describing magnetic domain-wall dynamics [16, 17] or the dependence of domain wall pinning potential landscapes on domain wall chirality [18].

As said in the previous section, and as seen in Figure 1.3 despite a spontaneous magnetization under Curie temperature, the magnetization of a ferromagnet is not always uniaxial. Indeed, the material is divided mesoscopically in magnetic domains, defined as regions where the magnetization is uniform. This is made, as seen before, to minimize the magnetostatic energy.

F. Bloch in the late 30s developed the first ideas on domain walls. Domains mainly come from the competition between several energies listed before. Hence, two neighboring magnetic domains next to each other with opposite moment can not have an ultrathin infinite surface that separate each other: the exchange energy in it would be too important so the free energy couldn't have a minimum. To decrease the contribu-

Figure 1.3: Magnetic imaging of domains in {Ir|Co|Pt} multilayered sample, without applied field and after demagnetization process (see Chapter 3 for further details about demagnetization).



tion of the exchange energy, the transition has to rely on several atoms so that the angle between two neighbors is the smallest possible. In that case, the problem is that when we are away from the easy axis, the magnetocrystalline energy increases (Figure 1.4).



Figure 1.4: Scheme of magnetization reversal according to the width of the domain wall (the reversal is abrupt in a very thin domain wall and continuous in a large domain wall). A narrow domain wall has a high exchange energy (**left**) and a wide domain wall has a high anisotropy energy (**right**).

Hence, it is the competition [19] between these two effects that define a domain wall: a high anisotropy will tend to reduce the width of the wall whereas a high exchange interaction will increase it. This competition is illustrated by the relation:

$$\Delta \propto \sqrt{\frac{A}{K}}, \quad (1.23)$$

where  $\Delta$  is the domain wall width,  $A$  is the exchange energy and  $K$  is the anisotropy energy as seen in the previous sections.

### 1.2.2 Domain walls in thin films with perpendicular anisotropy

The Domain Wall (DW) is described by its width and its structure. The latter is the spatial distribution of the magnetization inside the DW. In an ultrathin layer with perpendicular anisotropy, to go from a domain where the magnetization is pointing up

to another one pointing down, the magnetization is reversing by turning in the plane or perpendicularly to the plane of the DW. For these two configurations, the DW is called respectively Bloch DW or Néel DW. Indeed, the distribution of the magnetostatic charges is different between the case of a DW in an ultrathin layer and one in a layer structured in band of width  $w$ .

In the case of an infinite ultrathin layer ( $w = \infty$ ), Bloch walls are favored. Indeed, when the demagnetization field goes through the DW, a Néel-type structure appears, magnetostatic energy is minimized for a Bloch DW because the magnetic charges are pushed to infinite. In the case of a layer structured in strip, the type of the DW depends on the dimensions of the systems. If the bandwidth is less than the one of the DW, the system prefers a Néel configuration to lower the demagnetizing field [20]. Indeed, if  $w < \Delta$ , the charges are further from the Néel wall than from the edges of the wire, opposite to the case of a Bloch wall. Finally, if  $w \sim \Delta$ , magnetization inside the DW will be in between a Bloch wall and a Néel wall.

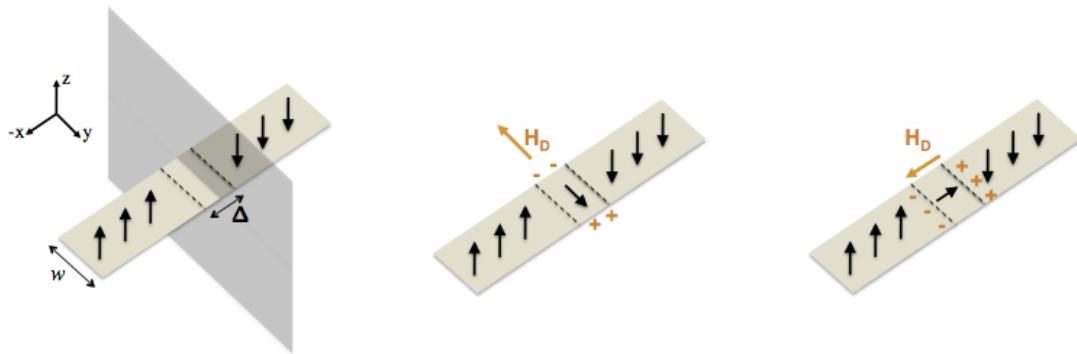


Figure 1.5: Scheme of DW in material with perpendicular anisotropy. The structure of the DW is dictated by the dipolar energy. It depends on the dimensions of the system and the width of the DW. Magnetostatic charges are represented in orange and  $\mathbf{H}_D$  indicates the direction of the demagnetizing field. **(middle)** Bloch wall. **(right)** Néel wall.

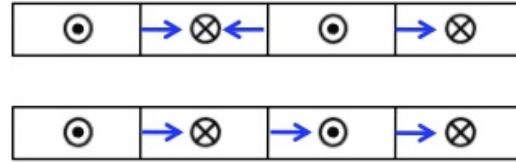
Materials with perpendicular anisotropy are particularly interesting in the study of the dynamics of DW. Indeed, be it Bloch or Néel, DWs have a simple and stiff structure: they are topological solitons. Their small size is also attractive when thinking about their potential application in memory chips where high density is required.

### 1.2.3 Domain wall dynamics

There are at least two different ways to move a DW. The first one is to apply a magnetic field along the easy axis of magnetization. In this case, domains with magnetization pointing in the same direction as the field are favored and increase their volume. On the contrary, domains with magnetization pointing in the opposite direction are shrinking

and tend to disappear. The result is in a displacement of the DWs. Another means is to use electrical current. In this case, the displacement is due, for example, to the Spin Transfer Torque (STT). When conduction electrons go through the system, they polarize themselves and then transfer an angular momentum. This interaction leads to a displacement of the DW. This method is more convenient for applications because in that case, all the DW move in the same direction. Thereby, domains keep the same width and information can be transmitted without modification.

Figure 1.6: Direction of DW's displacement under **(top)** an applied magnetic field (pointing towards the reader) or **(bottom)** an electric current (with electron flow pointing to the right).



### 1.2.3.1 Dynamics with applied magnetic field

The dynamics of a DW is described by the Landau-Lifschitz-Gilbert (LLG) equation. This equation, describing more generally the dynamics of magnetization considers the whole micromagnetic system. Thereby, the different energies involved in the system are gathered into an effective local field  $\mathbf{H}_{\text{eff}}$ :

$$\frac{\partial \mathbf{m}}{\partial t} = \gamma_0 \mathbf{H}_{\text{eff}} \times \mathbf{m} + \alpha \mathbf{m} \times \frac{\partial \mathbf{m}}{\partial t}, \quad (1.24)$$

where  $\mathbf{m} = \frac{\mathbf{M}}{M_s}$  with  $\mathbf{M}$  the local magnetization and  $M_s$  the spontaneous magnetization of materials. Equation (1.24) describes the temporal evolution of magnetization under magnetic field. When the magnetization and the field are not parallel, the system is out of equilibrium. It is then described by two terms. The first one is a conservative torque describing the precession of the magnetization around the effective field  $\mathbf{H}_{\text{eff}}$ . The angular speed of the precession is proportional to the effective field and the gyromagnetic ratio  $\gamma_0$ . The second term is dissipative and tend to get the system back to equilibrium. This torque is proportional to the damping parameter  $\alpha$  and to the temporal variation of the magnetization. It is perpendicular to the magnetization and to its trajectory.

Walker showed in 1974 [21] that, in presence of a magnetic field  $\mathbf{H}_{\text{app}}$  applied along the easy axis, a domain wall would move according to two different regimes: one with high mobility at low field and one with low mobility at high field. In presence of this field, the magnetization at the center of the domain wall will tilt until finding an equilibrium angle. The domain wall will then move continuously in a stationary regime. Above a critical field (called the Walker field), the magnetization at the center of the domain wall no longer finds equilibrium. The field destabilizes the domain wall which enters a turbulent regime: here the magnetization at the center of the DW precesses which diminishes so that it lowers the average speed of the DW motion.

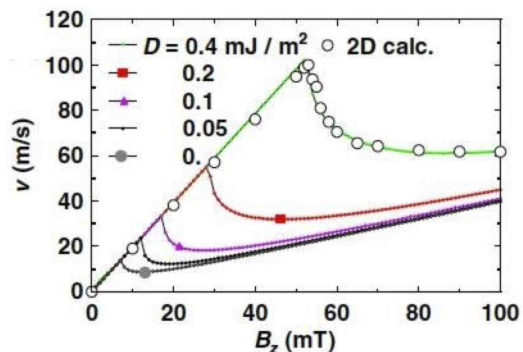


Figure 1.7: Variation of the domain wall speed with applied out-of-plane magnetic field in Pt|Co|AlO<sub>x</sub> systems and for different values of DMI [8].

Tretiakov et al. [22] and Thiaville et al. [8] recently investigated the influence of DMI on DW dynamics. For instance, Thiaville and coworkers used the material parameters of Pt|Co<sub>0.6</sub>|AlO<sub>x</sub>, as shown in Figure 1.7. The DMI will extend the range of perpendicular field value for the stationary regime, without changing the domain wall mobility. Hence, the maximum DW velocity is increased with  $D$ . We also note that the DMI amplitude in this case is only few 0.1 mJ/m<sup>2</sup>, which will be a good comparison with the values found in Chapter 5.

### 1.2.3.2 Current induced domain wall motion

**Introduction** In magnetic microstructures, applying current can induce domain wall motion either along or opposite to the electric current. The torque responsible for current induced DW motion can be of two types: Spin Transfer Torque (STT) and Spin-Orbit Torque (SOT). In the following paragraphs, the different aspects of physics associated with STT and SOT will be discussed.

**Spin Transfer Torque (STT)** Possibility to move magnetic DW by spin polarized current injection was first proposed by Berger in 1978 [23]. In a 3d-transition metal ferromagnet, the electrical current is naturally spin polarized thanks to  $s-d$  interaction which tend to align the spins of conduction electrons with local magnetization. When an electrical current goes through a DW, the spin of conduction's electrons tend to align with the local magnetization. This change of direction of spin leads to a torque on the magnetization inside the DW. This torque, called Spin Transfer Torque, is a transfer of the angular momentum of the conduction electron to localized moments. In literature, two main contributions have been identified to describe STT: the adiabatic torque (A) and the non-adiabatic one (NA) [8]. To summarize, the current induced domain wall motion exhibits the same features as those of the field induces domain motion. The current induced domain wall motion can be steady or oscillatory, depending on the current density.

From the application point of view, the usefulness of the current induced DW motion depends on two parameters: the current required for the depinning of the DW and the DW velocity. The DW can be trapped in the pinning potential created by the

imperfections in the sample. Thus, a large current may be required for the depinning of the DW. Recently, large DW velocities, too large to be explained by STT, were observed in systems with structural inversion asymmetry (trilayers made of a thin magnetic layer sandwiched between two-different non-magnetic layers). The DW motion was against the electron flow in contradiction with the STT model. To explain these observations, additional torque mechanisms were introduced, explained in the next paragraphs.

**Spin-Orbit Torque (SOT)** The ability to reverse the magnetization of nanomagnets by current injection has attracted increased attention ever since the spin-transfer torque mechanism was predicted in 1996. P. Gambardella and I.M. Miron have reviewed the basic theoretical and experimental arguments supporting a novel current-induced spin torque mechanism taking place in ferromagnetic (FM) materials, the so-called SOT. For more details, one can refer to this reference [24]. SOT originates from the exchange of angular momentum between the crystal lattice and the magnetization, which makes it possible to control the magnetization of a single ferromagnetic layer without transferring the magnetization in spin momentum from a second ferromagnet. It has been recently demonstrated that magnetic devices composed of a single ferromagnet and a heavy metal can be switched by an electric current injected in the heavy material [25, 26]. Magnetization switching induced by in-plane current has been investigated mainly in Pt|Co|AlOx [25, 27, 28], Pt|Co|MgO [29], Ta|CoFeB|MgO [30, 31, 32, 33], W|CoFeB|MgO [34] for systems with oxides, or for all-metal structures in Pt|Co|Ni [27], Ta|Ni<sub>20</sub>Fe<sub>80</sub> [35], Ta|Co<sub>20</sub>Fe<sub>60</sub>B<sub>20</sub>|MgO [36], Pt|Co|Pt [37] or Co|Pd [38] multilayers. A current applied parallel to the interface plane in trilayers with break of the inversion symmetry generates two different types of spin torques: a transverse (field-like) torque [39, 40]  $\mathbf{T}^\perp \sim \mathbf{m} \times \mathbf{y}$  and a longitudinal (damping-like) torque [25, 27]  $\mathbf{T}^\parallel \sim \mathbf{m} \times (\mathbf{y} \times \mathbf{m})$ , where  $\mathbf{y}$  denotes the in-plane axis perpendicular to the current direction  $\mathbf{x}$ , and  $\mathbf{m}$  is the magnetization unit vector. The effect of these torques is equivalent to two effective field:  $\mathbf{B}^\perp = \mathbf{m} \times \mathbf{T}^\perp$  and  $\mathbf{B}^\parallel = \mathbf{m} \times \mathbf{T}^\parallel$ .

**SOT driven current induced DW motion in presence of DMI** The study of current assisted DW depinning by P.J.J. Haazen et al [37] showed that the damping like component of the SOT is efficient in moving DWs if these DWs have a Néel component. If the DW has a Bloch structure, the magnetization in the DW is aligned with the field-like torque and the effective field from the damping-like torque is zero. In the case of Néel DW structure, since the magnetization is perpendicular to the field-like torque, the damping like torque can be very efficient in moving a DW, as seen in Figure 1.8.

However, in the case where two consecutive DWs are aligned along the same direction (up/down and down/up), they feel the same damping-like torque and the two Dws move opposite to each other: the domain expands. This points out the important role of DMI in the mechanism proposed by Thiaville and coworkers [8]. Since the interaction is promoting a chiral DW, the in-plane magnetizations inside two consecutive DWs are opposite to each other. Hereby, they feel opposite damping like fields and the two DWs move in the same direction.

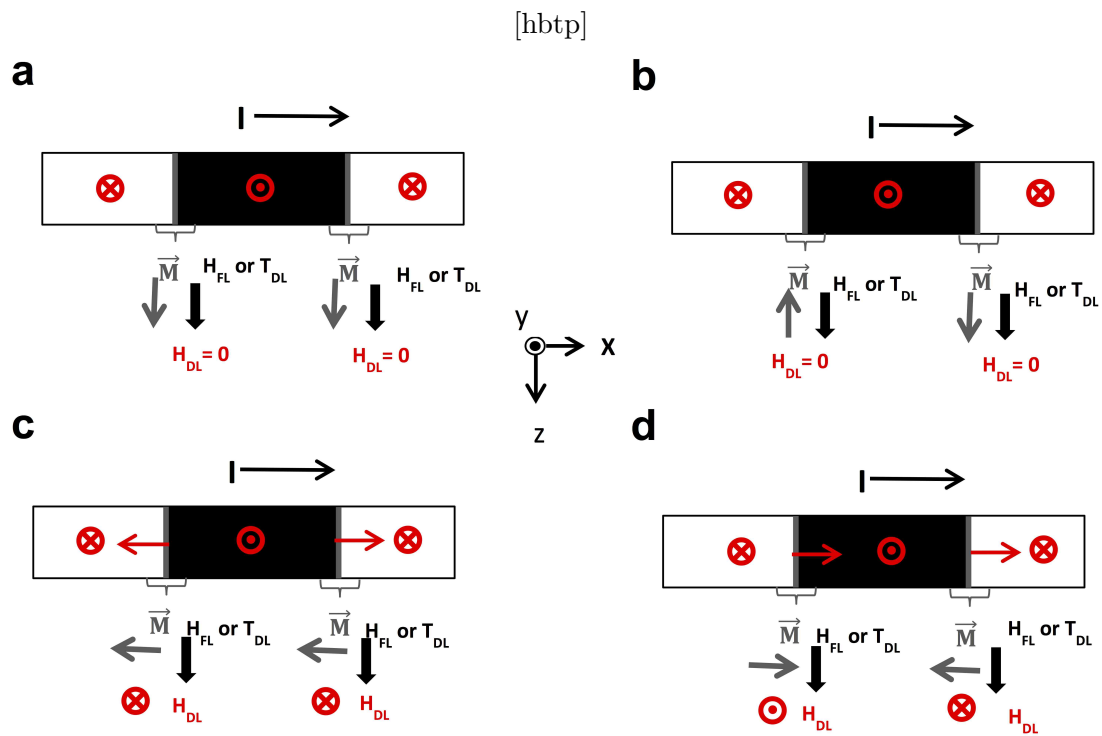


Figure 1.8: Schematic diagram of the action of SOT on different domain wall structures. The magnetization at the center of the domain wall is represented by a grey arrow. The direction of the DW motion is represented by the red arrows. **(a,b)** No DW motion. **(c)** Domain expands. **(d)** The two adjacent DW move along the same direction.

Moreover, the sign of the DMI defines the chirality of the DW as we have seen. Similarly, depending on the multilayer system, the damping-like torque can either be positive or negative. These two parameters give four possible combinations: two of them move the DW along the current direction (when  $D$  and  $T^{\parallel}$  are from opposite signs) while the other two move the DW against the current direction (when  $D$  and  $T^{\parallel}$  are from same signs) [27, 30, 6].

### 1.2.3.3 DMI estimation

The DMI amplitude can be experimentally estimated by a study of the DW dynamics. Je et al. [41] first introduced a method relying on DW dynamics with applied magnetic field. In this experiment, we consider a magnetic bubble in a thin film with an out-of-plane easy axis, as shown in Figure 1.9.

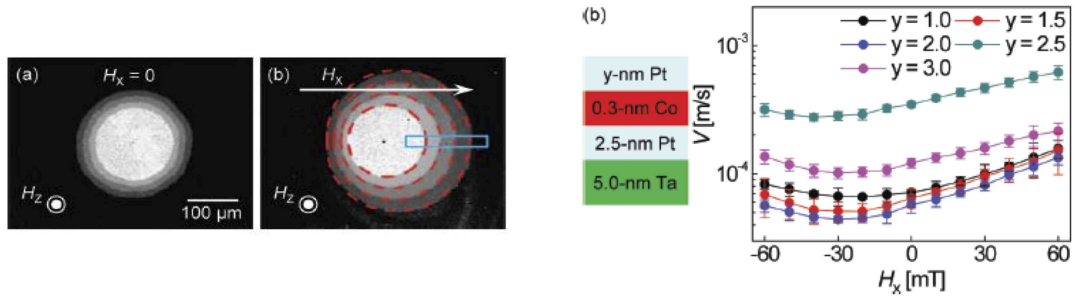


Figure 1.9: **(left)** (a) Expansion of a bubble domain in asymmetric Pt|Co|Pt trilayer, induced by an out-of-plane magnetic field  $H_z$ , observed by differential Kerr microscopy; (b) asymmetric expansion of the same domain in the presence of an in-plane magnetic field  $H_x$ . **(right)** velocity of a domain wall under the action of a  $H_z$  field in the presence of a positive or negative in-plane field. For around  $-30$  mT the  $H_x$  field compensates the DMI field [41].

Because of the chirality of the domain walls, a different behavior is expected to the up/down and down/up domains under in-plane field, a static in-plane field is applied. Velocities of up/down and down/up domains are compared when out-of-plane magnetic field pulses are applied to the system [41, 7, 42, 43]. The in-plane field, is breaking the symmetry and the effective field felt by the two different types of DW is hereby different. This effective field is composed of the static field and the effective DMI field (DMI acting as a chiral field in the plane of the sample). DW velocity increases when  $H_{eff}$  and  $m$  are parallel and decreases in the antiparallel situation. Hereby, the determination of the minimum speed lead to a quantitative estimation of the DMI amplitude. This approach has been used to estimate DMI amplitude in different systems such as Pt|Co|Pt [41], Pt|Co|Ir [7] and Pt|Co|GdOx [43] samples.

We have seen in this first chapter the micromagnetic energies involved in the samples

studied throughout this PhD work, and a first type of soliton, the domain walls, other candidate to next generation devices. As we will see in Chapter 2, skyrmions share a significant amount of properties with chiral Néel domain walls.

## Chapter 2

# Topological properties and dynamics of magnetic skyrmions

### Contents

---

|            |                                                                                      |           |
|------------|--------------------------------------------------------------------------------------|-----------|
| <b>2.1</b> | <b>Topological properties and skyrmion spin texture . . . . .</b>                    | <b>27</b> |
| 2.1.1      | Skyrmion spin texture . . . . .                                                      | 27        |
| 2.1.2      | Topological properties . . . . .                                                     | 28        |
| <b>2.2</b> | <b>Observation of skyrmions in magnetic materials . . . . .</b>                      | <b>31</b> |
| 2.2.1      | Skyrmions in non-centrosymmetric magnets . . . . .                                   | 32        |
| 2.2.2      | Skyrmions at interfaces . . . . .                                                    | 41        |
| <b>2.3</b> | <b>Topological phenomena related to skyrmions: Topological Hall Effect . . . . .</b> | <b>46</b> |
| <b>2.4</b> | <b>Dynamics of skyrmions . . . . .</b>                                               | <b>48</b> |
| <b>2.5</b> | <b>Conclusions and motivations . . . . .</b>                                         | <b>49</b> |

---

In this chapter, we will introduce the notion of magnetic skyrmions and make an overview of the state of the art on the subject at the beginning of my PhD.

## 2.1 Topological properties and skyrmion spin texture

### 2.1.1 Skyrmion spin texture

A magnetic skyrmion is the smallest possible perturbation to a uniform magnet: a point-like region of reversed magnetization, surrounded by a whirling twist of spins. Such skyrmions are quasiparticles - they do not exist in the absence of a magnetic state - and they give rise to emergent electrodynamics that cannot be simply described by Maxwell's equations. The particles are also attractive candidates for transporting information because they are only a few nanometers in size, very stable, and can be easily manipulated

with low-density spin-polarized currents. Although skyrmions are often described as particle like, a nearly two-decades old theory [44] makes detailed predictions for a skyrmion's size and shape. These properties determine the particle's response to a spin current and an external magnetic field, but are difficult to test because skyrmions are often only a few tens of atoms wide. Niklas Romming and colleagues at the University of Hamburg, Germany, have now imaged the internal structure of magnetic skyrmions in a metal film using a magnetically sensitive scanning tunneling microscopy technique [45]. The high spatial resolution of the technique allowed the researchers to confirm that both the size and shape of the skyrmions are consistent with theory.

The mathematical concept of the skyrmion was invented over fifty years ago by high-energy physicist Tony Skyrme [46]. In quantum field theory, particles are wavelike excitations with a finite lifetime. Skyrme proposed that the stability of hadrons (protons, neutrons, and mesons) could be explained if they were described as topological defects in a quantum vector field. These defects could be considered "protected" because they were characterized by a topological integer that cannot be changed through any continuous deformation of the field. Skyrme's idea for hadrons did not ultimately become part of the mainstream particle physics theory, but several examples of skyrmion-like topologies exist in condensed-matter systems [47]. The concept can, for example, describe quantum Hall systems, certain liquid-crystal phases, and Bose-Einstein condensates.

Skyrmions only form in magnets in which spin interactions favor a magnetic structure with chiral symmetry, such as a twist that is either left- or right-handed. Two decades ago, theorists predicted such twists could occur when spins felt a competition between aligning with their neighbors and being perpendicular to them [44]. In this picture, the strongest interaction between spins is Heisenberg exchange. The energy of this interaction, which favors the collinear alignment of neighboring spins and drives the ordering of many magnets, is given by the Heisenberg exchange integral  $J$ . A weaker interaction that favors perpendicular neighboring spins can occur in certain Heisenberg magnets in which electrons experience spin-orbit coupling. The energy of the Dzyloshinskii-Moriya Interaction (DMI) causes spins in a Heisenberg magnet to cant, leading in a natural way to a chiral structure (Figure 2.1).

### 2.1.2 Topological properties

Topological defects refer to field configurations or order parameter that are topologically distinct from vacuum in the sense that they cannot be smoothly connected to vacuum and are characterized by nontrivial value of topological invariant and properties that are stable against perturbations. In the context of magnetism, topological defects refer to configurations of magnetization vector field (in classical magnetism) or of spins (in quantum magnetism) that are topologically distinct from vacuum in the form of smooth configuration of magnetization or spins such as ferromagnetically ordered state. Ferromagnetic order is characterized by magnetization vector field uniformly polarized in parallel direction along certain orientations. Deformations away from this uniform

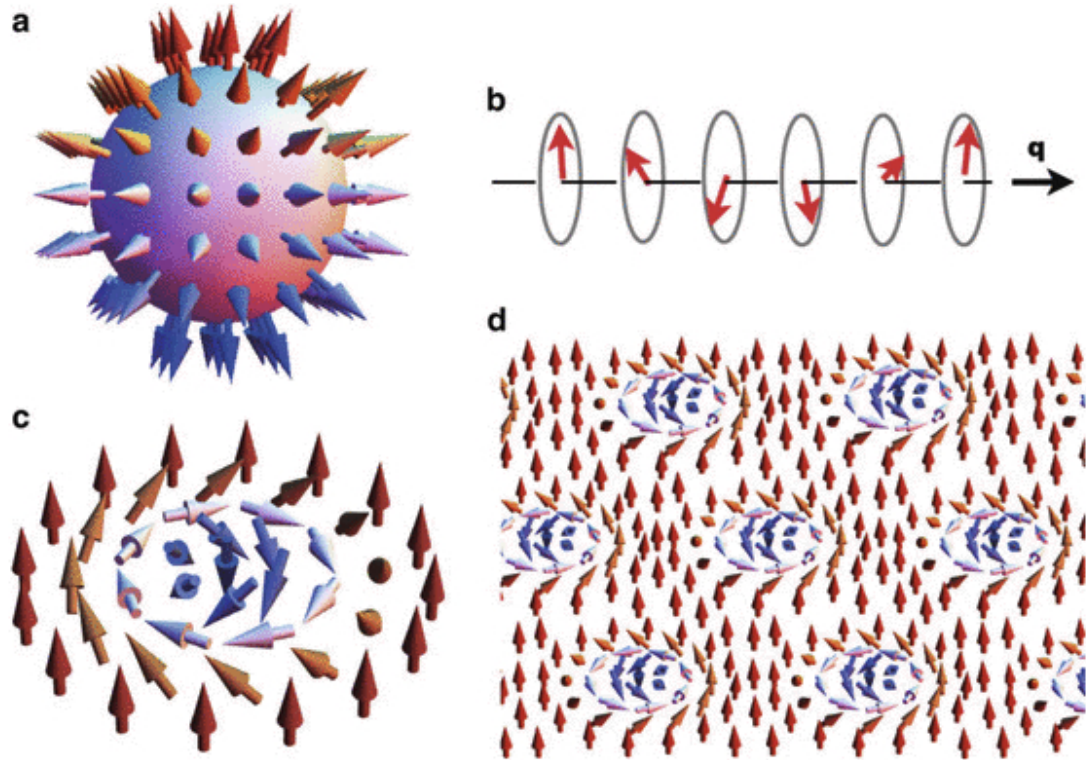


Figure 2.1: **(a)** Schematic of a hedgehog-type skyrmion, whose magnetization points in all direction wrapping a sphere. **(b)** Schematic of the helical state realized in chiral-lattice magnets as a consequence of the competition between the DMI and the exchange interaction. **(c)** Schematic of a skyrmion recently discovered in chiral-lattice magnets, which corresponds to a projection of the vortex-type skyrmion on a 2D plane. Its magnetization also points in all directions wrapping a sphere. **(d)** Schematic of the skyrmion crystal realized in chiral-lattice magnets under an external field in which skyrmions are hexagonally packed.

magnetization represent defects. Small deformations of magnetization vector fields in a ferromagnet lead to spin waves in configurations that are still smoothly connected to parallel magnetization configuration of a ferromagnet. There can however exist deformations, *i.e.* defects, which are not smooth and cannot be smoothly connected to the uniform magnetization of the ferromagnetic state. These deformations (defects) turn out to be also topological in character; *i.e.* they acquire nontrivial topological structure. These are topological defects in magnet. Topological defects are interesting both from pure scientific interest and potential practical applications. One of the most active subjects of research with regard to topological defects is their dynamics. Topological defects in magnet have been found to display nontrivial dynamics when subject to external driving forces such as applied magnetic field or spin-orbit torques. Topological defects normally involve variations of magnetization configuration. Oldest studies of topological defects in magnets started with the simplest of those structures; the domain wall. Straight domain walls and their dynamics were first studied by Walker and others [21]. We will focus on topological defects called skyrmions.

Topological defects in magnet have long been studied and classified based on the topological properties satisfied by the configuration of magnetization that makes up the defects [48]. In general, topology ensures the stability of the magnetization texture against weak perturbation once the structure is formed.

In the language of geometry, a magnetization pattern on  $2D$  plane is a mapping from  $\mathbb{R}^2 \rightarrow \mathbb{R}^3$ . At temperatures below Curie temperature however, the magnetization magnitude is fixed and therefore it is reduced to a  $\mathbb{R}^2 \rightarrow \mathbb{R}^2$  mapping. From physical considerations we know that any magnetization configuration has a (bounded) finite energy and the magnetization vector must take a fixed constant value at infinite distances. This is also the case with the skyrmion structure (above) where either  $\mathbf{m} = m\hat{\mathbf{z}}$  or  $\mathbf{m} = -m\hat{\mathbf{z}}$  at  $r \rightarrow \infty$ . Mathematically speaking, such vector configurations originally living in  $\mathbb{R}^2$  can be mapped to  $\mathbb{S}^2$ , the three-dimension sphere, where the fixed magnetization vector at infinite distances is stereo graphically projected to a point on the sphere, *e.g.* the north pole. If we consider an infinite  $2D$  (*e.g.*  $xy$ ) plane, it can also be mapped to a  $\mathbb{S}^2$  sphere with points at infinite distance on the plane mapped to the north pole of the sphere 2.1. Therefore, our magnetization structure including this skyrmion we are studying, can be classified as a mapping  $\mathbb{S}^2 \rightarrow \mathbb{S}^2$ .

Moreover, a skyrmion can be characterized by its topological charge:

$$q = \frac{1}{4\pi} \int \mathbf{m} \cdot (\partial_x \mathbf{m} \times \partial_y \mathbf{m}) dx dy, \quad (2.1)$$

with  $\mathbf{m} = \frac{M(\mathbf{r})}{|M(\mathbf{r})|}$  is the unit magnetization vector. A skyrmion has topological charge  $q = \pm 1$ . This topological invariant is protected by the topology and is stable against weak perturbations or disorder. This topological number is preserved during the motion of the skyrmion as long as there are no such processes as the creation or annihilation of the skyrmions or application of strong external field that can change the topological invariant.

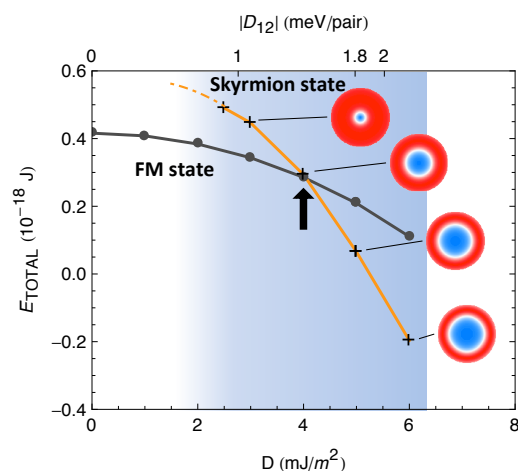
**Critical  $D$  value** We can define a skyrmion's domain wall by the region where the magnetization is in plane, meaning the region where  $m_z = 0$ . Then, the energy of this domain wall stabilized by DMI, typically in the order of few  $\text{mJ}/\text{m}^2$  can be calculated as followed:

$$\sigma = 4\sqrt{AK_{\text{eff}}} \pm \pi D. \quad (2.2)$$

In this equation, the first term is the same for a domain wall without DMI and the second term is just the integration of the DMI. It is interesting to note that DMI introduces chirality, of a sign fixed by  $D$ . For the most favorable chirality, it lowers the energy. The limit of this situation is when  $\sigma$  goes to zero. This defines the critical DMI energy constant [49]:

$$D_c = \frac{4\sqrt{AK_{\text{eff}}}}{\pi} \quad (2.3)$$

Figure 2.2: Evolution of the total energy with increasing DMI amplitude, for two different initial states: skyrmions and ferromagnet. The curves are crossing at a certain value of  $D$ , definition of the critical value for  $D$ :  $D_c$  [50].



Above it, the domain wall energy is negative so that the domain walls proliferate in the sample. As shown on Figure 2.2, below  $D_c$ , isolated magnetic skyrmions can exist in a ferromagnetic ground state, and above  $D_c$ , skyrmions lattices are the ground state.

## 2.2 Observation of skyrmions in magnetic materials

Experimentally, skyrmion spin textures are observed in various magnetic systems with distinctive characteristics. In this section, we introduce some typical environments that are favorable to skyrmionic spin textures:

- *Non-centrosymmetric ferromagnets.* These are systems with broken space-inversion symmetry, and thus, the DMI is active and serves as key source for stabilizing skyrmion spin texture.

- *Surface/interface* of ferromagnetic layers. As for the non-centrosymmetric ferromagnets, because of the broken space-inversion symmetry, skyrmions are stabilized by DMI.

### 2.2.1 Skyrmions in non-centrosymmetric magnets

We first introduce skyrmions in non-centrosymmetric ferromagnets [51, 44, 52]. In such environments with broken space-inversion symmetry, The DMI becomes active and stabilizes a modulated spin texture. In this class of materials, experimental observations of skyrmions reported here, have been made for chiral cubic ferro/ferrimagnets. In Figure 2.3, two material systems hosting skyrmion spin textures are indicated. One representative example is in a series of metallic or semiconducting materials called B20 alloys (such as MnSi,  $\text{Fe}_{1-x}\text{Co}_x\text{Si}$  [53, 54, 55, 56, 57], FeGe [58, 59, 60, 61] and  $\text{Mn}_{1-x}\text{Fe}_x\text{Ge}$  [62, 63], which have a common lattice form, as shown in Figure 2.3. They are usually characterized by an itinerant ferromagnetic exchange interaction. Another example is insulating  $\text{Cu}_2\text{OSeO}_3$  [64, 65, 66, 67]. This material contains two distinctive magnetic  $\text{Cu}^{2+}$  ( $S = 1/2$ ) sites, as shown in Figure 2.3, and shows a local ferrimagnetic spin arrangement between them. These two systems belong to the same chiral space group, indicating that the global symmetry is common between them. In both cases, their magnetic interactions consist of three hierarchical energy scales [68]: the strongest is the ferromagnetic or ferrimagnetic exchange interaction favoring a collinear spin arrangement, which is followed by the DMI giving rise to a long-period modulation of spin texture. Magnetic anisotropy is relatively weak as compared with the above two interactions but still plays an important role in determining the spin modulation direction. Because the two systems are characterized by similar magnetic phase diagrams shown in Figure 2.3, we focus initially on the case of B20 alloys.

Figure 2.3c shows the phase diagram for a bulk sample of MnSi in the temperature ( $T$ ) - magnetic field ( $\mathbf{B}$ ) plane [53]. Below the magnetic ordering temperature  $T_c \sim 29$  K without an applied magnetic field, a helical spin order characterized by a single magnetic modulation vector  $\mathbf{q}$  shown in Figure 2.3c is stabilized as a result of the competition between the ferromagnetic exchange interaction and DMI. The favorable  $\mathbf{q}$  direction is determined by magnetic anisotropy, and multiple equivalent helimagnetic  $\mathbf{q}$  domains coexist because of the original cubic lattice symmetry. The period of the helical spin modulation  $\lambda \sim 190$  Å is much larger than the crystallographic lattice constant  $a \sim 4.56$  Å, implying a rather weak coupling of magnetic and atomic structures. The application of a magnetic field leads to a single-domain helical spin state so as to satisfy the relation  $\mathbf{B} \parallel \mathbf{q}$  because anti-ferromagnetically aligned spins favor lying normal to an external  $\mathbf{B}$ . Here, a helical spin texture has a uniform magnetization component along an applied  $\mathbf{B}$  direction and thus can be considered to be conical. A further increase of the applied  $\mathbf{B}$  realizes a forced ferromagnetic state.

Another distinctive magnetic phase, the so-called "A phase", has also been identified in a narrow  $B - T$  region just below  $T_c$  with a moderate magnitude of  $B$ , which causes

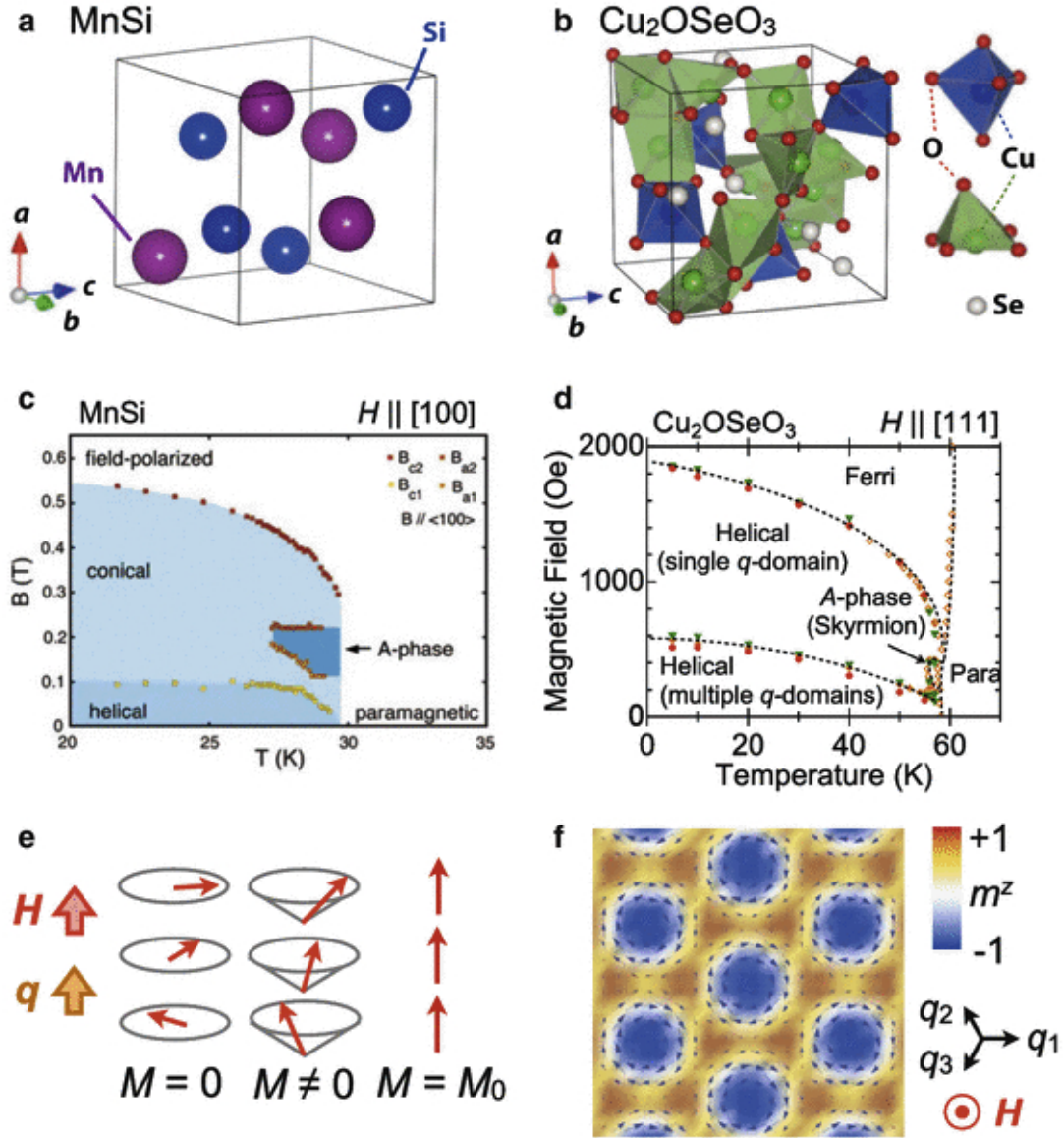


Figure 2.3: (a),(b), Crystalline structures of (a) MnSi and (b)  $\text{Cu}_2\text{OSeO}_3$ , both of which belong to the same cubic space group. (c),(d) Temperature versus magnetic field phase diagrams for the bulk samples of (c) MnSi and (d)  $\text{Cu}_2\text{OSeO}_3$ . Because of the isotropic nature of cubic lattice, similar magnetic phase diagrams can be obtained for any direction of  $\mathbf{B}$ . (e) Development of a helical spin texture characterized by a single magnetic modulation vector  $\mathbf{q}$  as a function of an applied magnetic field  $B$  for MnSi. (f) Schematic of a triangular lattice of skyrmions (*i.e.* skyrmion crystal) found for the above-mentioned materials, which is characterized by a triple magnetic modulation vectors  $\mathbf{q}_n$  ( $n = 1, 2, 3$ ) within a plane normal to the  $\mathbf{B}$  direction. Background color indicates the out-of-plane component of local magnetization  $m_z$ . Local magnetization at the core (edge) of each skyrmion is anti-parallel (parallel) to  $\mathbf{B}$  direction. [64]

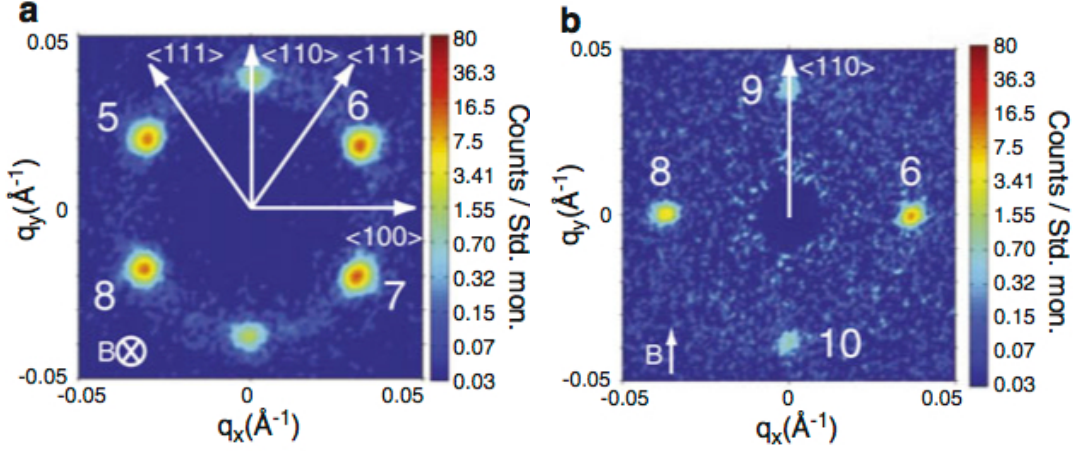


Figure 2.4: Results of small-angle neutron-scattering (SANS) measurements performed at the magnetic A phase of bulk MnSi under a magnetic field (a) normal and (b) parallel to an observation plane. The background color indicates the intensity of magnetic Bragg reflections at each point of reciprocal space[53].

anomalies in several macroscopic properties such as magnetic susceptibility, magnetoresistance [69], electronic spin resonance [70] and ultrasonic absorption [71]. While the spin texture in this A phase remained unresolved for several decades, Pfeleiderer and co-authors [53] revealed skyrmion lattice formation *via* small-angle neutron-scattering (SANS) experiments in 2009. In this method, an incident neutron beam was scattered by a sample and magnetic Bragg reflections within a reciprocal plane normal to the neutron-incident direction could be detected (see Figure 2.4). Figure 2.4 indicates the typical SANS data recorded for the magnetic A phase. Six-fold magnetic Bragg reflections always appear within a plane normal to  $\mathbf{B}$  irrespective of the  $\mathbf{B}$  direction. On the basis of these data, the spin texture  $\mathbf{m}(\mathbf{r})$  described by the summation of three magnetic helices:

$$\mathbf{m}(\mathbf{r}) \propto \mathbf{e}_z M + \sum_{a=1}^3 [\mathbf{e}_z \cos(\mathbf{q}_a \cdot \mathbf{r} + \theta_a) + \mathbf{e}_a \sin(\mathbf{q}_a \cdot \mathbf{r} + \theta_a)] \quad (2.4)$$

was proposed.  $\mathbf{q}_a$  denotes one of the three magnetic modulation vectors normal to  $\mathbf{B}$ , which forms an angle of 120 deg with respect to one another.  $\mathbf{e}_z$  is a unit vector parallel to  $\mathbf{B}$ , and  $\mathbf{e}_a$  is a unit vector orthogonal to both  $\mathbf{e}_z$  and  $\mathbf{q}_a$ , defined such that all  $\mathbf{q}_a \cdot (\mathbf{e}_z \times \mathbf{e}_a)$  have the same sign.  $M$  scales with the relative magnitude of net magnetization along the  $\mathbf{B}$  direction. When the phase shift of each of the magnetic helices  $\theta_a$  takes some specific value, the spin texture of Equation (2.4) can be considered to be a triangular lattice of skyrmions, i.e. the skyrmion crystal (SkX) shown in Figure 2.3. Combined with an additional theoretical calculation of free energy as well as the observation of the topological Hall effect [72], the formation of such a skyrmion crystal has been established for the A phase of bulk MnSi. Note that theories also predict that

thermal fluctuation is essential to stabilize the skyrmion crystal state over a helical spin state in a chiral cubic ferromagnet, which explains why a skyrmion crystal appears only in a limited temperature range just below  $T_c$ .

This breakthrough finding in the bulk sample was further followed by a real-space observation of a skyrmion crystal in thin-plate-shaped samples [73]. For this purpose, the Lorentz transmission electron microscopy (LTEM) technique is employed. When an electron beam passes through a magnetic material, each electron slightly changes its propagation direction as it experiences Lorentz force from local magnetization in the sample. As a result, by taking over- and under-focused images and performing some additional numerical analysis, it is possible to obtain the real-space distribution of in-plane components of local magnetization. Figure 2.5 indicates the LTEM data taken for a  $\text{Fe}_{1-x}\text{Co}_x\text{Si}$  ( $x = 0, 5$ ) single crystal with a thickness of several tens of nanometres [59]. Here, the thin-plate-shaped sample is prepared by thinning a bulk single crystal to obtain an observable amount of electron transmission, and a magnetic field is applied normal to the sample plane. Real-space images of lateral magnetization distributions in helical ( $B = 0$ ) and skyrmion crystal ( $B = 50$  mT) states are shown in Figure 2.5. Consistent with the previous SANS data and the proposed spin texture shown in Figure 2.3, skyrmions form a triangular lattice. Here, the spin helicity, i.e. the clockwise or counter-clockwise manner of spin rotation, is fixed by the chirality of an underlying crystal via the sign of the DMI in both magnetic states.

When the spin helicity changes sign, grey-scale contrasts in over- and under-focused images are reversed, as shown in Figure 2.6. Figure 2.6 indicates lateral magnetization distributions as well as under-focused LTEM images obtained around the boundary between two opposite chiral crystallographic domains in FeGe. The spin helicity or the grey-scale contrast in under-focused images of skyrmions is clearly reversed for the opposite chiral crystallographic domain, which experimentally confirms the coupling between spin helicity and crystallographic chirality. The LTEM technique can also capture formation and annihilation processes of skyrmions, as shown in Figure 2.5. At the phase boundary between ferromagnetic and skyrmion crystal states, a magnetic skyrmion can exist as an independent defect rather than a crystallized form, as shown in Figure 2.5. Figure 2.5 summarizes the  $B$ - $T$  phase diagram for the thin-plate-shaped single crystal of  $\text{Fe}_{1-x}\text{Co}_x\text{Si}$  ( $x = 0.5$ ). Here, the skyrmion crystal state is stabilized down to the lowest temperature, which is in sharp contrast with the case for the bulk crystal shown in Figure 2.3 where skyrmions appear only in a narrow temperature range just below  $T_c$ . This finding demonstrates that the stability of a skyrmion state essentially depends on the dimension or sample thickness of the system. Such a tendency is more clearly observed in the sample thickness  $t$  dependence of  $B$ - $T$  phase diagrams for FeGe, as shown in Figure 2.6. The skyrmion crystal state is stable in a relatively wide  $B$ - $T$  region for  $t \sim 15$  nm, whereas it gradually shrinks for larger  $t$  and finally turns into a narrow magnetic A phase in a bulk limit [74]. When a magnetic field is applied normal to the sample plane, the helical spin order with  $\mathbf{q} \parallel \mathbf{B}$  can no longer be stabilized given that the sample

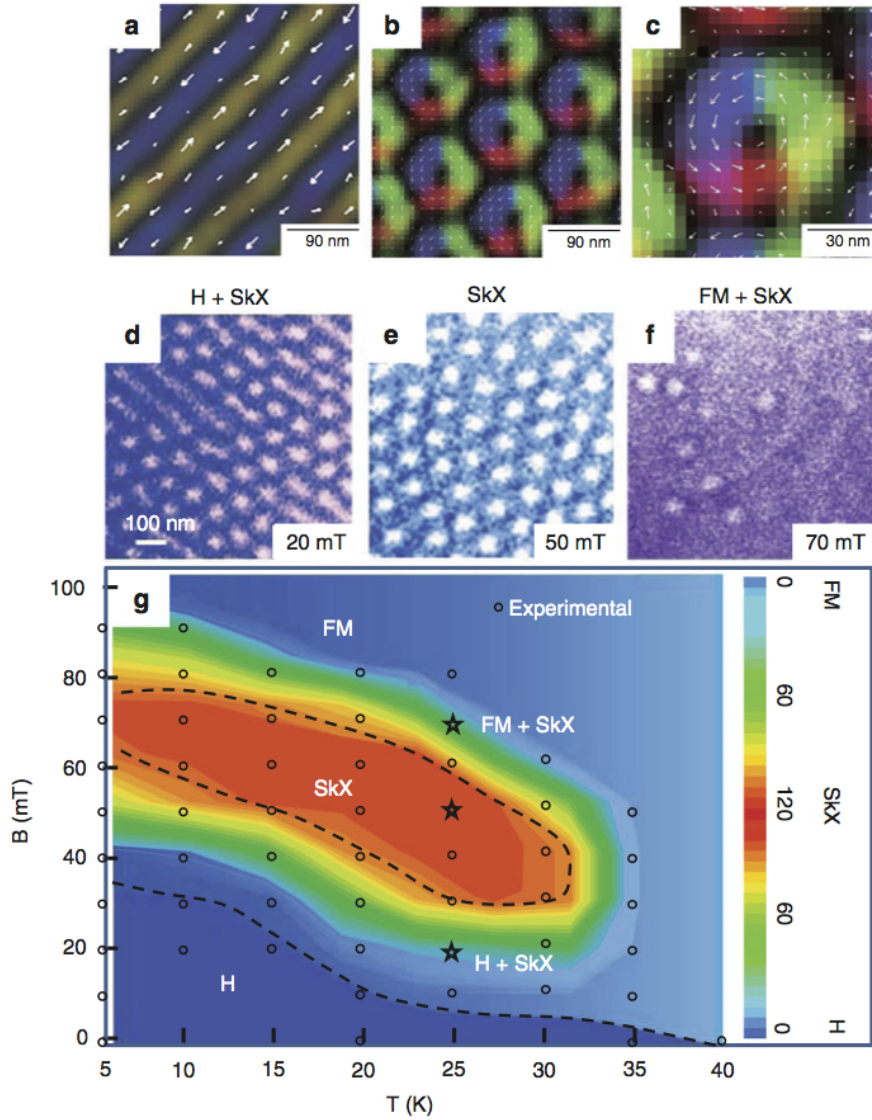


Figure 2.5: Lorentz transmission electron microscopy (LTEM) data for  $\text{Fe}_{0.5}\text{Co}_{0.5}\text{Si}$  with a thickness of several tens of nanometres. **(a)**–**(c)** Experimentally observed real-space images of lateral magnetization distributions obtained through the transport-of-intensity equation (TIE) analysis of LTEM data: **(a)** Helical spin structure with  $H = 0$ , **(b)** skyrmion crystal structure for  $H = 50$  mT applied normal to a thin plate and **(c)** a magnified view of **(b)**. The color map and white arrows represent magnetization direction at each point. **(d)**–**(f)** Magnetic field dependence of LTEM (overfocus) images. **(g)** Temperature versus magnetic field phase diagram, where H, SkX and FM denote helical, skyrmion crystal and ferromagnetic spin states, respectively. The color bar indicates skyrmion density per  $10^{12} \text{ m}^{-2}$ . [59]

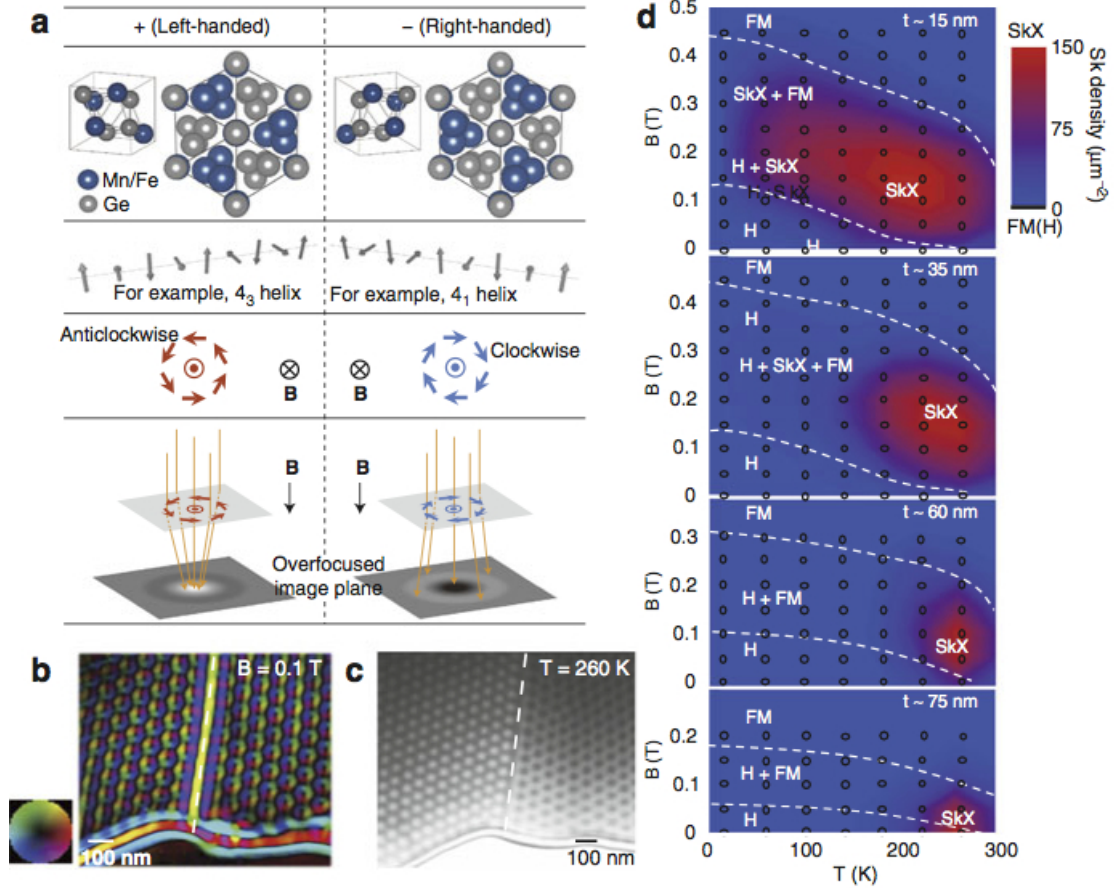


Figure 2.6: LTEM data for FeGe with a thickness of several tens of nanometres. (aa) Crystal structure, magnetic moment configurations of helical order, in-plane magnetic moment configuration of skyrmions when an external magnetic field  $B$  is applied downward and the corresponding over-focused LTEM images for left- and right-handed crystals. (b) In-plane magnetization distribution and (c) under-focused image of the skyrmion crystal state obtained by LTEM observation at the boundary of left- and right-handed crystallographic domains. (d) Sample thickness dependence of temperature versus magnetic field phase diagram, where H, SkX and FM denote helical, skyrmion crystal and ferromagnetic spin states, respectively. The background color indicates skyrmion density. (a) Ref [62], (b)-(d) Ref [74]

thickness is smaller than the helimagnetic modulation period. Such destabilization of the helical spin state leads to the relative stabilization of the competing skyrmion crystal state in the thin-plate-shaped sample; the possible relevance of additional uniaxial strain has also been proposed [75].

Similar magnetic phase diagrams and their sample thickness dependence are non-commonly observed for other  $B20$  alloys. Despite many differences in atomic arrangement,  $\text{Cu}_2\text{OSeO}_3$  can also be regarded as an insulating analogue of  $B20$  alloys by considering the similarity in the crystal symmetry and magnetic phase diagram characterized by a narrow A phase (skyrmion crystal state) just below  $T_c$  (Figure 2.3). This implies that chiral-lattice cubic ferro/ferrimagnets may ubiquitously host skyrmion spin texture regardless of their metallic or insulating nature. The list of materials showing a skyrmion spin texture is summarized in Table 2.1. Depending on the material, various magnetic transition temperatures (up to  $T_c \sim 280$  K for FeGe) and helimagnetic modulation periods (ranging from 3 nm (MnGe) to 200 nm ( $\text{Fe}_{1-x}\text{Co}_x\text{Si}$ )) have been reported. Note that theories predict that a skyrmion crystal can be stabilized down to  $T = 0$  in the case of uniaxial non-centrosymmetric ferromagnets and the emergence of magnetic skyrmions in non-centrosymmetric anti-ferromagnets has also been discussed [76]. Because various unique forms of magnetic skyrmions with different spin textures have been proposed for these systems [77], further searches for new materials and the establishment of a material design strategy are highly anticipated.

In addition to SANS for bulk samples and LTEM for thin-plate samples, the magnetic force microscopy (MFM) technique can be employed for the real-space imaging of spin textures at the surface of bulk magnetic materials with typical spatial resolutions of  $\sim 30$  nm [61]. Figure 2.7 indicates the real-space distribution of vertical magnetization components obtained by MFM measurement under various magnitudes of a magnetic field along the out-of-plane direction for  $\text{Fe}_{1-x}\text{Co}_x\text{Si}$  ( $x = 0.5$ ). The triangular lattice of skyrmions is observed at  $H = 20$  mT, and they gradually turn into a helical spin texture when  $B$  is reduced. In this process, two skyrmions appear to merge into a single elongated skyrmion. The corresponding Monte-Carlo simulation suggests that the original spin texture in the skyrmion crystal state is rod-like (i.e. almost uniform along the applied  $B$  direction), as shown in Figure 2.7, and the transition into the helical spin state is accompanied by the merging of two skyrmion lines. Because this causes a change of the topological winding number, hedgehog-like point defects with finite winding number ( $\pm 1$ ) will always appear at a merging point. Thus, the observed merger of skyrmions in MFM measurements implies that such defects pass through the sample surface. This topological point defect can be considered to be an emergent magnetic monopole or anti-monopole and will have profound effects on the dynamics of associated conduction electrons.

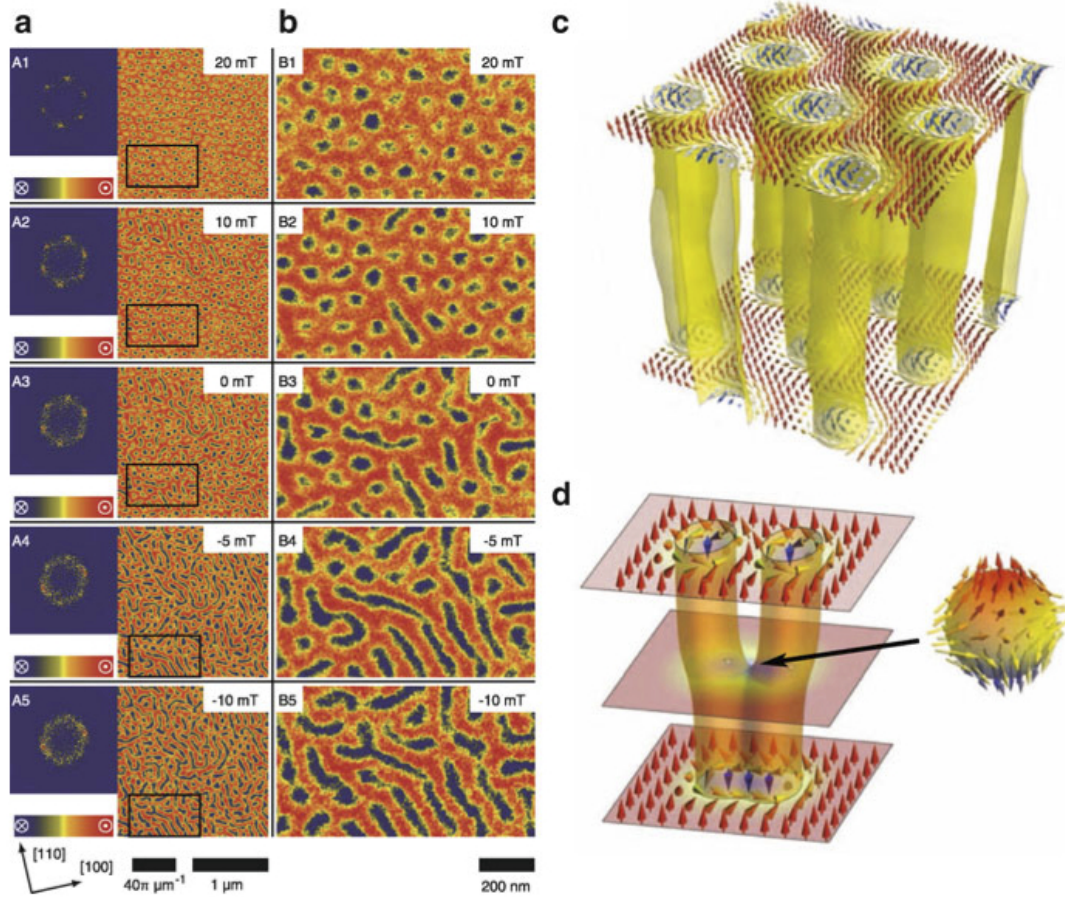


Figure 2.7: Typical magnetic force microscopy data at the surface of  $\text{Fe}_{1-x}\text{Co}_x\text{Si}$  ( $x = 0.5$ ). Blue (red) colors correspond to magnetization pointing parallel (anti-parallel) to the line of sight into (out of) the surface. (a) Data recorded as a function of a magnetic field after field cooling at 20 mT down to  $T = 10$  K. Panel (A1) displays data immediately after field cooling. After the initial cool down, the field is reduced at a fixed temperature of 10 K (A2–A5). During this process, skyrmions, visible as blue spots, merge and form elongated line-like structures. The left inset shows the Fourier transform of a real-space signal. Magnified images at corresponding field strengths are also shown in (b). (c) Typical spin configuration of a skyrmion lattice obtained by Monte Carlo simulation. (d) Sketch of a magnetic configuration describing the merging of two skyrmions. Magnetization vanishes at a singular merging point. This defect can be interpreted as an emergent magnetic anti-monopole, which acts similar to the slider of a zipper connecting two skyrmion lines[61].

| Category                    | Material                              | $T_c$ (K)          | $\lambda_m$ (nm) | Conductivity   | Reference    |
|-----------------------------|---------------------------------------|--------------------|------------------|----------------|--------------|
| Chiral-lattice ferromagnets | MnSi                                  | 30                 | 18               | Metal          | [53]-[57]    |
|                             | $\text{Fe}_{1-x}\text{Co}_x\text{Si}$ | $< 36$             | $40 \sim 230$    | Semiconductor  | [58]-[59]    |
|                             | MnGe                                  | 170                | 3                | Metal          | [78]         |
|                             | FeGe                                  | 278                | 70               | Metal          | [74]         |
| Interface                   | $\text{Cu}_2\text{OSeO}_3$            | 59                 | 62               | Insulator      | [64]-[67]    |
|                             | Fe/Ir (111)<br>FePd/Ir (111)          | $> 300$<br>$> 300$ | 1<br>7           | Metal<br>Metal | [79]<br>[80] |

Table 2.1: List of materials hosting skyrmion spin textures. Magnetic ordering temperature  $T_c$  and spin modulation period  $\lambda_m$  are also indicated.

## 2.2.2 Skyrmions at interfaces

### 2.2.2.1 Introduction

As said, one of the main objectives of the experiments lead in this thesis, is to observe skyrmions and be able to confirm that the magnetic spin textures observed are indeed skyrmions. Circular magnetic bubbles stabilized by the dipolar interaction are not revolutionary and have been studied since the years 1960s.

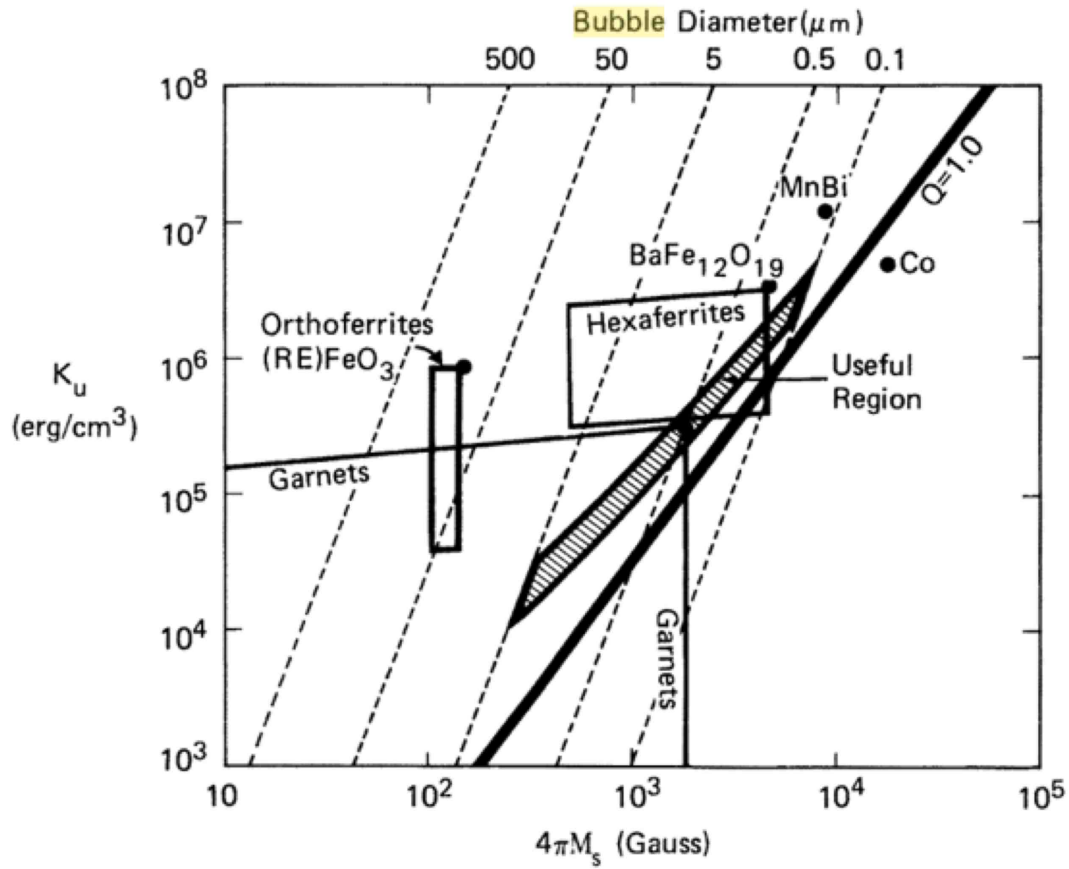


Figure 2.8: Phase diagram of magnetic bubbles diameter according to Magnetization at saturation and anisotropy energy.[81]

As seen on Figure 2.8, magnetic bubbles exist in different systems such as garnets or hexaferrites, but their diameter always exceed 500 nm.

Indeed, we can also refer to the work of Malozemoff and Slonczewski [82]. They have determined a phase diagram of magnetic bubbles stabilized by the dipolar interaction as seen in Figure 2.9.

In Figure 2.9, different phases of bubbles exist according to the field applied  $H$ , the magnetization at saturation  $M$ , the ratio between the thickness of the sample  $h$  and a

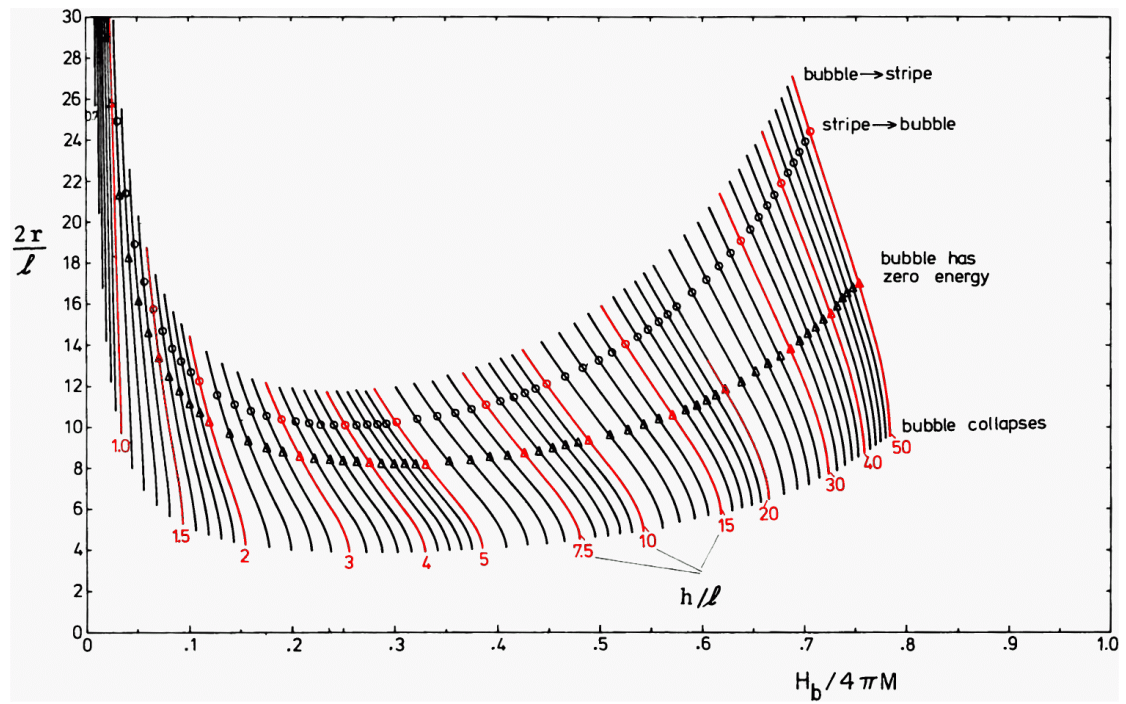


Figure 2.9: Phase diagram of magnetic bubbles stabilized by the dipolar interaction. with this graph it is possible, giving the experimental datas, to determine what kind of magnetic structure is stabilized by the dipolar interaction.

material length parameter  $l$ . We have also the possibility to determine the diameter of these bubbles according to the material length parameter  $l$ . We observe that, for every range of these parameters, the diameter of the existing bubbles are at least 4 times larger than the material length parameter  $l$ .

In this theory, they have defined a material length parameter:  $l_{\text{eff}} = \frac{\sigma_0}{4\pi M_s^2}$  where  $\sigma_0$  represents the energy of the domain wall. It is written as:  $\sigma_0 = 4\sqrt{AK_{\text{eff}}}$ , where the magnetization at saturation, effective anisotropy and  $A$  can be known by SQUID and AGFM measurements. For example, we can take typical values of  $A$ ,  $M_s$  and  $K_{\text{eff}}$  that are going to be used in the following chapters :  $A = 10$  pJ/m,  $M_s = 1.2$  MA/m and  $K_{\text{eff}} = 0.3$  MJ/m<sup>3</sup>. We then proceed to calculate the material length parameter and find  $l = 380$  nm, meaning that the smallest magnetic bubble stabilized by the dipolar interaction that can exist, has a diameter wider than  $1.5 \mu\text{m}$ .

### 2.2.2.2 Observation of skyrmions in multilayers system

As said in the introduction of this section, the Dzyaloshinskii–Moriya interaction emerging under the non-centrosymmetric environment can stabilize helimagnetism and skyrmion spin textures. This scenario is valid not only for ferromagnetic materials endowed with a non-centrosymmetric crystal lattice but also for interfaces or surfaces of ferromagnets where the spatial inversion symmetry is always broken. Here, we mainly discuss two material systems: (i) Fe monolayer on an Ir(111) surface [79] and (ii) a PdFe bilayer on an Ir(111) surface [80]. The Fe (PbFe) layer provides magnetic moments with a ferromagnetic exchange interaction whose thickness is just one (two) atomic units. The large nuclear number of the underlying Ir leads to a strong spin–orbit coupling and thus can serve as a source of significant DMI. Because magnitudes of relevant magnetic interactions are different between cases (i) and (ii), each system shows distinctive properties in the resultant spin texture and its development under an external field.

To investigate the detail of the spin texture at the surface of a magnetic mono/bilayer with atomic-scale spatial resolution, the spin-polarised scanning tunneling microscopy (SP-STM) technique has been employed. The ferromagnetic tip used for this measurement is magnetized along some specific direction in advance, and spin-polarised tunnel current scales as the cosine of the angle between the tip and local sample magnetization. As a result, this method enables the detection of a local magnetization component parallel to the tip magnetization direction. The pioneering work by Wiesendanger et al. for a Mn monolayer on a W(110) surface revealed the emergence of a helical spin texture of fixed spin helicity with the period of 12 nm, confirming the importance of the DMI at the surface or interface [83]. They further discovered the formation of a square lattice of skyrmions (with skyrmion number +1) for the Fe/Ir(111) system (Figure 2.10) by taking SP-STM images with various directions of tip magnetization and comparing them with simulated patterns [79]. This unique skyrmion spin texture appears even without the application of an external magnetic field and is characterized by two orthogonal magnetic modulation vectors within a film plane. The typical size of an individual magnetic

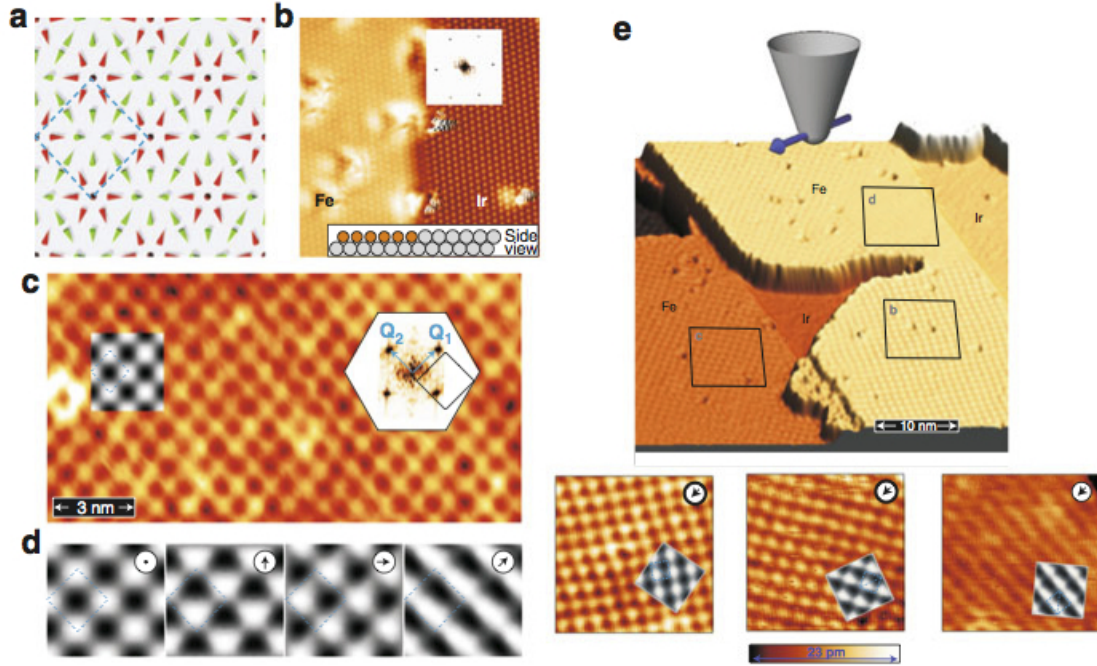


Figure 2.10: Skyrmion lattice observed by a spin-polarised scanning tunneling microscopy (SP-STM) measurement for the Fe monolayer on Ir(111). (a) Sketch of the nanoskyrmion lattice: cones represent atoms of a hexagonal Fe layer and point along their magnetization directions; red and green represent up and down magnetization components, respectively. (b) Atomic-resolution STM images of a pseudomorphic hexagonal Fe layer at an Ir step edge. Upper inset: The Fourier-transformed image. Lower inset: A side view of the system. (c) and (e) SP-STM images obtained with a tip magnetized along the (c) out-of-plane and (e) in-plane directions, respectively. Bright (dark) spots indicate areas with magnetization parallel (anti-parallel) to tip magnetization. In the latter case, images corresponding to three 120 deg rotational domains are obtained for different square regions shown in the upper panel. The tip magnetization direction is indicated by arrows. In (c), the Fourier transformation of the experimental SP-STM image is also indicated. (d) Simulations of SP-STM images of a skyrmion lattice with the tip magnetized in different directions as indicated. Here, the image size and unit-cell position are identical to those in (a). Simulated patterns are also overlaid on experimentally obtained images in (c) and (e), which agree well with each other. [79]

skyrmion is as small as  $\sim 1$  nm, with a magnetic modulation period incommensurate with the underlying crystalline lattice. The following theoretical analysis suggests that the Dzyaloshinskii-Moriya interaction play crucial roles in the stabilization of the observed skyrmion lattice as well as the short-range four-spin interaction.

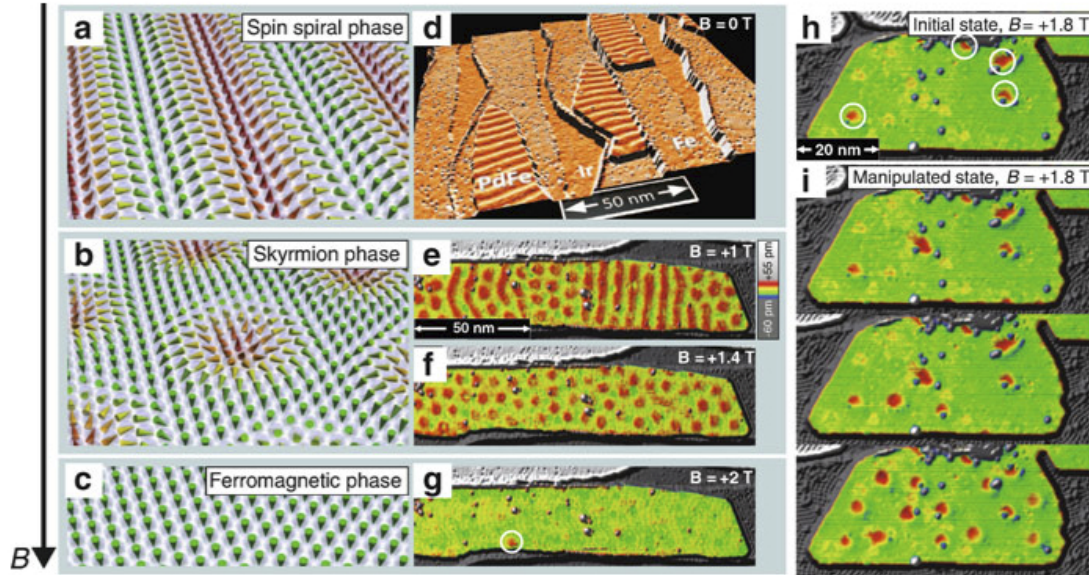


Figure 2.11: Magnetic field dependence of a PdFe bilayer on the Ir(111) surface at 8 K. (a)–(c) Perspective sketches of magnetic phases. (d) Overview image obtained by SP-STM, perspective view of constant-current image colorized with its derivative. (e)–(g) Distribution of the out- of-plane component of magnetization for a PdFe bilayer at different magnetic fields along the out-of-plane direction. (e) Coexistence of spin spiral and skyrmion phases. (f) Pure skyrmion phase. (g) Ferromagnetic phase. A remaining skyrmion is marked by the white circle. In (h) and (i), the manipulation of magnetic states by a local current injection through a magnetic tip is demonstrated at 4.2 K. (h) SP-STM image of the initial state at  $B = +1.8$  T after sweeping the magnetic field down from +3 T. Four skyrmions are marked by circles. (i) Successive population of an island with skyrmions by injecting higher-energy electrons through local voltage sweeps. [80]

In contrast, the magnetic behavior for the PdFe/Ir(111) system is rather close to that for the film of chiral-lattice ferromagnets [80]. Without an external magnetic field, this system shows a helical spin order characterized by unidirectional spin modulation with a period of  $6 \sim 7$  nm (Figure 2.11). The application of  $H \sim 1.4$  T normal to the film leads to the formation of a hexagonal lattice of skyrmions whose lateral magnetization components are not vertical but rather radiative. A further increase of  $B$  ( $> 2$  T) stabilizes the uniform ferromagnetic state, while isolated skyrmion particles often survive through pinning at atomic defects. Notably, when  $B$  is tuned around the phase boundary between ferromagnetic and skyrmion spin states, the local injection of electrons through a ferro-

magnetic tip enables the reversible writing and deleting of single magnetic skyrmions. The probability of skyrmion formation after current injection strongly depends on the sign of applied electric current, suggesting that the spin-transfer torque provided by spin-polarised tunneling current affects the directionality of switching. The above procedures enable the local "writing" and "reading" of individual skyrmion particles of an extremely small size, i.e. less than 10 nm, which demonstrates the potential of magnetic skyrmions as an information carrier for high-density storage/logic devices.

### 2.3 Topological phenomena related to skyrmions: Topological Hall Effect

In metallic materials, non-collinear or non-coplanar spin textures such as skyrmions, helices or domain walls give rise to intriguing phenomena via coupling to conduction electrons. In this section, we introduce the emergent electromagnetic fields generated by a skyrmion spin texture acting on conduction electrons. These cause the topological Hall effect and the electric-current-driven motion of skyrmions with a significantly small threshold current density  $j_c$  of  $10^5 - 10^6$  A/m<sup>2</sup>, which is five or six orders of magnitude smaller than that of a ferromagnetic domain wall and a helical magnetic structure.

Conduction electron passing through a non-coplanar spin texture characterized by the non-zero spin chirality give rise to additional contribution to the Hall resistivity or conductivity. This phenomenon is called the topological Hall effect. To obtain the finite topological Hall resistivity due to a non-coplanar spin texture, (i) a crystallographic lattice with a non-trivial geometry (ii) a special topology of the spin texture characterised by a non-zero skyrmion number is required [60].

$\rho_{xy}$  can be decomposed into three contributions:

$$\rho_{xy} = \rho_{xy}^N + \rho_{xy}^A + \rho_{xy}^T \quad (2.5)$$

where  $\rho_{xy}^N$ ,  $\rho_{xy}^A$  and  $\rho_{xy}^T$  correspond to the normal Hall term proportional to the external field  $B$ , the anomalous Hall term proportional to the magnetization  $M$  and the topological Hall term proportional to the emergent magnetic field. Figure 2.12 indicates the contribution  $\rho_{xy}^T$  for MnSi[84, 85, 72].

Compared with  $\rho_{xy}^T \sim 0.004\mu\Omega\text{cm}$  for MnSi with a spin modulation period  $\lambda_m \sim 17$  nm [78], a 40-times- larger  $\rho_{xy}^T \sim 0.16\mu\Omega\text{cm}$  has been reported for MnGe with  $\lambda_m \sim 3$  nm (Figure 2.12c) [86].

For MnGe, the topological Hall effect is observed in a much wider H–T range than the case for other B20 compounds characterized by a narrow magnetic A phase with a triangular lattice of skyrmions (Figure 2.12d) [78]. Combined with a recent analysis by neutron-scattering experiments, the possible emergence of a unique cubic or square lattice of skyrmions has been proposed for MnGe (Figure 2.12d) [86].

Moreover, the B20-ordered Fe<sub>0.7</sub>Co<sub>0.3</sub>Si epilayers grown on Si(111) substrates display a giant topological Hall effect due to the combination of three favorable properties:

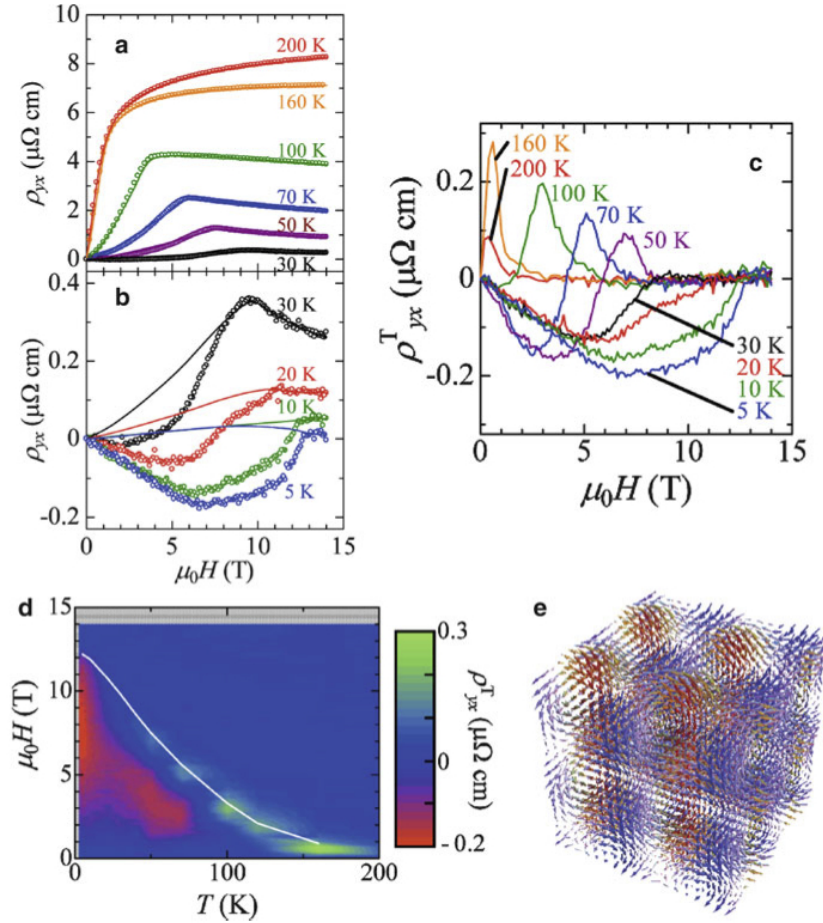


Figure 2.12: (a) Schematic of the topological Hall effect caused by skyrmion spin texture. (b) Hall resistivity for single-crystal MnSi, where a magnetic field is applied parallel to (110) and current is applied along (001). (c) Hall resistivity  $\rho_{xy}$  near  $T_c$  in the temperature and field range of the A phase. (d) Additional Hall contribution  $\rho_{xy}$  in the A phase. (e) Schematic of a cubic skyrmion lattice proposed as the magnetic ground state of MnGe.(a)-(d) Ref. [74], (e) Ref.[62]

they have a high spin-polarization, a large ordinary Hall coefficient, and a large emergent magnetic field. Furthermore, they show enhanced ordering temperatures due to the presence of epitaxial strain [87]. The topological Hall resistivity is as large as  $\sim 750 \text{ n}\Omega\text{cm}$  at helium temperatures [88], an order of magnitude larger than in MnSi [89] and roughly four times that found in MnGe [78].

Interestingly, the topological Hall effect originating from a scalar spin chirality has also been reported for several material systems without a long-range magnetic order, such as pyrochlore  $\text{Pr}_2\text{Ir}_2\text{O}_7$  with a “chiral spin liquid” state [90] and MnSi under high pressure [89]. In a high-pressure state, several anomalous transport properties such as non-Fermi liquid behaviour ( $\rho_{xx} \propto T^{\frac{3}{2}}$ ) [91] and the topological Hall effect have been reported [89].

## 2.4 Dynamics of skyrmions

The real advantage of skyrmions [47] compared with other magnetic nanostructures lies in their peculiar dynamics especially when combined with the conduction electrons or electrical polarization. Intensive interest has been triggered by the experimental discovery of current-driven skyrmion crystal motion by an ultralow current density of the order of  $10^6 \text{ A/m}^2$ , which is five or six orders of magnitude smaller than that needed for domain wall motion in ferromagnets. The current-driven motion of the skyrmion crystal in a thin film of FeGe has been studied by LTEM [92]. By comparing the motion of the helical and the skyrmion crystal phases, it was observed that a current density less than  $10^6 \text{ A/m}^2$  can drive the motion only in the latter case. This small critical current density enables the manipulation of information with low-power consumption per bit in the slow-speed regime. However, high-speed manipulation requires a similar current density than for domain wall motion.

Once the skyrmion moves, an emergent electric field is induced by the relation:

$$\nabla \times \mathbf{E} = -\frac{\partial \mathbf{B}}{\partial t} \quad (2.6)$$

or more explicitly  $\mathbf{E} = \mathbf{v}_d \times \mathbf{B}$  where  $\mathbf{v}_d$  is the drift velocity of the skyrmion crystal. As a function of the current density  $j$ ,  $\mathbf{v}_d$  vanishes below a critical value  $j_c$ , and begin to increase for  $j > j_c$ . Correspondingly, the induced emergent electric field  $\mathbf{E}$  gives a Hall effect in the opposite direction to the Topological Hall effect [93]. Therefore  $\Delta\rho_{xy}$  as a function of  $j$  shows a characteristic behavior, which is observed experimentally in MnSi [94].

Deriving the equation of motion of the center of mass of a skyrmion can be achieved by the method originally proposed by Thiele and its generalization [95, 5]. It results in the following Equation [96]:

$$M_s \frac{d\mathbf{v}_g}{dt} + \mathbf{G} \times (\mathbf{j} - \mathbf{v}_d) + \kappa (\alpha_g \mathbf{v}_d - \beta \mathbf{j}) = -\nabla U \quad (2.7)$$

where  $\mathbf{v}_g = \frac{d\mathbf{R}}{dt} = (\dot{X}, \dot{Y})$ , ( $\mathbf{R} = (X, Y)$  are the coordinates of the center of mass),  $M_s$  is the mass of the skyrmion,  $\kappa$  is a dimensionless constant of the order of unity, and  $\mathbf{G}$

the gyrovector.  $U$  is the potential for the skyrmion due to boundary effects, magnetic fields and impurities. The mass term in the equation comes from the deformation of the moving skyrmion compared with the static solution, and it can be neglected in the low-frequency limit. Then Equation (2.7) indicates a canonical conjugate relation between  $X$  and  $Y$ . The velocity is perpendicular to the force or along the equal potential contour, as in the case of a charge particle in a magnetic field.

The essential difference of motion between a skyrmion and a domain wall comes from the fact that the emergent field is finite for skyrmions, whereas it vanishes for a domain wall, and the tilting angle from the easy plane is the conjugate variable to  $X$ . Thereby, the pinning effect is enhanced compared with the case of skyrmion. Rosch et al. [98] introduced a phenomenological expression for the pinning force. Iwasaki et al. [97, 99] studied the current-driven motion of both the helical state and skyrmion crystal in a model with DM interaction taking into account the impurity pinning effect due to the easy-axis anisotropy. They observed a universal current-velocity relation for the skyrmion crystal in sharp contrast to the motion of the helical state that shows current-velocity relations similar to those of a magnetic domain wall [97, 99] (Figure 2.13). The reduced critical current density for the skyrmion crystal was attributed to the deformation of the crystal and of individual skyrmions to avoid the impurity potential [97, 100]. Skyrmion dynamics in constricted geometries are an important issue to consider for applications. An example is shown in Figure 2.13 where skyrmion motion in a finite-width geometry, and in the presence of a notch, has been simulated [5, 99, 50]. Sampaio et al. [50] also studied the stability and nucleation of skyrmion in nanodisks.

## 2.5 Conclusions and motivations

From the previous sections, we understand that at the beginning of this PhD work, skyrmions research was also at its beginning. Moreover, for applicative devices, it is necessary to manipulate skyrmions at room temperature. Hence, the first and main objective of this work was to be able to observe isolated magnetic skyrmions at room temperature. We have decided to work on multilayers systems meaning that the skyrmions ideally observed would be stabilized by DMI created by the broken symmetry at the interfaces between a ferromagnet and a heavy metal with large SOI. Also, working on multilayers would allow the possibility to vary a certain number of parameters such as materials or thicknesses. Moreover, it allows also the possibility to pattern the films and study the stabilization of skyrmions in confined structures (nanodisks, racetracks) and eventually in the motion of skyrmions in racetracks. It is also noteworthy to point out that by working on multilayers, we can increase the volume of the magnetic layers (by increasing the number of repetitions of the layers or increasing the thickness of the ferromagnet layer) and hereby increase the thermal stabilization, which is crucial for the observation of isolated skyrmions at room temperature. For the realization of multilayers, as seen in Figure 2.2, we should try to be in a region of  $D$  around  $D_c$  allowing the presence of isolated skyrmions stable or metastable in a ferromagnetic ground state.

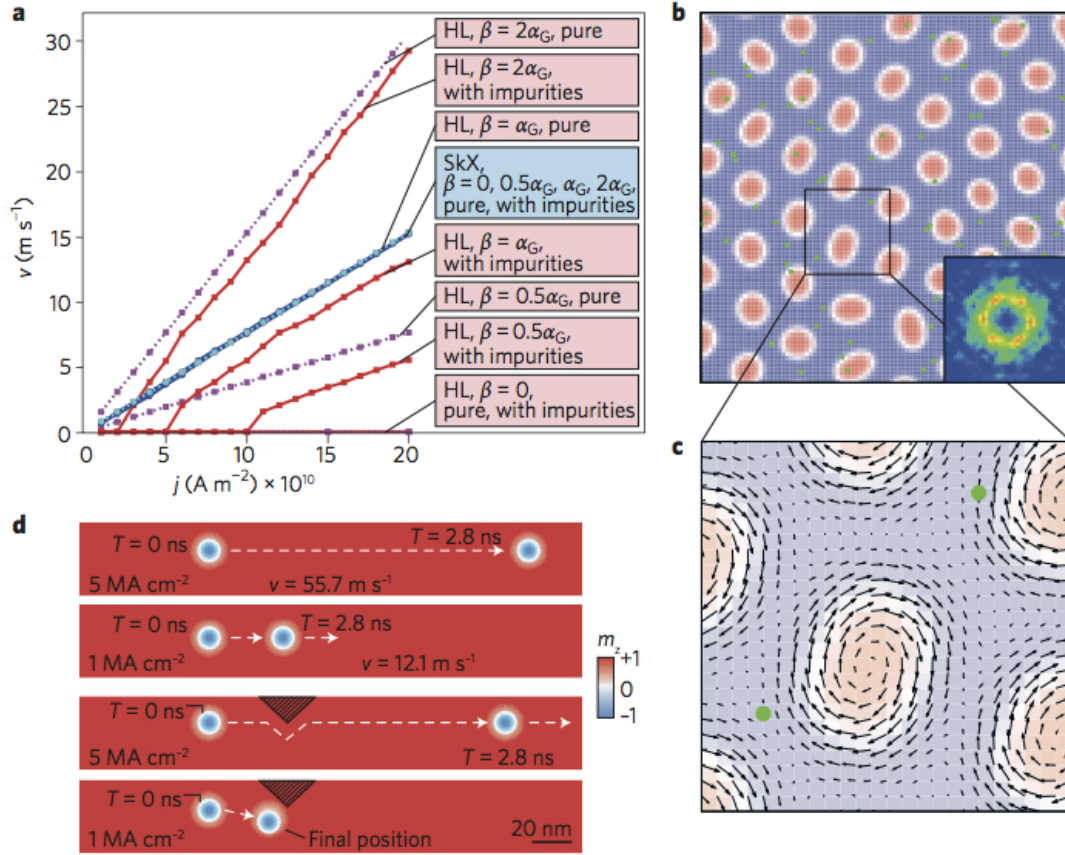


Figure 2.13: Simulations of the skyrmion motion driven by current. (a) Current–velocity relation for the helix structure (HL) and skyrmion crystal (SkX) calculated by solving the Landau–Lifshitz–Gilbert equation numerically. The  $j$ - $v$  characteristics for a skyrmion crystal (blue) are universal, and independent of  $\alpha_G$ ,  $\beta$  and the impurity pinning effect, while the  $j$ - $v$  characteristics for the helical phase are sensitive to these factors (red and pink). (b) Snapshot of the skyrmion crystal in motion and its Fourier transformation (inset). The green dots specify the position of impurities. (c) Zoom-in view showing the deformation of an individual skyrmion as well as of the skyrmion lattice at motion. (d), Motion of a skyrmion under the application of current in a stripe-shaped sample without (upper panels) and with (lower panels) a notch structure. (a)-(c) Ref.[97], (d) Ref.[5]

## Chapter 3

# Selection of materials and experimental techniques

### Contents

---

|            |                                                                          |           |
|------------|--------------------------------------------------------------------------|-----------|
| <b>3.1</b> | <b>Materials and growth methods</b>                                      | <b>51</b> |
| 3.1.1      | Choice of materials                                                      | 52        |
| 3.1.2      | Magnetron sputtering deposition                                          | 55        |
| <b>3.2</b> | <b>Preparation and characterization and physical analysis techniques</b> | <b>56</b> |
| 3.2.1      | X-ray reflectivity: characterization of the interfaces                   | 56        |
| 3.2.2      | Magnetometry characterizations: AGFM and SQUID                           | 57        |
| 3.2.3      | Demagnetization                                                          | 60        |
| 3.2.4      | Electron Energy-Loss Spectroscopy (EELS)                                 | 61        |
| 3.2.5      | Lorentz Transmission Electron Microscopy (LTEM)                          | 62        |
| <b>3.3</b> | <b>Magnetic Imaging</b>                                                  | <b>64</b> |
| 3.3.1      | Synchrotron techniques                                                   | 64        |
| 3.3.2      | Laboratory technique: MFM                                                | 68        |

---

In this chapter, the experimental techniques used to fabricate and investigate the thin films used for this work are presented. Sputtering was used exclusively to fabricate the films and is presented first. A variety of investigative techniques were used, including magnetic characterization and x-ray reflectivity. For each experimental technique an introduction to the physical principle and the origin of the effect is presented first, followed by a discussion of the experimental methodology associated with the measurement itself.

### 3.1 Materials and growth methods

This work is focused on ultrathin asymmetric multilayers with perpendicular anisotropy, grown by sputtering. Different samples were grown to optimize different parameters: perpendicular anisotropy, roughness of the interface or magnetization at remanence. The

first and most important goal was to optimize the parameters in order to be able to observe isolated skyrmions at room temperature (Chapter 4). Then, these observations enable us to estimate the DMI amplitudes (Chapter 5). Finally, by changing some parameters, we show that we can tune DMI amplitudes and skyrmions' behavior (Chapter 6).

### 3.1.1 Choice of materials

#### 3.1.1.1 Introduction

The interface contributes energetically, whereby there is an energy contribution associated with the surface anisotropy constant. As the ferromagnetic film thickness is reduced, the surface contribution can be so strong that the energy cost due to the demagnetisation field associated with out-of-plane magnetisation can be overcome [101]. This has found applications in the latest generation of magnetic hard-disk drives, since perpendicularly magnetised domains have better scalability, allowing much higher storage densities than their longitudinal counterparts. Another main advantage is that the perpendicular orientation improves the write field geometry so higher field can be created to switch smaller bits with high stability.

The interface has a structure that defines the transition between adjacent layers of the multilayer. It has been shown that the physical structure of the interface is crucial for the spin-mixing conductivity and the efficiency of the spin-orbit torques [102]. Furthermore, experiments where the interface has been systematically modified using focused ion beam irradiation have shown it is possible to modify the magnetic damping [103] and also perpendicular magnetic anisotropy [104].

Alongside the physical structure, the way in which the magnetism changes at an interface can also be important, particularly when a ferromagnet is interfaced with a late transition metal such as Pt or Ir. In these circumstances the ferromagnetism extends past the physical interface and into the non-magnetic layer [105, 106]. This spontaneous polarisation of paramagnetic metals is known as proximity induced magnetism (PIM) and occurs due to the hybridisation of atomic orbitals at the interface. Since the spin-orbit interaction scales with atomic weight, the PIM in Pt and Ir results in a magnetic region with a significant SOI at the interface.

#### 3.1.1.2 *ab initio* predictions

In order to obtain higher information storage density for application, it is critical to reduce skyrmion radius, which requires strong effective DMI. Furthermore, the velocity of domain wall motion is also known to be strongly dependent on DMI. We have considered some *ab initio* calculations to help us understand how, in theory, it is possible to strengthen DMI in multilayers. Even though *ab initio* calculations consider very theoretical and perfect interfaces, whereas, from an experimental point of view, this is hardly realistic, we believe that these predictions are giving very good guidelines.

First, we will see that the DMI can be magnified via multilayer stacking of ferromagnetic (FM) and non-magnetic heavy metals (HM). The key ingredient for DMI enhancement is to choose FM and HM material combinations processing the required DMI chiralities for additive effects at successive FM/HM interfaces.

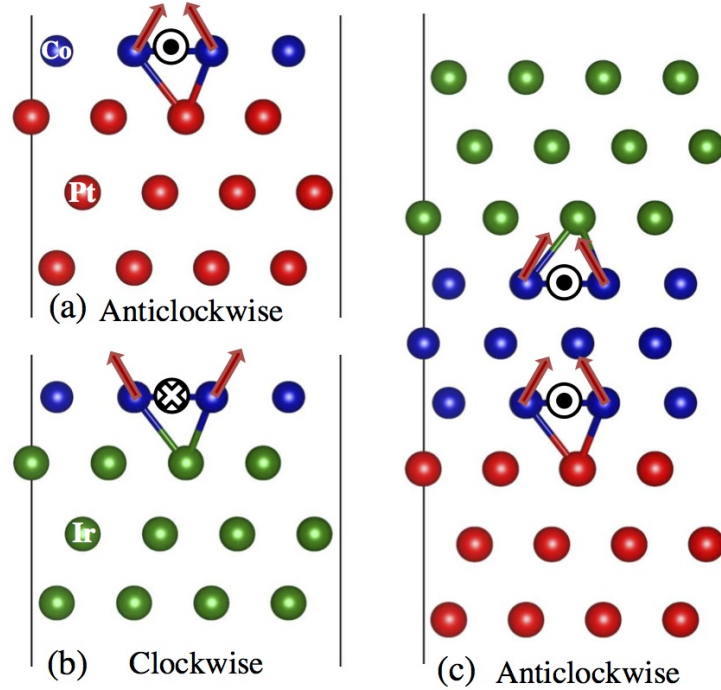


Figure 3.1: (a) Schematic structures with anticlockwise DMI in Pt|Co bilayers, (b) clockwise DMI in Ir|Co bilayers and (c) enhanced DMI in Pt|Co|Ir trilayers.[107]

Our approach is thus to consider asymmetric trilayers such as Pt|Co|Ir trilayers, where the DMI at both Pt|Co and Co|Ir interfaces add up due to the opposite sign of the DMI, as predicted by *ab initio* calculations [108, 109, 110, 111] (see Figure 3.1), resulting in an overall enhanced anticlockwise DMI. In order to design metallic trilayers with efficiently enhanced DMI, DMI was systematically investigated in FM/HM bilayers by *ab initio* calculations. The calculated results are summarized in Figure 3.2 (upper panel). We can notice that DMI chirality is anticlockwise for Pt|Co bilayers while for Co on Au, Ir, Pb and Al substrates, DMI shows a clockwise chirality. We also note that the DMI magnitude is much larger for Fe on top of Ir compared to the Co on Ir case.

Moreover, interfaces of opposite DMI chiralities with reverse stacking of the second interface so that both interfaces in the resulting Pt|Co|Ir structure possess anticlockwise chirality were combined. As summarized in the bottom panel of Figure 3.2, the resulting

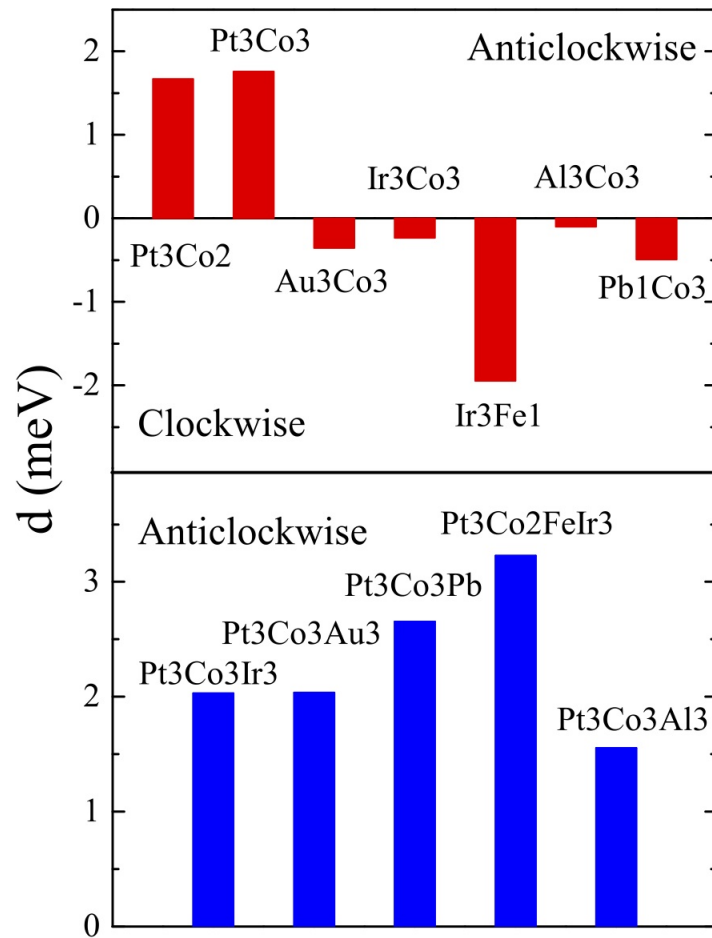


Figure 3.2: Calculated microscopic DMI,  $d$ , for bilayer structures (**upper panel**), and trilayers (**lower panel**).<sup>[107]</sup>

DMI strength is approximately equal (even higher) to the sum of the DMI amplitudes of two interfaces.

### 3.1.1.3 Fe-based samples and Co-based samples

At the beginning of my Ph.D, we have tried to grow different samples with different ferromagnets in order to have multilayers with out-of-plane anisotropy. We have grown Co-based samples and Fe-based samples in parallel. Nonetheless, despite multiples attempts we have never succeeded in growing Fe-based multilayers with large enough out-of-plane anisotropy. Indeed, several parameters were changed: the technique of deposition (be it by sputtering or evaporation), the thickness of iron deposited (4, 6, 8, and 10 Å were tried), the heavy metals layers beneath and above the iron (platinum, iridium, tungsten, with different thicknesses), the pressure of deposition when considering sputtering, and finally we have also tried annealing the grown samples. In parallel, we have succeeded in growing Co-based samples and have therefore decided to concentrate our efforts our Co-based samples.

## 3.1.2 Magnetron sputtering deposition

### 3.1.2.1 Description

Magnetron sputtering is a thin film deposition technique. It consists of the ejection of atoms from a target by bombardment of energetic particles. The atoms ejected form a plasma and will condense on a substrate facing the target.

### 3.1.2.2 Principle

More specifically, a potential difference is applied between the target and the substrate in a controlled gas atmosphere (Ar in our set-up). Ionic species will accelerate in the direction of the target, triggering collision cascades. The magnetic field created by the magnetron will impose an helicoidal trajectory to the electrons, leading to a higher collision rate. Following the electrical potential, the negative Argon ions will be accelerated towards the target(cathode).

If the incoming energy of the accelerated particles is greater than the binding energy of the target material, neutral atoms will be sputtered. At the collision, the target also releases secondary electrons that will contribute to the ionization process of Ar atoms. A cold plasma (electrons, ions, neutral Ar and atoms of the target, photons) is formed between the substrate and the target. The species extracted from the target are neutral, they can freely recombine on the substrate surface.

Materials are usually deposited in DC mode, meaning that the voltage applied between the target and the substrate plate is constant in time. However it is possible to use an RF mode when the target is insulating. For example RF mode was used to grow W. The alternating electric field will prevent the target from charging. It is also possible to

invert the anode and cathode position: the gas ions in the plasma will then be accelerated towards the sample plate. In the proper conditions, that configuration can be used to clean or etch a sample/substrate surface.

## 3.2 Preparation and characterization and physical analysis techniques

### 3.2.1 X-ray reflectivity: characterization of the interfaces

#### 3.2.1.1 Principle

The XRR measurement technique described here is used to analyze X-ray reflection intensity curves from grazing incident X-ray beam to determine thin-film parameters including thickness, density, and surface or interface roughness.



Figure 3.3: Reflection and refraction of X-Rays on material surface.

In the case of X-rays, which are incident electromagnetic waves, the refractive index of a material is slightly less than 1. Therefore, the X-rays undergo total external reflection when incident on a flat surface of a material at a grazing angle is smaller than the critical angle for total reflection  $\theta_c$  (Figure 3.3). Thus X-ray reflectivity is related to the values of refractive index and X-ray wavelength. It should be noted that  $\text{Cu} - K_\alpha$  X-rays is used throughout the following measurements (wavelength of 0.15418 nm).

We can distinguish different cases when the incident angles are smaller, equal to, and greater than the critical angle for total reflection,  $\theta_c$ :

$\theta < \theta_c$  All the incident X-Rays are reflected

$\theta = \theta_c$  Incident X-Rays propagate along the sample surface

$\theta > \theta_c$  Incident X-Rays penetrate into the material refraction

#### 3.2.1.2 Information provided by an X-ray Reflectivity measurement: thickness and roughness

The observed scattering X-rays are the sum of individual electron scatterings. The intensity of X-ray reflectivity is calculated from each layer which is constructed from elemental species and filling rate of space. As shown in Figure 3.4, the reflectivity profile shows oscillations caused by this X-ray interference. These oscillations were first observed in 1931 by Kiessig and is called Kiessig fringes. The oscillations depend on the film thickness, and the thicker film, the shorter the period of the oscillations.

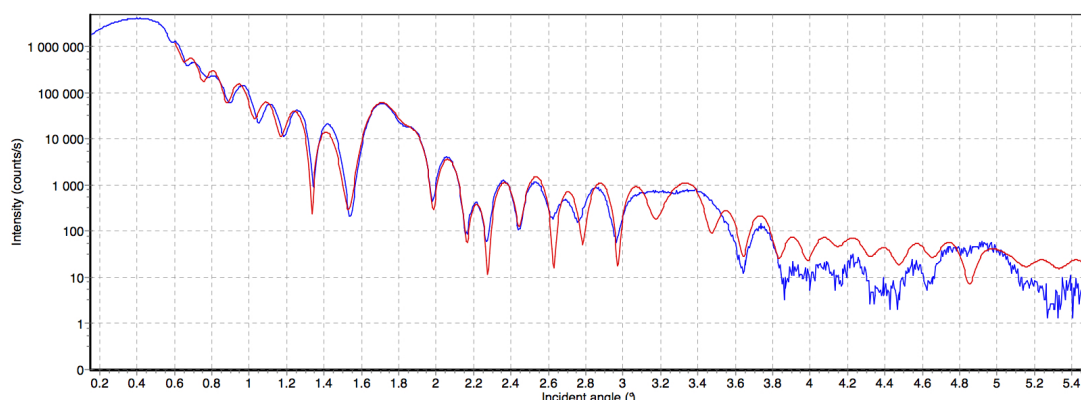


Figure 3.4: Reflectivity of Pt10|{Ir1|Co0.8|Pt1}5|Pt3. The blue line corresponds to the experimental data and the red line to the fitting curve.

The amplitude of the oscillations decrease with increasing interface roughness. The term “interface roughness” includes that physical uneven interface and transitional boundary layer which continually changes in density. Interface roughness is recognized to a continuous variation of electric density along the thickness direction.

Figure 3.5 shows the summary of the effect of film thickness, density, roughness of surface and interface on the X-ray reflectivity curve of a thin film deposited on a Si substrate. Therefore, the X-ray reflectivity technique is a method for determining the layer structure of a thin film multilayer.

## 3.2.2 Magnetometry characterizations: AGFM and SQUID

### 3.2.2.1 AGFM

A force technique to measure magnetization is the Alternative Gradient Force Magnetometer (AGFM). The principle of this method is to use the fact that the net translational force on a magnetic dipole depends on the gradient of the magnetic field, and then by varying this gradient in a controlled way to produce a time-varying force at the same frequency. This signal can then be measured with the advantages of noise and offset rejection that are possible by detecting only signals which occur at the known excitation frequency.

The AGFM, introduced by Flanders [112], is in many respects a variant of the Vibrating Sample Magnetometer (VSM). However, its sensitivity exceeds  $10^{-11}$  Am<sup>2</sup> for measurement of magnetic moment, and is therefore typically 1000 times more sensitive than a conventional VSM. The output of the AGFM is obtained by measuring the amplitude of the motion of the magnetic sample. The amplitude depends on the force experienced by the sample, and if the field gradient is known the magnetic moment can be calculated.

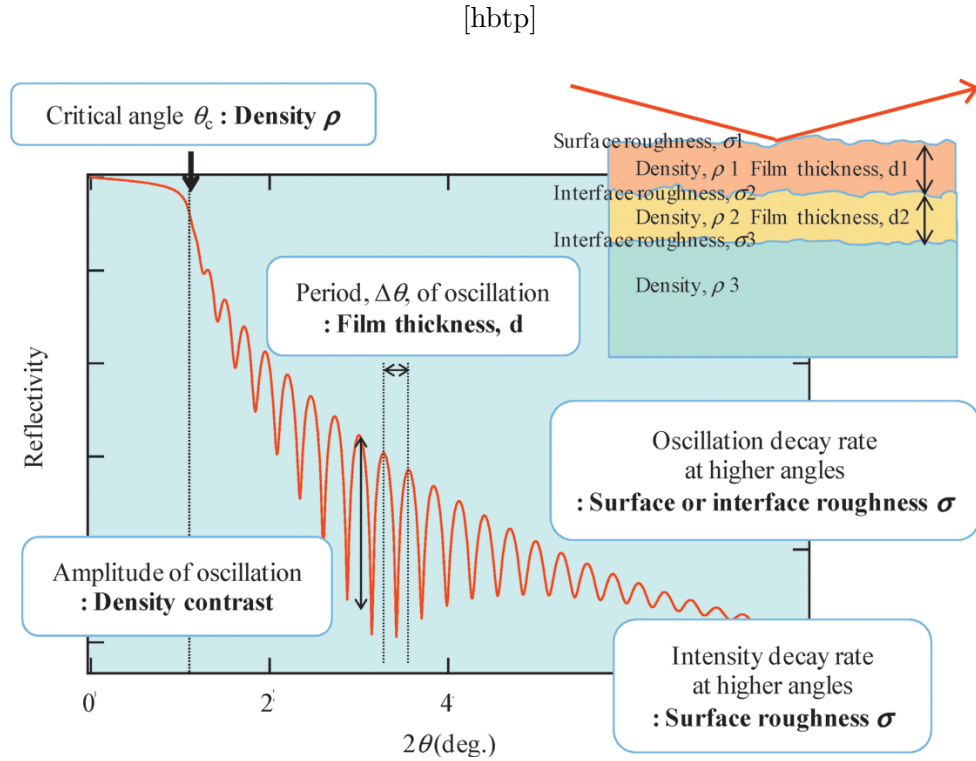


Figure 3.5: Information provided by X-ray reflectivity profile.

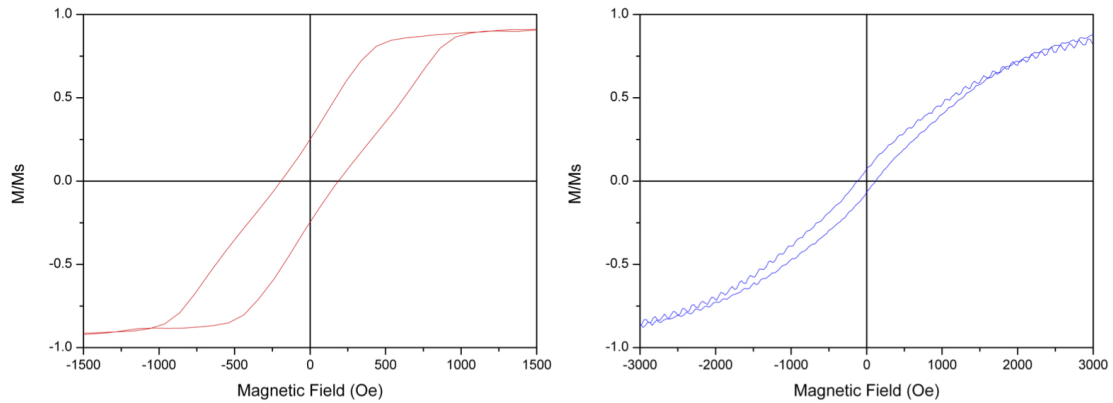


Figure 3.6: Typical profile of hysteretic loops obtained by AGFM. The red curves corresponds to the hysteresis loop obtained by applying out-of-plane field to the sample (**left**); the blue line corresponds to the hysteresis loop obtained by applying in plane field to the sample (**right**). The shape of the red curve indicates that the anisotropy is out of plane and here the remanence is around 25%.

In the present work, AGFM measurement have been performed on every sample. First, to measure both hysteresis loops with out-of-plane and in plane fields, and then to estimate the anisotropy field and energy (the anisotropy field corresponding to the saturation field). Thus, both loops are normalized to 1. Typical graph obtained by AGFM is shown in Figure 3.6.

### 3.2.2.2 SQUID

A Superconducting Quantum Interference Device (SQUID) is a magnetometer. It is used to measure extremely weak magnetic signals under a large range of magnetic fields and temperatures. We used a Quantum design SQUID with a 5.5 T magnet and a temperature ranging from 4 K to 400 K. A SQUID device consists of two Josephson junctions symmetrically disposed in parallel on a superconducting loop. The Josephson junction consists of two superconductors separated by a thin insulating layer. In a superconducting state, the electrons form Cooper pairs and condense in a unique collective quantum wave. As all electrons share the same quantum state, the pairs can tunnel through the insulating barrier by tunnel effect, and induce a spontaneous current through the barrier. In an entirely superconducting loop, only certain values of magnetic flux are allowed to pass through its center. The wave function of the electron condensate expands in the whole superconducting ring and thus imposes the continuity of the wave function's phase along the ring. When a magnetic flux passes through the superconducting loop, the phase is modified and must at all times fulfill the periodic boundary conditions. So only certain values of the field can fulfill the phase conditions, the flux is then quantized, with a flux quantum  $\phi_0 = 2.07 \cdot 10^{-15} \text{ Tm}^2$ . If the magnetic flux is smaller than  $\frac{\phi_0}{2}$ , a screening current will form to cancel the external magnetic flux. Now if the magnetic flux increases and exceeds half the flux quantum, the current in the loop will invert to help the flux reach  $\phi_0$ . The electric current is DC and its value is proportional to the sine of the phase difference between the two superconductors. The current is then also sensitive to the magnetic flux going through the loop as it tends to modify the phase difference at the junction interface. This effect is periodic, with a period  $\phi_0$ . The voltage of the SQUID device will also be periodic with progressive increase or decrease of the magnetic flux. This voltage is recorded and the number of periods indicates the overall magnetization of the measured sample.

We used the SQUID to characterize ultrathin magnetic films. Hence, only quarter cycle were registered (from zero field to 0.7 T), but obviously complete cycle can be registered as shown in Figure 3.7, showing also the possibility to record the evolution of the magnetization for different temperatures. Indeed, SQUID measurements have also been performed to characterize the evolution of the magnetization at saturation with temperature (see Chapter 4).

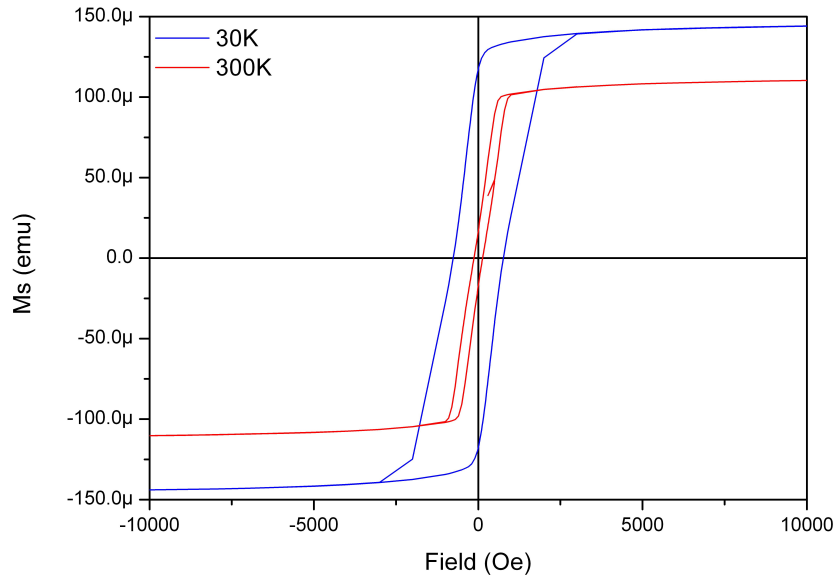


Figure 3.7: Typical profile obtained by SQUID measurement for a sample with out-of-plane anisotropy. Measurements for two different temperatures are reported here.

### 3.2.3 Demagnetization

Before trying to image the samples, in order to avoid the maximum of perturbations, we have decided to demagnetize them. Demagnetization may be carried out in several ways. Heating the specimen or component above the Curie point causes the substance to lose completely its ferromagnetic properties. Such heating followed by cooling in the absence of any external field results in the most complete demagnetization.

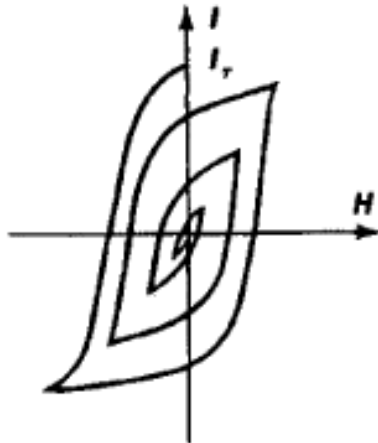


Figure 3.8: Curve of the demagnetization of a specimen with residual magnetization  $I_r$ , by an alternating field  $H$  that decreases to zero.

In most cases however, such as ours, this method of demagnetization cannot be used, since the heating may alter mechanical and other properties of the material. Another widely used technique for demagnetization, the one we used in the present work, called

AC demagnetization, consists in the alternating magnetization of the component or specimen by an alternating magnetic field whose amplitude decreases smoothly to zero (Figure 3.8).

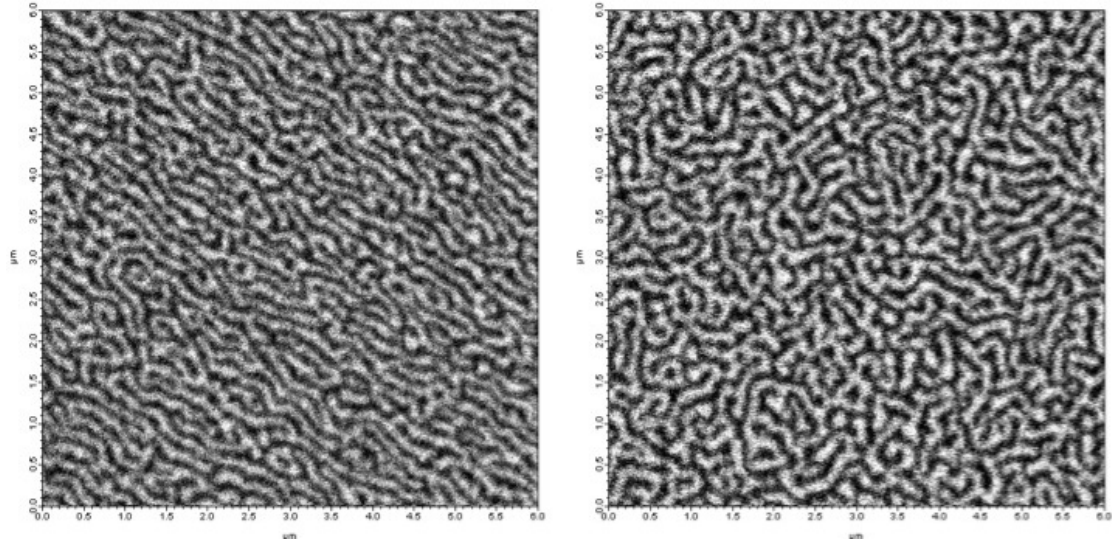


Figure 3.9:  $6 \times 6 \mu\text{m}^2$  images of magnetic domains of  $\text{Pt}_{10}\{\text{Ir}_1|\text{Co}_{0.6}|\text{Pt}_1\}_{20}|\text{Pt}_3$  after demagnetization with field parallel (**left**) or perpendicular (**right**) to the plane of the sample.

Here, two options are possible: we can use either an external field perpendicular or parallel to the plane of the sample. Since the magnetization of the sample is out-of-plane, it seems more natural to use a perpendicular field. Nonetheless, we have studied the influence of both demagnetization on our samples, as seen in Figure 3.9. Labyrinth-shaped domains are visible in both images. However, it seems that these domains follow a certain direction when the field is in plane. More precisely, the direction of the trend is guided by the direction of the field used to demagnetize the sample. As we are going to see in the next chapters, the mean domain width after demagnetization is going to be important to determine properties of our samples. Therefore it is quite important to check that, no matter the direction of the field used to demagnetize our samples, the mean domain width obtained in both cases is equal. Because this is the case, unless we want a special direction for the domains obtained after demagnetization, in the rest of this work, we are going to demagnetize samples with perpendicular field.

### 3.2.4 Electron Energy-Loss Spectroscopy (EELS)

Electron energy-loss spectroscopy (EELS) is an analytical technique that measures the change in kinetic energy of electrons after they have interacted with a specimen. When carried out in a modern transmission electron microscope, EELS is capable of giving

structural and chemical information about a solid, with a spatial resolution down to the atomic level in favorable cases. The energy resolution is typically 1eV but can approach 0.1eV if an electron-beam monochromator is used.

### 3.2.5 Lorentz Transmission Electron Microscopy (LTEM)

Electron moving through a region of space with an electrostatic field  $\mathbf{E}$  and a magnetic field  $\mathbf{B}$  experiences the Lorentz force  $\mathbf{F}_L$ :  $\mathbf{F}_L = -e(\mathbf{E} + \mathbf{v} \times \mathbf{B})$ .  $\mathbf{F}_L$  acts normal to the travel direction of the electron, a deflection will occur. Only the in-plane magnetic  $\mathbf{B}$  induction will contribute to the deflection. The deflection angle is linked to the in-plane magnetization and the thickness sample.

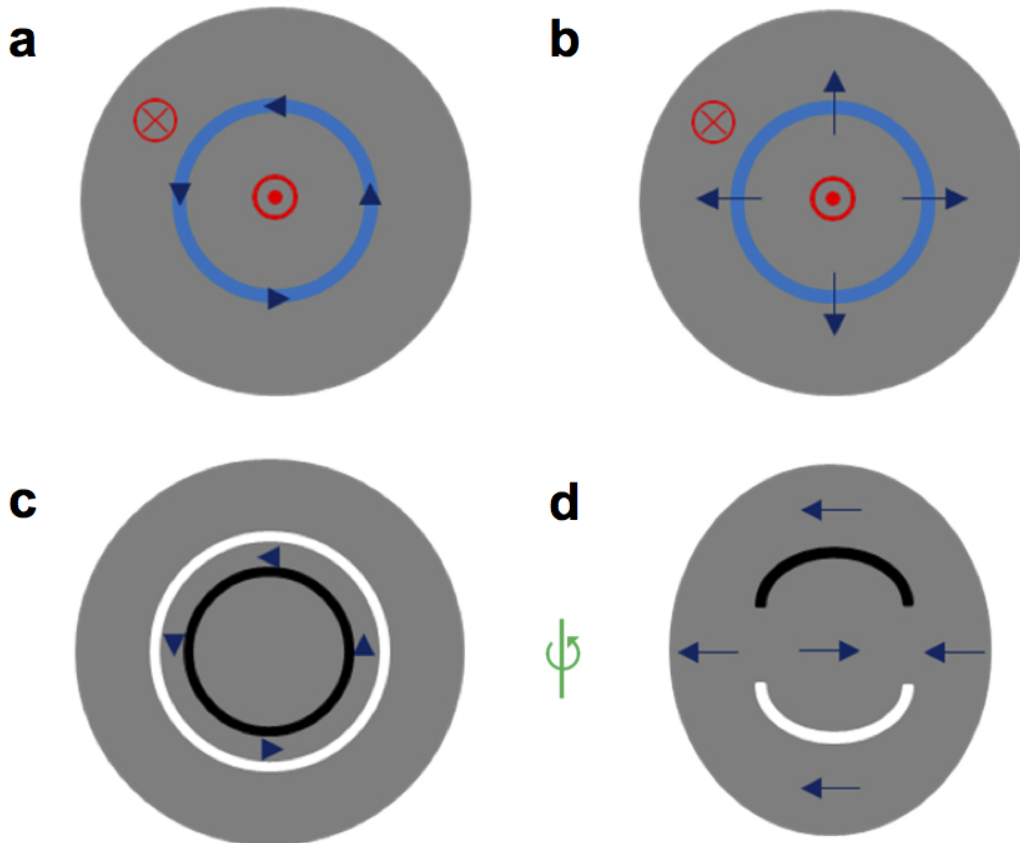


Figure 3.10: Schematic of (a) Bloch and (b) Néel wall in thin film with perpendicular magnetic anisotropy. Schematic of Fresnel images of (c) Bloch wall in untilted film and (d) Néel wall in tilted film. The tilt axis is shown by the green line and arrow.

There are two modes in Lorentz microscopy: the Fresnel mode, in which you observe domain walls and magnetization ripples, and the Foucault mode, where domains are

imaged. In the Fresnel mode, underfocusing or overfocusing is used to image the walls (minimum of contrast indicating the in-focus position of the sample where domain walls do not appear). Holograms are recorded and post-treatments are necessary to extract the phase shift from the holograms.

Magnetic imaging was performed, however in order to image the magnetic structure, the objective lens must be switched off. The field from this lens when fully excited is around 2.0 T which is more than enough to fully saturate the magnetization of samples. Imaging here was performed in TEM with the Fresnel defocused mode in operation. For sample with in-plane magnetization, the Lorentz deflection of the electron beam either side of a domain wall will cause the electron to converge or diverge. By defocusing the walls then appear as bright and dark lines depending on the sign of defocus. In the case of the samples imaged here they possess out of plane (perpendicular) anisotropy. Therefore, at normal incidence, the domains will provide no deflection of the beam and hence no contrast. However, in the region of the domain wall the magnetization will have an in-plane component. Two possibilities exist for a simple one dimensional wall, being either Bloch or Néel-type. To illustrate this, the structure of these walls are shown for a circular domain wall in Figure 3.10a-b for Bloch and Néel wall respectively. The Bloch wall is divergent free and the in-plane magnetization (induction) within the wall will cause a divergent/convergent effect of the electron beam at either side resulting in black/white contrast at normal incidence of the beam. This is shown schematically in Figure 3.10c where black and white contrast is shown either side of the wall on a grey background. In comparison the Néel wall has in-plane magnetization, but in this case this component of magnetization is has divergence and the resulting stray field cancels and deflection to the magnetization. The wall is therefore invisible at normal incidence. However, on tilting the sample, the magnetization from the domains then produces a component of induction perpendicular to the electron beam resulting in domain wall contrast as shown schematically in Figure 3.10d. It should be noted that the wall contrast is seen where the magnetization either side of the wall lies parallel to the wall, whereas where the magnetization points head to head or tail to tail no contrast is visible. The latter is gain due to the divergence of the magnetization. Thus whilst the Néel wall becomes visible there is no continuous contrast along the wall, the discontinuity indicates the tile axis. The main point to note here is that by analyzing the structure of the domain walls and their effect on the electron beam it is possible to distinguish between Bloch and Néel walls. Tilting of the sample with Bloch walls would show a superposition of the contrast seen in Figure 3.10c-d. Bloch walls are expected for materials with perpendicular magnetic anisotropy due to magnetostatic considerations, whilst the presence of an interfacial DMI will favor Néel walls.

When imaging these multilayers in the TEM, it is necessary to be aware of some of the challenges faced due to the fact that the majority of the magnetization lies out of the film plane. As already stated at normal incidence of the electron beam this component of magnetization gives no contribution to magnetic contrast. When tilted away from this orientation by an angle  $\theta$ , the component of magnetization which gives a Lorentz

deflection becomes  $M \sin \theta$ . For the TEM membrane samples the tilt is restricted to around 25 deg due to the etching of the silicon support. This means that with the small thickness of sample the resulting Lorentz deflection angles from the domain will be very small. A further complication is that the electrons have to traverse the whole stack. This increases inelastic scattering of the electrons and will degrade the magnetic contrast.

### 3.3 Magnetic Imaging

The imaging of magnetic systems is much more than just taking aesthetic pictures, which for sure is part of the beauty of the job. It reveals the microscopic details of the functionality of magnetic systems, enabling the understanding of their behaviors and engineering of their properties [113].

#### 3.3.1 Synchrotron techniques

We have performed the scanning transmission x-ray experiments on two different beamlines: X07DA (PolLux) beamline at the Swiss Light Source, Paul Scherrer Institute, Villigen, Switzerland, and the Maxymus beamline, BESSY II, Adlershof, Germany.

##### 3.3.1.1 In absorption: XAS and XMCD

Scanning Transmission X-Ray Microscopy (STXM), as most of magnetic imaging techniques with x-rays, is based on x-ray absorption spectroscopy (XAS). The contrast in the images originates from local variations of the x-ray absorption coefficient of the sample, which depends on the x-ray energy and polarization.

To image magnetic domains, the polarization properties of x-ray must be employed. The contrast for imaging domains of ferromagnetic systems arises now from X-ray Magnetic Circular Dichroism (XMCD). For magnetic images, it is essential to select the corresponding photon energy, and to find the right energy, the underlying absorption spectra must be measured. Employing XMCD, ferromagnetic domains can be imaged by tuning the X-ray energy to the  $L_3$ -edge (corresponding to the  $2p - 3d$  transitions). Here, in our sample Co-based, we scan the samples at the Co  $L_3$ -edge at 779.95 eV. The absorption spectra for different orientations of the magnetization in a Co film with respect to the x-ray polarization vector are shown in Figure 3.11. Dividing two images taken with left and right circular polarized light at the  $L_3$  edge leads to an image with increased magnetic contrast, which we refer to as an XMCD image as contributions to the image that do not depend on the polarization cancel out.

Assuming that the intensity of the circularly polarized x-ray beam going through a layer can be written as:

$$I = I_0 \exp(-\mu t) \quad (3.1)$$

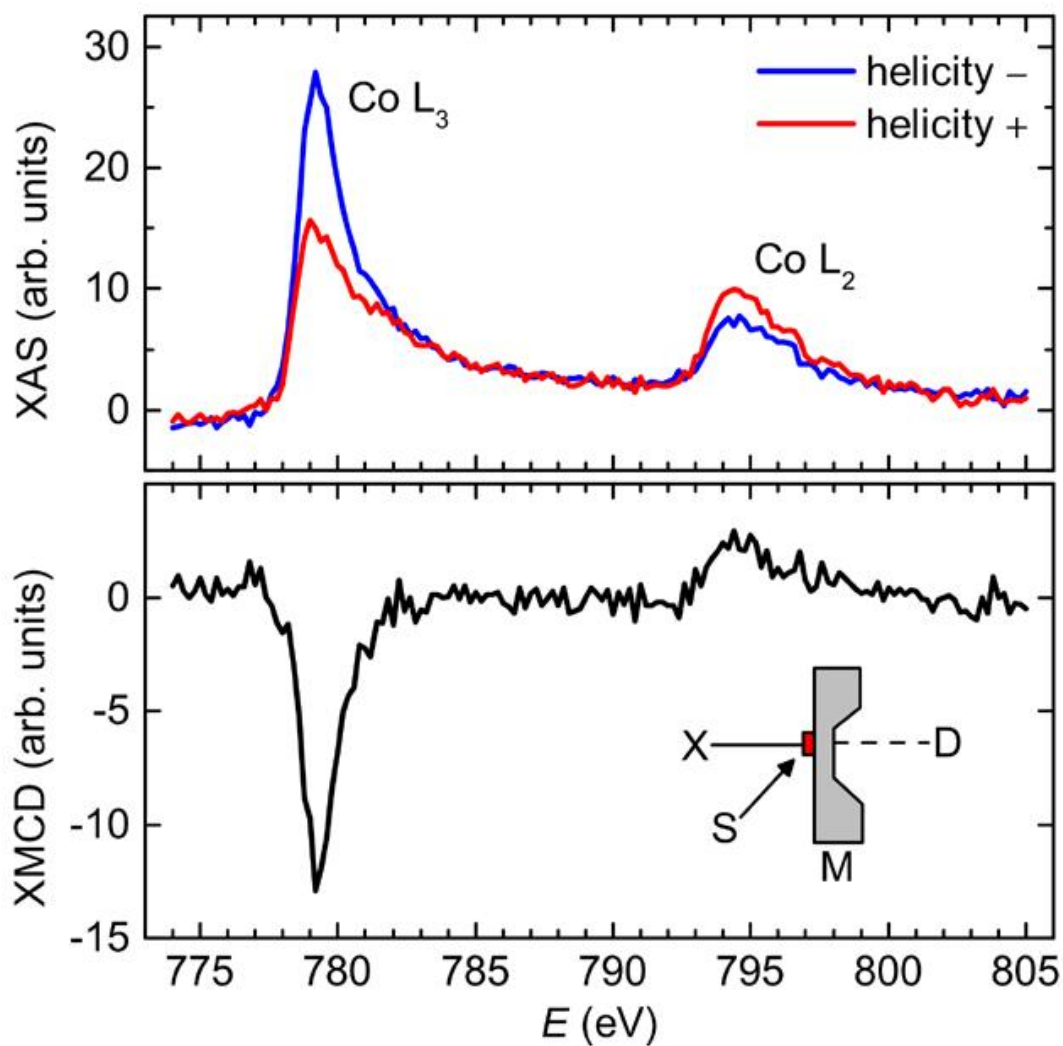


Figure 3.11: XAS of the  $L_{3,2}$  peaks of Co and the corresponding XMCD obtained on  $(\text{Co}_{0.6}\text{Pt}_{1})_{10}$  at the PolLux beamline. The XAS were obtained by normalizing intensity by the intensity of the nearby membrane and then offset to bring the pre-edge value to zero. XMCD is obtained from the difference of these XAS. The inset shows a very schematic cut diagram of the incoming x-ray beam (X), the sample (S) on top of the membrane (M), and the photon counter (D).[114]

where  $I_0$  is the intensity of the incoming light,  $\mu$  the absorption and  $t$  the thickness of the layer. Then, it can be shown that the quantity  $\mu_p - \mu_m$  where  $p$  and  $m$  are for the different helicities, is proportional to the out-of-plane magnetization  $m_z$ . This remains true even in the case of an x-ray beam that is not 100% circularly polarized or if the positive helicity has not the same level as the negative one. Therefore, all the experimental maps of the magnetic configurations presented in this work are obtained by calculating the maps of the absorption difference  $\mu_p - \mu_m$ .

**rules with XMCD** From the XAS and XMCD signals, it is possible to extract quantitative information about the magnetic spin moment and the orbital magnetic moment of each species. It is done through a set of relations called "sum rules". Thole et al. [115] and Carra et al. [116] first derived the sum rules for single ions in a crystal field and later validated for Fe and Co 3d metals by Chen et al. [117] For dipolar  $2p^{3/2}$  and  $2p^{1/2}$  to 3d empty valence states, the orbital and spin magnetic moments,  $m_l = -\mu_B \langle L_z \rangle$  and  $m_s = -2\mu_B \langle S_z \rangle$  can be derived from the XAS and XMCD spectra through the following equations:

$$m_l = -\frac{4(\mu_+ - \mu_-)}{3(\mu_+ + \mu_-)} \frac{dE}{dE} (10 - n_{3d}) \quad (3.2)$$

$$m_s = -6 \frac{(\mu_+ - \mu_-)}{(\mu_+ + \mu_-)} \frac{dE}{dE} (10 - n_{3d}) \left( 1 + \frac{7\langle T_z \rangle}{2\langle S_z \rangle} \right) \quad (3.3)$$

with  $n_{3d}$  the number of 3d electrons for a given atom,  $\langle T_z \rangle$  the expectation value of the magnetic dipole operator ( $\langle T_z \rangle = 0$  for textured Co and Fe). In absorption spectra lies a contribution from photoelectron excitations up to the continuum states that do not account from magnetic dependent transition from 2p to 3d states. In order to apply the sum rules, one should not include these contributions in the integrates signal. This background is usually removed by subtraction of a step function [117] supposed to take into account the number of electrons in the core states.

### 3.3.1.2 In transmission: STXM

To measure X-ray absorption, one way is to measure in transmission, for example the x-ray transmitted through a sample with a photodetector. This can be done in a scanning mode, STXM [118, 119].

A schematic for a STXM is shown in Figure 3.12. The Fresnel zone plate (FZP) focuses the soft X-ray light to a diffraction limited spot. The focal length of the FZP depends on the photon energy. Higher diffraction orders are filtered out using an order sorting aperture (OSA), located between the FZP and the sample. The distance between the OSA and the sample is typically less than 1 mm, depending on the photon energy. The sample is deposited on a semi-transparent  $Si_3N_4$ -membrane. Images are formed by raster scanning the sample through the focal point while measuring the transmitted intensity using an X-ray detector. The spatial resolution is given by the spot size of the

focused x-rays which in turn is determined by the outer width of the zone plate (Figure 3.12) In the presented experiments, the full width at half maximum (FWHM) of the beam is 45 nm at Maxymus and 91 nm at PoLLux (depending on the beamline and the experimental conditions such as apertures slits, divergence and zone plate). However, assuming a typical circular shape of the magnetic skyrmions, it is possible to fit the experimental images and thus deduce the actual skyrmions diameter down to 20 nm, as explained in the next section.

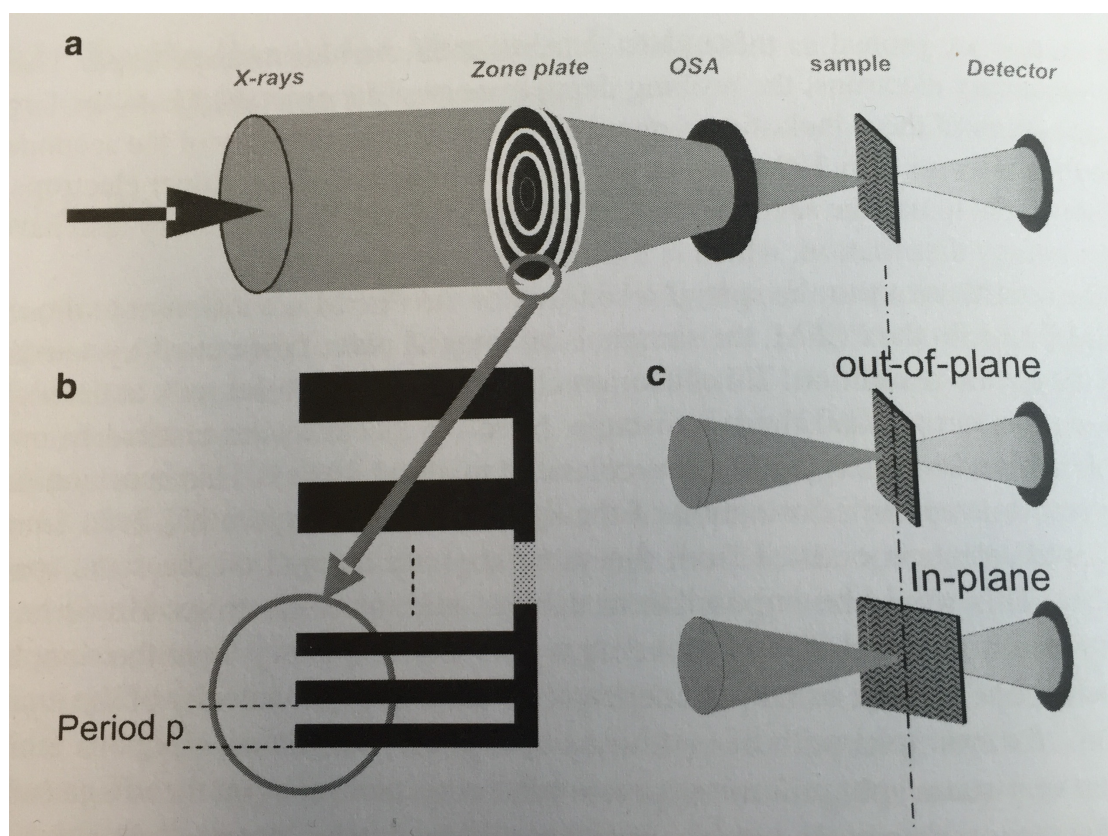


Figure 3.12: STXM. (a) Arrangement of the Fresnel Zone Plate, the ordering selecting aperture, sample and detector. (b) The Fresnel zone plate has a varying period of the lines starting with a larger period in the middle and a smaller period at the outer diameter. The outer width of the zone plate is determining the spot size. (c) Changing from out-of-plane measurements to in-plane measurements by rotating the sample. [120]

As one has understood, for magnetic imaging with x-rays, it is essential to control the polarization. The time to switch polarization should be short so that there is a minimum drift between two images. There are two different concepts: the first one is based on having two undulators (concept used on Maxymus line), and the second one is based on a bending magnet as source with control over the electron path in the synchrotron

(this solution was adopted for PolLux).

For imaging with the undulator solution, a simple way is to use the fact that the photon energy generated from an undulator has a specific, finite width in the range of a few electron-volt as shown in Figure 3.13. The energy emitted from an undulator depends on the strength of the magnetic field, which, in turns, depends on the gap between the upper and low row of magnets. Usually, the monochromator is set to the same energy as the center of the energy distribution of the undulator (tuned). Detuning the undulator [121] by moving now the gap by a few millimeters will shift the center of the emitted photon energy away from the energy of the monochromator, such that nearly no intensity passes the monochromator. Setting one undulator to circularly left polarization and the other to circular right polarization, one can switch rapidly between these two undulators, having one tuned to the energy of the monochromator and the other one detuned.

For the second concept, a bending magnet produces linearly polarized x-rays in the central plane of the synchrotron. The light is circularly polarized above and below the plane. A way to change the polarization is to tilt the electron beam in the section of the bending magnet, with the apertures fixed [122]. The tilt of the electron beam is introduced by means of a vertical asymmetric bump produced by four successive dipole correctors. This set-up is implemented at the PolLux beamline at the SLS and enables to switch polarization in about 1s.

It should be noted that the degree of circular polarization of a bending magnet is in practice between 60 and 80%, in contrast with the undulator where 100% polarization can be reached.

Finally, it is possible to apply high out-of-plane magnetic fields during the measurement, up to 250 mT. The size of the magnetic field is limited here by geometrical restrictions as the distance between the samples and the FZP is very narrow.

## 3.3.2 Laboratory technique: MFM

### 3.3.2.1 Introduction

The Magnetic Force Microscopy (MFM) is a variant of the Atomic Force Microscopy (AFM) [123]. It records the magnetostatic forces or force gradients between a sample and a small ferromagnetic tip. Starting from pioneering work the method has been extremely used and useful in the field of imaging magnetic patterns in magnetic recording media. The two most prominent advantages of the technique contributing to its success are its potential insensitivity to non-magnetic surface coatings and reliefs, and good resolution down into the nanometer range. The magnetic transition geometry and stray field configuration in perpendicular recording media is illustrated in Figure 3.14.

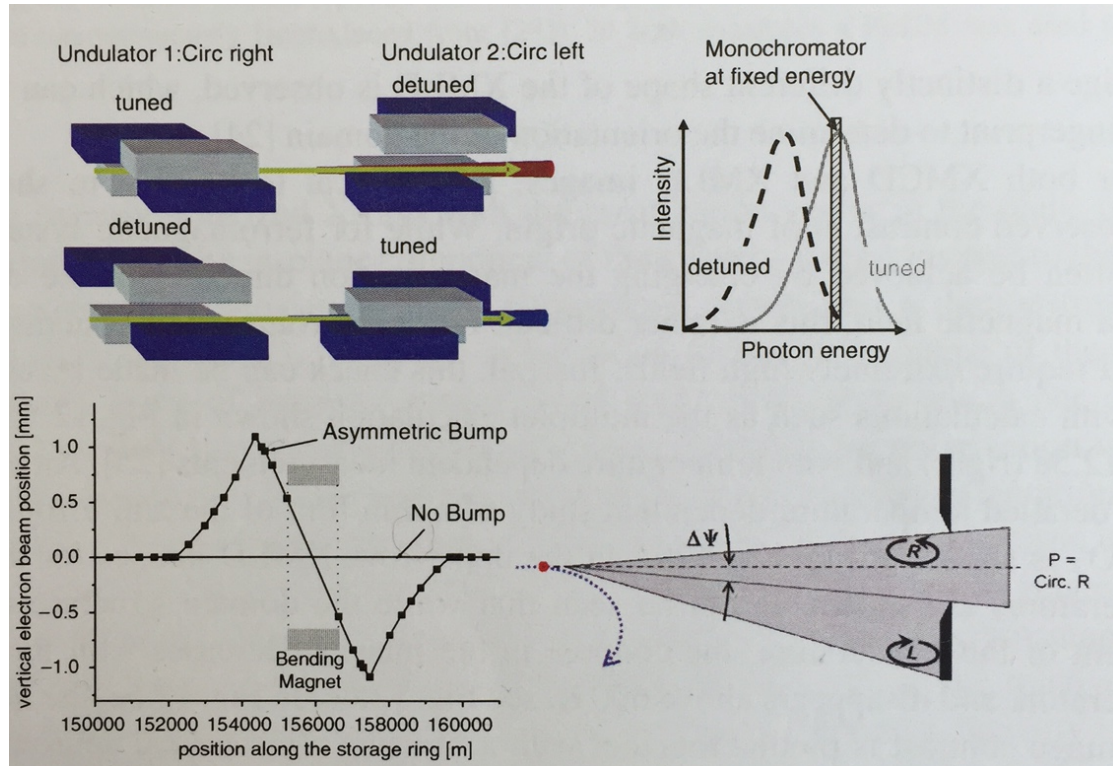


Figure 3.13: **(top)** The photon energy generated from an undulator has a specific, finite width in the range of a few electron-volt, which must be tuned to the energy of the monochromator to get photons of the sample. If the energy of the undulator is detuned and does not match the energy of the monochromator, no photons will hit the sample. With two undulators, it is now possible to switch between them by having one tuned and the other one detuned as only photons from the tuned undulator will hit the sample, while the photons from the detuned undulator will not pass the monochromator. If now the first undulator is set to circular right polarization and the second one to circular left polarization, one can switch the polarization within a few seconds. **(bottom)** The polarization from a bending magnet can be changed by tilting the synchrotron. This can be realized by an asymmetric bump of the electron beam in the bending magnet, and now the circular polarized fraction of the produced X-rays is passing the aperture. [120]

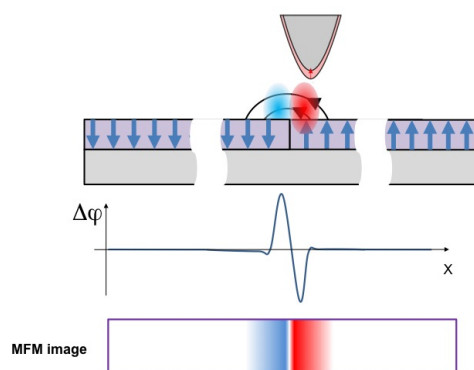


Figure 3.14: on top: the tip of the MFM scanning a sample with several perpendicular magnetic domains. In the middle, the shift in the phase induced by the interaction between the tip and the stray-field of the sample. On the bottom: the image obtained with MFM.

### 3.3.2.2 Basic of magnetic contrast formation

The principle of the AFM is based on the detection of inter-atomic forces between a small tip affixed to a micro-cantilever of a known spring constant, and the surface of the sample under observation. The vertical movements of the tip moving over the sample are detected, for example optically using a laser diode shined onto a mirror on the back of the cantilever and reflected towards a four quadrant detector. Indeed, in force microscopy, forces are measured by the deflection of a flexible beam (the so-called cantilever), which carries the tip-shaped probe at its free end. More precisely, it means that under the influence of a probe-sample interaction, the cantilever behaves as if it had a modified spring,  $c_f = c - \partial F / \partial z$  where  $c$  is the natural spring constant and  $\partial F / \partial z$  is the derivative of the interaction force relative to the perpendicular coordinate  $z$ . The beam can be adjusted by a piezoelectric actuator and its position can be detected by a wide variety of sensors.

The essential adaptation from AFM to MFM which allows the tip to probe local magnetic field of the sample is quite simple. The tip is coated with a continuous film of ferromagnetic material about 10 nm thick. This coating can be magnetized parallel or anti-parallel to the long axis of the tip, and its direction of magnetization can be flipped by approaching a sufficiently strong permanent magnet. As the magnetized tip interacts with the magnetic textures of the sample, a force of magnetic origins is exerted on the tip. This force results in the deflection of the cantilever and hence a signal, which can be observed.

At first sight, a description of the force between the magnetic tip and the sample seems straightforward: the force is the gradient of the interaction energy, which can be

written in two equivalent forms:

$$E = - \int_{tip} \mathbf{J}_{tip} \cdot \mathbf{H}_{sample} dV = - \int_{sample} \mathbf{J}_{sample} \cdot \mathbf{H}_{tip} dV \quad (3.4)$$

The force acting on a MFM tip can thus be calculated by:  $\vec{F} = -\vec{\nabla} E$ . The first integral supports the interpretation of the magnetic force microscopy where the magnetization distribution of the tip (supposed to be known) interacts with the stray field of the sample. The interaction energy should therefore offer information about the stray field. Hence, different magnetization patterns with the same stray field cannot be distinguished. The second integral tells us that two tips with different magnetization patterns but with the same stray fields are also equivalent.

### 3.3.2.3 Imaging procedures

Quantitative data about the sample stray field can only be derived from MFM images when topographic signal contributions are not included. This is especially important when the tip is brought very close to the sample (in order to improve resolution), since non-magnetic forces become increasingly stronger. The solution to this problem is to keep the topography influence constant by letting the tip follow the surface height profile. First the surface profile is recorded by measuring repulsive forces; then in the second run the forces gradients are recorded at an adjustable distance above the previously measured topographic profile. the specific method employed to separate signal contributions is called lift mode (Figure 3.15).

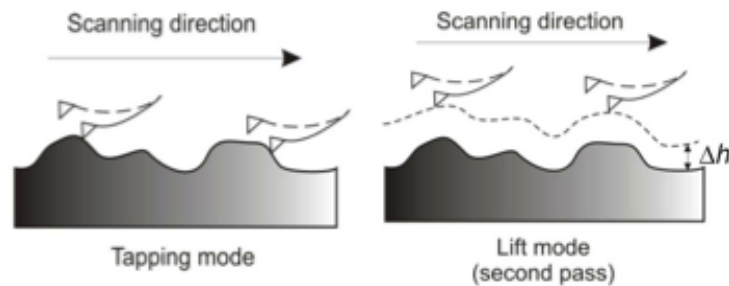


Figure 3.15: Outline of the lift mode principle. Magnetic information is recorded during the second pass (right panel). The constant height difference between the two scan lines is the lift height  $\Delta h$ .

It involves measuring the topography on each scan line in a first scan (left panel), and the magnetic information in a second scan of the same line (right panel). The difference in height Outline of the lift mode principle. Magnetic information is recorded during the second pass (right panel). The constant height difference between the two scans, the so-called lift height, is selected by the

user. Topography is measured in dynamic AM mode and the data is recorded to one image. This height data is also used to move the tip at a constant local distance above the surface during the second (magnetic) scan line, during which the feedback is turned off. In theory, topographic contributions should be eliminated in the second image.

#### 3.3.2.4 Magnetic field

A powerful tool for understanding the behavior of a magnetic sample is applying magnetic field. The Asylum MFM available at the laboratory is equipped with an Asylum Research Variable Field Magnet (VFM) module. It relies on a rare-earth permanent magnet to apply a field to the sample. By rotating the magnet, different amounts of magnetic flux can be channeled through the sample. By using permanent magnets, using electromagnetic coils that can require significant current to maintain a large magnetic field is avoided. A motor controls the magnet rotation, and the motion of the motor is controlled through menu settings in a control panel of the software interface. The out-of-plane field will explore values from +150 mT to -150 mT.

#### 3.3.2.5 Lift Height

To have a better insight, we have performed some preliminary simulations to verify the role of the height chosen for the MFM lift. Indeed, the nominal value chosen to image our sample is 20nm, but, in order to have a better control on the error margin due to the experiment, it was necessary to study the different size of skyrmions and mean domain width versus the height of the MFM lift. To perform such study, we have chosen to work with micromagnetic simulations on Mumax3. Mumax3 has built-in generation of MFM images from a 2D magnetization. The MFM tip lift can be freely chosen. By default the tip magnetization is modeled as a point monopole at the apex. This is sufficient for most situations. Nevertheless, it is also possible to model partially magnetized tips by setting MFMDipole to the magnetized portion of the tip, in meters. In this study, we have considered that the MFM tip as a point monopole.

This means that, at the end of the simulation, we are no longer only recording the map of magnetization, but we are also generating a simulated MFM image corresponding to the MFM lift height we've put in the parameters. The general lift height chosen for imaging all the samples is 20 nm.

Figure 3.16 shows the evolution of a skyrmion's diameter in an extended film according to the MFM lift height and same experiment for worm-domains ; the left image corresponding to the actual magnetization map. Note that the difference of size between a MFM lift of 10 nm and 30 nm for a skyrmion is less than 5%, and for the worm domains, the Fourier transformation of the different images gives also a mean domain width equivalent in the error margin of 5%. Nonetheless, as we can observe in the different images of Figure 3.16, it is quite clear that the higher the lift, the blurrier the image, increasing the challenge to estimate qualitatively the evolution of the magnetic behavior of our sample.

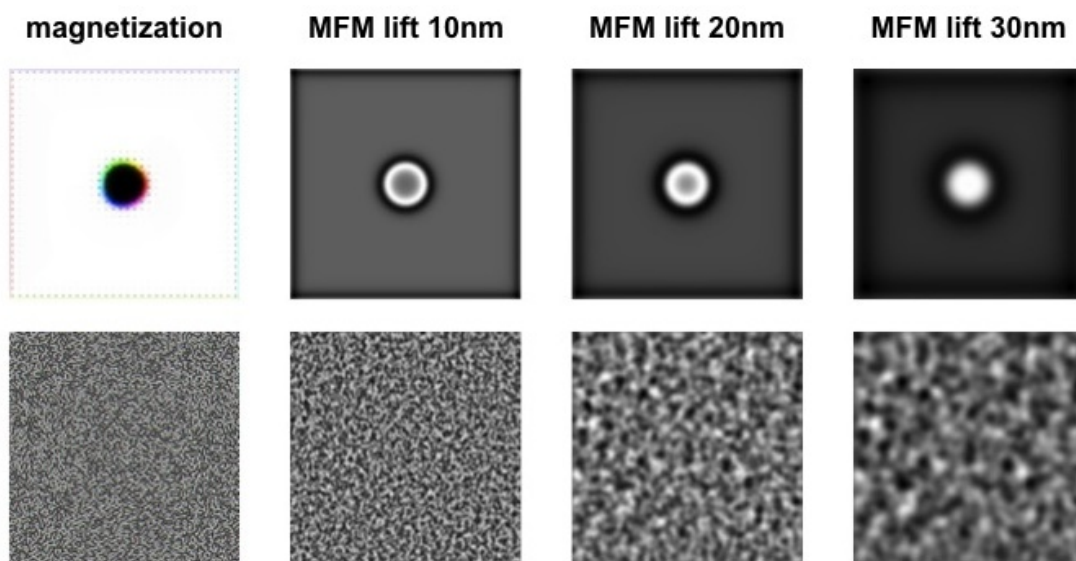


Figure 3.16: Different outputs obtained with Mumax3. From left to right, the magnetization map, the simulated cliché for a MFM lift height of 10, 20 and 30 nm, for (**top**) a skyrmion and (**bottom**) domains. Even though the image is blurrier as we are increasing the height of the MFM lift, the size found for the skyrmion or the mean domain width is not significantly changed.

### 3.3.2.6 Choice of tips and spatial resolution

A large choice of tips exist. However when using classical MFM tips, we noticed that it is influencing the sample. Moreover, since the coercitive field of the samples studied is quite low, it is better to use low moment tip because it will yield weaker interaction with the sample. The counterpart is that the signal recorded is weaker.

In our study, we used exclusively Asylum Low Moment tips which are silicon probes coated with 15 nm of CoCr. The magnetic moment due to the tip is about  $3 \cdot 10^{-14}$  emu and its coercitive field of 40 mT. In practice, we have found that the tip is switching magnetization direction around 15 mT. Hence the contrast is changing around this field because of the switching of the tip and not because of a sudden change of magnetic behavior of the sample. For more comprehensible results, we have post-treated the images so that the switching of the tip is not visible.

It is also noteworthy that we have performed some studies to evaluate the actual spatial resolution we can achieve. Theoretically, the spatial resolution achieved with room temperature MFM is between 30 and 50 nm.

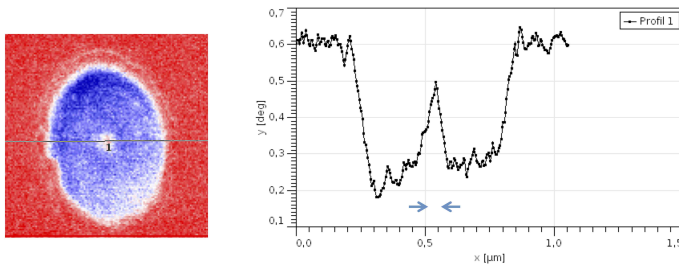


Figure 3.17: MFM image obtained in Py50|Pt5 of a vortex in a 600 nm patterned disk. On the right is plotted the profile of the vortex core. The full width half maximum leads to a resolution of 50 nm.

Indeed, as seen in Figure 3.17, with a MFM lift height of 20 nm, with a Low Moment Asylum tip, we are able to observe a vortex with a core of 50 nm. For information, when the lift height is decreased to 10 nm, the MFM resolution goes down to 35 nm.

We have seen in this chapter the different processes used for the fabrication of the ultrathin multilayers systems. We have also made an overview of the different techniques for characterizing the samples and two different methods for the observation at room temperature of the magnetization: a synchrotron technique (STXM) and a laboratory technique (MFM).

## Chapter 4

# Observation of isolated skyrmions at room temperature in ultrathin multilayers

### Contents

---

|            |                                                                    |            |
|------------|--------------------------------------------------------------------|------------|
| <b>4.1</b> | <b>Observation by STXM</b>                                         | <b>76</b>  |
| 4.1.1      | Observation of Pt10 Co0.6 Pt1 {Co0.6 Pt1} <sub>10</sub>  Pt3       | 76         |
| 4.1.2      | Observation of Pt10 Co0.6 Pt1 {Ir1 Co0.6 Pt1} <sub>10</sub>  Pt3   | 77         |
| 4.1.3      | Discussion                                                         | 91         |
| <b>4.2</b> | <b>Observation by Magnetic Force Microscopy</b>                    | <b>94</b>  |
| 4.2.1      | Observation at remanence after demagnetization                     | 95         |
| 4.2.2      | Observation under out-of-plane magnetic field of {Ir Co Pt} sample | 96         |
| <b>4.3</b> | <b>Comparison with other experiments</b>                           | <b>96</b>  |
| <b>4.4</b> | <b>Perspective: Moving small skyrmions in nanotracks</b>           | <b>101</b> |

---

In this chapter, we present the first images of magnetic skyrmions at room temperature in ultrathin multilayers. We have been able to observe different magnetic structures, including skyrmions, and this study was performed on two different samples: an asymmetric Co-based multilayer: Pt10|Co0.6|Pt1|{Ir1|Co0.6|Pt1}<sub>10</sub>|Pt3 and a symmetric Co-based multilayer: Pt10|Co0.6|Pt1|{Co0.6|Pt1}<sub>10</sub>|Pt3. The concept of having two different samples is that, because the two interfaces are the same in {Co|Pt} sample, we expect that the two components of DMI annihilate whereas, as seen with the prediction of *ab initio* calculations in the previous chapter [108, 109, 110], the DMI amplitudes at the interfaces of {Ir|Co|Pt} sample should add to each other. Moreover, these samples have been imaged by two different techniques: a synchrotron technique (STXM) and a laboratory one (MFM), both explained in the previous chapter. We have chosen to work with two different techniques which have their own pros and cons and compare the results.

## 4.1 Observation by STXM

In this section, we present results obtained on both  $\{\text{Ir}|\text{Co}|\text{Pt}\}$  and  $\{\text{Co}|\text{Pt}\}$  samples by STXM. The run were made at two different synchrotron facilities: PolLux, Swiss Light Source, Paul Scherrer Institute, Villigen, Switzerland and Maxymus, BESSY, Max Planck Institute, Berlin, Germany. This work was in collaboration with PSI team, especially with Christoforos Moutafis. It was the first technique used to try observing isolated magnetic skyrmions at room temperature. The very powerful advantage of this technique is that we are observing the direct magnetization (out-of-plane component) of the sample. Moreover, it is also possible to apply out-of-plane magnetic field, which is really important when trying to understand the magnetic behavior of objects. Nonetheless, this technique has obviously some disadvantages: beside the fact that the sample has to be grown on a fragile very thin transparent membrane, it is a long-term feed back technique. Indeed, the timelapse between two runs (which lasts around one week) is generally of few months - meaning that the time needed to perform a complete study is quite important.

### 4.1.1 Observation of $\text{Pt}_{10}|\text{Co}_{0.6}|\text{Pt}_1|\{\text{Co}_{0.6}|\text{Pt}_1\}_{10}|\text{Pt}_3$

#### 4.1.1.1 Sample's characterization

Prior to the synchrotron experiment, samples were characterized by AGFM and SQUID measurement. Figure 4.1 shows the hysteresis loops obtained for both out-of-plane and in plane applied magnetic field.

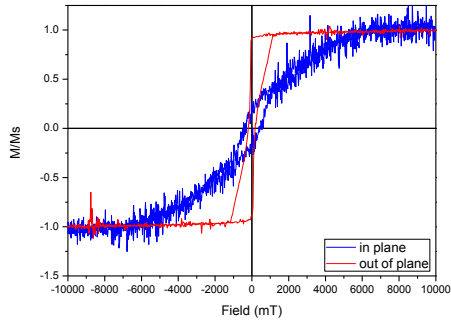


Figure 4.1: Hysteresis loops of  $\{\text{Co}|\text{Pt}\}$  sample for applied out-of-plane (red) and in plane (blue) magnetic field.

$\{\text{Co}|\text{Pt}\}$  sample shows a clear out of plane anisotropy with a strong magnetization at remanence of 96%. Moreover, the SQUID measurement gives us a magnetization at saturation of  $1603 \pm 80$  kA/m and effective anisotropy energy of  $0.25 \pm 0.07$  MJ/m<sup>3</sup>.

#### 4.1.1.2 Observation in plain films

Our first work on this sample was to image its magnetic behavior after demagnetization. As expected, without any applied magnetic field, we can see some magnetic domains.

As noticed on Figure 4.2, we obtain a very good contrast: the magnetization goes from black to white, representing the out-of-plane magnetization. As the STXM probes the total thickness, these images correspond to an average of the magnetic configurations throughout the eleven layers of Co. As we mainly observe two opposite contrast amplitudes (corresponding to  $m_z = \pm 1$ ), we conclude that these magnetic configurations run throughout the magnetic thickness of the multilayers [124].

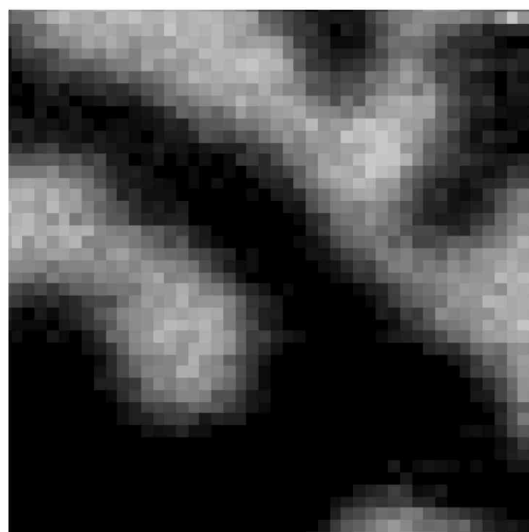


Figure 4.2:  $2.5 \times 2.5 \mu\text{m}^2$  out-of-plane magnetization ( $m_z$ ) map obtained by STXM at room temperature under no field on {Co|Pt}

We can notice that the size of the observable domains is quite large. Indeed, the quantitative analysis of Figure 4.2 reveals that the mean periodicity of perpendicular magnetic domains obtained after demagnetization is  $320 \pm 30$  nm.

We have mapped the distribution of the vertical component of the magnetization in our sample and to *follow* its evolution as a function of the external perpendicular magnetic field  $H_{/perp}$

After saturation at large negative field, we first observe a worm domains configuration at  $-160 - -120$  mT on Figure 4.3. By increasing the field, the white configuration is favored by the field and hence it is extending. Whatever the field applied, we can only observe labyrinth-shaped domains, with size depending on the amplitude of applied field. No circular-shaped domains seem to be stabilized by this structure and we can expect a very low DMI amplitude in this sample. Thereby, even if very low DMI magnitude can not be excluded, this sample's behavior will be of good comparison when studying the asymmetric structure in the following sections.

#### 4.1.2 Observation of Pt<sub>10</sub>|Co<sub>0.6</sub>|Pt<sub>1</sub>|{Ir<sub>1</sub>|Co<sub>0.6</sub>|Pt<sub>1</sub>}<sub>10</sub>|Pt<sub>3</sub>

##### 4.1.2.1 Characterization of the sample

**EELS** {Ir|Co|Pt} samples were also grown on ultrathin Si<sub>3</sub>N<sub>4</sub> membrane (30nm-thick) to be analyzed with EELS at the University of Glasgow by M. Krajnak and S. McVitie.

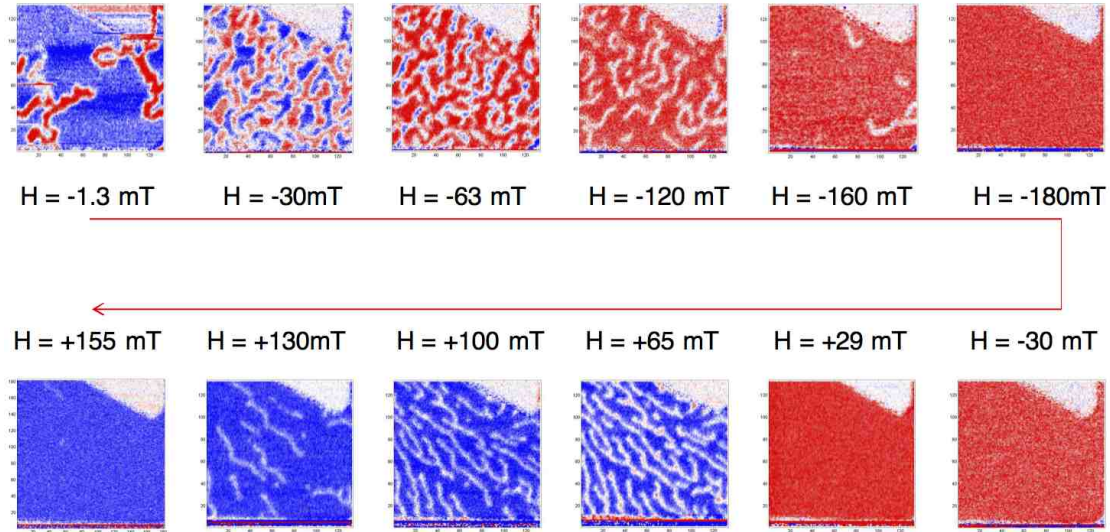


Figure 4.3:  $4 \times 4 \mu\text{m}^2$  out-of-plane magnetization ( $m_z$ ) map obtained by STXM on {Co|Pt} sample at room temperature for applied perpendicular magnetic fields of  $-180$ ,  $-160$ ,  $-120$ ,  $-63.2$ ,  $-29.8$  and  $-1.3$  mT.

This analyze were made on cross-section samples prepared using focused ion beam (FIB) “lift out” methods to image the quality of the interface.

The electron beam of the TEM is parallel to the interfacial planes, hence the interfaces can be imaged. Figure 4.4 shows the results of high resolution imaging and EELS on the cross-section. High Annular Dark Field (HAADF) images of the section as shown in Figure 4.4a, are sensitive to atomic number, meaning that elements with higher atomic number appear brighter. The 10 dark Co layers are shown clearly in the center of the image, indicating well-defined and continuous layers clearly separated by the lighter contrast Ir and Pt layers. The green area highlighted in Figure 4.4a was then investigated with EELS and processing of the EELS data provided elemental maps of the key components of the structure. These are shown in Figure 4.4b for Pt, Ir, Co, Cu and N. This nicely shows the definition of the key active layers of Pt, Co and Ir. Cu was also investigated because it was used as a protective capping layer put on the surface, before the usual protective Pt capping layer, both administered in the FIB. The N locates the silicon nitride substrate.

Furthermore, the data can be plotted as elemental profiles and this is displayed in Figure 4.4c for the active elements in the multilayer. Again the quality of the layer definition is clearly shown here. The pixel spacing of  $0.5$  nm is sufficient to sample multilayer structure with layers of  $0.6$  and  $1.0$  nm. It should be noted that the percentage level shown on the vertical axis suggests that the layers have much less than  $100\%$  of the elements in each of the active layers, apart from the thicker (wider in this case) Pt layers. The reason for this is the thickness of the cross-section ( $60$ - $70$  nm) which means that the electron

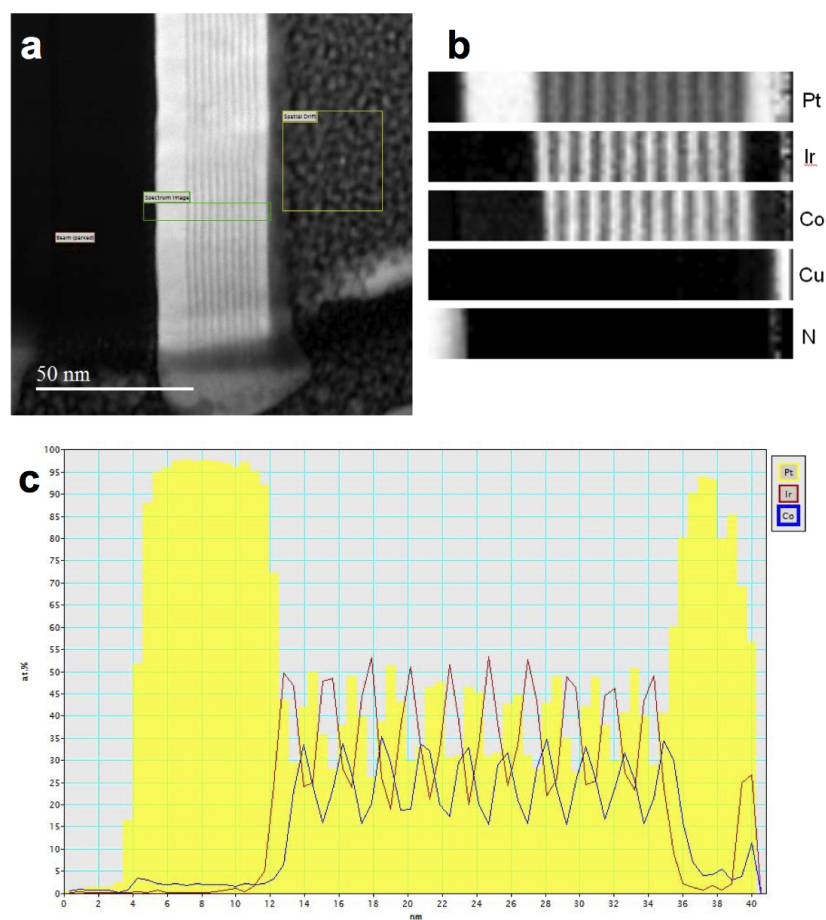


Figure 4.4: (a) HAADF image of cross-section of  $\text{Pt}_{10}\{\text{Ir}_1|\text{Co}_{0.6}|\text{Pt}_1\}_{10}\text{Pt}_3$  showing layers and area (green) for EELS analysis. (b) Elemental distribution in region defined in (a) highlighting well defined active Pt, Ir and Co layers plus substrate (N) and protective layer (Cu). (c) Linetraces of variation of active elements in ML stack.

beam samples the adjacent layers for the thinnest (narrowest) layers here. Thinner cross-sections will give better quantification of the percentages however the data here gives very powerful evidence of the high quality layer structure and definition of multilayered stackings.

**Magnetic characterization** Prior to the synchrotron experiment, the sample was characterized by AGFM and SQUID measurement. Figure 4.5 shows the hysteresis loops obtained for both out-of-plane and in plane applied magnetic field.

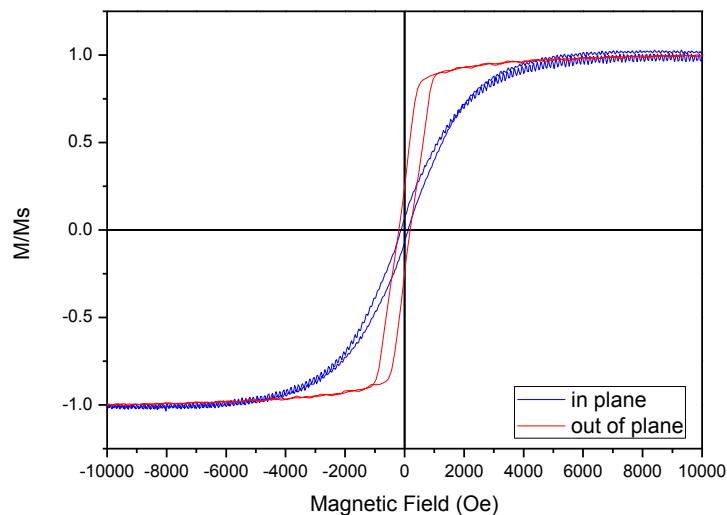


Figure 4.5:  $M(H)$  of  $\{\text{Ir}|\text{Co}|\text{Pt}\}$  sample for applied out-of-plane (red) and in plane (blue) magnetic field.

$\{\text{Ir}|\text{Co}|\text{Pt}\}$  sample shows a clear out of plane anisotropy with a strong magnetization at remanence. Moreover, the SQUID measurement gives us a magnetization at saturation of  $960 \pm 50$  kA/m and effective anisotropy energy of  $0.17 \pm 0.04$  MJ/m<sup>3</sup>. The bulk value for Co magnetization is of 1400 kA/m. Generally the magnetization value for Co in ultrathin multilayers is taken between 1000 and 1300 kA/m [50, 49, 7, 125]. The value founded experimentally here is in good agreement with these expectations.

We can notice that the hysteresis loop for out-of-plane applied magnetic field presents a tilt leading to a magnetization at remanence close to zero. This very low magnetization at remanence let foresee the observation of magnetic domains without any applied field.

#### Evolution of $M_s$ with temperature and evaluation of the exchange stiffness

In order to have a complete picture samples, we have performed SQUID measurement of

the evolution of the magnetization with applied out-of-plane magnetic field. Figure 4.6 shows the hysteresis loops for two different temperatures: 30 and 300 K. We can clearly see that the magnetization at saturation increases with decreasing temperature and the coercitive field is also higher with low temperature.

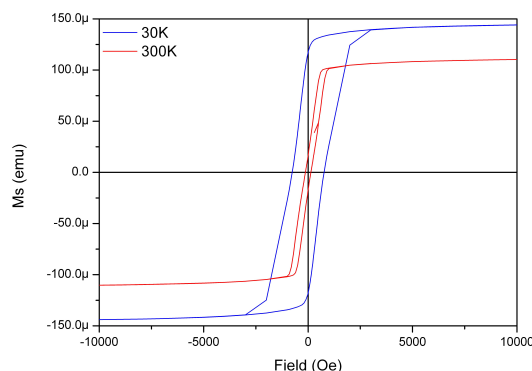


Figure 4.6: Evolution of the magnetization of {Ir|Co|Pt} sample with applied out-of-plane magnetic field for two different temperatures: 30K (blue curve) and 300 K (red curve).

As expected, this kind of measurements allow us to have an estimation of the exchange stiffness. Indeed,  $A$  is linked to the Curie Temperature and the evolution of the magnetization at saturation with temperature below Curie Temperature. For memory, ferromagnetism appears only below a certain temperature, simply known as the Curie Temperature. This temperature depends on the material, and is about 1380 K for bulk Co. But, for Co-based multilayers, Curie-Temperature is expected to be between 500 and 1100 K [11]. We can use the *Bloch Law*:  $M(T) = M(0) \left(1 - \left(\frac{T}{T_c}\right)^{\frac{3}{2}}\right)$  and the magnetization at saturation can be written as [126, 127]:  $M_s(T) = M_s(0) - \left(\beta T^{\frac{3}{2}}\right)$  where  $M_s(0)$  is the magnetization at saturation at 0K.  $\beta$  is then defined by:  $\beta = \frac{V_0}{\langle S \rangle} \frac{k_B}{V_0 A}$  where  $V_0$  is the atomic volume,  $\langle S \rangle$  is the average spin per atom and  $k_B$  is the Boltzmann's constant.

When applying this formula to the data obtained by SQUID, we result in Figure 4.7. This allows us to estimate the exchange stiffness in {Ir|Co|Pt} sample to be  $\sim 10$  pJ/m, and a Curie Temperature of  $T_c = 960 \pm 50$  K, which is in good agreement with the prediction made by Bruno [11]. It has also been observed recently in similar stacking of Co thin films with heavy metals [128] that  $A$  is significantly influenced by the surface/volume ratio and evolves from 15 pJ/m for multilayers with 7 nm-thick Co layers (a typical bulk value for Co) down to about 7 pJ/m for a 2 nm-thick Co layers. However, we find here a value for 0.6 nm higher than the value found in the work of C. Eyrich and coworkers for 2 nm of Co. Nonetheless, their work is based on trilayers, whereas we work here with multilayers composed of repeated trilayers. The total thickness of Co in our stacking is 6.6 nm and we can expect that the value of  $A$  should be between 15 and 7. With and experimental estimation of  $\sim 10$  pJ/m, we are in a good agreement with this expectation.

The value obtained for the exchange stiffness is in good agreement with theory and other experimental observations. However, it is important to keep in mind that the

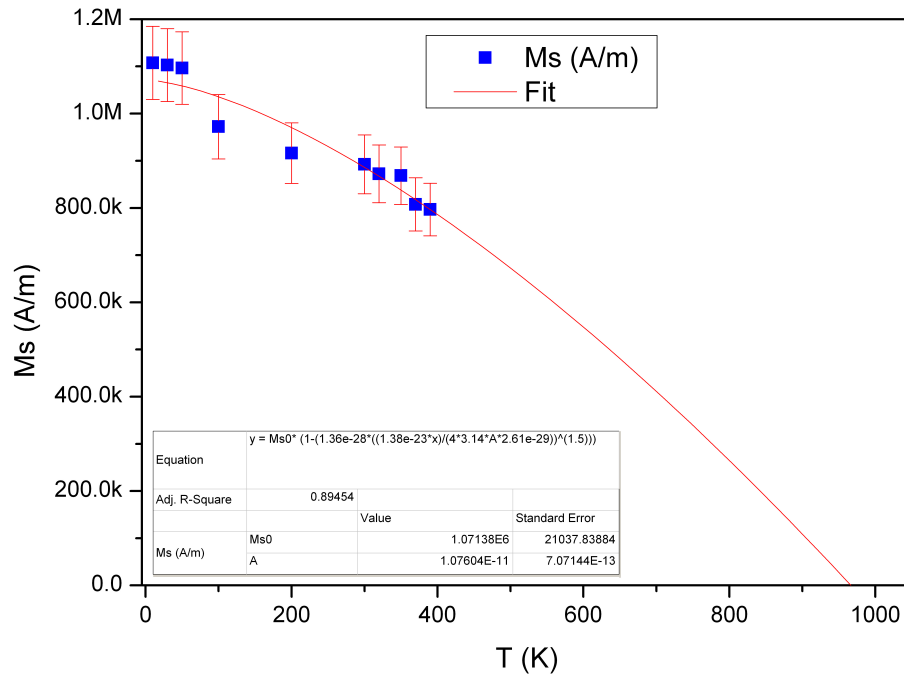


Figure 4.7: Evolution of the magnetization at saturation with temperature. Fitting curve gives an estimation of  $A$  at  $\sim 10$  pJ/m

value of the exchange stiffness is extracted with partial datas because no measurements were made above 400 K and no doubt that these measurements would change (even slightly) the value of the exchange stiffness. The study would have been improved by the possibility to make measurements of the evolution of the magnetization with applied magnetic field for higher temperatures, closer to Curie Temperature. Unfortunately the SQUID device available at the laboratory doesn't enable to heat the sample more than 400 K. The error bars of the determination of the exchange stiffness value would be smaller thanks to a wider range of temperature applied to the sample.

#### 4.1.2.2 Plain films

**Without applied magnetic field** As for the {Co|Pt} sample, we have first image {Ir|Co|Pt} sample without applied field. The result presented here are not images straight after demagnetization. Indeed, some external out-of-plane magnetic field was first applied to the sample, and because of constraints due to the functioning of the STXM, it was not possible to demagnetize properly the sample. We have performed a very rough demagnetization by applying field of both signs as in the demagnetization process explained in Chapter 3. However, even without a proper demagnetization, we expected, at remanence, some magnetic domains because of the low magnetization at remanence measured by AGFM. As it is observable on Figure4.8, we obtain a very good contrast: the magnetization goes from red to blue, representing the out-of-plane

magnetization, and white color representing in-plane magnetization.

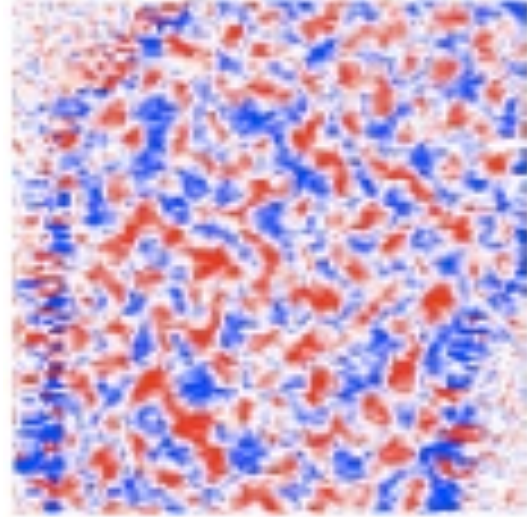
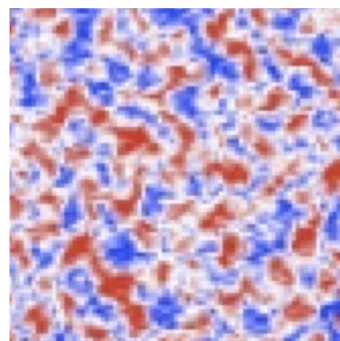


Figure 4.8:  $1.5 \times 1.5 \mu\text{m}^2$  out-of-plane magnetization ( $m_z$ ) map obtained by STXM at room temperature under no field of  $\{\text{Ir}|\text{Co}|\text{Pt}\}$  sample.

Comparison with  $\{\text{Co}|\text{Pt}\}$  sample (Figure 4.9) allows us to notice that the size of the domains observed are smaller in the case of  $\{\text{Ir}|\text{Co}|\text{Pt}\}$ . Indeed, Fast Fourier Transformation of the image allow us to determine the the mean domain width and this quantitative analysis of Figure 4.8 reveals that the mean periodicity of perpendicular magnetic domains obtained after demagnetization is  $106 \pm 20 \text{ nm}$ . As explained in the Chapter 1, the domain pattern contain information about the DMI amplitude, because it results from an equilibration of magnetostatic, wall energies and DMI. Through the latter, the equilibrium domain configuration and the DMI are linked. The domains are narrower in  $\{\text{Ir}|\text{Co}|\text{Pt}\}$  than in  $\{\text{Co}|\text{Pt}\}$  one, which indicates a stronger DMI in  $\{\text{Ir}|\text{Co}|\text{Pt}\}$  (which is expected).

Figure 4.9:  $800 \times 800 \text{ nm}^2$  comparison of the out-of-plane magnetization ( $m_z$ ) map obtained by STXM at room temperature under no field. (**left**)  $\{\text{Ir}|\text{Co}|\text{Pt}\}$  sample and (**right**)  $\{\text{Co}|\text{Pt}\}$  sample.



Asymmetric sample



Symmetric sample

**Applying out-of-plane magnetic field** Our main study was to map the distribution of the vertical component of the magnetization in our sample and to *follow* its evolution as a function of the external perpendicular magnetic field.

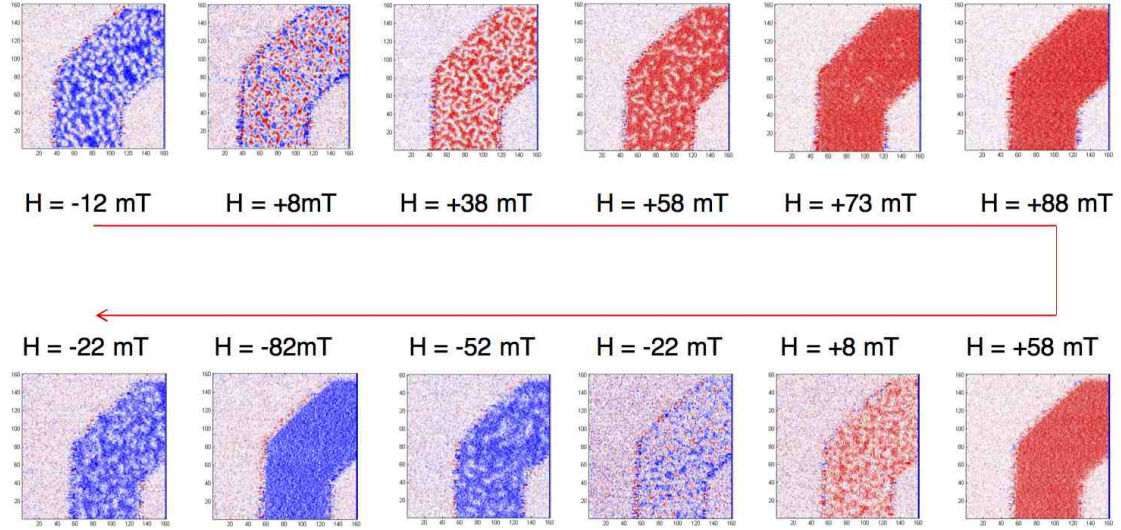


Figure 4.10:  $1.5 \times 1.5 \mu\text{m}^2$  out-of-plane magnetization ( $m_z$ ) map obtained by STXM at room temperature for applied perpendicular magnetic fields of 8, 38, 68, 73, and 83 mT.

After saturation at large negative field and inversion of the field, we first observe a domain configuration at 8 mT on Figure 4.10 that combines some labyrinth-shaped domains with other domains having almost a circular shape. As expected, when the field is increasing, it favors the one direction of the magnetization (here corresponding to the red color). When reaching  $\mu_0 H_{\perp} = 38$  mT, we note the size augmentation of the red domains. Obviously, this means that the domains of the other direction of magnetization are shrinking. These shrinking domains should be in blue, but, because of the size of the beam (see next paragraph) the blue domains being smaller, we can only observe white contrast. Eventually, there are becoming small enough so that we can no more observe the complete switching of the magnetization (the Figure at  $\mu_0 H_{\perp} = 63$  mT does not show any blue component of the magnetization). Nonetheless, at  $\mu_0 H_{\perp} = 63$  mT we can observe isolated magnetic domains of an approximately circular shape. Furthermore, they persist with higher field up to 80 mT in an almost totally perpendicularly polarized sample.

**Estimation of the size** The actual diameter of the circular-shape domains is found to be often smaller than the actual dimension of the polarized x-ray beam, as we have seen with the blue domains. In fact, in the presented STXM experiments, the full width at half maximum (FWHM) of the beam was either 45 or 91 nm depending on the beamline (45 nm on Maxymus beamline and 91 nm on PolLux beamline) and the

experimental conditions (aperture slits, divergence, zone plate). However assuming a typical circular shape of the magnetic skyrmions (which is the typical definition of a skyrmion) and convoluting it with a Gaussian x-ray beam profile, it is then possible to fit the experimental images and thus deduce the actual skyrmion diameters down to 20 nm (see Figure 4.11).

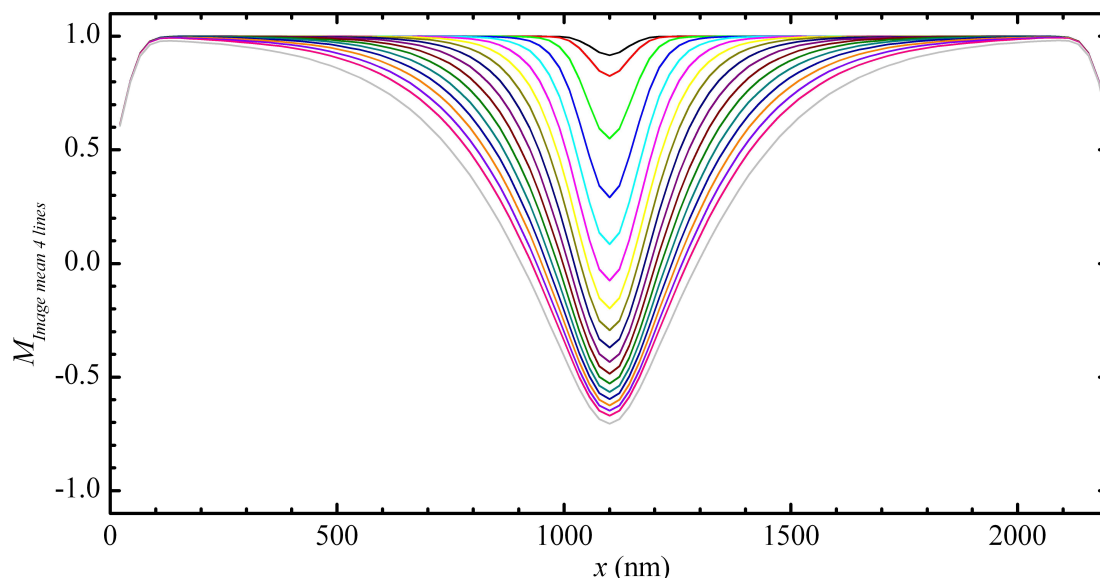


Figure 4.11: Simulations of different magnetization profile of skyrmions for different sizes: from 20 nm diameter to 360 nm diameter.. Here we have the result of the convolution between the theoretical magnetization  $m_z(r)$  and the beam profile. Theoretical magnetization is defined by  $m_z(r) = \cos\left(\frac{\pi r}{2r_s}\right)$  for  $r < 2r_s$  [129].

More precisely, the assumed magnetization profiles are corresponding to circular skyrmions for which the magnetization  $m$  is rotating continuously with the distance from skyrmion center  $r$ , *i.e.*  $m_z(r) = \cos\left(\frac{\pi r}{2r_s}\right)$  for  $r < 2r_s$  [129, 45]. To improve the signal/noise ratio, we average over a few lines, typically corresponding to the beam FWHM. However, it is quite clear that determining the actual size of the skyrmion with this technique is leading to some errors, mainly because the theoretical profile lines are quite close to each other as seen on Figure 4.11, and it is sometimes not obvious to determine which line the experimental profile is closer to. We have chosen to be quite cautious and illustrate the largest possible error margins given the datas. The skyrmion profiles are then compared to the ones determined in micromagnetic simulations. In Figure 4.12, we illustrate such image analysis and comparison to ideal profiles for two different perpendicular applied magnetic fields for the {Ir|Co|Pt} multilayers.

We can now focus on the dimensions of these circular-shaped domains as well as on their increase when  $H_{\perp}$  is decreased. We find that the diameter of the circular shaped domains goes from about 30nm at  $\mu_0 H_{\perp} = 73$  mT to 80 nm at  $\mu_0 H_{\perp} = 12$  mT, as

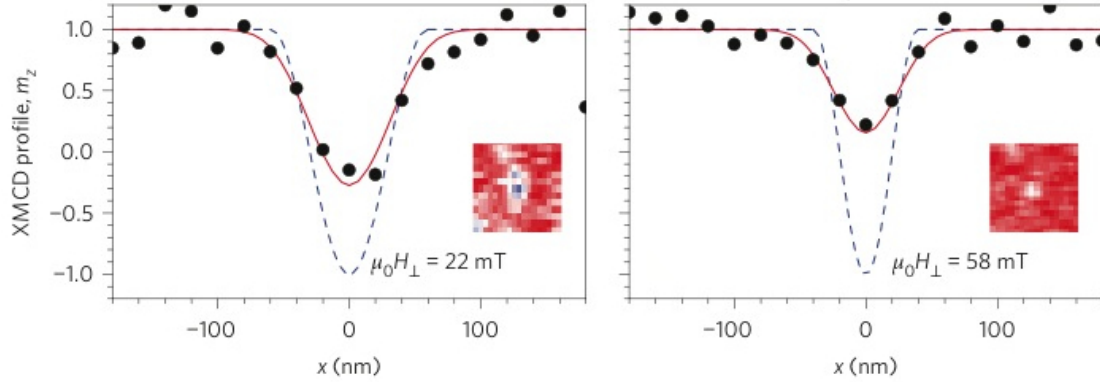


Figure 4.12: Black dots: Experimental X-ray magnetic circular dichroism (XMCD) signal through a magnetic circular domain (skyrmion) as observed at 22 mT (left) and 58 mT (right). The blue dashed curves are the magnetization profiles of an ideal 60 nm-diameter (right) and 40 nm-diameter (left) skyrmion and the red curves derive from the model described in the previous section. The images and data presented here result from the same skyrmion evolution in the field. The actual image size of the insets is 360 nm

reported in Figure 4.13. At lower field (closer to zero), the magnetic contrast evolves towards worm-like domains from which a proper diameter can no longer be defined. These values are consistent with a large DMI amplitude, which was expected by the comparison of the mean domain width at remanence between  $\{\text{Ir|Co|Pt}\}$  and  $\{\text{Co|Pt}\}$  samples. And indeed, in the next chapter we are going to show two techniques we have developed to estimate the DMI.

**Discussion about the size** From Malozemoff and Slonczewski theory on magnetic bubbles stabilized by dipolar interaction [82] seen in Chapter 2, we conclude that only magnetic bubbles of diameter larger than few micrometers can be stabilized by the dipolar interaction, which is in contradiction with the observation of circular shaped domains of 80 nm diameter. This confirms that the circular-shape domains observable in the  $\{\text{Ir|Co|Pt}\}$  sample is not only stabilized by the dipolar interaction but also by a strong DMI. This conclusion is also applicable partially for  $\{\text{Co|Pt}\}$  sample : eventhough no skyrmions were observed, the worm domains and especially their sizes confirms that DMI is needed to understand the stabilization of such magnetic domains.

The first important conclusion drawn from this analysis is that the presence of circular-shape domains in the 30 – 90nm size range cannot be accounted for by the dipolar interaction [82, 130, 131, 132, 133]. Indeed, the diameter of the circular-shape domains (around 80 nm) that we observe at very low field values remains extremely small compared to the usual values observed in the classic bubble systems in which the driving mechanism for bubble stabilization is the dipolar interaction. The micromagnetic analysis performed in next chapter will indeed confirm that classic bubbles can never be stabilized with such parameters (magnetization at saturation and anisotropy) with such

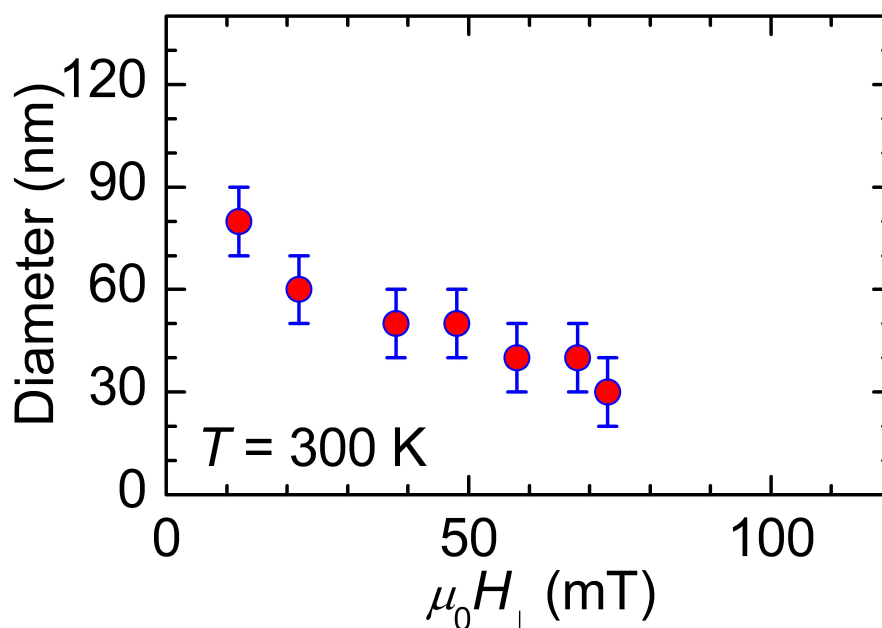


Figure 4.13: Evolution of the size of the observable skyrmions with applied perpendicular magnetic field in {Ir|Co|Pt}

low diameters, and thereby confirming the observation of isolated magnetic skyrmions in {Ir|Co|Pt} sample at room temperature.

#### 4.1.2.3 Nanostructures

**Motivation** In the previous paragraph, we have presented some observations of isolated magnetic skyrmions in extended films. The next step to our work was to study the magnetic behavior of magnetic disks lithographed on our sample, to observe the influence of the confinement on skyrmions behavior. Indeed, as predicted by J.Sampaio et al. and S. Rohart et al. [50, 49] in their study of the confinement of skyrmions in ultrathin film nanostructure in the presence of DMI, the edges of nanostructures allow for the isolation of single skyrmions for a large range of the DMI parameter. In their work, they categorized different case according to the value critical DMI called  $D_c$ . In nanostructures, for the smallest DMI value (compared to  $D_c$ ), the skyrmion diameter is found to be independent of the disk diameter and coincides with the plain film solution. These skyrmions are so small and their shape is not impacted by the edge. In the case where the DMI value is quite similar to  $D_c$ , they do not observe the divergence of the skyrmion diameter because these skyrmions are in fact confined in the dots which limits the diameter increase. Moreover, for DMI values larger than  $D_c$  and if the dot diameter is not too large, a single skyrmion can be isolated in the dot.

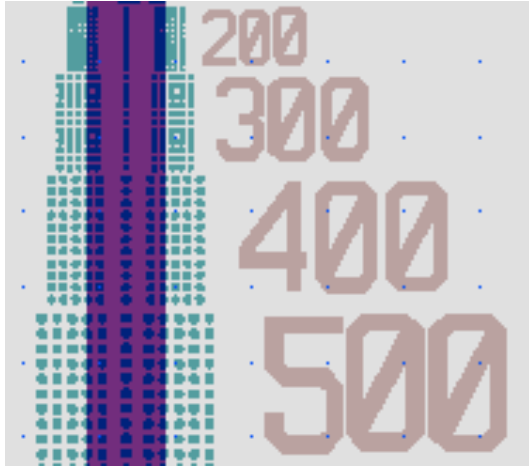


Figure 4.14: Patterns of the mask used to study the magnetic behavior of  $\{\text{Ir}|\text{Co}|\text{Pt}\}$  in nanostructures. Different sizes of nanodisks are patterned, diameters are being patterned on the right of the disks arrays.

**Technical details** On the same sample as the one studied in plain film in the previous section, we are now looking at some nanostructures patterned by e-beam lithography and ion-beam etching (by Karin Garcia). The patterns of the mask used for this study are showed in Figure 4.14. After e-beam, the samples are ion-etched to remove the insulated part of the structure. The Ion-Beam Etchnig (IBE) available at the laboratory has the possibility to control the process thanks to a secondary ion mass spectrometer for the analysis of secondary ions from the ion beam etch process, as seen on figure 4.15.

It is possible to follow different elements, and different isotopes by element. In our case, we focused on Pt (black curve), Ir (blue curve) and Co (green curve), as well as Si (red curve) for the substrate. When looking at the Co curve, after the ten peaks corresponding to the ten layers of the stack, we observe a decrease of the element, as well as for Pt and Ir. Few times later, the Si curve start to drop, meaning that we start to etch the substrate and hereby it's time to stop the etching. As one can see, the process is very well controlled.

**Observations** We have performed the same protocol of field cycling on an array of nine 500 nm-diameter nanodisks (Figure 4.16). As we can notice, four different magnetic configurations are again observable: apparent saturation at large field (negative at  $-52$  or  $-72$  mT, or positive at  $+68$ mT), partition of the space by labyrinth-shape domains (for example at  $+28$  and  $+48$  mT), a mix combination of worms and circular-shape domains (both  $-12$  mT and  $-32$  mT) and finally some isolated magnetic skyrmion at  $-52$  mT. Nonetheless, we can notice that the saturation appears at lower field ( $-52$  mT) compared to the plain films of Figure 4.10 where saturation was obtained at  $-80$  mT. Hereby, we observe an effect of the confinement on the magnetic behavior of  $\{\text{Ir}|\text{Co}|\text{Pt}\}$  sample. Moreover, the skyrmions are stable down to very small fields ( $\sim 8$  mT). Their dimension go from 90 mT at very small field down to 50 mT when applying out-of-plane magnetic field.

We also have performed a similar study on 300 nm-diameter disks with the same

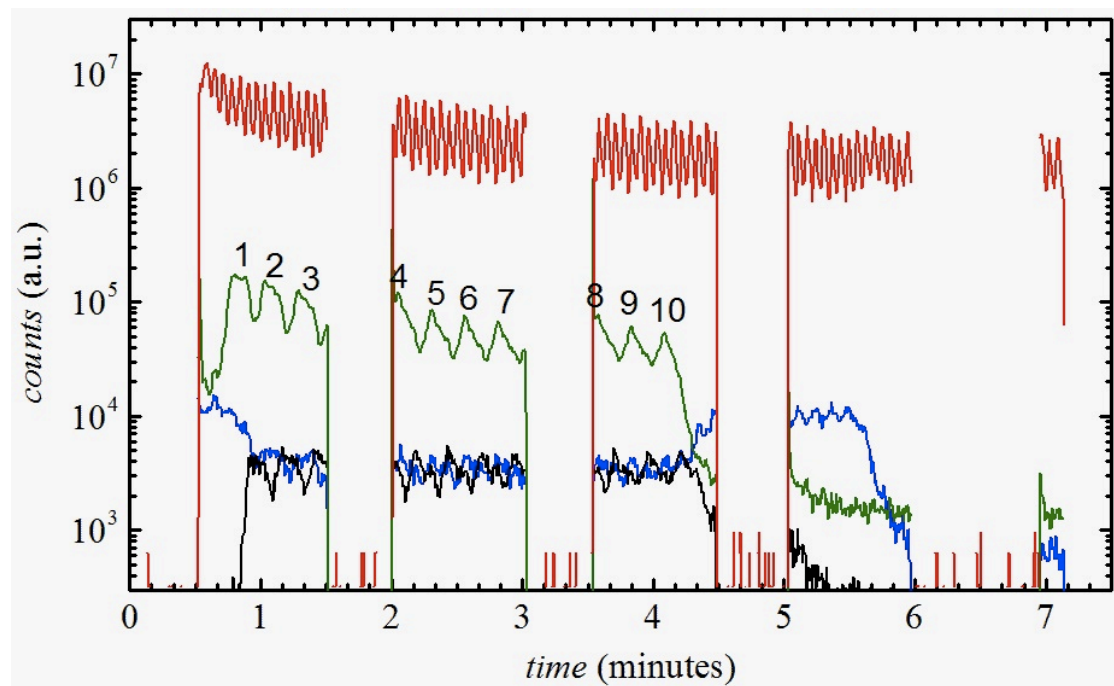


Figure 4.15: Secondary Ion Mass Spectrometer (SIMS) image of the ion etching of  $\{\text{Ir}|\text{Co}|\text{Pt}\}$ . Red curve is Si, Green curve is Co, blue curve is Ir and black curve is Pt.

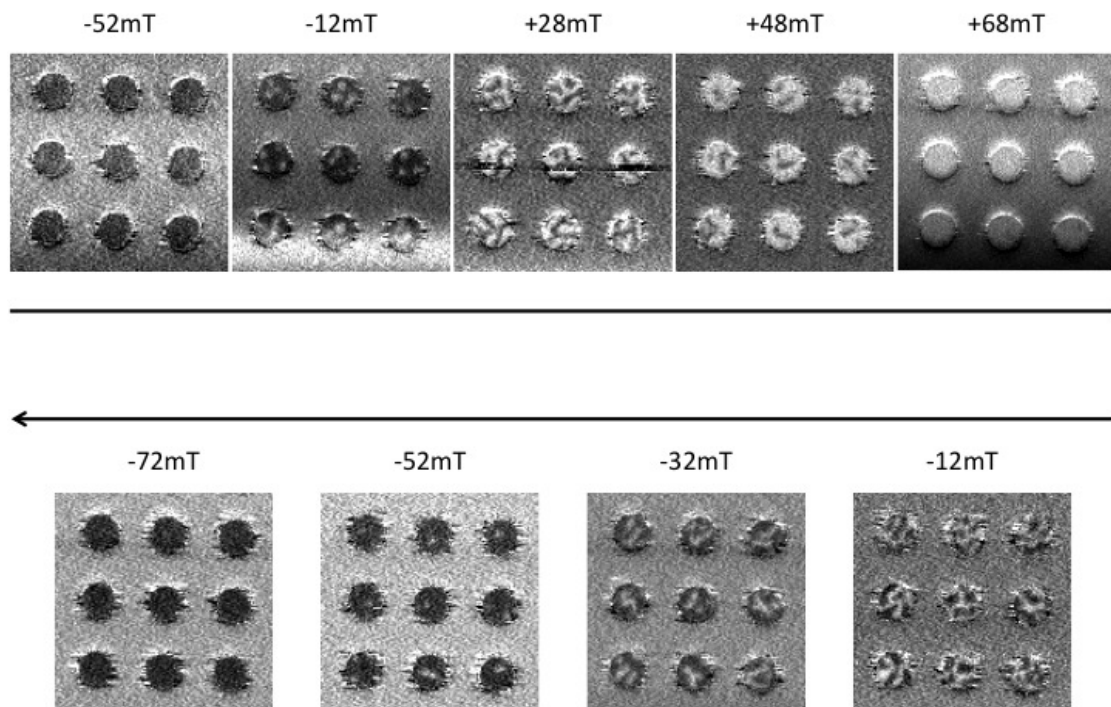


Figure 4.16: Field cycling on an array of nine nanodisks of 500 nm diameter. The applied out-of-plane magnetic field is swept from  $-52$  mT up to  $+68$  mT and then decreased down to  $-72$  mT. Four different configurations can be observed: apparent saturation (at  $-52$ ,  $+68$  and  $-72$  mT), worm-shaped domains (at  $+28$  and  $+48$  mT), a mix between worm-shaped domains and skyrmions (both  $-12$  and  $-32$  mT), and finally isolated magnetic skyrmions at  $-52$  mT.

result, except that the state with the mix existence of worms and skyrmion does not really exist anymore: with the field sweeping, we pass more easily from the apparent saturation to the isolated magnetic skyrmion to the worms. We can conclude that the confinement due to the smaller size of the nanodisks favors the sweeping from one state to another without letting possible the coexistence of mixed states.

The dimension of the skyrmions observed at in nanodisks of 300 nm-diameter are quite similar to the one found in the 500 nm-diameter nanodisks. Indeed, it rather depends on the effective ratio between the DMI amplitude and the exchange interaction, as long as the DMI magnitude remains smaller than the threshold value that corresponds to negative domain wall energy, and we'll see in next chapter that we are indeed below  $D_c$ .

Finally, we also have considered smaller nanodisks of 200 nm diameter. Note that, at that size, we are close to the spatial limit for resolution. Indeed, because of the size of the Fresnel Zone Plate (FZP, see Chapter 3 for details) used for the experiment (20 nm for these measurements performed on Maxymus beamline), the pixel size will be of 20 nm so that there are only 5 or 6 pixels for one dot. Meaning that for smaller nanodisks (100 nm-diameter in our patterns as seen on Figure 4.14), these dots would be seen only on 3 or 4 pixels which don't allow a clear map of the magnetization of the sample. On those nanodisks, we have decided to record more statistics and observe a larger array of it. Also, we have performed similar field cycling as for the larger disks and we have observed only two different magnetic behavior : saturation and isolated magnetic skyrmions. Therefore, we have decided to lead another field experiment. We stay at one field where every dots present an isolated magnetic skyrmion. From that state (here at 8 mT), we are increasing the field up to apparent saturation (here at 88 mT) take an image and then go back to the field where we were just before. When doing this operation a couple times, we can notice on Figure 4.17 that the magnetic skyrmions are reappearing at the same location of the nanodisks. One final move was to go up to the higher field possible (183 mT) and go back to 8 mT.

### 4.1.3 Discussion

#### 4.1.3.1 Determination of the chirality of the domain walls

As explained in the Chapter 3, some LTEM measurement in Fresnel mode were performed at the University of Glasgow by S. McVitie. Firstly, images were taken with {Ir|Co|Pt} sample untilted and tilted to determine the wall type. An example of an untilted and tilted image is shown in Figure 4.18a-b respectively. Both images are defocused with a defocus distance of 10 nm. It can be seen from Figure 4.18a that there is little in the way of black-white contrast, the main contrast is a darkening of the image in the upper left corner due to some bending resulting from stress experienced by the membrane. Imaging of the same region but tilted by 25° shows distinctive small scale black-white contrast which is eliminated by applying a field. The latter indicates the contrast is indeed magnetic, and the non-visible magnetic contrast untilted is consistent

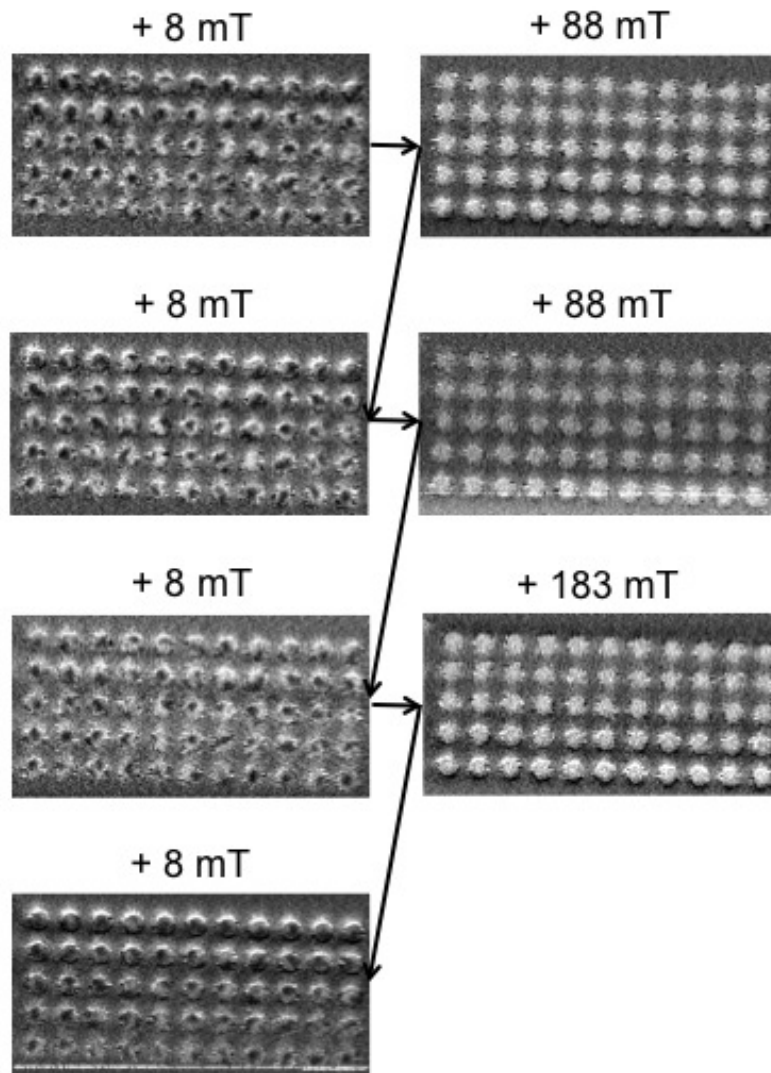


Figure 4.17: Field hopping in {Ir|Co|Pt} sample, between (**left**) 8 mT where isolated skyrmions are observable and (**right**) magnetic saturation 88 mT or maximum field possibly applied 183 mT. The nanodisks are of 200 nm-diameter and the skyrmions diameter are 80 nm.

with the walls being Néel in character, as explained in Chapter 3.

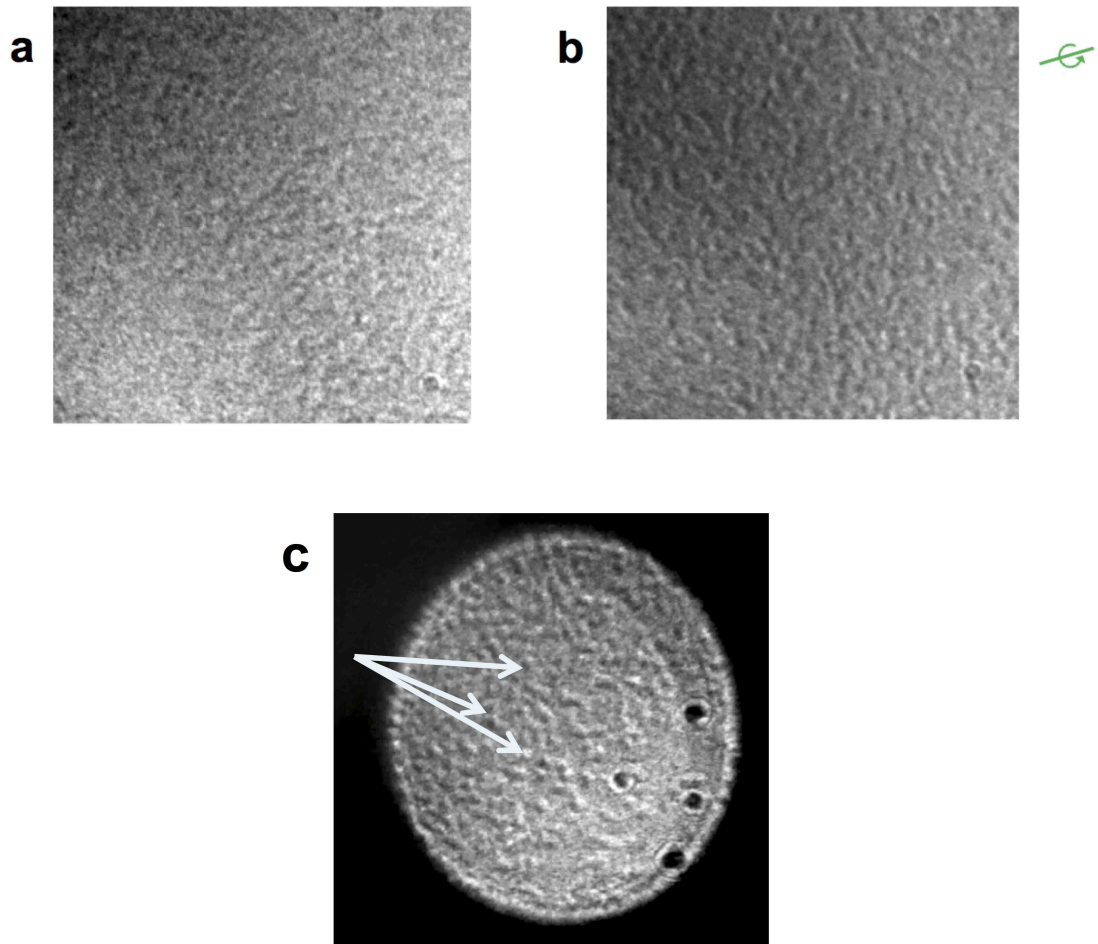


Figure 4.18: (a) Untilted Fresnel image showing no magnetic contrast. (b) Fresnel image from same area as (a) but tilted by 25 deg in the direction indicated by the by the green axis and arrow, showing magnetic contrast. (c) Tilted Fresnel image showing magnetic skyrmions under external out-of-plane magnetic field of 3.5 mT. Some skyrmions are pointed with the help of white arrows for the reader.

Additionally, Fresnel imaging can be used to characterize the domain sizes and therefore deduce the magnitude of the DMI constant  $D$ . This is done by looking at the remanent state of the films where there is equal up-down magnetised regions. As example of this is shown in Figure 4.19a which is a Fresnel image taken from the ten repetitions  $\{\text{Ir}|\text{Co}|\text{Pt}\}$  sample. The image is analysed by taking a fast Fourier transform, which is shown in Figure 4.19b. As the image is defocused there are a series of rings visible which

effectively show the contrast transfer function of the microscope. Also visible are two arcs which relate to the spatial frequency associated with the skyrmion domains. From these arcs the domain size can be measured and here the domain size was measured 120 nm, effectively identical to the quantitative analysis performed with STXM images ( $106 \pm 20$  nm for memory) within error.

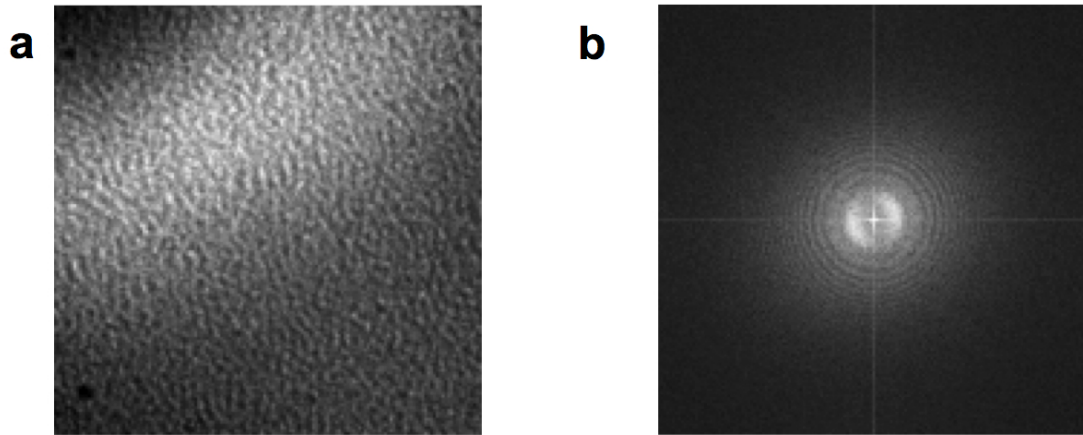


Figure 4.19: **(a)** Tilted Fresnel image showing magnetic contrast. **(b)** Fast Fourier Transform of (a) showing distinct spatial frequency associated with magnetic structure allowing estimate of domain size.

#### 4.1.3.2 Conclusions

The main results of this study are:

- First observation at room temperature of isolated magnetic skyrmions in asymmetric multilayers system by STXM
- Néel chirality of the skyrmion's domain wall confirmed by LTEM imaging
- Comparison with symmetric sample foresee a significantly larger DMI amplitude in the asymmetric sample

## 4.2 Observation by Magnetic Force Microscopy

In this section, we present results obtained for the observation of isolated magnetic skyrmions at room temperature in  $\{\text{Co|Pt}\}$  and  $\{\text{Ir|Co|Pt}\}$  samples by Magnetic Force Microscopy (MFM). The MFM technique has the main advantage that, since it is a laboratory technique, it is possible to have a really quick feedback on the magnetic behavior of different multilayers and it is possible to perform numerous studies without waiting for few months. Besides, it is also possible to apply some out-of-plane magnetic field up

to 150 mT. Nonetheless, the main disadvantage is that the component observed by MFM is the gradient of the magnetization and not the magnetization itself. This results in a more difficult analysis of the images obtained. Moreover, the spatial resolution is slightly less good than the one of the STXM measurements (40nm compared to 20 – 30 nm). We stress out the fact that the very same samples were studied by STXM and by MFM.

#### 4.2.1 Observation at remanence after demagnetization

Both samples were demagnetized (see previous chapter) before any imaging. The main objectives of this experiment were to see if we were able to observe the same kind of magnetic structures by MFM and by STXM and moreover if these magnetic structures presented the same parameters. Since our first study by STXM was to observe the magnetic domains in both samples at remanence, we have followed the same steps by MFM.

We have imaged  $3 \times 3 \mu\text{m}^2$  regions in plain films and the results are shown in Figure 4.20.

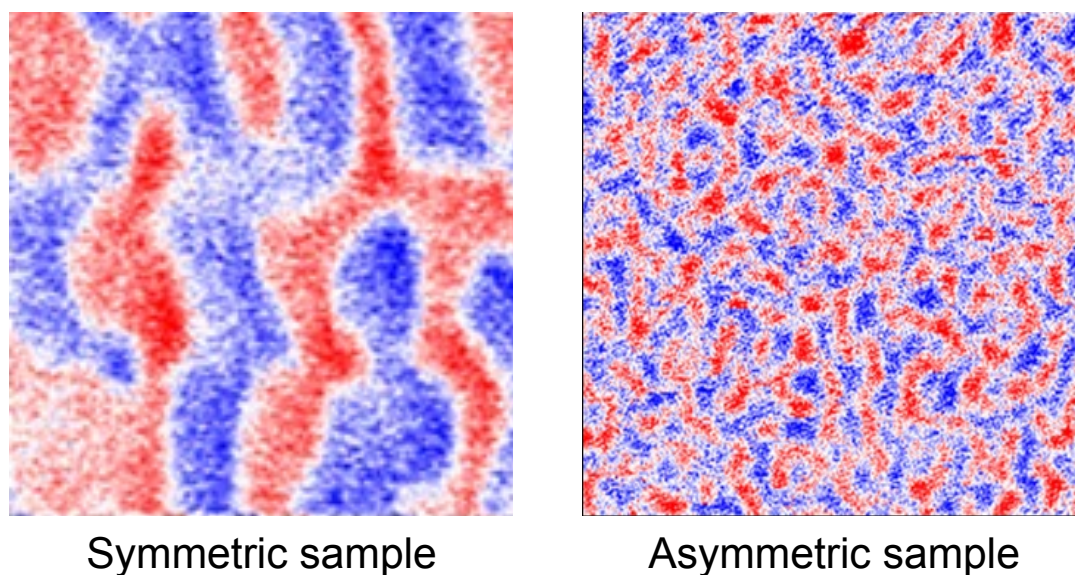


Figure 4.20:  $1.5 \times 1.5 \mu\text{m}^2$  MFM images of  $\{\text{Co|Pt}\}$  and  $\{\text{Ir|Co|Pt}\}$  samples after demagnetization and without applied magnetic field.

This figure allows us to conclude several important points:

- By comparing Figure 4.9 and Figure 4.20, it is clear that the same kind of magnetic behavior is observable by STXM and MFM under the same conditions,
- From eyesight, the domain width of  $\{\text{Co|Pt}\}$  and  $\{\text{Ir|Co|Pt}\}$  samples seem to be identical by STXM or MFM imaging,

- More quantitatively, by Fourier transformation, we deduce a mean domain periodicity of  $117 \pm 20$  nm for {Ir|Co|Pt} sample and  $318 \pm 20$  nm for {Co|Pt} one, which is in excellent agreement with the ones found by STXM imaging. This means that the parameters of the magnetic worm domains observed by MFM and STXM are significantly equal and quantitative analysis can be performed equally with STXM and MFM measurements, as far as worm domains are concerned.

### 4.2.2 Observation under out-of-plane magnetic field of {Ir|Co|Pt} sample

Even if the observation of magnetic worm domains can give us important information such as the estimation of the DMI in the sample studied, the main objective of my PhD was to be able to observe isolated magnetic skyrmions at room temperature. If it has been achieved by STXM experiments, the main question here is to know if we are able to have the same kind of observation by MFM. Therefore, we have imaged {Ir|Co|Pt} sample by MFM with applying out-of-plane magnetic field. We have first saturated the sample up to very high positive field (1 T) and then we have decreased the field down to the region where the magnetization tends to switch in the other direction (see Figure 4.5, red curve)). We have then imaged a  $3 \times 3 \mu\text{m}^2$  region every 2.5 mT steps of field. Results are shown in Figure 4.21.

It is clear that we are observing small magnetic skyrmions (diameter of about 50 mT). When decreasing more the field, some skyrmions remain visible but some burst into larger domains (as visible in Figure 4.20). Additional data taken in different regions show the same magnetic behavior. It is also interesting to notice that the skyrmion density vary with the applied out-of-plane field.

Indeed, if we plot the skyrmion density (corresponding to the number of skyrmions divided by the area of the region imaged), we obtain the Figure 4.22, and we see that it shows that skyrmion density increases when decreasing the magnetic field as expected. Indeed, by decreasing the field, we are favoring one direction of the magnetization and more domains of this magnetization should appear. Because of the DMI, these domains are skyrmions and we observe an increase of the skyrmion number with a decrease of the out-of-plane external magnetic field. Moreover we can notice that there is a plateau at low negative field. And indeed, when decreasing the magnetic field, we increase the number of skyrmion presents in the area, meaning that skyrmions have to coexist, before eventually bursting into wider worm-domains. We can thereby expect a range of field where the maximum number of skyrmions in an area is reached before a critical field where the energies involved lead to a burst of the skyrmions into worm-domains.

## 4.3 Comparison with other experiments

In Chapter 2, the state-of-the-art of the experimental observation of skyrmions ended at the beginning of this PhD. Since the end of 2013, different imaging techniques have been used to observe skyrmions at room temperature stabilized by interfacial chiral interaction.

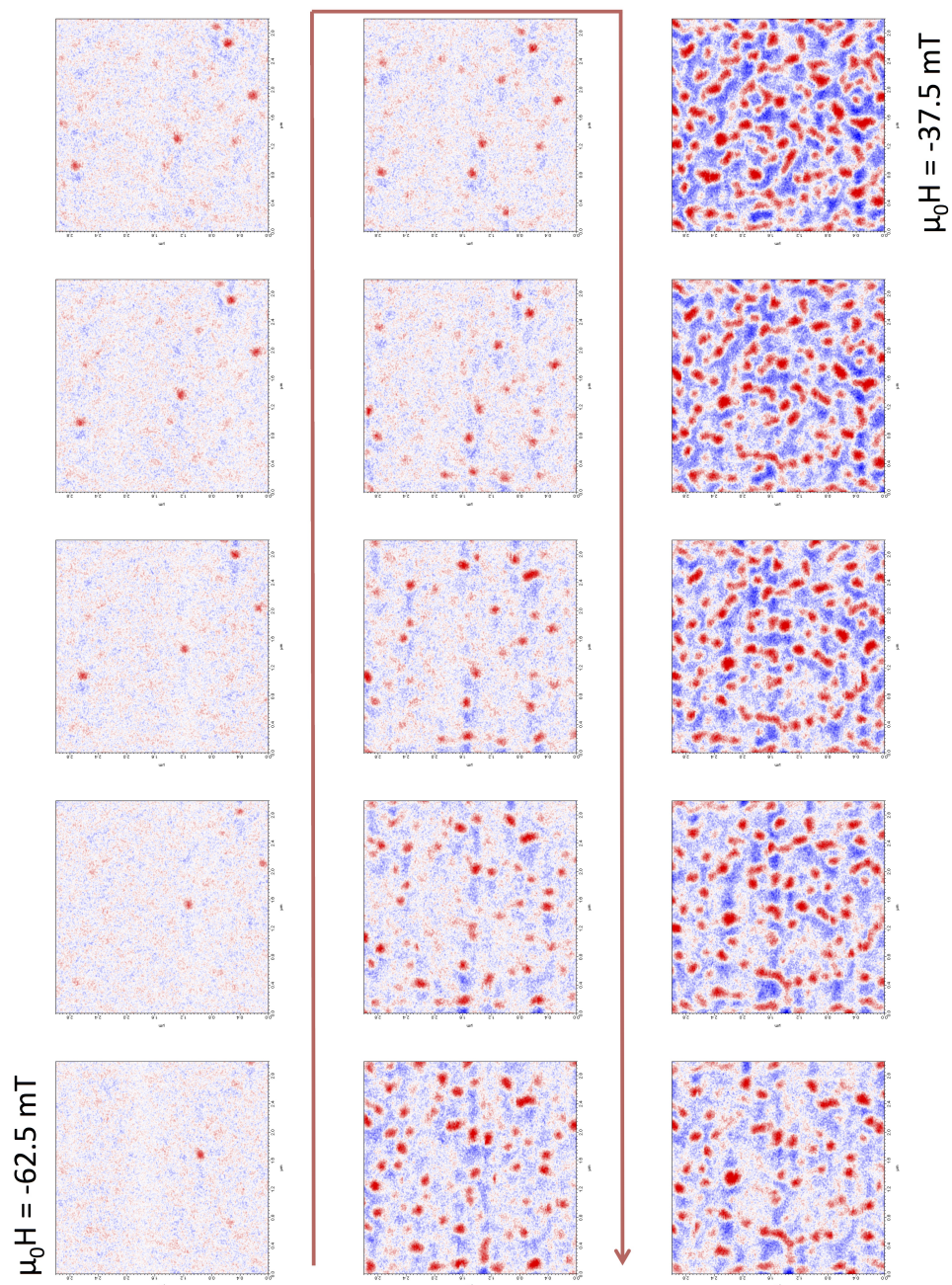


Figure 4.21:  $3 \times 3 \mu\text{m}^2$  MFM images of  $\{\text{Ir}|\text{Co}|\text{Pt}\}$  sample from  $-62.5 \text{ mT}$  to  $-37.5 \text{ mT}$  with  $2.5 \text{ mT}$  steps of out-of-plane magnetic field.

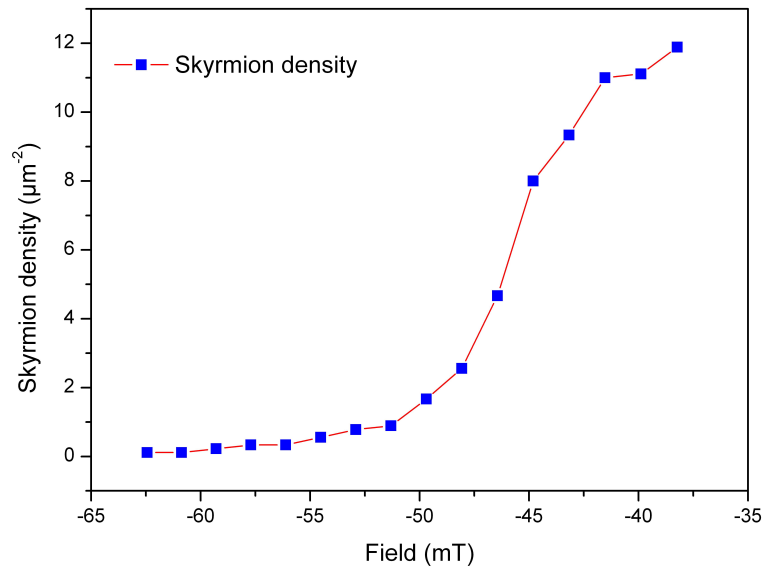


Figure 4.22: Evolution of the skyrmion density of {Ir|Co|Pt} sample with out-of-plane magnetic field

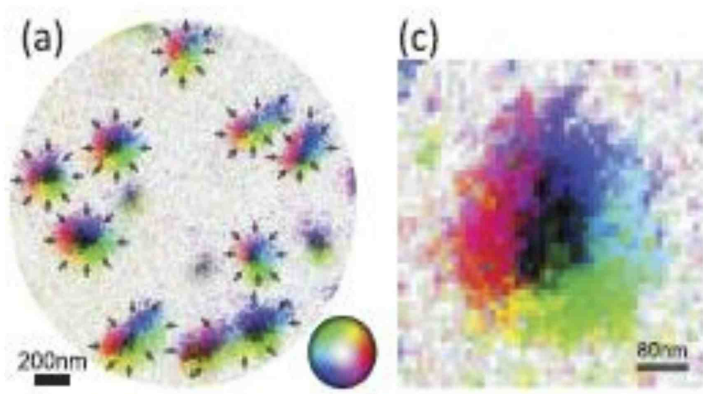


Figure 4.23: spin-polarized LEEM (SPLEEM) imaging for the investigation of the skyrmion ground state at room temperature of continuous films of Ni15ML|Cu x|Ni2ML|Fe2–3ML.[134]

**Spin-Polarized Low-Energy Electron Microscopy** G. Chen et al. [134] describe the use of Spin-Polarized Low-Energy Electron Microscopy (SPLEEM) imaging. In LEEM, real-time observations of dynamic processes at surfaces are possible, such as magnetic microstructure. SPLEEM introduces an additional physical dimension by allowing control of the spin-polarization of the electron beam. Spin-Spin coupling of illumination electrons with electrons in the sample generates new contrast mechanisms that permit imaging of magnetic properties and phenomena. They have investigated skyrmion ground states at room temperature of continuous films of Ni(15ML)|Cu (x)|Ni(2ML)|Fe(2–

3ML) (with different thicknesses of the Cu layer) multilayers grown on Cu(001) substrates (Figure 4.23). Here, multiple skyrmions with a size of  $\sim 200$  nm were stabilized (at no applied out-of-plane magnetic field). A spatial resolution of about 20 – 30 nm can be deduced from the reported SPLEEM images. It is noteworthy to stress out that the in-plane components of the skyrmion domain walls could also be completely resolved by the SPLEEM imaging.

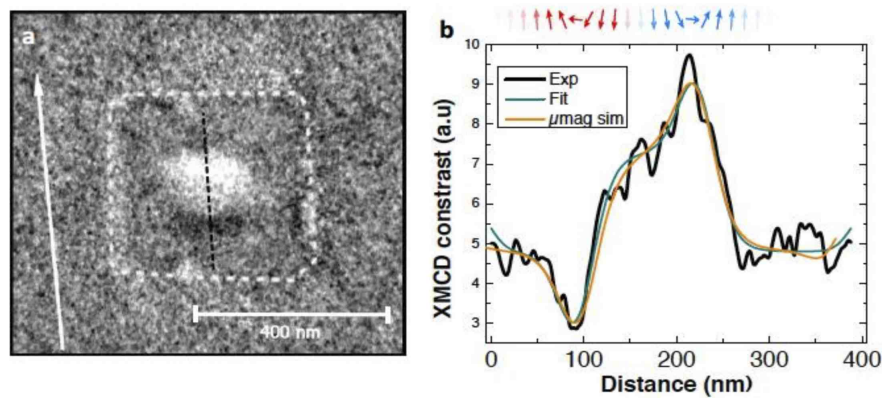


Figure 4.24: (a) XMCD-PEEM image of a 420 nm square dot (indicated by the dotted line) and (b) line scan along the dotted black line (black line) on a Pt|Co|MgO. The blue line in (b) is a fit to the data using a Gaussian convoluted 360 deg DW profile. The orange line is the contrast predicted by the micromagnetic simulations for a left-handed skyrmion. [125]

**PhotoEmission Electron Microscopy (PEEM)** O. Boule et al. [125] investigated micrometer-sized structures (fabricated by electron-beam lithography followed by ion milling) with different geometries out of thin films of Ta<sub>3</sub>|Pt<sub>3</sub>|Co<sub>0.5-1</sub>|MgO x|Ta<sub>1</sub> multilayers exhibiting interfacial DMI with XMCD-PEEM imaging at room temperature. The group reports left-handed Néel magnetic skyrmion. The analysis of the XMCD-PEEM images allows deducing a skyrmion diameter of 130 nm as seen on Figure 4.24. The comparison with experiments allowed the authors to highlight that not only the interfacial DM but also the magnetostatic interaction play an important role to determine the skyrmion size, even in the case of ultrathin magnetic films. Spatial resolutions down to 25 nm were reported for XMCD-PEEM imaging.

**STXM and MXM** S. Woo et al. [135] investigated multilayered {Pt<sub>3</sub>|Co<sub>0.9</sub>|Ta<sub>4</sub>}<sub>15</sub> and {Pt<sub>4.5</sub>|CoFeB<sub>0.7</sub>|MgO<sub>1.4</sub>}<sub>15</sub> exhibiting interfacial DMI with STXM imaging (with reported spatial resolutions of about 25 nm - Figure 4.25). Here, the groups use X-ray imaging similar to our approach. This technique has advantages in imaging not only statically but also in imaging the dynamics of magnetic domains (here, skyrmions). Both

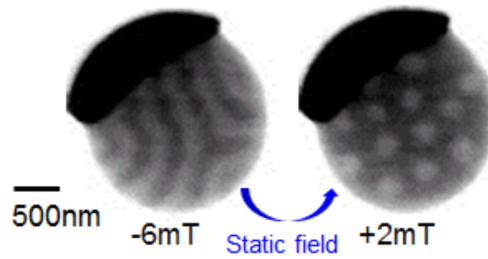


Figure 4.25: STXM investigation of  $\{\text{Pt}3|\text{Co}0.9|\text{Ta}4\}_{15}$  and  $\{\text{Pt}4.5|\text{CoFe}0.7|\text{MgO}1.4\}_{15}$ . By applying magnetic field, the group has been able to image magnetic worm domains and magnetic skyrmions.[135].

isolated magnetic skyrmions and hexagonal magnetic skyrmion lattices were observed for these multilayered materials at room temperature. Room temperature observation of multiple skyrmions of relatively large diameter (around 400 nm) in 2 –  $\mu\text{m}$ -diameter disks is reported.

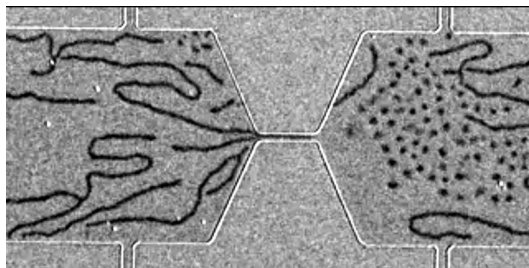


Figure 4.26: Kerr investigation of  $\text{Ta}5|\text{CoFe}1.1|\text{TaOx}3$  multilayers.[109]

**Kerr Microscopy** Magneto-optical imaging techniques, such as Polar Kerr microscopy, has also been employed for the investigation of skyrmionic bubbles, as reported in the publication of W. Jiang et al. [109]. However, due to the relatively low spatial resolution achievable by optical microscopy (diffraction limited), this technique is limited to the analysis of micrometer-sized skyrmionic bubbles. In the work, microstructures of  $\text{Ta}5|\text{CoFe}1.1|\text{TaOx}3$  multilayers were analyzed by dynamical Kerr microscopy (with temporal resolutions on the  $10^{-1}$  s timescale). The stabilization of multiple skyrmions (not organized in a lattice) of diameters varying between 700 nm and  $2\mu\text{m}$  (dependent on the magnitude of the externally applied out-of-plane magnetic field) was reported.

**MFM** MFM has also been used to image magnetic skyrmions, as reported in the work of A.Soumyanarayanan et al. [136] and M. Baćani and coworkers [137]. As seen in this work, we have already completed a full imaging study of multilayers with MFM tuning their properties by engineering number of layers and interfaces. It is also noteworthy

that the evolution of the density of skyrmions with the applied magnetic field has the same trend than in our study. They have investigated  $\{\text{Ir}_1|\text{Fe}_x|\text{Co}_y|\text{Pt}_1\}_{20}$  ( $x$  between 0 and 0.6 nm, and  $y$  between 0.4 and 0.6 nm) multilayer stacks, and imaged by MFM (typical spatial resolutions of about 30-50 nm, strongly dependent on the lift height of the MFM tip) and MTXM. Both isolated skyrmions and hexagonal skyrmion lattices were observed at room temperature, with reported skyrmion diameters between 50 and 70 nm (dependent on the magnitude of the externally applied out-of-plane magnetic field). A key point materializing in the community is the tunability of the magnetic skyrmions.

**Conclusion** As seen in all the previous paragraphs, we have seen that similar work with similar or different techniques were lead to investigate, image and try to tune magnetic isolated skyrmions in ultra thin multilayers. Skyrmions with similar sizes (or larger) were also reported.

## 4.4 Perspective: Moving small skyrmions in nanotracks

**Background** Magnetic skyrmions might become the basic building block of a new generation of spintronic devices only if they can be easily inserted in real devices and can be moved or excited at low energy costs. Jonietz et al. observed a current-induced rotation of the orientation of the skyrmion lattice in a B20 MnSi crystal. Recently, current-induced motion of skyrmions was imaged by Yu et al. [92] using Lorentz microscopy. It is established that there is a correlation between the current-induced motion of the skyrmion lattice in MnSi and the deviation  $\Delta\rho_{xy}$  of the Hall resistivity from the normal behavior, from which the skyrmion velocity can be estimated (Figure 4.27). Two important comments can be formulated. First, the current densities required to move skyrmions lattices are very small, a few  $10^6$  A/m<sup>2</sup>, which is about  $10^5$  to  $10^6$  smaller than current densities needed to move DWs ( $\sim 10^{11}$  to  $10^{12}$  A/m<sup>2</sup>). Second, the skyrmion velocities in Figure 4.27 are small ( $\sim 10^{-4}$  m/s), and a linear extrapolation indicates that a current density as large as for DWs ( $\sim 10^{11}$  to  $10^{12}$  A/m<sup>2</sup>) would be necessary to reach typical DW velocities of 10-100 m/s. This reflects the fact that the motion is due to the same spin-transfer mechanism in both skyrmions and DWs, and follows the same spin-conservation rules. However, we stress that the important difference is that the depinning current,  $j_c$  in Figure 4.27, is greatly reduced in the case of skyrmions, allowing them to move with small currents and small speeds.

For the theory of current-induced motion of skyrmions, we refer to the work of Schultz et al. [94] that is based on Berry phase arguments, and of Everschor et al. [138, 96] that uses the Thiele equation to describe the spin dynamics induced by spin torque. Iwasaki et al. [97] compare predictions from the Thiele equation with numerical simulations directly based on the Landau–Lifshitz–Gilbert equation with spin-transfer terms for different non collinear configurations including a skyrmion lattice. They presents the results of simulations with and without pinning, as well as for different values of the damping

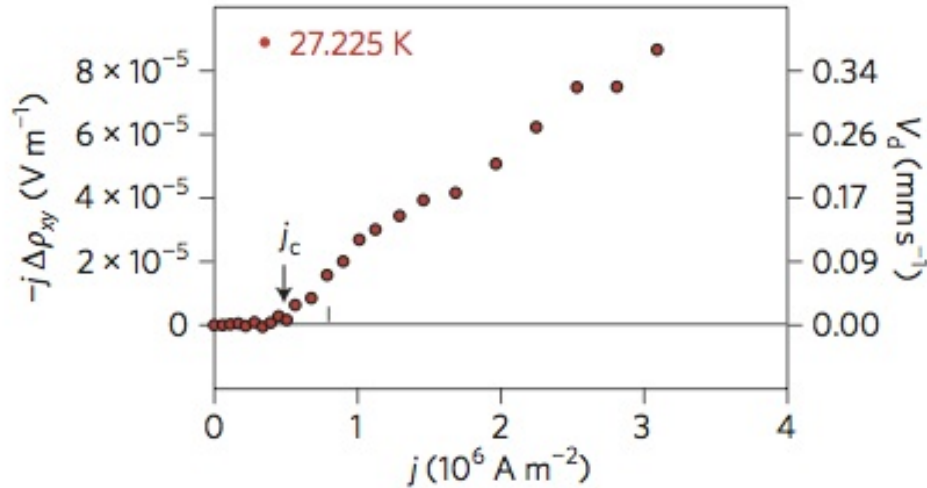


Figure 4.27: Skyrmion velocity. Deviation of the MnSi Hall resistivity from the normal behaviour (left y-axis), and the calculated corresponding velocity of the skyrmion lattice along the current direction (right y-axis) as a function of the current  $j_c$ , depinning current.[92]

coefficient  $\alpha$  and the non-adiabatic coefficient  $\beta$  of the spin-transfer torques.

As the only results on current-induced motion are for skyrmion lattices, micromagnetic simulations have been performed for individual skyrmions with a modified OOMMF code [50], see also Figure 4.28). It turns out that from these new calculations:

- metastable (stable) individual skyrmions can be found in a stable (metastable) ferromagnetic state,
- they can be moved by a current along narrow stripes with large velocities, identical to those of current driven DW motion,
- realistic strong pinning sites give rise to depinning currents that are larger than those derived from Hall effect measurements [94] or simulations [97] with skyrmion lattices but are still much smaller than in most experiments with DWs,
- the generation of skyrmions in tracks similar to those in Figure 4.28 is the next important experimental challenge on the way towards realizing devices. At present, we are using the same types of simulation to test several possible mechanisms.

**Observation by MFM** Very preliminary experimental observations have also been obtained by Post-Doc Davide Macarriello and new PhD Student William Legrand. New

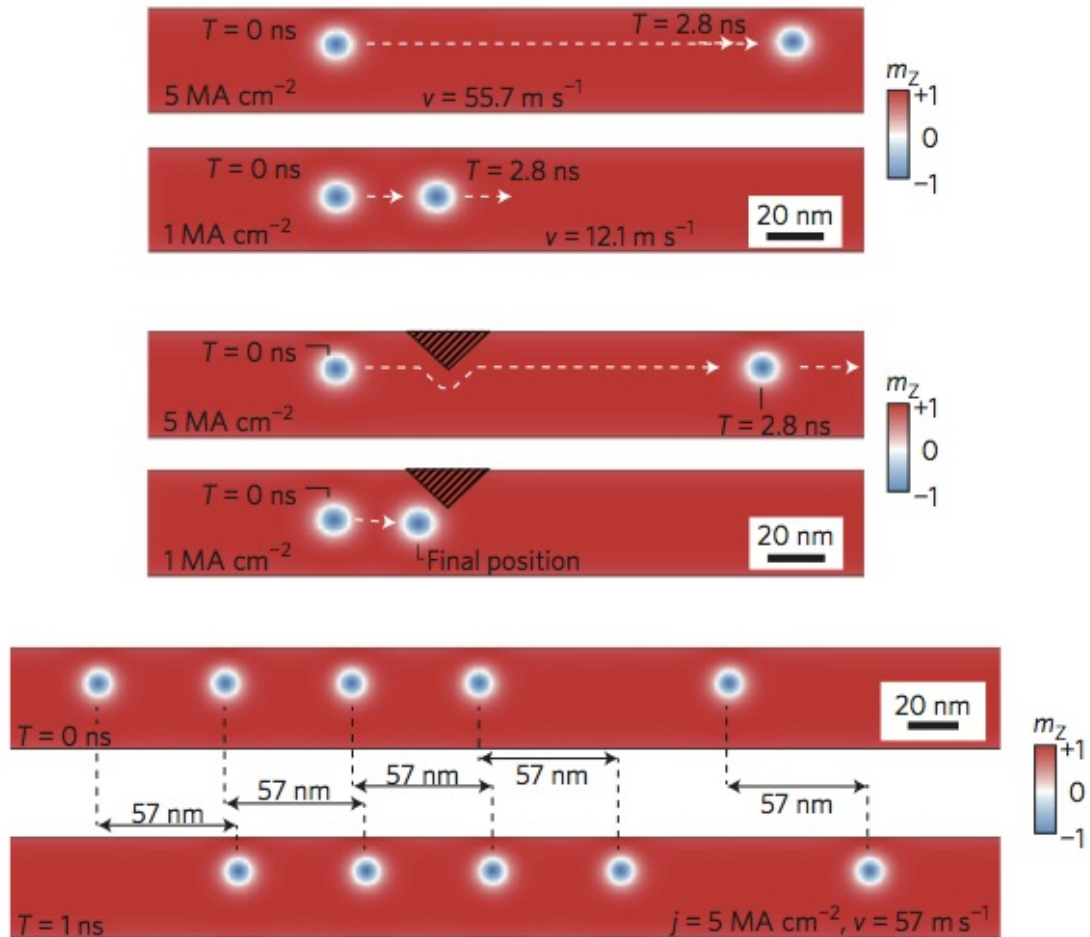


Figure 4.28: Micromagnetic simulations of current-induced motion of individual skyrmions or chains of skyrmions in  $500 \times 40 \times 0.4 \text{ nm}^3$  Co stripes with DMI of  $1.4 \text{ meV}$  per atom for the interface atoms and the different spin current densities indicated. The positions are indicated at  $t = 0$  and either  $t = 2.8 \text{ ns}$  or  $1 \text{ ns}$ , the corresponding velocity is also shown. (**top, middle**) Individual skyrmions in perfect stripes (**top**) and stripes with pinning (**middle**) shown by the shaded triangle of enhanced anisotropy ( $j_c$  is between the two current values). (**bottom**), Individual skyrmions and chains of skyrmions exhibit the same velocity. The spacing between skyrmions can be smaller than shown in the figure and of the order of their diameter. The color scale shows the out-of-plane component of magnetization,  $m_z$ . [50]

samples were designed for this purpose, to improve the stacking, allowing better electrical flow. We present here the results obtained on  $\text{Ta5|Pt10|}\{\text{Co0.8|Ir1|Pt1}\}_{20}\text{|Pt}x$ . Several changes were performed on this sample compared to the one studied by STXM: a 5 nm-thick layer is added to the usual 10 nm-thick buffer layer, Pt and Ir have been exchanged (platinum is now under the cobalt layer, enabling the electrons' flow through the sample), Co thickness has increased and the number of repetition of the main trilayer is 20 (instead of 10 in the study by STXM/MFM reported above). Nonetheless, it was possible to observe isolated magnetic skyrmions under applied out-of-plane magnetic field by MFM.

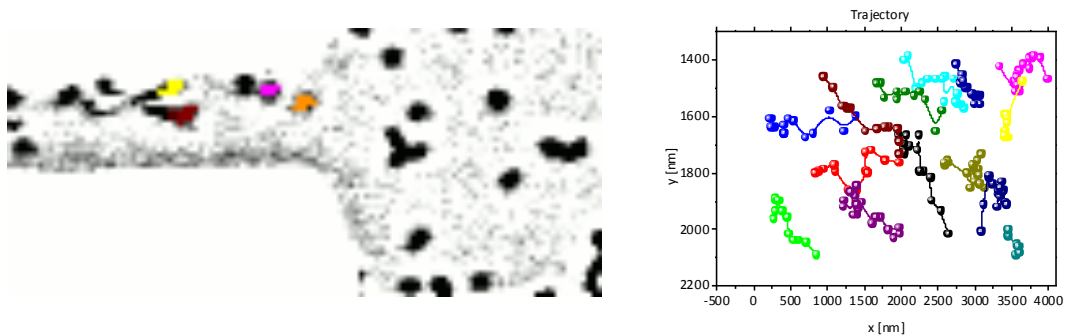


Figure 4.29: **(left)** MFM image. A post treatment enables the coloration of skyrmions to facilitate the visualization of the skyrmions trajectory. **(right)** Trajectories of the skyrmions. The colors correspond to the color attributed to the skyrmion in the treatment of the MFM images.

We have lithographed a structure as seen in Figure 4.29 so the skyrmion could move in the micrometer wide stripe and the larger form on the right of this track would become a large area of skyrmions. Pulses of 200 ns and  $2.10^{11}$  A/m<sup>2</sup> are generated so the electron flow is coming from the left of the track to the nucleation side. We observe here what seems to be an opposite direction of longitudinal skyrmion motion for opposite current sign. And finally, as seen on Figure 4.29, we have deduced a skyrmion velocity of  $\sim 0.5 - 1$  m/s, which is a moderate value compared to Woo et al. [135] or Hrabec et al. [139]. But, in the work of Woo et al., skyrmions may move faster ( $\sim 100$  m/s) but are significantly larger in size ( $\sim 1$   $\mu\text{m}$  of diameter) ; same configuration in the work of Hrabec et al with velocities up to 60 m/s for skyrmions of 300 nm diameter.

These observations are very good preliminary results on the motion of small skyrmions in racetracks. Several paths to improve the motion are being investigated, as well as for transport characterization of skyrmion based multilayered systems.

## Chapter 5

# Quantitative estimation of the interfacial chiral interaction

### Contents

---

|                                                                                          |            |
|------------------------------------------------------------------------------------------|------------|
| <b>5.1 Principles</b> . . . . .                                                          | <b>105</b> |
| 5.1.1 Introduction . . . . .                                                             | 105        |
| 5.1.2 Determination of $D$ using mean domain periodicity after demagnetization . . . . . | 106        |
| 5.1.3 Determination of $D$ using the evolution of skyrmion size with field . . . . .     | 106        |
| <b>5.2 DMI amplitude estimated with mean domain width</b> . . . . .                      | <b>107</b> |
| <b>5.3 Estimation with the evolution of skyrmions with out-of-plane field</b> . . . . .  | <b>109</b> |
| 5.3.1 Plain films . . . . .                                                              | 109        |
| 5.3.2 DMI estimation in nanostructures . . . . .                                         | 113        |
| 5.3.3 Influence of the proximity effect . . . . .                                        | 114        |
| <b>5.4 Conclusions</b> . . . . .                                                         | <b>121</b> |

---

We develop two main approaches to estimate the interfacial chiral interaction (DMI) amplitude in our systems, both of them based on the comparison between the experimental datas and micromagnetic simulations under the same conditions. The first one concerns the study of the mean domain periodicity of the system at remanence and the other one of the evolution of the skyrmion size with applied out-of-plane magnetic field.

## 5.1 Principles

### 5.1.1 Introduction

All the micromagnetic simulations were performed on MuMax3 [140]. These simulations are using as inputs some experimental values: the magnetization at

saturation, anisotropy energy and exchange stiffness. The magnetization at saturation and the anisotropy energy are usually obtained by normalizing the value found by AGFM and/or SQUID with the total Co thickness, meaning that we are not taking into account any induced proximity effect. However, in the following chapter, we have studied the influence of the induced proximity effect on the amplitude of the DMI.

Moreover, as seen in the previous chapter, we have estimated  $A$  to be around 10 pJ/m in our samples. Nonetheless, for the determination of the DMI amplitude in the asymmetric sample described in the previous chapter, we have decided to compare the experimental results with three series of simulations obtained with different exchange parameters that range from 15 down to 5 pJ/m.

### 5.1.2 Determination of $D$ using mean domain periodicity after demagnetization

For the approach considering the mean domain periodicity at remanence, we have considered a  $1.5 \times 1.5 \mu\text{m}^2$  square region with the experimental values for the magnetization and the anisotropy constant. We have tried different techniques to evaluate  $D$  from remanent magnetic configuration. Our first idea was to simulate the width of regular stripe domains and minimize the total energy of the system. For each value of  $D$ , we obtain a certain domain width periodicity that minimize the energy of the system and hereby we obtain the evolution of the mean domain periodicity with the DMI amplitude. Difficulties have emerged from this approach. The main one is that the experimental domains observed differ from regular stripe pattern and therefore the simulations don't rely on experimental observations. Therefore, we have chosen to work with a different initial state: an image of the sample after demagnetization provided by STXM or MFM imaging is uploaded and chosen in the simulation as initial state. We then relax the system so that the energy is minimized, for different amplitudes of DMI. For each DMI magnitude, the mean domain periodicity of the final state is obtained (as for the experimental data) by Fourier-Transformation. A comparison between the simulated evolution of the mean domain width with DMI amplitude and experimental data give an estimation of the DMI magnitude in the system.

We note that the approach taking regular stripes domains gave us smaller values of  $D$ , result also reported in the work of Baćani et al [137].

### 5.1.3 Determination of $D$ using the evolution of skyrmion size with field

For the approach considering the evolution of an isolated skyrmion under applied magnetic field, we consider a square region of  $500 \times 500 \text{ nm}^2$  with the experimental values obtained for the magnetization at saturation and the anisotropy constant, just as in the previous approach. The initial state is an isolated skyrmion under no magnetic field. Then we apply perpendicular magnetic field and make the system relax until minimizing its energy. We record the size of the skyrmion for different values of the magnetic field and reproduce the simulations for different magnitudes of DMI.

**With MFM images** Mumax3 has built-in generation of MFM images from a 2D magnetization. The MFM tip lift can be freely chosen. By default the tip magnetization is modeled as a point monopole at the apex. This is sufficient for most situations. Nevertheless, it is also possible to model partially magnetized tips by setting MFMDipole to the magnetized portion of the tip, in meters. In this study, we have considered that the MFM tip as a point monopole.

This means that, at the end of the simulation, we are no longer only recording the map of magnetization, but we are also generating a simulated MFM image corresponding to the MFM lift height that we have used as input. The general lift height chosen for imaging all the samples is 20 nm. We record the size of skyrmions after the generation of the MFM image, for different values of the magnetic field applied and  $D$ .

Again, comparison between the simulated evolution of the skyrmions size with applied magnetic field for several values of  $D$  and experimental data lead to the determination of the DMI magnitude in our samples.

## 5.2 DMI amplitude estimated with mean domain width

As shown in Figure 5.1, we have measured the average domain periodicity in  $\{\text{Ir}|\text{Co}|\text{Pt}\}$  system to be  $106 \pm 20$  nm. The same analysis was made for  $\{\text{Co}|\text{Pt}\}$  sample, and led to a mean domain periodicity of  $303 \pm 30$  nm. In Figure 5.1, these experimental values are compared with those obtained in a series of micromagnetic simulations as a function of the DMI, which allows an estimation of  $|\mathbf{D}|$ , as explained in the previous section.

From this approach, we find that the DMI is about  $1.6 \pm 0.2 \text{ mJ/m}^2$  for the asymmetric multilayers or  $0.2 \pm 0.2 \text{ mJ/m}^2$  for the symmetric sample.

This first approach lead to some conclusions:

- The value found for  $\{\text{Co}|\text{Pt}\}$  sample confirms that because the two interfaces around the Co layer are the same, the two components of DMI are almost compensating and the average DMI is close to zero. However, since the growth of Co on top of Pt is different from the growth of Pt on top of Co (the roughness at the interfaces is not the same for example: 0.08 nm for Co|Pt compared to 0.02 nm for Pt|Co), the two interfaces are not strictly equal and it may explain why the average DMI found for  $\{\text{Co}|\text{Pt}\}$  sample is close to zero but not equal to zero.
- The value found for  $\{\text{Ir}|\text{Co}|\text{Pt}\}$  sample is a very large value of DMI amplitude and confirms that the magnetic skyrmions observed in the previous chapter are stabilized mainly by a strong DMI.
- This technique, relying on a single experimental image, gives a first estimation of the DMI amplitude. To improve the precision of this value, we have developed another approach, as explained in the following section. However, we will show

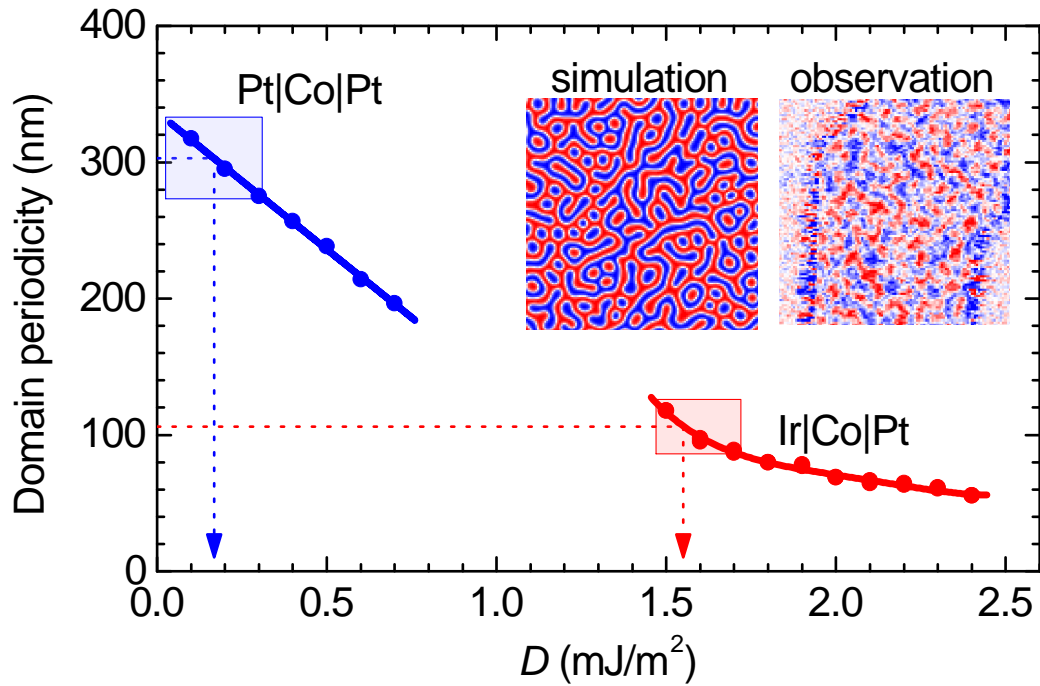


Figure 5.1: Micromagnetic simulations and experimental measurements of mean domain-width evolution with DMI after demagnetization. Comparing the simulation with experimental domain-width value (dotted horizontal line) allows us to estimate  $|\mathbf{D}|_{\text{Ir|Co|Pt}} = 1.6 \pm 0.2 \text{ mJ/m}^2$  and  $|\mathbf{D}|_{\text{Pt|Co|Pt}} = 0.2 \pm 0.2 \text{ mJ/m}^2$ . The box height represents the error margins on the experimental domain-size evaluation; its width gives the resulting error on  $|\mathbf{D}|$  for the used simulation parameters. The inset shows a simulated worm pattern for  $|\mathbf{D}| = 1.6 \text{ mJ/m}^2$  in Ir|Co|Pt ( $1.5 \times 1.5 \mu\text{m}^2$ ) and a corresponding experimental observation at the same scale.

that this first approach lead to a value that is very similar to the one found with the next approach.

## 5.3 Estimation with the evolution of skyrmions with out-of-plane field

### 5.3.1 Plain films

#### 5.3.1.1 With STXM experiments

Since no skyrmions/bubbles have been observed in {Co|Pt} sample, we focus our efforts here on {Ir|Co|Pt} sample.

We compare in Figure 5.2 the experimental data for the field dependence of the size of the skyrmions with micromagnetic simulations of DMI-induced skyrmions. The simulated diameters versus out-of-plane magnetic field curves that correspond to different values of the DMI are compiled in Figure 5.2. Here, we have chosen to perform the simulations for three different values of  $A$  to point out the influence of the exchange stiffness in the estimation of the DMI value.

It is noteworthy to point out that, with the DMI taken into account and whatever the value of  $A$ , bubble-like configurations relax for  $|\mathbf{D}| \geq 1 \text{ mJ/m}^2$  in a stable configuration of an isolated skyrmion having a winding number equal to 1. With the smallest exchange constant  $A = 5 \text{ pJ/m}$ , isolated skyrmions are not stable in our range of magnetic field for DMI magnitude larger than  $1.6 \text{ mJ/m}^2$ , and deform into labyrinth-worm structures. Thus, we considered that the exchange constant in our system is closer to the intermediate value of  $10 \text{ pJ/m}$ . For this value, the best agreement between the experimental size of skyrmions with the micromagnetic simulations lead to an estimation of the DMI magnitude of  $1.9 \pm 0.1 \text{ mJ/m}^2$ .

This value is close, but larger than the value found with the previous approach. The difference between the two approaches could come from the fact that when considering the mean domain width, the experimental data are represented by a single value. In the case of the evolution of the skyrmion size with applied out-of-plane magnetic field, there are several experimental points to compare with the micromagnetic simulations, hence the difference of amplitude between the two approaches is not incompatible and one would believe that the actual value should be closer to the one estimated by the skyrmion size evolution. Moreover, this value is in good agreement with theoretical predictions that add the DMI magnitudes predicted for Pt/Co (three monolayers) and Ir/Co (three monolayers) [107].

Actually, this range of DMI is indeed close to optimal for the stabilization of isolated skyrmions instead of skyrmions lattices. Indeed, the critical value for  $D$  is  $D_c = 2.1 \pm 0.2 \text{ mJ/M}^2$ , by using the experimental values obtained for the magnetic parameters. Finally, this approach is along the lines of the experimental characterization of skyrmions developed by Romming et al. [80], in which the evolution of the size and shape of

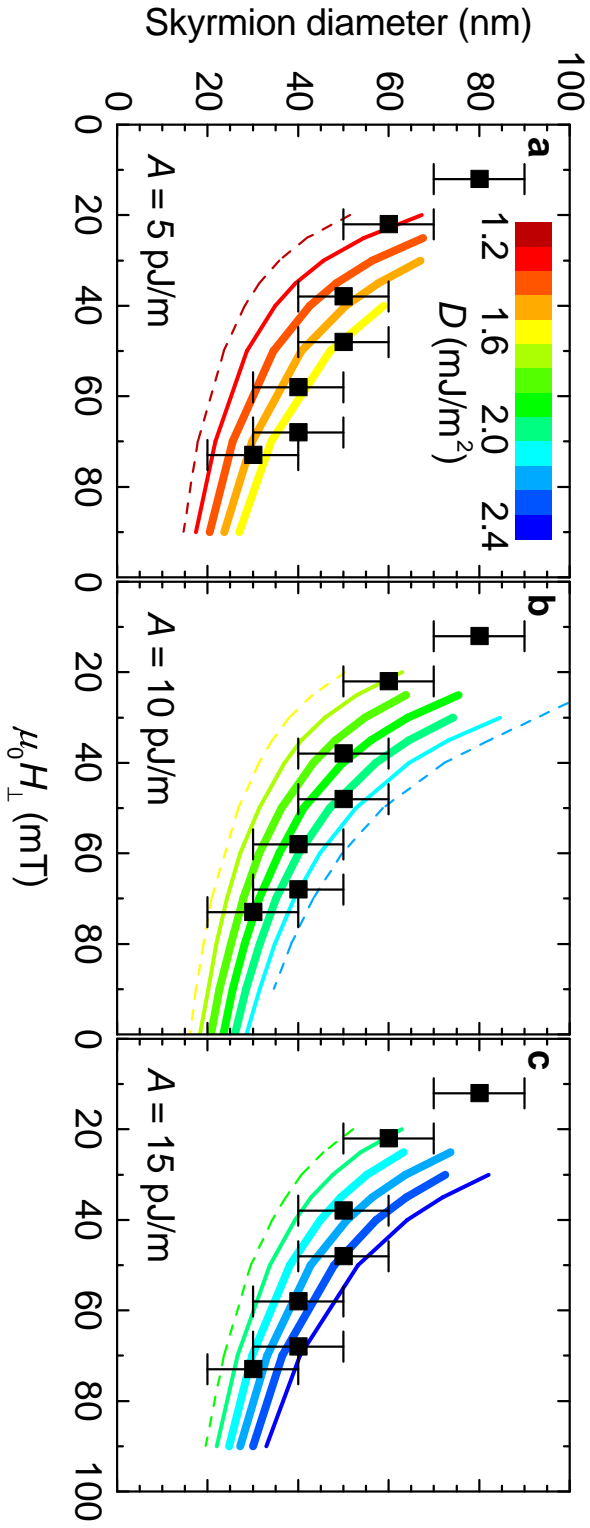


Figure 5.2: Skyrmion diameter as a function of the external out-of-plane magnetic field  $H_{\perp}$ . Experimental diameters (squares) can be compared with micromagnetic simulations for different values of  $|D|$  (lines) and different values of the exchange interaction  $A$  (panels). Simulations were obtained in the case where the induced proximity effect is not taken into account. For  $A = 5$  pJ/m, circular skyrmions are stable for  $|D| \geq 1.7$  mJ/m<sup>2</sup> and deform into labyrinthic worm-like structures. The deviation of the data compared with the simulations at a low field can be explained by the interaction with the other domains.

skyrmions as function of the magnetic field is proposed to compare experimental spin-polarized scanning transmission microscopy images with theory.

**Comparison with results of other groups** This large DMI is comparable, for example, with that derived recently in Pt|Co|AlO<sub>x</sub> trilayers from asymmetric domain-nucleation experiments [141], domain wall annihilation, non-reciprocal spin wave propagation and scanning microscopy [142]. More precisely, M. Belmeguenai et al. have studied Pt|Co|AlO<sub>x</sub> trilayers with varying Co thicknesses and the DMI amplitudes are found between  $|D| = 2.71 \pm 0.16$  mJ/m<sup>2</sup> for 0.6 nm of Co, and  $|D| = 1.57 \pm 0.18$  mJ/m<sup>2</sup> for 1.2 nm of Co. These DMI amplitudes were much larger than what was measured on perpendicularly magnetized Pt|CoFeB ( $|D| \sim 1$  mJ/m<sup>2</sup> [143]) for example. Even more recently, O. Boulle et al. [125] worked on Pt|Co|Pt|MgO trilayers and report a very large DMI amplitude estimated by BLS:  $|D| = 2.05 \pm 0.3$  mJ/m<sup>2</sup>, which is the highest reported value so far for sputtered magnetic ultrathin film. However, it is also noteworthy to point out that the value found for our sample is comparable to what is found by BLS, but still, the structure of the sample is quite different. Aside from the fact that Co is sandwiched between a heavy metal and an oxide (compared to two heavy metals in our systems), in the BLS experiments, only trilayers are studied, meanwhile we have focused on multilayers, here with ten repetitions of the same trilayer. We have tried to perform similar BLS measurements on {Ir|Co|Pt} sample, but due to the repetitions of the trilayer, the results were more complex to analyze, with a DMI amplitude estimated much lower than the value found with the two approaches described above. Moreover, the exchange stiffness needed to fit the experimental data of the BLS had to be taken smaller than 5 pJ/m and we have seen that the SQUID measurement in temperature allowed us to extract an exchange stiffness of  $\sim 10$  pJ/m.

### 5.3.1.2 With MFM experiments

Since we have seen in the previous chapter that we are able to observe isolated magnetic skyrmions at room temperature also by MFM, and it was a concern to study the possibility to estimate in the sample the DMI amplitude with this technique and if it is the case, if the value found is the same as the one extracted with the STXM experiments. From Figure 5.3 we have extracted the size of the skyrmions observable by MFM and compared them with the skyrmion size simulated with Mumax3. The results are presented in Figure 5.4.

From this measurement, we find that the DMI magnitude for {Ir|Co|Pt} sample is found to be  $|D| = 1.9 \pm 0.1$  mJ/m<sup>2</sup>, which is exactly the same value as the one found with the STXM experiments.

We can conclude from this comparison that not only MFM experiments allow us to observe magnetic skyrmions at room temperature; but even more, by comparing the skyrmions size evolution as seen by MFM with simulated skyrmion size with MFMlift, we are able to estimate the DMI magnitude exactly as if we were observing the out-of-plane component of the magnetization of the sample as in STXM experiments.

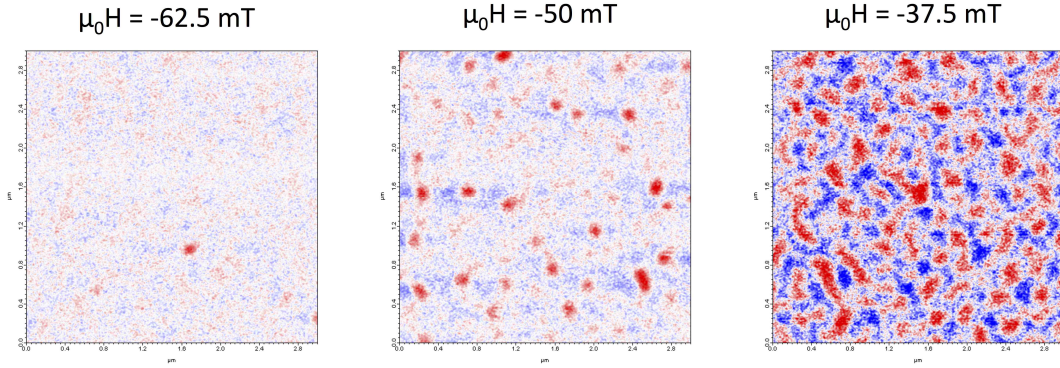


Figure 5.3: MFM  $3 \times 3 \mu\text{m}^2$  MFM images of  $\{\text{Ir}|\text{Co}|\text{Pt}\}$  sample at  $-62.5$  mT,  $50$  mT and  $-37.5$  mT out-of-plane magnetic field.

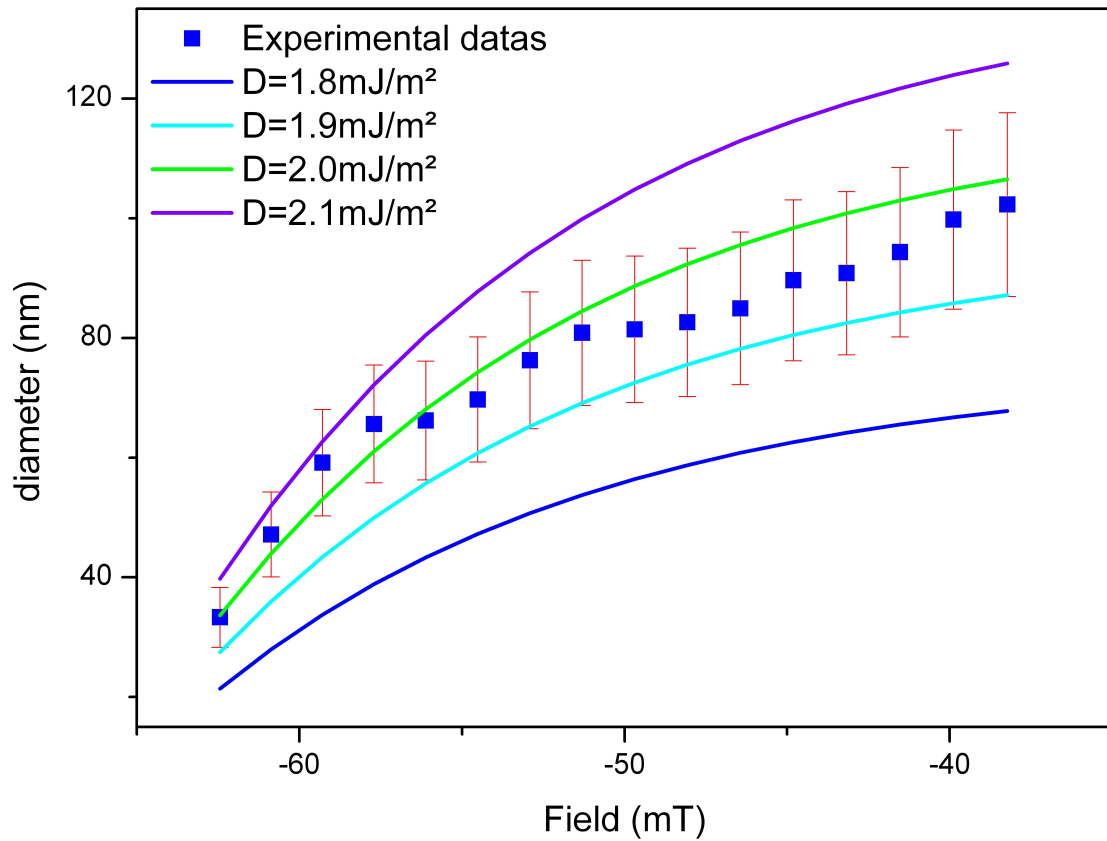


Figure 5.4: Evolution of the skyrmion size observed by MFM in extended film for  $\{\text{Ir}|\text{Co}|\text{Pt}\}$  sample. Magnetic evolution of the skyrmion size derived from micromagnetic simulations realized for  $A = 10$  pJ/m (lines for different amplitude of DMI) and sizes of the observed skyrmions (squares).

### 5.3.2 DMI estimation in nanostructures

As described in the previous sections, we found from two different independent analyses on the magnetic configurations that very large DMI and skyrmions exist at room temperature in asymmetric  $\{\text{Ir}|\text{Co}|\text{Pt}\}_{10}$  multilayered films. Here, we demonstrate that isolated nanoscale skyrmions can be stabilized at room temperature in nanodisks. Figure 5.6 shows the field dependence of the diameter of an approximately circular domain located close to the center of a 500 nm-diameter disk, and this dependence is once again compared to what is obtained in micromagnetic simulations.

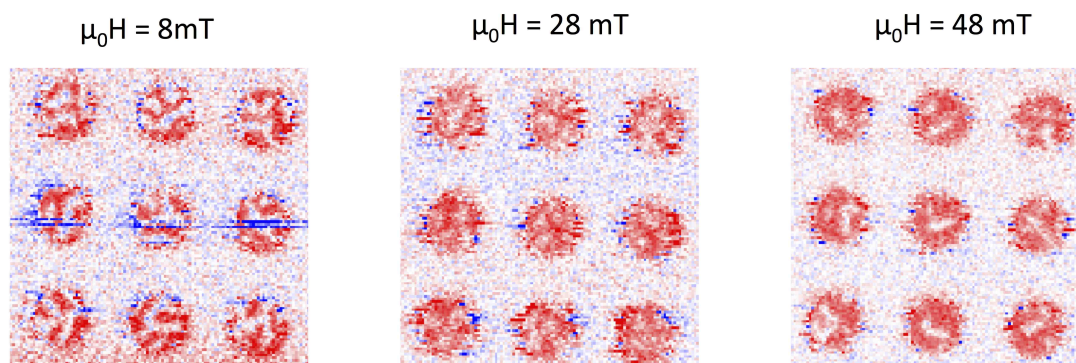


Figure 5.5: STXM imaging of nine nanodisks of 500 nm diameter of  $\{\text{Ir}|\text{Co}|\text{Pt}\}$  sample. Three different external out-of-plane field are presented here: 8, 28 and 48 mT.

Even though the agreement is not as good as the one in extended film shown in Figure 5.2, especially in the low field region, again, a major outcome of these simulations is that it is not possible to stabilize any bubble-like domain in submicrometer-sized disks without introducing large DM values of at least  $1.5 \text{ mJ/m}^2$ . In the low field region, we can explain the less good agreement by the fact that in this field range, skyrmions are no longer alone, but we can observe several ones and a better agreement should be found by simulating several skyrmions in the same area. As the winding number of the simulated circular domain is, after stabilization, always equal to one, we can conclude that the experimental images correspond to nanoscale skyrmions with chirality fixed fixed by the sign of  $D$ .

If we want to try to understand why the agreement is less good in this case, we can notice that, at low field in Figure 4.16, the skyrmions are not completely isolated, but coexist with other skyrmions and/or with labyrinth-shaped domains. Thereby, because of the repulsive interaction between those domains, the skyrmion's size in our experimental structure is lower than the one calculated in micromagnetic simulations where it stands alone in a circular disk.

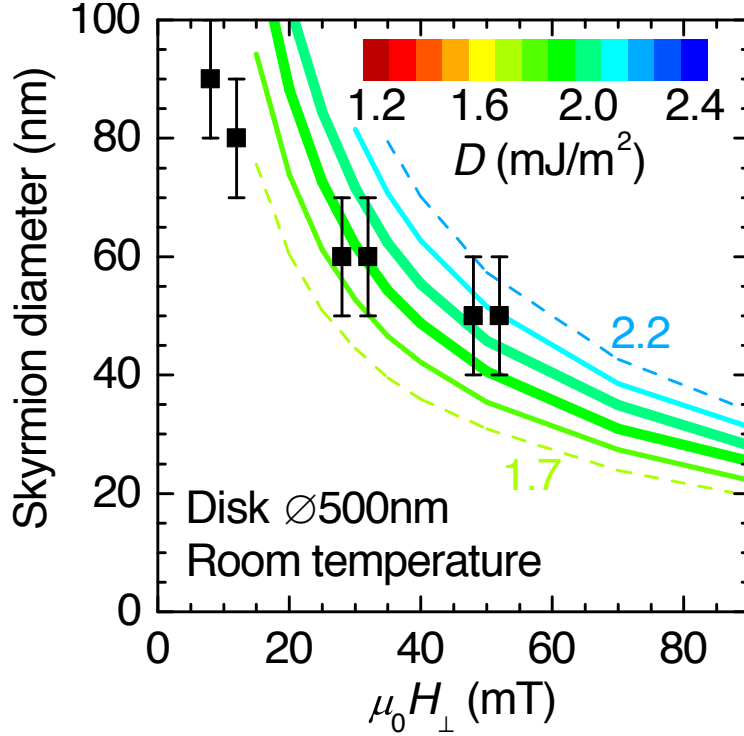


Figure 5.6: Evolution of the skyrmion size in patterned nanoscale disks. Magnetic evolution of the skyrmion size derived from micromagnetic simulations realized for  $A = 10$  pJ/m (lines for different amplitude of DMI) and sizes of the observed skyrmions (squares) for 500 nm-diameter disks.

### 5.3.3 Influence of the proximity effect

#### 5.3.3.1 Proximity induced magnetism in paramagnetic metals

We consider magnetic interactions that can be induced in a material which is usually paramagnetic but can become magnetized under certain conditions. There are a variety of ways that this can occur, for example, alloying the paramagnet with a ferromagnet [144, 145] or forming the paramagnet from nanoparticles [146], but they all originate from local modifications of the electronic density of states and the subsequent satisfaction of the *Stoner criterion*.

Here, we focus on proximity induced magnetism (PIM), and in particular that which occurs in the paramagnetic metals Pt and Ir. The paramagnet can obtain a spontaneous magnetic polarization at the interface with a ferromagnet that generally exists over a length of the order of 1 nm into the paramagnet.

Microscopically, PIM can be explained using a Hubbard model where the interaction energy between atomic sites is given some degree of spatial dependence [147]. From *ab initio* calculations, it was demonstrated that the induced moment can be attributed to orbital hybridisation between the ferromagnet and the paramagnet [148]. An enhanced density of states would then lead to Stoner enhanced paramagnetism in the non-magnetic layer.

In an x-ray magnetic circular dichroism study by Wienke *et al.* [149], it was found that all the *5d* series of elements take on some form of polarisation when introduced as

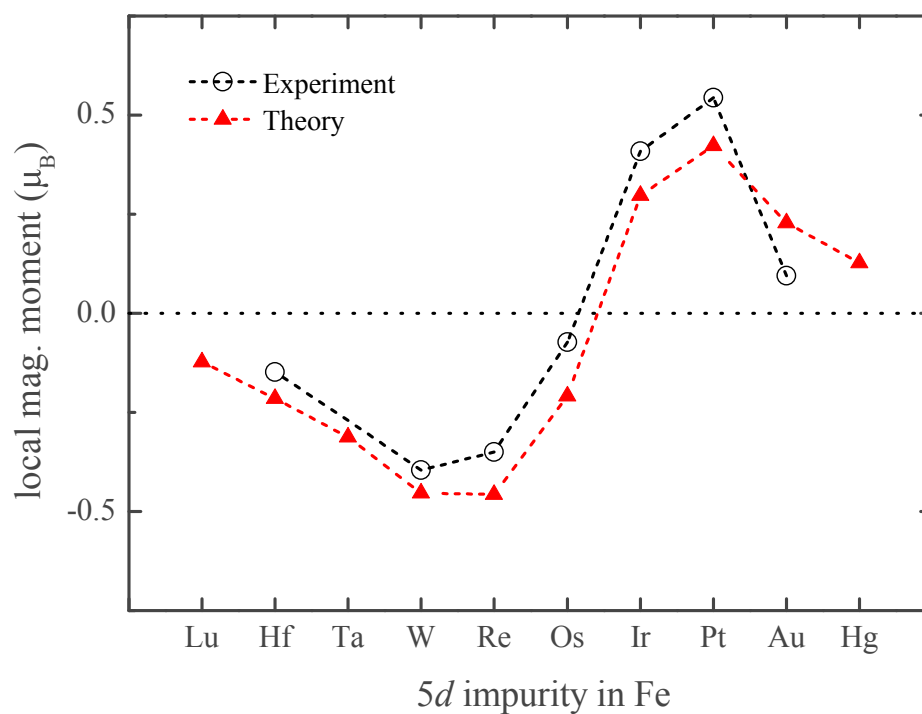


Figure 5.7: Magnitude of proximity induced moment and sign relative to the host Fe ferromagnet for 5d transition metal impurities. The measured moments from experiment are sourced from reference [149] and the theoretical values from reference [150]

an impurity within Fe. It can be seen from Figure 5.7 that the coupling between the impurity and the local moment changes from antiferromagnetic to ferromagnetic between Os and Ir. The reason for this is related to whether spin up or spin down electrons form the majority species from the spin-polarised density of states for the impurity [150]. It can also be seen that there is significant polarization of Pt, as expected from the Stoner enhanced paramagnetism.

These heavy metal elements, in particular Pt, are used regularly within the field of spintronics due to their significant SOI, which as discussed, gives rise to interesting phenomena such as the DMI. Connections are now beginning to be drawn between the interfacial PIM and these phenomena. In particular work by S. S. P. Parkin [151] has suggested a strong correlation between the DMI and PIM from observations of current-induced domain wall motion within perpendicularly magnetized Pt|Co|Ni|Co structures. However, *ab initio* calculations are in disagreement with this result, finding no link between PIM and DMI [107].

When Pt is deposited adjacent to a ferromagnet, a spontaneous magnetic polarisation of the Pt arises at the interface that persists through the first few atomic layers of Pt [105, 152, 153, 154, 155, 156]. This proximity induced magnetism (PIM) in Pt is associated with the large *Stoner factor* associated with higher-d transition elements. Some of the earliest indications of PIM came from the enormous moments measured in FePd alloys [144, 145]. Here the moment was too large to be accounted for by the itinerant ferromagnetism of Fe alone and the ferromagnetism persisted down to Fe concentrations as low as 1.25 at.% [144].

With the observations of perpendicular magnetic anisotropy in Pt/Co multilayers [157, 158] the role of interfacial PIM became of great interest with regard to these phenomena [159, 160].

Furthermore, the development of x-ray magnetic circular dichroism (XMCD) [161] opened up a method by which PIM could be measured directly. One of the first uses of XMCD was to study PIM in Pt/Co multilayers, which showed that there existed undoubtedly a significant induced moment in Pt [162, 163]. Subsequently numerous other studies using XMCD confirmed the existence of some degree of PIM across the entirety of the 5d transition elements, either in thin film multilayers or impurities in a ferromagnetic matrix [105, 149, 164, 165, 166, 167, 168].

These higher-d transition metals such as Ta, Ir, Pd and in particular Pt also have a history of use in magnetic heterostructures due to their large spin-orbit interaction. Recently, they have found considerable use in investigating the spin-Hall effect, Rashba effect [39, 40] and the DMI [7, 169].

Studies into the DMI by Ryu et al. [170, 151], within the group of S. S. P. Parkin, have provided compelling evidence for a strong association of PIM with DMI. However, *ab initio* calculations conflict with this, suggesting that the role of PIM is negligible with regard to DMI [107].

Fundamental to the experiments of Ryu et al. [151] was the use of interface engineering in which ultrathin Au spacer layers were used to modify the PIM. However, there was

no direct measurement of the PIM in these experiments only an inferred relationship with DMI from domain wall velocity measurements and spacer layer thickness.

In the literature, spacer layers have been used to separate the ferromagnetic layer from Pt when attempting to rule out PIM [151, 102, 171]. However, the lengthscale of this is based on existing measurements of the PIM lengthscale within the Pt, with a value of approximately the order of 10 Å [105].

### 5.3.3.2 Induced proximity effect in Ir|Co|Pt multilayers

In order to have a better understanding of the mechanisms arising at the interfaces of our sample, we have studied magnetic polarization of two 5d metals in Cobalt-based magnetic multilayers: Ir and Pt. Samples with the same kind of structure as the one studied in the previous were grown: Pt10|{Ir1|Co0.6|Pt1}<sub>10</sub>|Au6 and Pt10|{Ir0.6|Co0.6|Pt1}<sub>10</sub>|Au6. We choose to study two different samples with two different thickness of iridium and we also have replaced the capping layer by gold to have a better visualization of the proximity effect within the main trilayers without taking into account (at least the less possible) the buffer and capping layers.

XMCD measurements were performed at the European Synchrotron Radiation Facility in Grenoble (France) on the ID12 beamline. The XAS spectra were collected in the total fluorescent yield (TFY) at the Pt  $L_{2,3}$  and Ir  $L_{2,3}$  adsorption edges at room temperature, with an angle of the incident x-ray beam set at 15 deg. The element-selective XMCD signal was obtained by measuring the X-ray absorption near edge structure spectra for two circular polarizations of the incoming light on the saturated samples. The direction of the large out-of-plane applied magnetic field (2 T) was also reversed in order to make sure of the magnetic origin of the XMCD signal and to improve statistics in data treatment.

Figure 5.8 shows a large energy separation between the  $L_{2,3}$  edges. Therefore, in order to estimate induced magnetization for Pt and Ir, the scans have been taken separately and the magnetic moments were determined by applying the sum rules as explained in reference [115, 172]. The normalized spectra of the total absorption at the Ir  $L_{2,3}$  edges are shown on the left part of Figure 5.8. The non-zero XMCD signal for both studied samples indicates the polarization of the Ir by the adjacent Co layer. To determine the spin and orbital moments, we give the sum rules in a suitable form for our discussion:

$$\mu_L = \frac{4}{3} \frac{A_3 + A_2}{\mu_+ + \mu_-} N_h, \quad \mu_S^{eff} = \frac{A_3 - 2A_2}{\mu_+ + \mu_-} N_h \quad (5.1)$$

where  $A_3$  and  $A_2$  are the integras under the differences of XAS measured with the left and right circularly polarized light at the  $L_3$  and  $L_2$  edge, respectively. Here,  $\mu_+$  and  $\mu_-$  stand for the absorption coefficient of the photon in the case of same sign of spin polarization of excited electrons and unoccupied final states. To determine the white line, which is proportional with the number  $N_h$  of the  $d$  unoccupied stated, generally an arctan function (representing the continuum) is subtracted from the XAS. The step-like

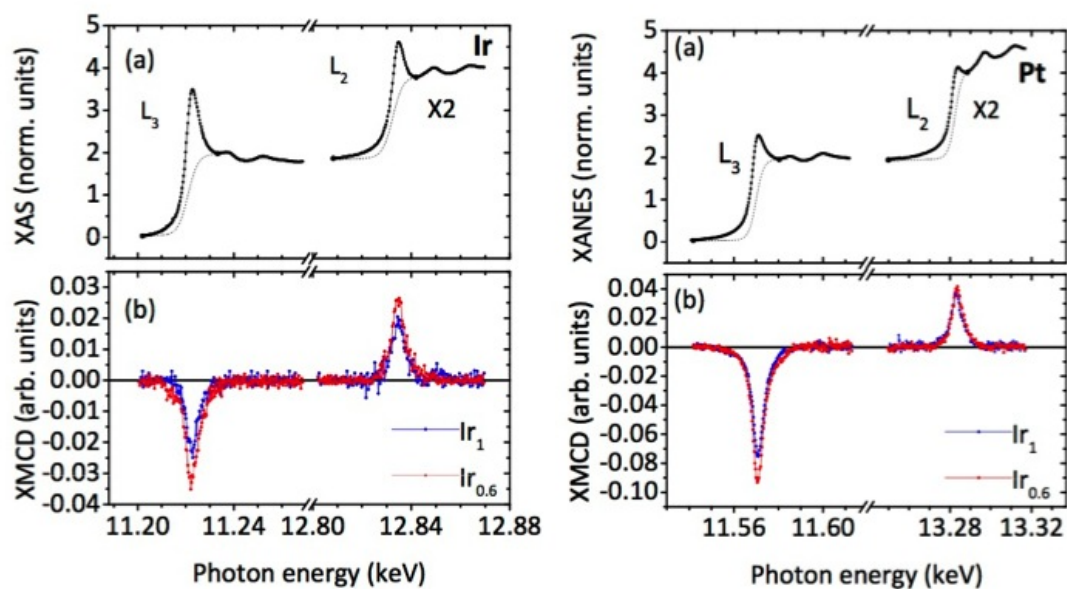


Figure 5.8: **(left)** (a) Normalized XAS at the Ir **(left)** and Pt **(right)**  $L_{2,3}$  edges in the samples. The continuum is represented by a step-like function (dotted line). (b) XMCD signal for the Ir thickness of 0.6 nm (red) and 1 nm (blue) at the Ir **(left)** and Pt **(right)**  $L_{2,3}$  edges.

|                                            | $\mu_S^{eff}$ | $\mu_L$ | $\mu_L/\mu_S^{eff}$ |
|--------------------------------------------|---------------|---------|---------------------|
| <b>Ir</b> Ir <sub>0.6</sub> $L_{2,3}$ edge | 0.150         | 0.014   | 0.09                |
| <b>Ir</b> Ir <sub>1</sub> $L_{2,3}$ edge   | 0.103         | 0.003   | 0.03                |
| <b>Pt</b> Ir <sub>0.6</sub> $L_{2,3}$ edge | 0.265         | 0.060   | 0.23                |
| <b>Pt</b> Ir <sub>1</sub> $L_{2,3}$ edge   | 0.235         | 0.042   | 0.18                |

Table 5.1: Values for spin and orbital moments (in units of  $\mu_B$  per atom) for Ir and Pt for both thicknesses or Ir. Induced Ir and Pt moments are larger for the sample for thinner Ir layers. the error bars are typically of about 10%.

function method is suitable for the case of Ir since its rather large white line intensity allows an estimation with small errors [168]. We find that the multilayer having thinner Ir layers shows a total magnetic moment of about  $0.16\mu_B$  per atom. This result is in very good agreement with the value of  $0.18\mu_B$  per atom reported for Fe1|Ir0.5 multilayers [168]. The total magnetic moment reduces to  $0.1\mu_B$  per atom for the thicker Ir multilayers (the one used for the STXM measurements).

The results obtained at Pt  $L_{2,3}$  edges are also shown in Figure 5.8 (right panel). We observe an induced magnetic moment in the Pt thin layer for both samples. The XAS spectra show that Pt white line is weaker than for Ir and this may strongly affect its estimation and a different approach should be adopted. Therefore, we decide to focus the discussion on the estimated values of  $m\mu_L/\mu_S^{eff}$ , in fact the denominator appearing in Equation 5.1 depends on the circular polarization rate of the light and on the magnetic saturation. For this reason, the ratio between the orbital and spin moment is generally used as reference because it is not affected by the choice of the continuum line for the application of the sum rules. The orbital  $\mu_L$  and spin  $\mu_S^{eff}$  moment and their ratio for Ir and Pt are reported in Table 5.1 for both samples. For the unoccupied states in the  $5d$  bands we used  $N_h = 2.7$  for Ir [168] and  $1.8$  for Pt [173]. The ratio  $\mu_L/\mu_S^{eff}$  obtained at the Pt  $L_{2,3}$  given in table 5.1 is in good agreement (within the 10% error bar) with the value previously published for proximity effects in other Pt/FM systems [173, 174]. The variation of this ratio with the Ir thickness can be considered negligible though its trend shows a good agreement with what is reported in reference [168].

With this study, we report on induced magnetic polarization in Ir and Pt respectively in contact with both faces of a Co thin film.

As explained before, the first series of simulation have been performed under the assumption that the total experimental measured magnetization and total experimental anisotropy energy of the multilayer is concentrated in eleven 0.6nm-thick Co layers having the stiffness constant of cobalt and separated by 2nm-thick vacuum layers. Consistently the effective magnetization of Co is simply obtained by dividing the total magnetization by the total Co thickness, *i.e.* 6.6nm. The effective anisotropy constant is deduced from the saturation field measured in both magnetic hysteresis curves. Herein, we have considered the case of that the interfacial Pt and Ir atomic layers can acquire a

small magnetic moment by proximity effect. In this case, the experimental magnetization (and the effective anisotropy thereof) is no more fully concentrated in the Co layers but is obtained by considering that one atomic plane of Pt and Ir is magnetized. As shown in Figure 5.9, this second case leads to a slightly different estimation of the DMI amplitude from the evaluation of the skyrmion diameter with field with a value equal to  $|\mathbf{D}| = 1.4 \pm 0.2 \text{ mJ/m}^2$ .

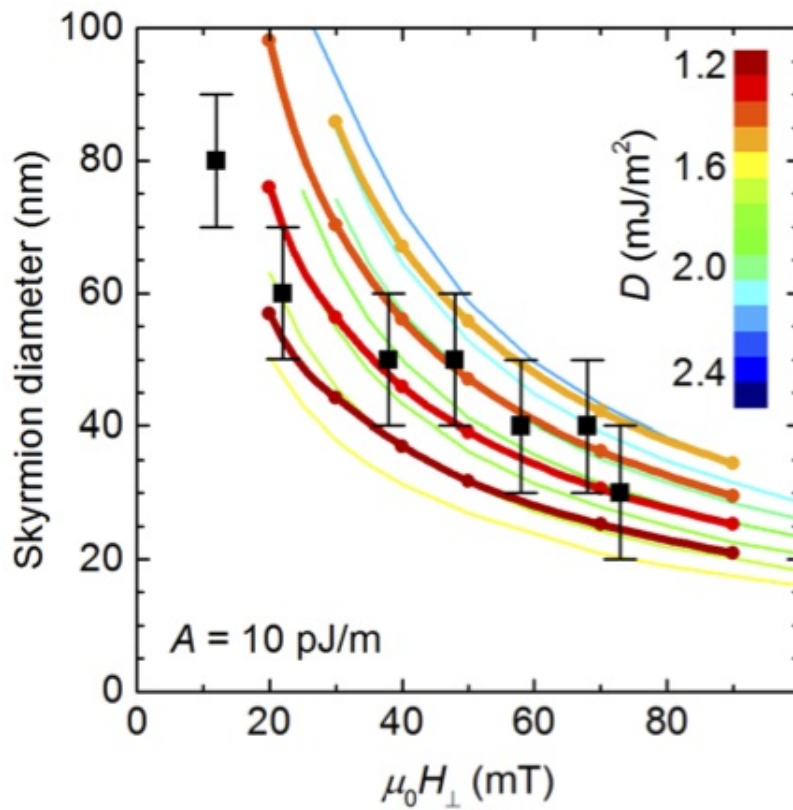


Figure 5.9: Comparison of the skyrmion diameter as a function of the external out-of-plane magnetic field for different values of the DMI amplitude, in the case where small magnetic moments on Pt and Ir atoms due to proximity effect with Co layer are considered, *i.e.* with a finite interlayer coupling (thick lines, see text for details). Thin lines correspond to simulations of Figure 5.2.

The actual value is probably being between this latter value and the one found without proximity effect. In consequence, all these results converge to a very large interfacial DMI, which enables the observation of skyrmions in technologically relevant systems of magnetic multilayers.

## 5.4 Conclusions

The main results of this study are:

- The observation of worm domains at remanence and the evolution of skyrmions size with applied out-of-plane magnetic field enable us the estimation of the average DMI amplitude,
- A very large DMI amplitude was found in the {Ir|Co|Pt} sample, of  $1.9 \text{ mJ/m}^3$  - in good agreement with similar samples measured by other groups,
- A very low, still non-zero, DMI amplitude was found for the {Co|Pt} sample of  $0.2 \text{ mJ/m}^3$ ,
- Both STXM and MFM experiments allow the estimation of DMI amplitude, and the value found is exactly the same for the two observations,
- Proximity induced magnetization was found in both Pt and Ir and estimated using XMCD in our structures,
- Proximity effect lowers the value estimated of the DMI in samples by about 20%.

## Chapter 6

# Tuning magnetic interactions and skyrmions properties

### Contents

---

|            |                                                         |            |
|------------|---------------------------------------------------------|------------|
| <b>6.1</b> | <b>List of samples and protocol . . . . .</b>           | <b>122</b> |
| 6.1.1      | List of the samples and motivation . . . . .            | 122        |
| 6.1.2      | Protocol . . . . .                                      | 123        |
| 6.1.3      | Characterization . . . . .                              | 124        |
| <b>6.2</b> | <b>Observations by MFM and DMI estimation . . . . .</b> | <b>129</b> |
| 6.2.1      | {Ir Co Pt} samples . . . . .                            | 129        |
| 6.2.2      | Changing Ir by W or AlOx . . . . .                      | 138        |
| <b>6.3</b> | <b>Conclusions and discussion . . . . .</b>             | <b>140</b> |
| 6.3.1      | DMI . . . . .                                           | 140        |
| 6.3.2      | Skyrmion density vs. $K_{\text{eff}}$ . . . . .         | 142        |
| 6.3.3      | Conclusion . . . . .                                    | 142        |

---

Here, we have performed a systematic study of different multilayers for the realization of possible tunable room temperature skyrmions platform based on multilayers stacks. All samples were designed on the same pattern:

$$\text{SiO}_2||\text{Buffer layer}|\{\text{Heavy metal}_1|\text{Co}| \tag{6.1}$$

## 6.1 List of samples and protocol

### 6.1.1 List of the samples and motivation

To have the most complete overview of the possibilities to tune the skyrmion's properties and enhance the DMI amplitude, we have varied multiple parameters:

- the number of repetition of the main trilayer. Indeed, increasing the number of repetitions of the main trilayer would increase the total magnetic volume, hence increasing the thermal stabilization to allow the observation of isolated magnetic skyrmions at room temperature. Moreover, for more technical reasons, it helps having more signal for magnetic imaging (either STXM or MFM). However, the multiplication of the trilayers may have an impact on the  $D$ -value and the behavior of the skyrmions observed.
- the thickness of the cobalt layer. Since the DMI is anticipated to be an interfacial interaction, the ratio surface/volume of the ferromagnet is an important parameter, and we expect that the increasing thickness of the ferromagnet lead to a lower DMI amplitude.
- the thickness of both heavy metals deposited below and above the ferromagnet. These heavy metals (here Pt and Ir) have different roughness, different induced proximity effect when in an interface with Co and hereby tuning their thickness should play a role in the DMI amplitude of the system. Moreover, changing their thickness lead to changing the space between two layers of ferromagnet (here Co) and hereby the coupling between two ferromagnet layers.
- the materials chosen for the heavy metals. For all the previous studies, we are in the classical scheme of this work with Pt, Ir and Co. From *ab initio* calculation, we know that the most important interface for the DMI is Pt|Co. We have kept it, but tried to change the material used for the other interface: W (to have another heavy metal) and AlOx (to replace the heavy metal with an oxide).

From all these considerations, the samples studied in this chapter are reported in the following table 6.1:

|                                            |                                          |
|--------------------------------------------|------------------------------------------|
| Pt10 {Ir1 Co0.6 Pt1} <sub>3</sub>  Pt3     | Pt10 {Ir1 Co0.6 Pt1} <sub>5</sub>  Pt3   |
| Pt10 {Ir1 Co0.6 Pt1} <sub>5</sub>  Pt3     | Pt10 {Ir1 Co0.8 Pt1} <sub>5</sub>  Pt3   |
| Pt10 {Ir1 Co0.6 Pt1} <sub>10</sub>  Pt3    | Pt10 {Ir1 Co1 Pt1} <sub>5</sub>  Pt3     |
| Pt10 {Ir1 Co0.6 Pt1} <sub>20</sub>  Pt3    | Pt10 {Ir0.6 Co0.6 Pt1} <sub>5</sub>  Pt3 |
| Pt10 {Ir1 Co0.6 Pt1} <sub>30</sub>  Pt3    | Pt10 {Ir0.8 Co0.6 Pt1} <sub>5</sub>  Pt3 |
| Pt10 {Ir1 Co0.6 Pt1} <sub>5</sub>  Pt3     | Pt10 {Ir1 Co0.6 Pt1} <sub>5</sub>  Pt3   |
| Ta5 Pt10 {Ir1 Co0.6 Pt1} <sub>3</sub>  Pt3 | Pt10 {Ir2 Co0.6 Pt1} <sub>5</sub>  Pt3   |
| Pt10 {Ir1 Co0.6 Pt1} <sub>5</sub>  Pt3     | Pt10 {Ir1 Co0.6 Pt0.7} <sub>5</sub>  Pt3 |
| Pt10 {W1 Co0.6 Pt1} <sub>5</sub>  Pt3      | Pt10 {Ir1 Co0.6 Pt1} <sub>5</sub>  Pt3   |
| Pt10 {AlOx1 Co0.6 Pt1} <sub>5</sub>  Pt3   | Pt10 {Ir1 Co0.6 Pt2} <sub>5</sub>  Pt3   |

Table 6.1: List of the samples studied for DMI enhancement tuning properties of skyrmions, thickness in nm.

### 6.1.2 Protocol

To perform a systematic study, all samples have followed the same steps, detailed below:

- Growth by sputtering
- Characterization by AGFM
- Characterization by SQUID
- XRR characterization
- Demagnetization
- Observation by MFM in extended films with no applied field
- Observation by MFM during field cycling with out-of-plane external magnetic field
- Quantitative analysis of the observations

### 6.1.3 Characterization

As detailed above, before observing samples by MFM, we have characterized them by AGFM, SQUID and XRR. This section reports the result of these characterizations.

#### 6.1.3.1 Magnetic characterization

**AGFM and SQUID** As explained in Chapter 3, AGFM and SQUID lead to the evaluation of two important parameters: the magnetization at saturation and the anisotropy energy. Table 6.2 is referencing the values for these parameters.

We can notice several points:

- For  $\{\text{Ir}|\text{Co}|\text{Pt}\}$  multilayers, the magnetization at saturation seems quite stable in the range 1200–1300 kA/m except for the samples varying the thickness of iridium, meaning that the cobalt layers are comparable from one sample to another.
- $\{\text{Ir}_{0.6-0.8-2}|\text{Co}_{0.6}|\text{Pt}_1\}$  and  $\{\text{W}_1|\text{Co}_{0.6}|\text{Pt}_1\}$  present value for magnetization at saturation lower than the rest of the samples. From these results, we would expect from the XRR characterization that the roughness at the interface Ir|Co and W|Co is higher than in the other samples. This unusual roughness would yield more intermixing of the species at the interfaces and hereby modify the magnetization at saturation of the samples. This would lead to a more complex (and maybe impossible) quantitative analysis of the observations by MFM (and hereby estimation of the DMI).

We also note that we have compared the characterizations of  $\{\text{Ir}|\text{Co}|\text{Pt}\}$  sample grown on  $\text{SiO}_2$  and  $\text{Si}_3\text{N}_3$  substrates and noticed no change be it on the magnetization at saturation, the effective anisotropy or the hysteresis loops with in plane or out-of-plane magnetic field.

Figures 6.1 and 6.2 report all the hysteresis loops for external applied out-of-plane and in-plane magnetic field. Comparison have been made for the variation of parameters listed in the first part of this chapter (number of repetitions, Co thickness, Ir thickness,

| Structure                 | Ms (kA/m) | $\pm$ (kA/m) | $K_{\text{eff}}$ (MJ/m <sup>3</sup> ) | $\pm$ (MJ/m <sup>3</sup> ) | K (MJ/m <sup>3</sup> ) | $\pm$ (MJ/m <sup>3</sup> ) |
|---------------------------|-----------|--------------|---------------------------------------|----------------------------|------------------------|----------------------------|
| Pt10{Ir1Co0.6Pt1}3 Pt3    | 1288      | 64           | 0.285                                 | 0.03                       | 1.33                   | 0.1                        |
| Pt10{Ir1Co0.6Pt1}5 Pt3    | 1256      | 63           | 0.208                                 | 0.02                       | 1.20                   | 0.1                        |
| Pt10{Ir1Co0.6Pt1}10 Pt3   | 1222      | 61           | 0.362                                 | 0.04                       | 1.30                   | 0.1                        |
| Pt10{Ir1Co0.6Pt1}20 Pt3   | 1245      | 62           | 0.425                                 | 0.04                       | 1.40                   | 0.1                        |
| Pt10{Ir1Co0.6Pt1}30 Pt3   | 1192      | 60           | 0.439                                 | 0.04                       | 1.33                   | 0.1                        |
| Pt10{Ir1Co0.6Pt1}5 Pt3    | 1256      | 63           | 0.208                                 | 0.02                       | 1.20                   | 0.1                        |
| Pt10{Ir1Co0.8Pt1}5 Pt3    | 1229      | 61           | 0.393                                 | 0.04                       | 1.34                   | 0.1                        |
| Pt10{Ir1Co1Pt1}5 Pt3      | 1273      | 64           | 0.289                                 | 0.03                       | 1.31                   | 0.1                        |
| Pt10{Ir0.6Co0.6Pt1}5 Pt3  | 1130      | 57           | 0.222                                 | 0.02                       | 1.03                   | 0.1                        |
| Pt10{Ir0.8Co0.6Pt1}5 Pt3  | 1013      | 51           | 0.220                                 | 0.02                       | 0.86                   | 0.09                       |
| Pt10{Ir1Co0.6Pt1}5 Pt3    | 1256      | 63           | 0.208                                 | 0.02                       | 1.20                   | 0.1                        |
| Pt10{Ir2Co0.6Pt1}5 Pt3    | 1127      | 56           | 0.280                                 | 0.03                       | 1.08                   | 0.1                        |
| Pt10{Ir1Co0.6Pt0.7}5 Pt3  | 1217      | 62           | 0.242                                 | 0.02                       | 1.17                   | 0.1                        |
| Pt10{Ir1Co0.6Pt1}5 Pt3    | 1256      | 63           | 0.208                                 | 0.02                       | 1.20                   | 0.1                        |
| Pt10{Ir1Co0.6Pt2}5 Pt3    | 1342      | 65           | 0.516                                 | 0.05                       | 1.65                   | 0.2                        |
| Pt10{Ir1Co0.6Pt1}5 Pt3    | 1256      | 63           | 0.208                                 | 0.02                       | 1.20                   | 0.1                        |
| Ta5Pt10{Ir1Co0.6Pt1}5 Pt3 | 1293      | 65           | 0.483                                 | 0.05                       | 1.53                   | 0.1                        |
| Pt10{Ir1Co0.6Pt1}5 Pt3    | 1256      | 63           | 0.208                                 | 0.02                       | 1.20                   | 0.1                        |
| Pt10{W1Co0.6Pt1}5 Pt3     | 771       | 39           | 0.231                                 | 0.02                       | 0.605                  | 0.06                       |
| Pt10{AlOx1Co0.6Pt1}5 Pt3  | 1512      | 76           | 0.450                                 | 0.05                       | 1.91                   | 0.2                        |

Table 6.2: Magnetic characterization of the samples studied.

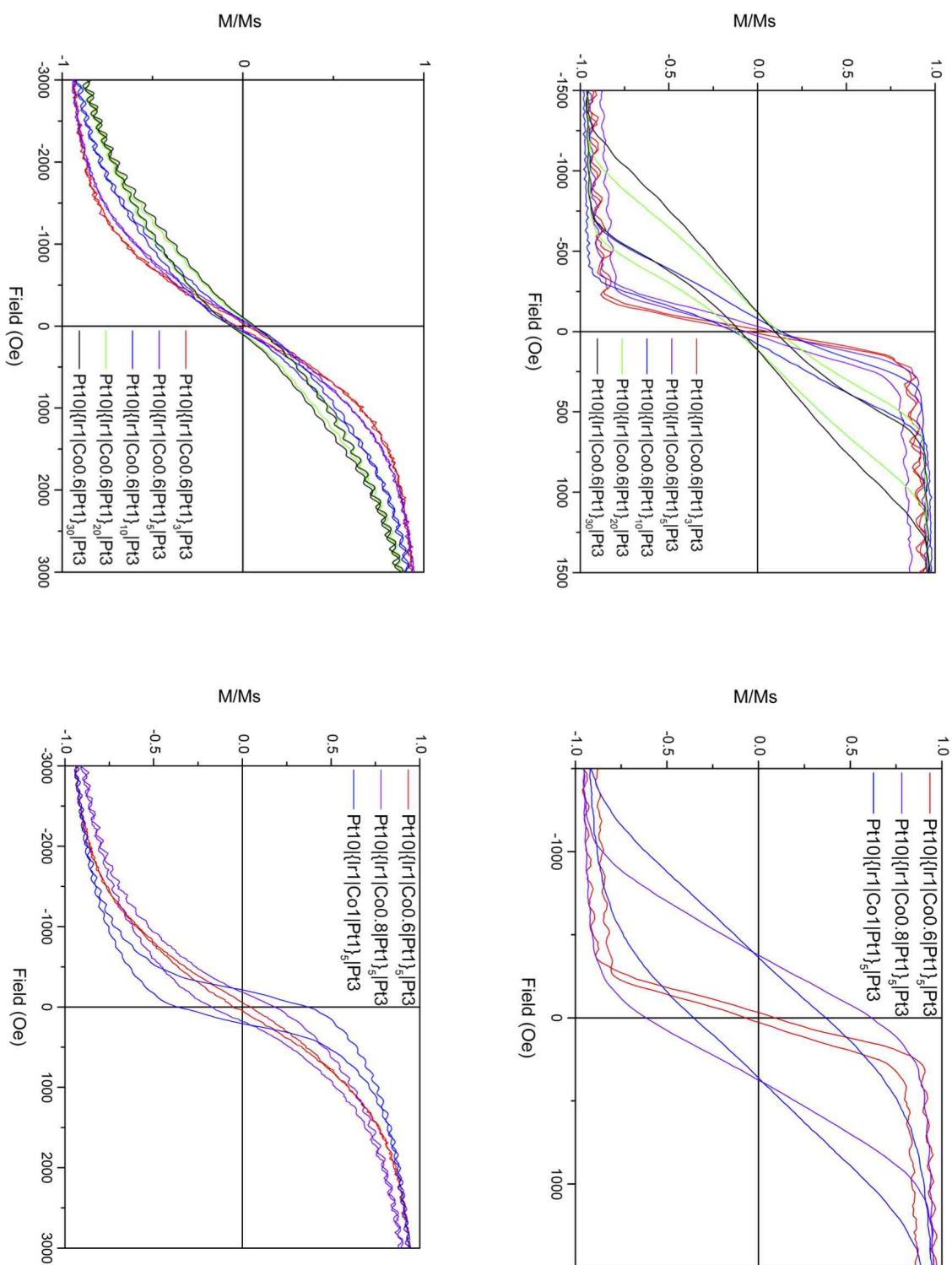


Figure 6.1: **(top)** Hysteresis loops with external applied out-of-plane and **(bottom)** in plane magnetic field for all samples studied in this chapter. Comparison have been made for the variation of the different parameters: from left to right: number of repetitions and Co thickness.

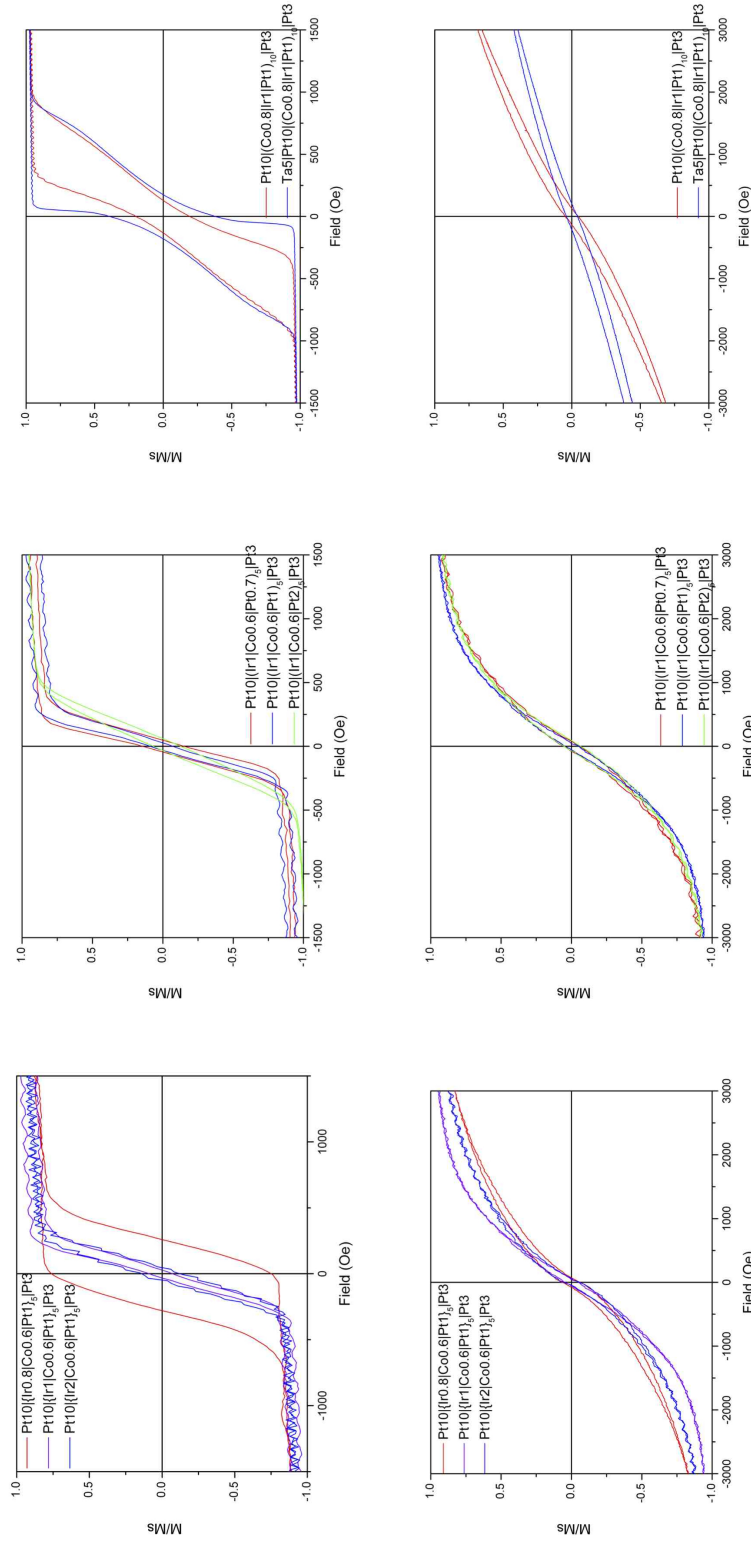


Figure 6.2: **(top)** Hysteresis loops with external applied out-of-plane and **(bottom)** in plane magnetic field for all samples studied in this chapter. Comparison have been made for the variation of the different parameters: from left to right, Ir thickness, Pt thickness, buffer layers.

Pt thickness and different buffer layers). From Figures 6.1 and 6.2 and , we report several remarks:

- The increasing number of repetitions of the main trilayers is increasing the coercitive field and tend to decrease the magnetization at remanence,
- By increasing the Co thickness from 0.6 to 0.8 nm, the coercitive field and the anisotropy energy are increased as well as the magnetization at remanence.
- 1 nm thick Co is the limit in {Ir|Co|Pt} samples to have an out-of-plane anisotropy.
- Comparing 0.8 nm and 1 nm of Ir, we notice that the coercitive field is increasing, whereas the magnetic characterization for Ir 1 and 2 nm seems quite equivalent.
- Note that the magnetic characterization for 0.6 nm is not reported because no qualitative image by MFM could have been acquired.
- We also observe that the hysteresis loops for Pt 0.7 and 1 nm are equivalent but 2 nm of Pt lowers the magnetization at remanence as well as the coercitive field.
- Finally the added Ta layer below the 10 nm-thick Pt buffer layer increases the coercitive field as well as the magnetization at remanence,

From table 6.2 and Figures 6.1 and 6.2, we conclude that by changing thicknesses, number of repetitions of the main trilayers or changing the buffer layer, magnetic properties of our samples are changing. Hence, we expect a change in the properties of the magnetic skyrmions observed by MFM and in the DMI amplitude of samples.

**Magnetization vs. thickness** In Figure 6.3, we plot the variation of  $M_s$  with thickness of Co ranging from 1.8 to 18 nm. Indeed, we have here reported the results for {Ir|Co|Pt} samples with different number of repetitions, and different thickness of Co. A notable property of the magnetization in thin films is the significant diminution of the maximum volumetric magnetization with thickness, indicating the presence of dead layers. Here, no such trend is visible on Figure 6.3. The growth of the trilayers is thereby stable and no dead layers seem to be observable in the stacks.

### 6.1.3.2 X-Ray Reflectivity

XRR characterizations have been made for all the samples listed in the first part of this chapter. From these measurements we can report several conclusions:

- Firstly, the experimental thickness is found to be really close to the nominal thickness (maximum deviation of 5%)
- As expected from the magnetic characterizations, the roughness estimated at the interface Ir|Co is more important than at the interface Co|Pt: 0.5 nm in the case or Ir 0.6, 0.3 nm for Ir 0.8, 0.2 nm for Ir 1 and 0.4 for Ir 2.

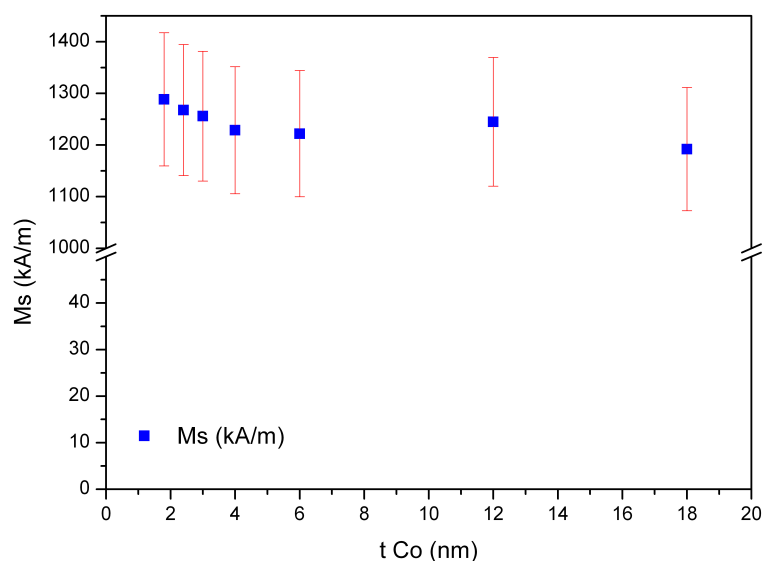


Figure 6.3: Evolution of the magnetization at saturation (in kA/m) versus the total thickness of Co in the sample for  $\{\text{Ir}|\text{Co}|\text{Pt}\}$  samples with different number of repetitions and different thicknesses of Co.

- Identically, roughness of W|Co interface is also more important than at other interfaces: 0.5 nm for a 1 nm-thick layer.
- We report in table 6.3 the average thickness (compared to the nominal one) and roughness of the layers.

## 6.2 Observations by MFM and DMI estimation

The first observation was of the magnetic domains after demagnetization with no applied field and have a first estimation of the average DMI amplitude in these samples. In the work reported here, we focus on the observation of isolated magnetic skyrmions and their evolution with applied external out-of-plane magnetic field.

### 6.2.1 $\{\text{Ir}|\text{Co}|\text{Pt}\}$ samples

Since the main goal of this PhD were achieved on  $\{\text{Ir}|\text{Co}|\text{Pt}\}$  sample, we have first varied parameters in this structure.

**Number of repetitions** Working with multilayers allows to tune several parameters, including the number of repetitions of the main trilayers. Hereby, increasing the number of repetitions would increase the total volume of magnetic material and increase the thermal stability, allowing the observation of isolated magnetic skyrmions at room temperature. However, as seen in the magnetic characterizations, increasing the number of

| Layer            | Nominal thickness (nm) | XRR thickness (nm) | Roughness (nm) |
|------------------|------------------------|--------------------|----------------|
| Pt buffer layer  | 10                     | 10.4               | 0.09           |
|                  |                        |                    |                |
| Ir               | 0.6                    | 0.654              | 0.5            |
|                  | 0.8                    | 0.765              | 0.3            |
|                  | 1                      | 1.08               | 0.2            |
|                  | 2                      | 1.98               | 0.4            |
|                  |                        |                    |                |
|                  |                        |                    |                |
| Pt               | 0.7                    | 0.695              | 0.03           |
|                  | 1                      | 0.984              | 0.02           |
|                  | 2                      | 2.04               | 0.01           |
| Co               | 0.6                    | 0.68               | 0.3            |
|                  | 0.8                    | 0.84               | 0.2            |
|                  | 1                      | 1.02               | 0.3            |
| Pt capping layer | 3                      | 3.069              | 0.1            |

Table 6.3: Table reporting average thickness and roughness for {Ir|Co|Pt} samples, measured by XRR characterizations.

repetition is not transparent for the magnetization at saturation, the anisotropy energy and even more for the coercitive field and the magnetization at remanence. Therefore, it was quite important to verify the influence of this parameter on the average DMI amplitude of samples.

Figure 6.4 reports the observation by MFM of isolated magnetic skyrmions at room temperature in Pt10|{Ir1|Co0.6|Pt1}<sub>5</sub>|Pt3 and Pt10|{Ir1|Co0.6|Pt1}<sub>10</sub>|Pt3, and the evolution of skyrmion size and density with changing out-of-plane magnetic field.

In Figure 6.5, we note that the evolution of the density of skyrmions with applied out-of-plane magnetic field is following the same trend for each samples: increasing when diminishing the field. However we also note that the density itself is not the same from one sample to another. In next section, we will discuss the evolution of the density at a field close to saturation compared to the anisotropy of the sample. Hitherto, we have seen that for different numbers of repetition of the main trilayer in {Ir|Co|Pt} sample, the magnetic parameters are changing and also the properties of the isolated magnetic skyrmions.

We have performed micromagnetic simulations as explained in Chapter 5 to compare the evolution of skyrmions diameters with applied out-of-plane magnetic field (in the same range of values as for the experimental datas) for different values of DMI amplitudes. The results are compared to the experimental datas and reported in Figure 6.6.

Here we can conclude that the magnetic characterizations of {Ir|Co|Pt} samples with different number of repetitions lead to different values of magnetization at saturation, coercitive field and anisotropy energy, and the observation of isolated magnetic skyrmions at room temperature by MFM lead to different densities of skyrmions, different size of skyrmions. However, the average DMI amplitude found for theses samples is large and equal, with  $|D| = 1.9 \pm 0.2 \text{ mJ/m}^2$ , as found in Chapter 5 for the 10 repetitions sample. We can conclude that, at least in the range of 3 to 30 repetitions, it is possible to tune magnetic properties of skyrmions without changing the average DMI value of the sample.

**Co thickness** Another way to increase the total volume of magnetic layer is to increase the thickness of the ferromagnet layer (here Co). Here we are comparing {Ir|Co|Pt} samples with 5 repetitions of the main trilayers and with Co thicknesses of 0.6, 0.8 and 1 nm. As expected, we find that the magnetic properties of the sample are changing with the changing thickness of cobalt (be it the magnetization at remanence, the coercitive field or the anisotropy energy). When applying out-of-plane magnetic field, we observe by MFM isolated magnetic skyrmions at room temperature, as reported in Figure 6.7.

Figure 6.7 reports different densities of skyrmions with applied magnetic field for Co 0.6 and Co 0.8 in Figure 6.8

In Figure 6.8, we also note that skyrmion density is increasing when decreasing the absolute value of the field. However, the density itself is not the same from one sample to another and will be compared with other samples versus the effective anisotropy in the next section. Hitherto, as for the repetitions of the main trilayers, we have seen that for different thicknesses of cobalt in {Ir|Co|Pt} sample, the magnetic parameters are

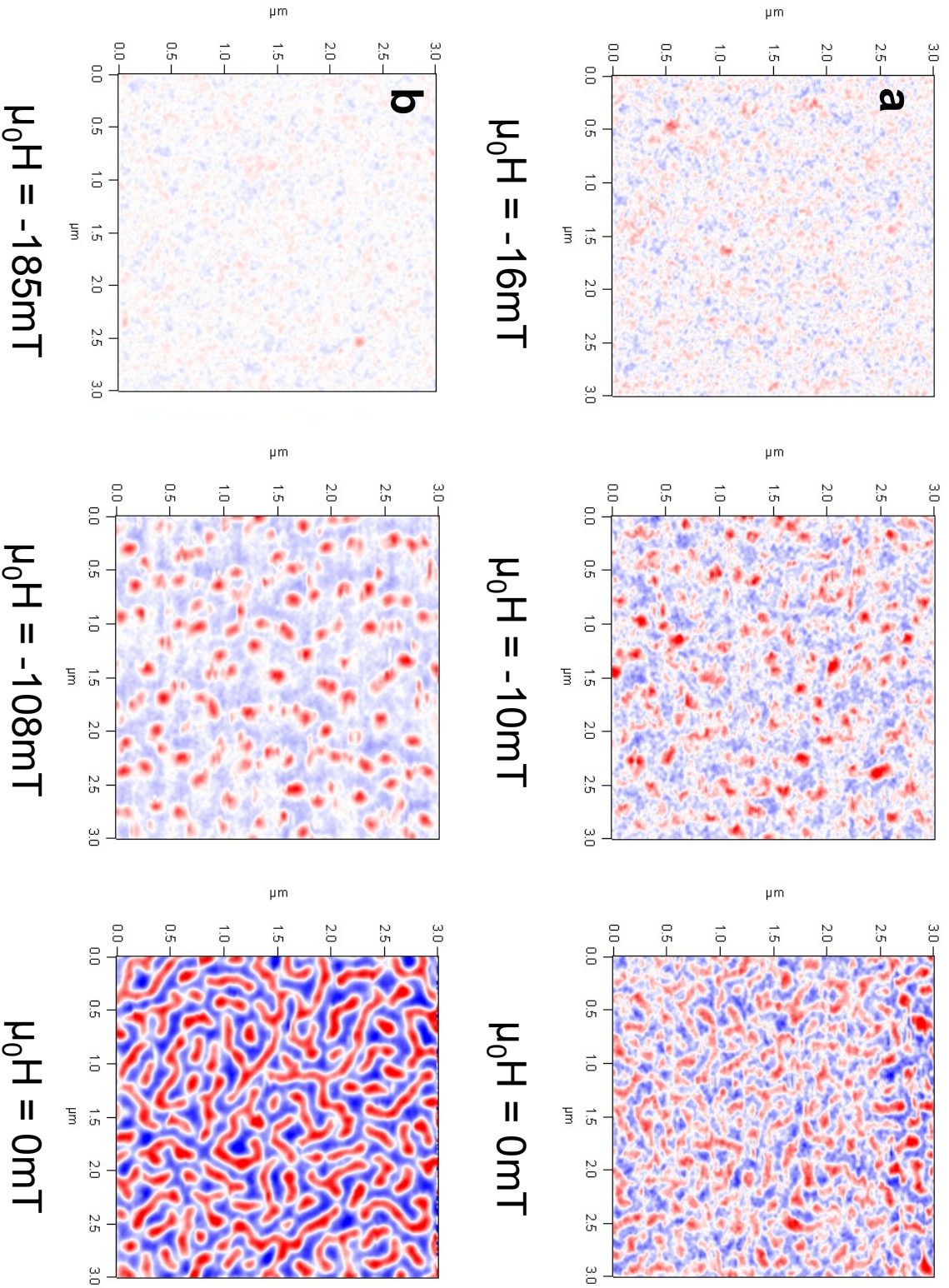


Figure 6.4:  $3 \times 3 \mu\text{m}^2$  MFM images of (a) Pt10|{Ir1|Co0.6|Pt1}<sub>5</sub>|Pt3 and (b) Pt10|{Ir1|Co0.6|Pt1}<sub>10</sub>|Pt3 with applied external out-of-plane magnetic field.

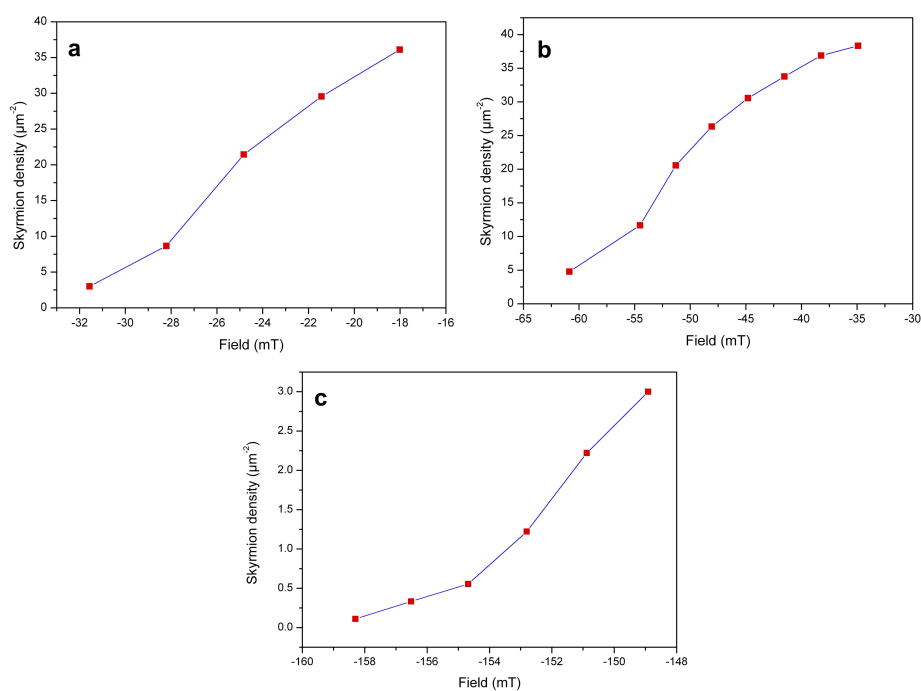


Figure 6.5: Evolution of the density of skyrmions with applied out-of-plane magnetic field for (a) Pt10{Ir1|Co0.6|Pt1}5|Pt3, (b) Pt10{Ir1|Co0.6|Pt1}10|Pt3 (c) Pt10{Ir1|Co0.6|Pt1}30|Pt3.

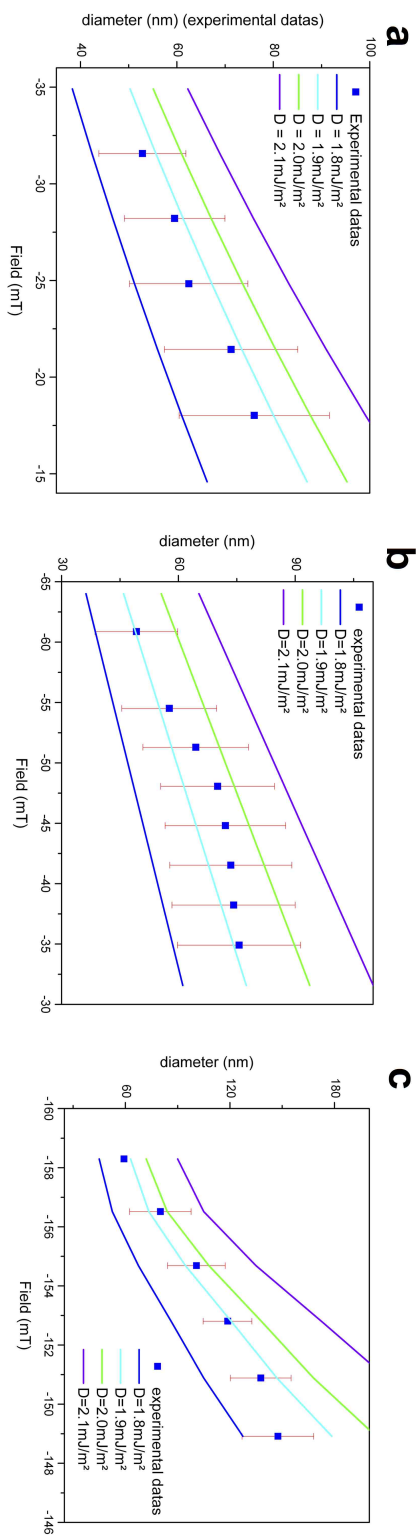


Figure 6.6: Evolution of the skyrmions diameter with applied out-of-plane magnetic field compared to Mumax3 simulations performed for different values of DMI amplitude, for (a)  $\text{Pt}_{10}\{\text{Ir}_1\text{Co}_0.6\text{Pt}_1\}_{30}\text{Pt}_3$ , (b)  $\text{Pt}_{10}\{\text{Ir}_1\text{Co}_0.6\text{Pt}_1\}_5\text{Pt}_3$  and (c)  $\text{Pt}_{10}\{\text{Ir}_1\text{Co}_0.6\text{Pt}_1\}_{10}\text{Pt}_3$

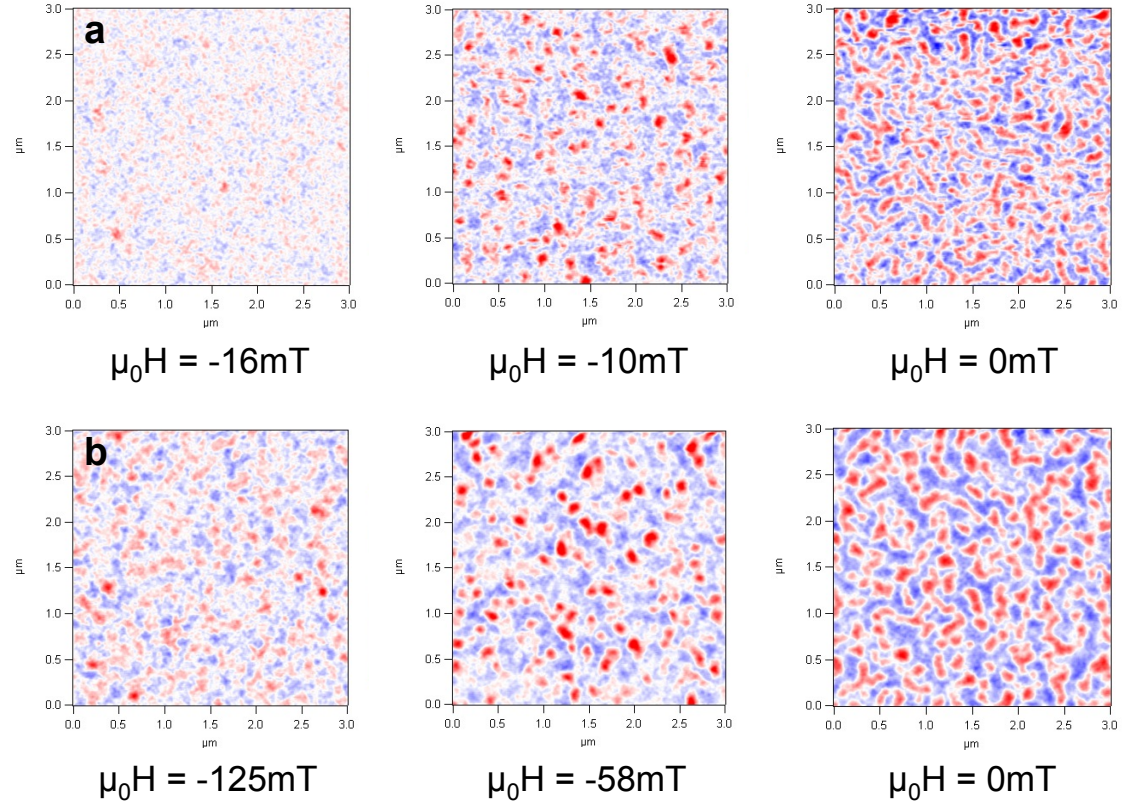


Figure 6.7:  $3 \times 3 \mu\text{m}^2$  MFM images of (top) Pt10|{Ir1|Co0.6|Pt1}5|Pt3 and (bottom) Pt10|{Ir1|Co0.8|Pt1}5|Pt3 with applied external out-of-plane magnetic field.

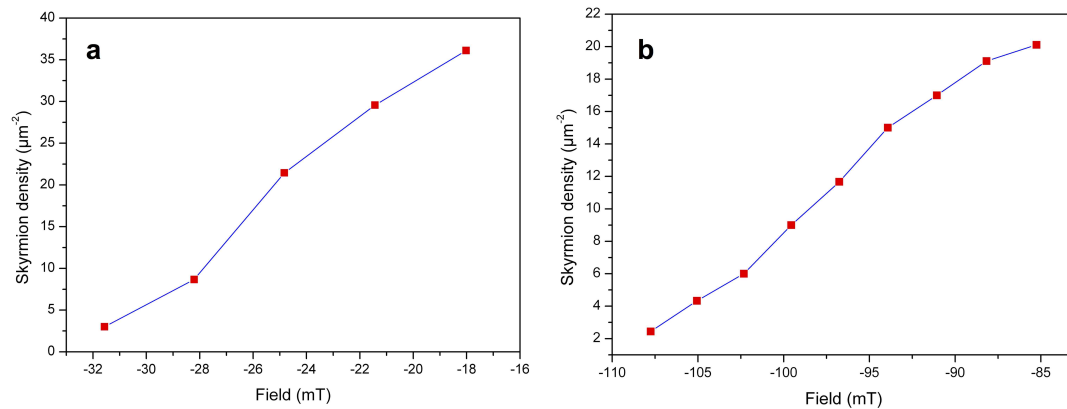


Figure 6.8: Evolution of the density of skyrmions with applied out-of-plane magnetic field for (a) Pt10|{Ir1|Co0.6|Pt1}5|Pt3 and (b) Pt10|{Ir1|Co0.8|Pt1}5|Pt3.

changing and also the properties of the observed isolated magnetic skyrmions. However, contrary to the case of the repetitions of the main trilayer, we expect here a change of the average DMI amplitude. Indeed, the DMI is an interfacial interaction and hereby is sensitive to the change of ratio surface/volume. An increase of the thickness of the magnetic layer should lead to a diminution of the DMI amplitude. To confirm this expectation, we have performed micromagnetic simulations for the evolution of the skyrmion diameter with applied out-of-plane magnetic field in the same range as in the experimental observations, and compared these simulations with experimental datas. Results are reported in Figure 6.9.

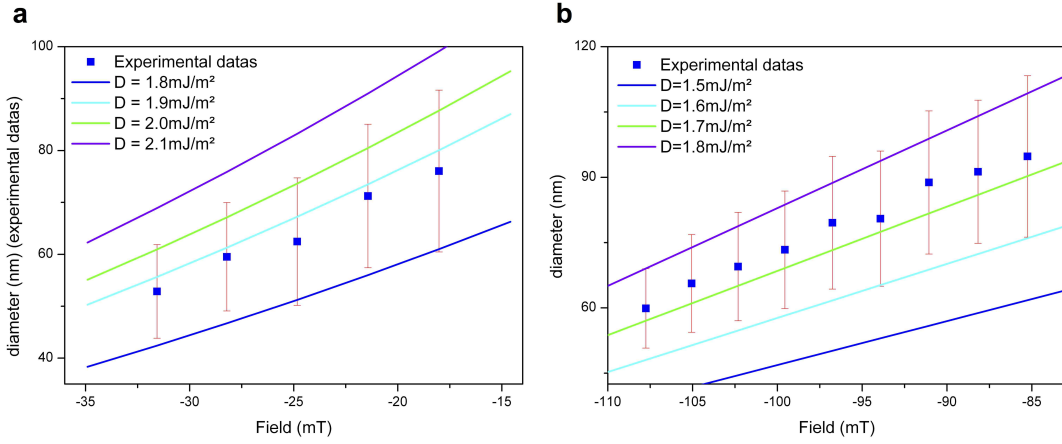


Figure 6.9: Evolution of the skyrmions diameter with applied out-of-plane magnetic field compared to Mumax3 simulations performed for different values of DMI amplitude, for (a) Pt10|{Ir1|Co0.6|Pt1}\_5|Pt3, and (b) Pt10|{Ir1|Co0.8|Pt1}\_5|Pt3.

In Figure 6.9, we demonstrate that, by changing the thickness of the Co layer, it is possible to tune the DMI amplitude. Indeed, for a thicker Co layer (0.8), we observe, as expected, that the average DMI amplitude is going from  $|D| = 1.9 \pm 0.2$  mJ/m<sup>2</sup> for 0.6 nm of Co to  $|D| = 1.7 \pm 0.2$  mJ/m<sup>2</sup> for 0.8 nm of cobalt. Now, a natural step would be to grow samples with thinner Co layer to enhance the DMI amplitude. Unfortunately, we have tried {Ir|Co|Pt} samples with Co layers of 0.5, 0.4 and 0.3 nm but never succeeded in having out-of-plane anisotropies; further studies have to be lead in that way.

Moreover, we also have to point out that results for 1 nm-thick Co is not reported in this study because, even though we have been able to observe isolated magnetic skyrmions at room temperature, the quantitative analysis of the results were quite complex. Indeed, as seen in the magnetic characterizations, the sample with 1nm thick Co shows hysteresis loops for in plane and out-of-plane field quite equivalent, meaning that the magnetic anisotropy of the sample is not completely out-of-plane. Thereby, it becomes quite complex to simulate the evolution of skyrmions with applied out-of-plane field for samples which anisotropy is not fully unidirectional.

**Ir thickness** In the previous paragraphs, we have studied the modifications in the properties of skyrmions and in the DMI amplitude when we are increasing the total magnetic volume (either by increasing the number of repetitions or increasing the ferromagnetic layer thickness). The next step of our study is to observe the influence of the thickness of the heavy metals deposited above or below the ferromagnet. We start here with the thickness of iridium, deposited below the Co in  $\{\text{Ir}|\text{Co}|\text{Pt}\}$  samples. To lead this study, as seen in the first part of this chapter, we have grown four different samples with four different thicknesses of Ir: 0.6, 0.8, 1, and 2 nm. Since we have already studied the 0.6 nm Ir sample in the study of the induced proximity effect in Chapter 5, we have focused here on the three remaining samples. As the previous studies, we find that the magnetic properties of the sample are changing with the changing thickness of iridium (be it the magnetization at remanence, the coercitive field or the anisotropy energy). When applying out-of-plane magnetic field, we observe by MFM isolated magnetic skyrmions at room temperature, as reported in Figure 6.10.

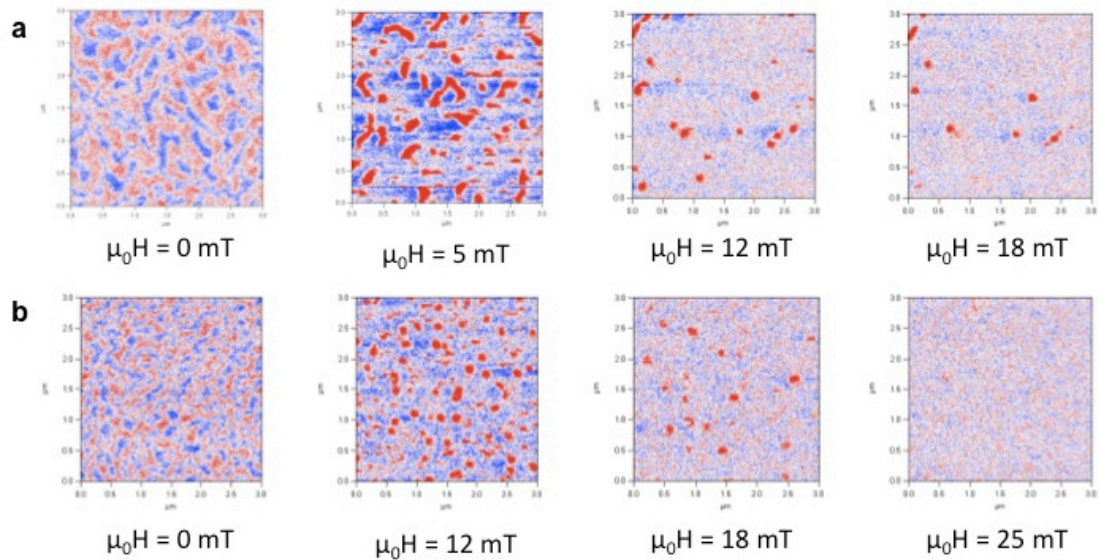


Figure 6.10:  $3 \times 3 \mu\text{m}^2$  MFM images of (a) Pt10|{Ir0.8|Co0.6|Pt1}5|Pt3 and (b) Pt10|{Ir2|Co0.6|Pt1}5|Pt3 with applied external out-of-plane magnetic field.

Figure 6.10 reports the observation of isolated magnetic skyrmions at room temperature and their evolution with applied out-of-plane magnetic field. We note that the quality of the images taken by MFM are slightly less good than for the previous measurements. This is probably due to rougher interfaces found by XRR leading to intermixing at these interfaces. We have performed micromagnetic simulations to evaluate the evolution of skyrmions size with applied out-of-plane magnetic field. By comparing these simulations with experimental datas, we found that the DMI amplitude is equal to  $|D| = 1.9 \pm 0.2 \text{ mJ/M}^2$  with no significant change from the changing thicknesses of iridium. However, because of the different quality of the image, the error margins in

the evaluation of the skyrmions diameter are larger than in the other experiments and thereby the estimation of the DMI is less precise. From this conclusion, we can point out that it seems that 1 nm thick Ir is the optimal thickness for the study of isolated magnetic skyrmions in {Ir|Co|Pt} samples. Finally, we can also conclude that, within the error margins, DMI amplitude is not influenced by the thickness of Ir.

**Pt thickness** As explained in the previous paragraph, the penultimate steps of our study is the thickness variation of the heavy metals deposited around the ferromagnet. So, we have also studied the importance of the Pt thickness. As seen in Chapter 5 the induced proximity effect in Pt is rather important and we would expect a change in the DMI amplitude with different thicknesses of Pt.

Figure 6.11 reports the observation by MFM of stable isolated magnetic skyrmions at room temperature. Here again, we observe different densities for skyrmions depending on the field applied, as seen in Figure 6.12.

Finally, micromagnetic simulations of the evolution of skyrmions diameter with applied out-of-plane magnetic field (in the range of the experimental observations) have been performed for different values of DMI amplitude. Comparison with experimental datas are shown in Figure 6.13.

Figure 6.13 shows that the variation of Pt thickness is not changing significantly the DMI amplitude within the error bars. However, a more complete study has to be performed with a wider range of thickness for Pt to verify completely its role in the DMI amplitude. From Figure 6.13, one would see that the DMI value for Pt 0.7 nm seems slightly above  $1.9 \text{ mJ/m}^2$ , but obviously the error margins inherent at the estimation of the skyrmions diameter don't allow any assurance of this trend.

## 6.2.2 Changing Ir by W or AlOx

Previous section reported results on observation of isolated magnetic skyrmions on {Ir|Co|Pt} samples with variation of several parameters. Our main efforts was lead on those kind of samples, but during this PhD, we have also tried other materials. We have seen in Chapter 3 that Co was no the only ferromagnet used for the realization of multilayers, but unfortunately all the attempts of Fe-based multilayers have failed in getting out-of-plane anisotropy. As far as Co-based samples are concerned, since it is known from *ab initio* calculations that the interface Co|Pt is the one with the most important component for DMI, we have tried to replace the Ir by other materials. Indeed, we have tried two other type of multilayers: {W|Co|Pt} and {AlOx|Co|Pt}. As shown in Figure 6.14.

Aside from these observations, we have performed micromagnetic simulations of the evolution of skyrmions size with applied magnetic field (in the same range of the experimental datas) and by comparing simulations with experimental data, we found that:  $|D|^W = 1.7 \pm 0.3 \text{ mJ/m}^2$  and  $|D|^{AlOx} = 2.3 \pm 0.2 \text{ mJ/m}^2$ . Results for AlOx are in very good agreement with experiments led by other groups [141] where  $|D|^{AlOx} = 2.2 \text{ mJ/m}^2$ . However, it is noteworthy to point out that sample with AlOx was grown by sputtering

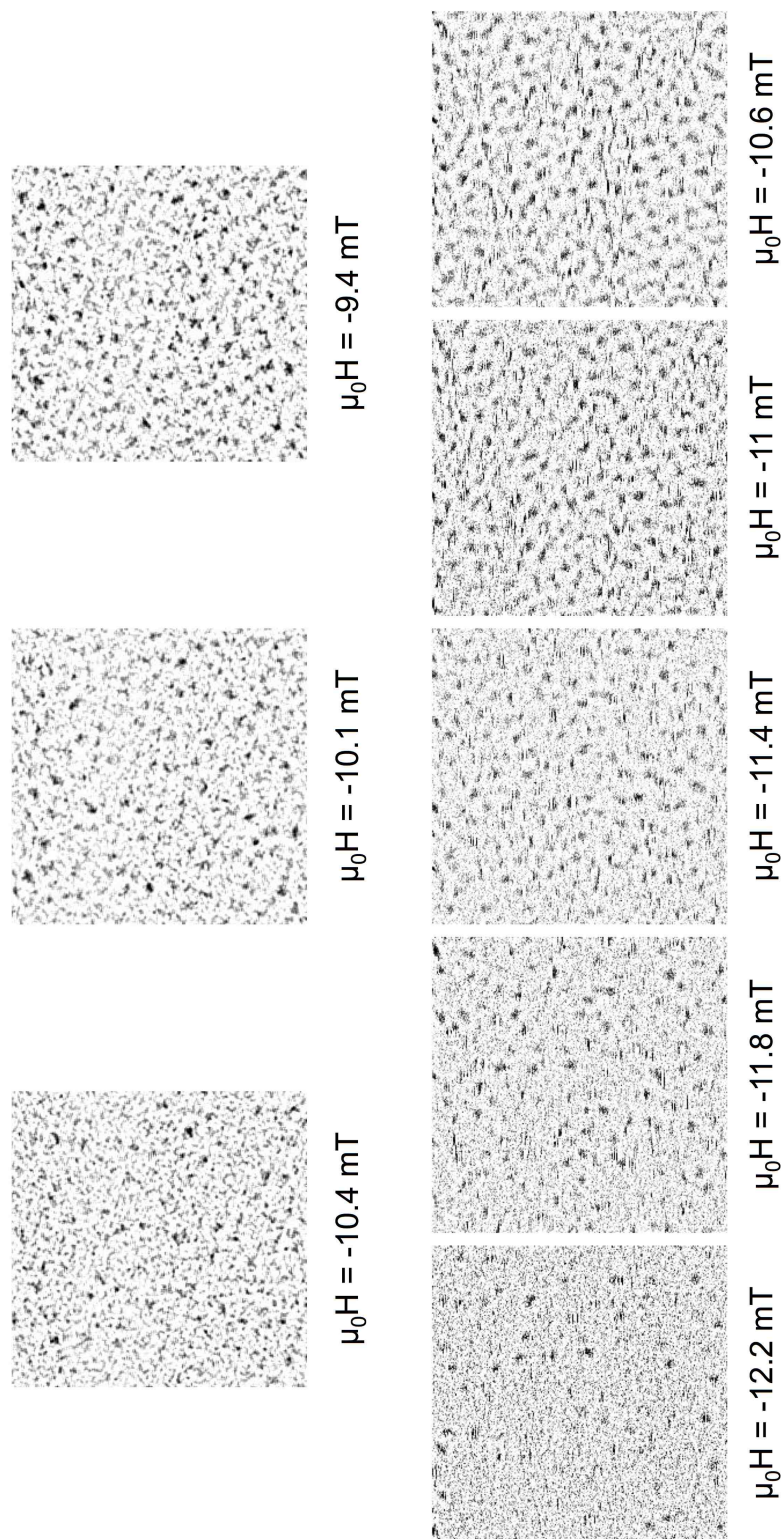


Figure 6.11:  $3 \times 3 \mu\text{m}^2$  MFM images of (top) Pt10|{Ir1|Co0.6|Pt0.7}5|Pt3 and (bottom) Pt10|{Ir1|Co0.6|Pt2}5|Pt3 with applied external out-of-plane magnetic field.

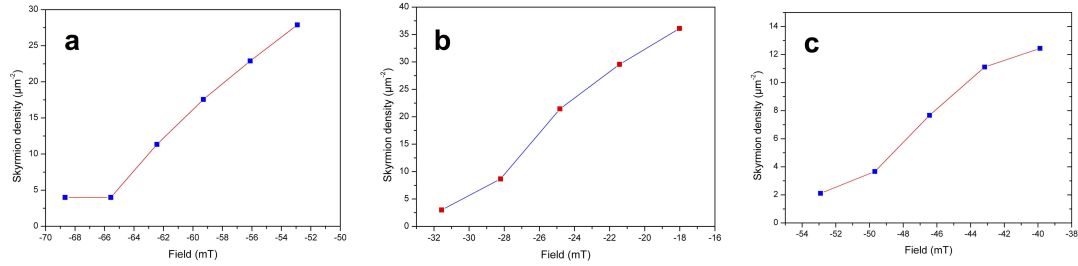


Figure 6.12: Evolution of the density of skyrmions with applied out-of-plane magnetic field for (a) Pt10|{Ir1|Co0.6|Pt0.7}5|Pt3 (b) Pt10|{Ir1|Co0.6|Pt1}5|Pt3 and (c) Pt10|{Ir1|Co0.6|Pt2}5|Pt3.

with a target of Al<sub>2</sub>O<sub>3</sub>, which might lead to structural differences with samples grown with etched Al.

## 6.3 Conclusions and discussion

Previous sections listed all the observations and quantitative analysis get from different studies. We can draw here some conclusions and prospects.

### 6.3.1 DMI

From the previous section, we can draw several conclusions considering the DMI amplitude:

- The number of repetitions of the main trilayer do not change the DMI amplitude in our {Ir|Co|Pt} samples
- Increasing the thickness of Co lead to a diminution of the average DMI amplitude
- The variation of Ir thickness is not changing the DMI amplitude although the roughness at the interfaces lead to an estimation of the DMI amplitude not as precise as in the other measurements
- The variation of Pt thickness do not seem to change the DMI amplitude, although a thinner Pt thickness might help enhance it. However more measurements have to be performed with a wider range of Pt thicknesses to confirm or infirm this possibility.
- Measurements on samples with replacement of Ir by W or AlO<sub>x</sub> have been performed. W sample lead to a DMI amplitude less important than Ir, although nice images of single skyrmion at the center of nanodisks have been observed at room temperature by MFM. AlO<sub>x</sub> sample lead to an enhancement of the DMI strength in the sample, as observed by other groups.

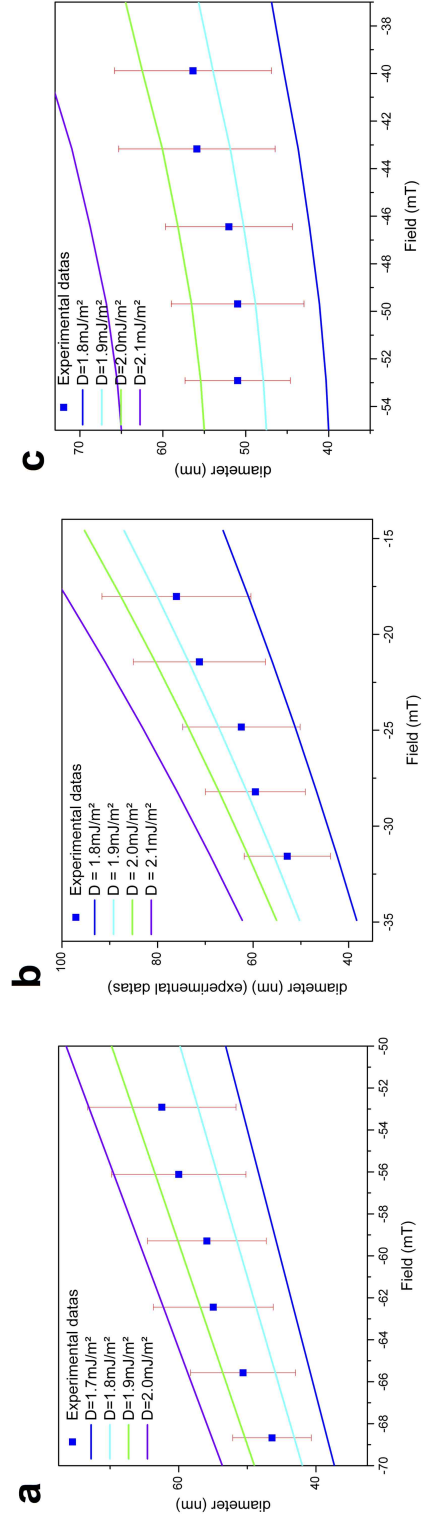


Figure 6.13: Evolution of the skyrmions diameter with applied out-of-plane magnetic field compared to Mumax3 simulations performed for different values of DMI amplitude, for (a) Pt10{Ir1Co0.6Pt0.7}5Pt3, (b) Pt10{Ir1Co0.6Pt1}5Pt3 and (c) Pt10{Ir1Co0.6Pt2}5Pt3

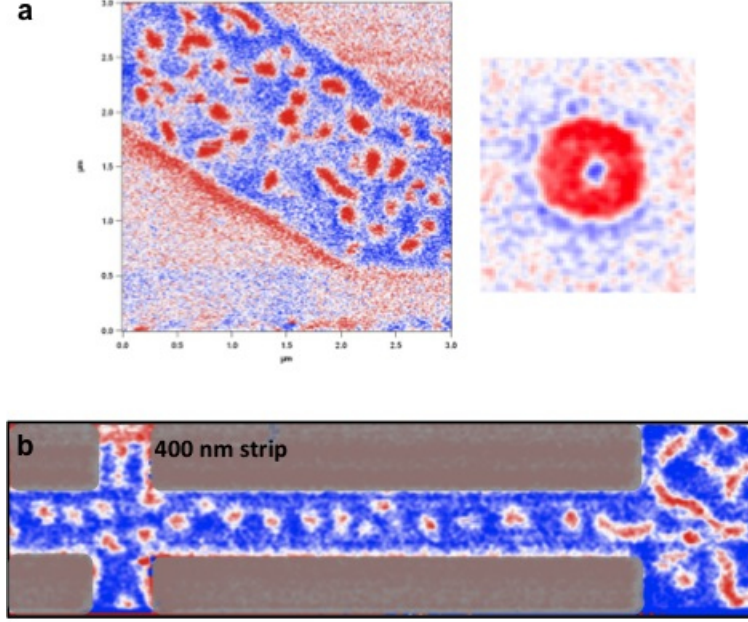


Figure 6.14: (a) MFM imaging with out of plane magnetic field of a plain film (left) and a 600nm disk (right) of  $\text{Pt}_{10}|\text{Co}_{0.6}|\text{Pt}_1|\{\text{W}_1|\text{Co}_{0.6}|\text{Pt}_1\}_{10}|\text{Pt}_3$  and (b) MFM imaging in a 400nm wide stripe of  $\text{Pt}_{10}|\{\text{AlOx}_1|\text{Co}_{0.6}|\text{Pt}_1\}_5|\text{Pt}_3$ .

### 6.3.2 Skyrmion density vs. $K_{\text{eff}}$

All along the previous sections, we have seen that the density of skyrmions with applied magnetic field is changing with the field and also from one sample to another. To be able to compare the density for every sample, we have chosen a field close to the saturation field, where skyrmions are observable:  $0.8 H_s$ . A. Soumyanarayanan et al. [136] have reported a diminution of the skyrmion density with increased effective anisotropy. We have also plotted the evolution of the skyrmion density with the effective anisotropy on Figure 6.15. The samples studied for this graph are :  $\{\text{Ir}_1|\text{Co}_{0.6}|\text{Pt}_1\}_5$ ,  $\{\text{Ir}_1|\text{Co}_{0.6}|\text{Pt}_1\}_{10}$ ,  $\{\text{Ir}_1|\text{Co}_{0.6}|\text{Pt}_1\}_{30}$ ,  $\{\text{Ir}_1|\text{Co}_{0.8}|\text{Pt}_1\}_5$ ,  $\{\text{Ir}_1|\text{Co}_{0.6}|\text{Pt}_{0.7}\}_5$ ,  $\{\text{Ir}_1|\text{Co}_{0.6}|\text{Pt}_2\}_5$ .

In Figure 6.15, we observe that the density of skyrmions is decreasing with increasing effective anisotropy. We also note a plateau for effective anisotropies above a certain value. While skyrmions in high  $K_{\text{eff}}$  samples are isolated, they form a dense pack in low  $K_{\text{eff}}$  sample, without being ordered in lattices. Additionally, skyrmions in low  $K_{\text{eff}}$  are stable over a wider range of value of out-of-plane field. It is also noteworthy to point out that skyrmions are wider in high  $K_{\text{eff}}$  samples (when the density is really low) and smaller in low  $K_{\text{eff}}$  samples (with large densities).

Here, we can conclude that the variation of  $K_{\text{eff}}$  has direct implications for skyrmion properties, such as their densities or their size.

### 6.3.3 Conclusion

We have described in this chapter the realization of multilayers with tunable room temperature skyrmions. The presence of these skyrmions was confirmed by MFM observa-

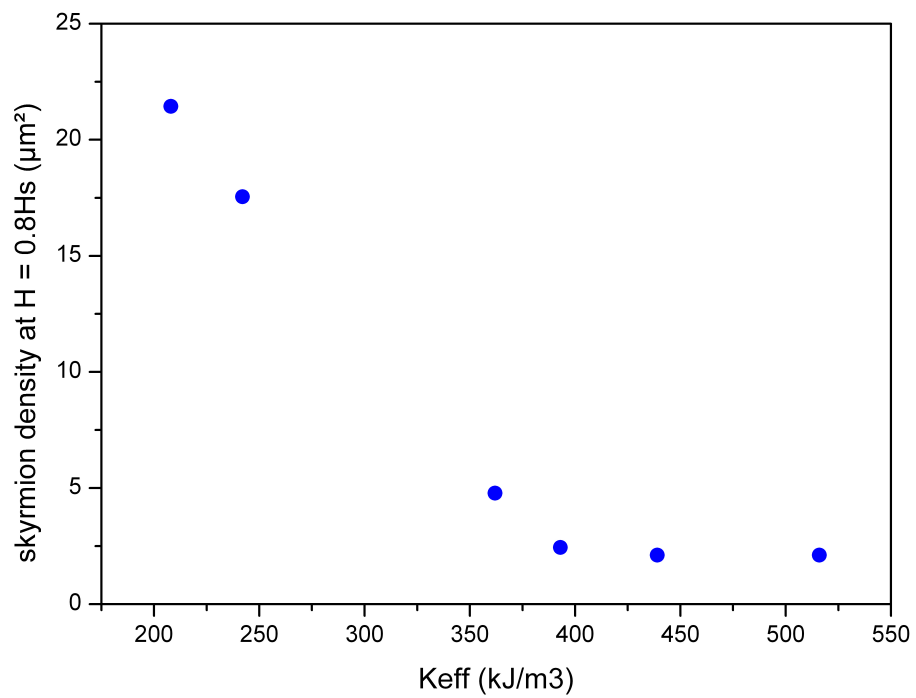


Figure 6.15: Evolution of the skyrmion density with effective anisotropy. The skyrmion density is taken at  $H = 0.8H_s$ , and is studied for samples with different number of repetitions, different Co thickness and different Pt thickness.

tions and the quantitative analysis performed lead to the conclusions that it is possible to control various skyrmions properties such as their size, their density and their stability with magnetic field.

# Conclusions and prospects

## Conclusions

At the beginning of my PhD, the main goal was to observe isolated magnetic skyrmions at room temperature. We have shown in this manuscript that we have been able to successfully achieve this goal with the observation of isolated sub-100nm skyrmions in {Ir|Co|Pt} samples. Moreover, we have been able to observe them with two different techniques : STXM - a synchrotron technique that maps the out-of-plane magnetization of a sample, and MFM - a laboratory technique that images the gradient of the magnetization. The quantitative analysis of the skyrmions sizes excluded the possibility of magnetic bubbles stabilized only by the dipolar interaction. Moreover, some LTEM measurements performed by our collaborators at the University of Glasgow, confirm the Néel chirality of the domains walls. Hence, we have been able to conclude that the circular-shape domains observed by STXM (and after by MFM) were indeed Néel magnetic skyrmions. We have also shown that we have stabilized them in extended films as well as in nanostructures (nanodisks with diameter from 200 nm to 1  $\mu\text{m}$ , as well as stripes with width from 400 nm to 1  $\mu\text{m}$ ). Comparison between the observations made by STXM and MFM lead to the conclusion that it was also possible to observe isolated magnetic skyrmions by MFM, but also that quantitative analysis was possible to determine the evolution of the skyrmion size with the external applied out-of-plane magnetic field.

Secondly, we have developed two different approaches to estimate the DMI amplitude in samples. The first one is based on the mean domain periodicity in samples after demagnetization. Fourier transformation allow the determination of this periodicity. Micromagnetic simulations performed on Mumax3, taking in input the magnetization at saturation, anisotropy energy and exchange stiffness evaluated experimentally for each sample, and with different values of  $D$ , give the evolution of the mean domain periodicity with  $D$ . The initial state of these simulations is an image of the actual domains of the sample after demagnetization. By comparing the simulations with experimental data, we found an estimation of the DMI strength. The second technique is based on the size evolution of skyrmions with applied out-of-plane magnetic field. Here we perform again micromagnetic simulations of the evolution of the skyrmion size with applied out-of-plane magnetic field. By comparing the experimental data with simulation, another estimation of  $D$  is obtained. Note that here, the experimental data are in higher number

and allow a more precise estimation of  $D$ . For the need of the micromagnetic simulations, we have also tried to determine the exchange stiffness of our samples, which is of  $10 \pm 3$  pJ. With this value, the DMI amplitude found in our samples is about  $2 \text{ mJ/m}^2$ . The precision of the determination of the exchange stiffness is not very high due to the experiments but, even in the lowest case, the DMI is still of great strength in the sample studied ( $1.5 \text{ mJ/m}^2$ ).

Since skyrmions are of great promise for next-generation information storage devices because of their small size, topological stability and (theoretical) ease of manipulation, it is also important to develop systems offering the possibility to tune skyrmions properties, such as their size, density and stability with applied field. Therefore, we have performed a systematic study on samples with variation of different parameters : number of repetitions of the main trilayers, Co thickness, Pt thickness, Ir thickness, composition of the buffer layers, and switching Ir with W or AlOx. We have shown that for every systems, we have been able to observe stabilized skyrmions at room temperature with MFM. We also reported that the number of repetitions of the main trilayer is not changing the DMI amplitude in our {Ir|Co|Pt} samples, increasing the thickness of Co leads to a diminution of the average DMI amplitude, the variation of Ir or Pt thickness is not influencing the magnitude of the DMI, although a thinner Pt thickness might help to enhance it, measurements on samples with replacement of Ir by W or AlOx have been performed. W sample lead to a DMI amplitude less important than Ir, although nice images of single skyrmion at the center of nanodisks have been observed at room temperature by MFM. Samples with top AlOx layer lead to an enhancement of the DMI strength in the sample, as observed by other groups. We also observed that the density of skyrmions is decreasing with increasing effective anisotropy. There is a plateau for effective anisotropies above a certain value. While skyrmions in high  $K_{\text{eff}}$  samples are isolated, they form a dense pack in low  $K_{\text{eff}}$  sample, without being ordered in lattices. Additionally, skyrmions in low  $K_{\text{eff}}$  are stable over a wider range of values of out-of-plane field. It is also noteworthy to point out that skyrmions are wider in high  $K_{\text{eff}}$  samples (when the density is really low) and smaller in low  $K_{\text{eff}}$  samples (with large densities). The variation of  $K_{\text{eff}}$  has direct implications for skyrmion properties, such as their densities or their size.

## Next steps

**Growth** On the path we opened, further efforts on the growth of Fe-based multilayers can lead to samples with out-of-plane anisotropy. This would enable the possibility to perform the same kind of study as the one lead in Chapter 6 and hence the possibility to tune in wider range the properties of skyrmions and maybe enhance the DMI strength observed in samples. Without changing the ferromagnet, it is also possible to change the materials chosen to be above Co. We have shown here some preliminary results with W and AlOx. AlOx is already quite well studied by other groups [141], but a more complete investigation of W is needed, although its growth by sputtering is quite

complex (reason why only few investigations on  $W$  have been performed during this PhD). Other materials can also be tried, such as Pd or Pb.

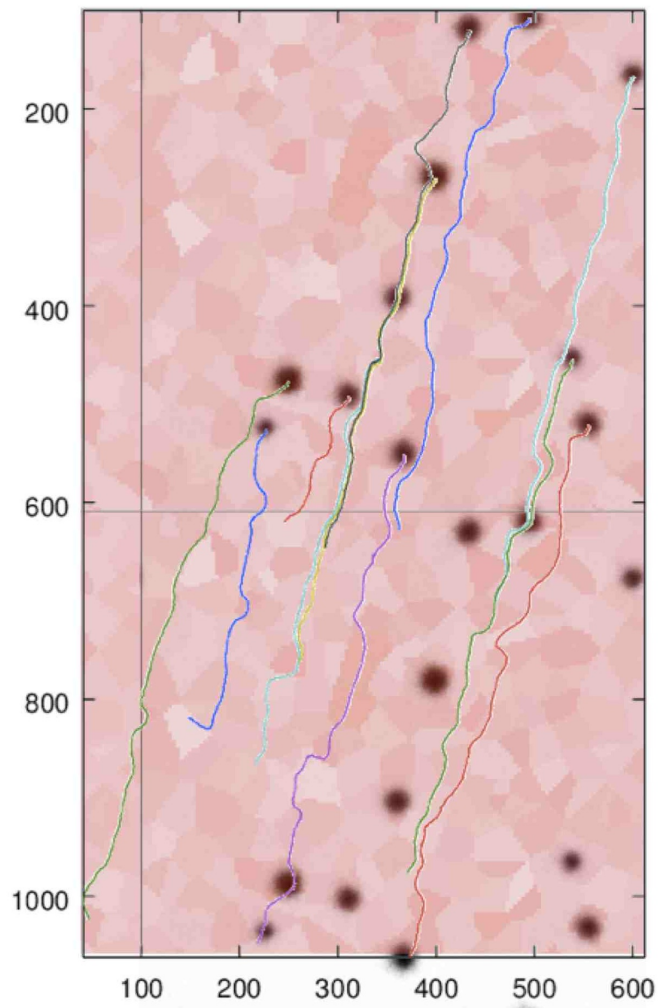
**Stability under in plane magnetic field** In this work, we have studied the nucleation and stabilization of magnetic skyrmions with applied out-of-plane magnetic field. Moreover, we have demonstrated the Néel chirality of the observed magnetic skyrmions. Hence, their behavior under in-plane magnetic field should be different according to the direction of the field. One can think about studying this phenomena.

**Dynamics** Another path to follow concerns the dynamics of skyrmions. We have seen some good preliminary results in this manuscript as well as in other groups [109, 135, 139]. In our experiments, further efforts have to be made to improve the velocity of skyrmions in racetracks, as well as concerning the pinning sites. Indeed, we have recent results concerning the motion of small skyrmions in racetracks. As proposed by M. Baćani et al. [137], it is very likely that the DMI amplitude is not homogeneous all over the surface of our sample, and that the value found by the several approaches explained above is only the average DMI amplitude of the sample. To understand more finely the behavior of the skyrmions motion observed by MFM, new PhD student William Legrand has simulated a distribution of the DMI variation all over the tracks. It was done with voronoi tessellation by Mumax3. It is a normal distribution of the DMI and we keep the same map for every experiments. Results are reported on Figure 6.16.

Several trends are noticed. Indeed, at low current densities, skyrmions are stabilized and are pinned in high- $D$  areas. When moving, they tend to avoid low- $D$  areas, and curve their trajectories into high- $D$  areas. We can also notice that pinned skyrmions are depinned by other skyrmions when their motion lead them in the area of pinned skyrmions. In the case of skyrmions that are forced to go in low  $D$  areas, they are vanishing. For larger current densities, skyrmion motion seems to be less brownian and deterministic trajectories are almost reproduced. It is also noteworthy to point out that skyrmions velocities depend on their size, hence skyrmion velocity is  $D$ -dependent.

Finally, a more complete study has to be performed on the skyrmion motion with different samples to improve the velocity and the pinning of skyrmions. Also, it is important to have a more complete picture of the influence of the distribution of  $D$  and probably also the anisotropy on the skyrmions velocity. Indeed, from the study of the role of defects (be it of anisotropy or DMI) in the nucleation of skyrmions by spin polarized injection (see appendix for details) that the non uniform distribution of anisotropy and/or DMI can help/thwart the nucleation and stabilization of skyrmions.

One can also think about the possibility to observe the different modes of skyrmions, predicted by micromagnetic simulations [175], or the possibility to detect magnetic skyrmion by transport measurements, for example thanks to the Topological Hall Effect.



$$J = 10 \cdot 10^{10} \text{ A m}^{-2}$$

Figure 6.16: Trajectories of skyrmions in race-tracks. The pink background corresponds to the normal distribution of DMI amplitude calculated by MUMax3. The darkest part represents higher values of  $D$  (10% higher) and the lightest part to lower value of  $D$  (10% lower).

**Antiferromagnetic coupling** We can also consider the possibility to study samples with antiferromagnetic coupling (with a layer of Ru between two layers of Co for example). This should allow us to decrease the dipolar interaction, at least mostly, and thereby to obtain smaller skyrmions. Moreover, we have seen that the skyrmions trajectories bend away from the driving current direction due to the Magnus Force [47]. Consequently, the skyrmions in constricted geometries may be destroyed when they reach the sample edges [176, 26]. This phenomenon is expected to be suppressed in the antiferromagnetically exchange-coupled bilayer system, since the Magnus forces in the top and bottom layers should be opposite. We anticipate that these systems should provide promising means to move magnetic skyrmions in a perfectly straight trajectory in ultra-dense devices with ultra-fast processing speed.

**Nucleation** Finally, in this work, we have demonstrated the possibility to nucleate skyrmions by applying external out-of-plane magnetic field. However, we also have seen the possibility to nucleate skyrmions by spin-polarized current, either theoretically [50, 97, 99, 177] (see also Appendix), or experimentally at very low temperatures [80]. Exploration of the possibility to experimentally write and delete single magnetic skyrmions at room temperature would be a great achievement.

# Appendix A

## Annex : Complementary micromagnetic simulations study

### Contents

---

|            |                                                  |            |
|------------|--------------------------------------------------|------------|
| <b>A.1</b> | <b>Mecanism of injection</b>                     | <b>150</b> |
| <b>A.2</b> | <b>Roles of defects</b>                          | <b>152</b> |
| A.2.1      | DMI defects                                      | 152        |
| A.2.2      | Anisotropy defects                               | 153        |
| <b>A.3</b> | <b>Skyrmions modes</b>                           | <b>154</b> |
| A.3.1      | Simulation model and method                      | 154        |
| A.3.2      | Dynamic response to driving perpendicular fields | 155        |

---

In this section, I will present micromagnetic simulations that study the nucleation of isolated skyrmions in nanostructures with spin polarized current. This study has been performed in the path of the work done by former Post-Doc Joao Sampaio, at the very beginning of this PhD.

### A.1 Mecanism of injection

In order to get insights on the skyrmion nucleation mechanism, we present in Figure A.1 [50] a series of snapshots of both the magnetization distribution along  $z$  direction and the DMI energy density in a 80nm disk obtained at different times after the injection of a pulse of spin polarized current. The initial state at  $t = 0$  was uniformly magnetized along  $+z$  (red). The pulse starts at  $t = 0$  and has a duration of 2 ns long pulse. The spin-polarized current ( $P = 0.4$  oriented along  $-z$ ) is injected, in the central region of the disk (40 nm). For these simulations, the  $D$  value is  $|\mathbf{D}| = 6 \text{ mJ/m}^2$ , the current density is  $J = 2.10^8 \text{ A/cm}^2$  and the magnetic damping is  $\alpha = 0.3$ .

At  $t = 0.21 \text{ ns}$ , the magnetization is still quasi uniform and oriented along  $+z$  with only a small tilt induced on the disk edge by the DMI (independently of the current) [49].

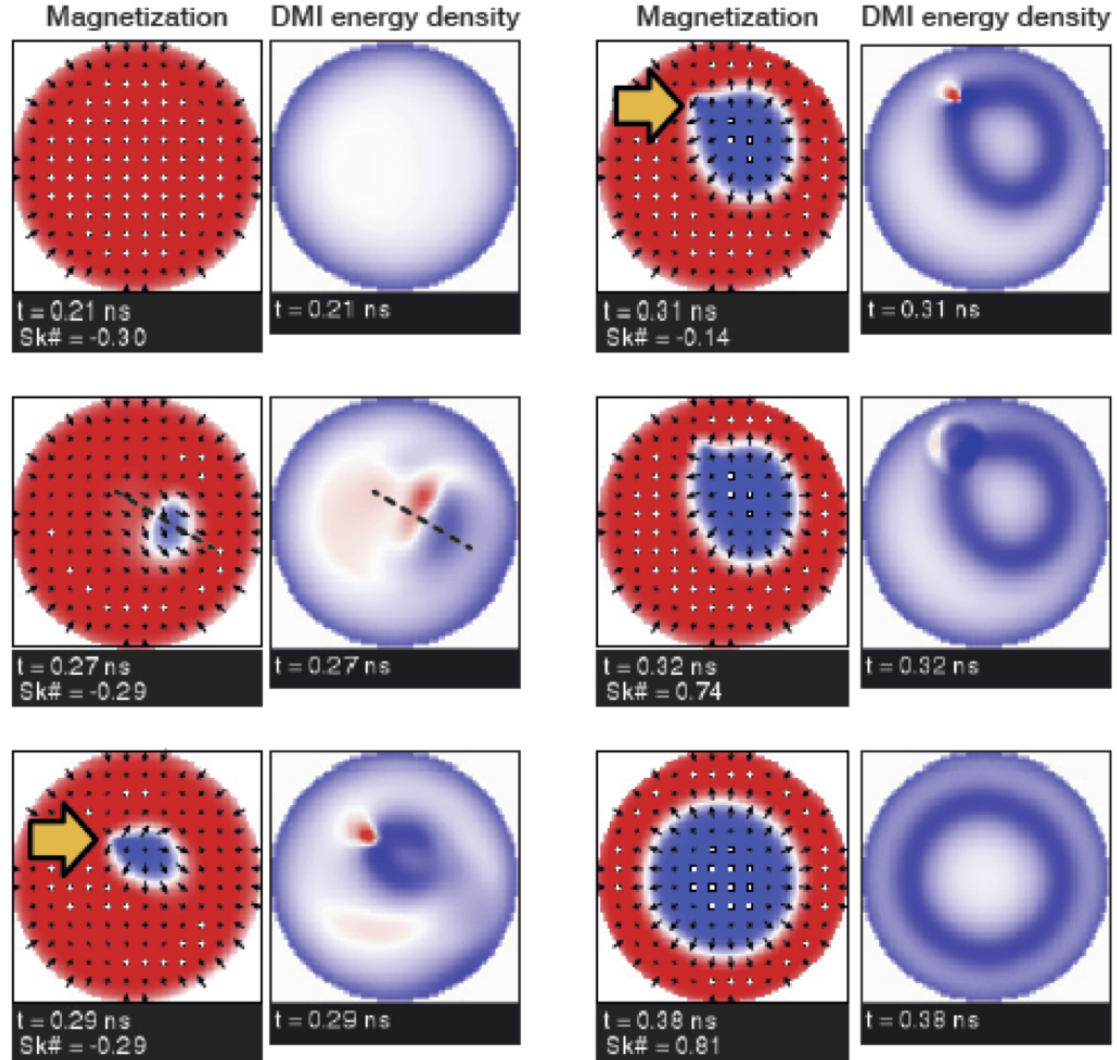


Figure A.1: Magnetization distribution along  $z$  (left) and DMI energy density distribution (right) in 80 nm nanodisks at different times ( $t = 0.21$  ns, 0.27 ns, 0.29 ns, 0.31 ns, 0.32 ns and 0.38 ns) during a 2 ns long pulse of spin-polarized current ( $P = 0.4$  along  $-z$ ) injected in the central region of the disk (40nm). The  $D$  value is  $|\mathbf{D}| = 6$  mJ/m<sup>2</sup>,  $J = 2 \cdot 10^8$  A/cm<sup>2</sup> and  $\alpha = 0.3$ . The initial state at  $t = 0$  was quasi-uniformly magnetized along  $+z$  (red). The yellow arrows at  $t = 0.29$  and 0.31 ns indicate the location of defect-like point inside the wall of the bubble having a strong positive DMI energy density. After the reversal of the spins in the defect (at  $t = 0.32$  ns for these parameter conditions), a skyrmion is stabilized at the center of the disk and remains stable even after the end of the current pulse [50].

The blue contrast on the edge of the right figure reflects the lowering of the DMI energy by this inward tilt. At  $t = 0.27$  ns, the magnetization inside a region under the injection contact region is reversed and this configuration corresponds to a magnetic bubble with a skyrmion number that remains close to zero. Then the spins inside the pseudo-wall of the bubble tend to be oriented very rapidly ( $t = 0.29$  ns) toward the direction that is favored by the DMI, compressing the portion of non-favored chirality into a small region (indicated by the yellow arrow) that concentrates a large amount of exchange and DM energy. The size of this small defect-like region, comparable to a Bloch point in classical bubble material, decreases with time and changes its position due to the spin transfer induced dynamics of the bubble. At  $t = 0.31$  ns, the defect size becomes small enough and eventually switches its configuration (with emission of spin waves across the disk) with an increase of the skyrmion number close to 1 (not exactly 1 because of the tilted magnetization on the edges) that corresponds to a single skyrmion. Once the skyrmion configuration is nucleated, this relaxed configuration remains stable during the remaining time of the current pulse and after the end of the pulse.

By changing the disk shape and the material parameters, we have found that in some cases that the small defect region reaches the disk edges due to the attractive interaction with the tilted magnetization, leading to the transformation of the bubble into an edge-to-edge domain wall. Finally, in other conditions, we have also observed some more complex nucleation process involved the nucleation of more than one skyrmion (sometimes together with edge-to-edge domain wall). However they eventually collapse before the end of the pulse in order to relax in a final configuration corresponding to a single skyrmion in the disk.

## A.2 Roles of defects

After the study of the nucleation of isolated skyrmions by spin-polarized current injection, we have tried to find possible improvement for this mechanism.

Our idea was that since the interfaces of our samples are not perfect and show some defects. These defects (either DMI or anisotropy defects in the following study) are expected to influence the nucleation of skyrmions.

### A.2.1 DMI defects

We present in Figure A.2 a series of snapshots of the magnetization distribution along  $z$  direction in a 80 nm disk obtained after the injection of a pulse of spin polarized current. The initial state at  $t = 0$  was uniformly magnetized along  $+z$  (red). The pulse starts at  $t = 0$  and has a duration of 1 ns long pulse. The spin-polarized current ( $P = 0.4$  oriented along  $-z$ ) is injected, in the central region of the disk (10 nm). For these simulations. The  $D$  value is  $|\mathbf{D}| = 4$  mJ/m<sup>2</sup> in the dark blue region and  $|\mathbf{D}| = 2$  mJ/m<sup>2</sup> in the light blue region, the current density is  $J = 2.10^8$  A/cm<sup>2</sup> and the magnetic damping is  $\alpha = 0.3$ .

Whenever the whole disk has a DMI value of  $|\mathbf{D}| = 2$  mJ/m<sup>2</sup> or  $|\mathbf{D}| = 4$  mJ/m<sup>2</sup>,

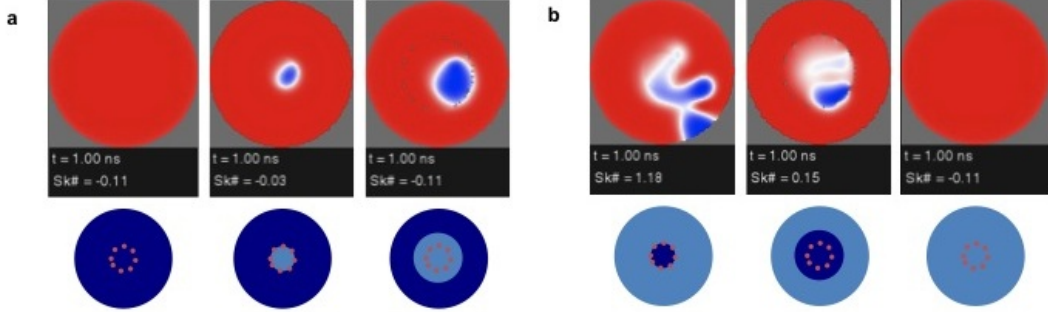


Figure A.2: Magnetization distribution along  $z$  in 80 nm nanodisks after a 1 ns long pulse of spin-polarized current ( $P = 0.4$  along  $-z$ ) injected in the central region of the disk (10 nm). The  $D$  value is  $|\mathbf{D}| = 4 \text{ mJ/m}^2$  in the dark blue region  $|\mathbf{D}| = 2 \text{ mJ/m}^2$  in the light blue region, and  $J = 2 \cdot 10^8 \text{ A/cm}^2$  and  $\alpha = 0.3$ . The initial state at  $t = 0$  was quasi-uniformly magnetized along  $+z$  (red). In the case of an inner region with DMI smaller than in the outer region, this DMI defect helps nucleate a bubble (skyrmion number of 0). But, at the end of the injection, when the nanodisk is relaxing, the bubble is not stable and eventually vanishes. Hence, DMI defects don't seem to help nucleate skyrmions.

in the "normal" case explained in the previous section, no skyrmion can be nucleated. Here, we wonder if some kind of DMI defect could help the nucleation of skyrmions. We can observe that in the case where the inner region (20 nm diameter) has a DMI amplitude smaller than in the outer region, a bubble is nucleated (skyrmion number of 0). In all the other cases, we notice that DMI defects as simulated here, don't help any kind of nucleation.

### A.2.2 Anisotropy defects

We present in Figure A.3 a series of snapshots of the magnetization distribution along  $z$  direction in a 80 nm disk obtained after the injection of a pulse of spin polarized current. The initial state at  $t = 0$  was uniformly magnetized along  $+z$  (red). The pulse starts at  $t = 0$  and has a duration of 1 ns long pulse. The spin-polarized current ( $P = 0.4$  oriented along  $-z$ ) is injected, in the central region of the disk (10 nm). For these simulations. The  $D$  value is  $|\mathbf{D}| = 4 \text{ mJ/m}^2$ , the current density is  $J = 2 \cdot 10^8 \text{ A/cm}^2$  and the magnetic damping is  $\alpha = 0.3$ . In the central region (20 nm diameter), we artificially create a region where the anisotropy energy is diminished : the value corresponds to 0, 25, 50, 75 and finally 100% of the anisotropy energy of the outer region.

We can see that when there is no defect of the anisotropy energy, no skyrmion can be nucleated under such conditions. Now looking at the cases where defects are created, we can notice that, except in the case where the anisotropy is artificially fixed to zero, every kind of defects help nucleating skyrmion (with a skyrmion number of 1). We remind

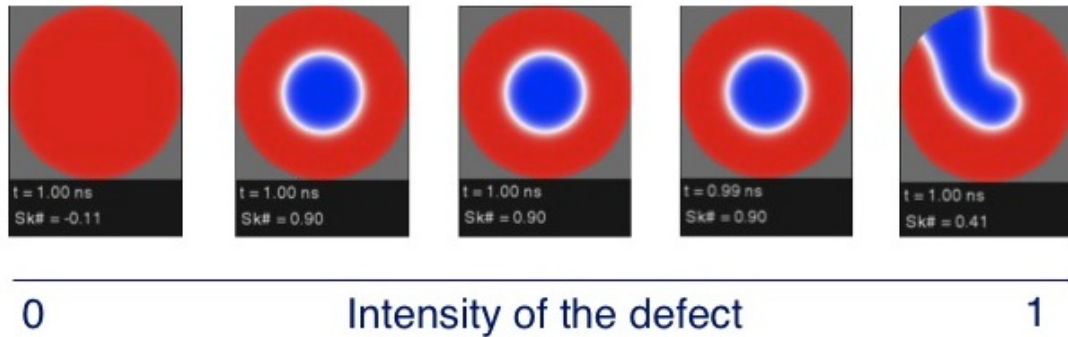


Figure A.3: Magnetization distribution along  $z$  in 80 nm nanodisks after a 1 ns long pulse of spin-polarized current ( $P = 0.4$  along  $-z$ ) injected in the central region of the disk (10 nm). The anisotropy is artificially diminish in the region of the injection with, from left to right, 0%, 25%, 50%, 75% and 100% or the value of the outer region. The  $D$  value is  $|\mathbf{D}| = 4 \text{ mJ/m}^2$  and  $J = 2.10^8 \text{ A/cm}^2$  and  $\alpha = 0.3$ . The initial state at  $t = 0$  was quasi- uniformly magnetized along  $+z$  (red). An isolated skyrmion is nucleate as soon as the anisotropy defect exist but without an anisotropy equal to zero. Hence anisotropy defects seem to help the nucleation of skyrmions.

that the skyrmion number calculated with simulation take into account the tilting spins at the edge of the nanodisk and hence a skyrmion number of  $\sim 0.9$  corresponds to a theoretical value of 1.

Hence a modification of the anisotropy of the system can help the nucleation of isolated skyrmions.

### A.3 Skyrmions modes

At the beginning of this PhD, some simulations have been performed in collaboration with IEF, Orsay, France to investigate the different skyrmions modes and find a skyrmion signature in those modes [175]. Indeed, meanwhile exploring the nucleation of skyrmions by injection of spin polarized current, we also started to explore the dynamics of individual skyrmions confined geometrically in ultrathin circular dots. In particular, the breathing dynamics of the skyrmion is studied, which is known to provide a distinct microwave response from experiments conduced on skyrmion crystals in helimagnetic insulators [178].

#### A.3.1 Simulation model and method

The static and dynamic states of the isolated skyrmion in a confined magnetic dot were studied using numerical micromagnetic simulations with a modified version of the Mumax2 code. The code performs a numerical time integration of the Landau-Lifschitz

equation of motion with Gilbert damping for the magnetization dynamics, as seen in Chapter 1:

$$\frac{d\mathbf{m}}{dt} = -|\gamma_0|\mathbf{m} \times \mathbf{H}_{eff} + \alpha\mathbf{m} \times \frac{d\mathbf{m}}{dt}, \quad (\text{A.1})$$

where  $\gamma_0$  is the gyromagnetic constant,  $\alpha$  is the phenomenological Gilbert damping constant,  $\|\mathbf{m}\| = 1$  is the unit vector representing the orientation of the magnetization, and  $\mathbf{H}_{eff}$  is the effective field,

$$\mathbf{H}_{eff} = -\frac{1}{\mu_0 M_s} \frac{\delta U}{\delta \mathbf{m}}, \quad (\text{A.2})$$

which represents the variational derivative of the total micromagnetic energy  $U$  with respect to the magnetization.

The micromagnetic parameters are chosen to correspond to a model thin film perpendicular anisotropy system: an isotropic exchange constant of  $A = 15$  pJ/m, a perpendicular anisotropy constant of  $K_u = 1$  MJ/m<sup>3</sup> and a saturation magnetization of  $M_s = 1$  MA/m.

The main focus of this work was the breathing response of individual skyrmion in a dot. To this end, the calculations performed involve the dynamic response of the perpendicular magnetization to perpendicular dynamic fields  $h_z$ :

$$m_z(\omega) = \chi_{zz}(\omega)h_z(\omega). \quad (\text{A.3})$$

In the absence of the DMI, the equilibrium ground state is uniformly magnetized along the easy z axis, which means that the linear susceptibility  $\chi_{zz}$  is significantly small. A finite  $\chi_{zz}$  in the linear response regime should provide a clear signature of individual skyrmions in magnetic dots.

The ground state of the magnetic dot with an individual skyrmion is first determined in the presence of a magnetic field applied perpendicular to the film plane at zero temperature. The initial state comprises an hedgehog skyrmion. For each value of the applied magnetic field, this initial state is then allowed to relax over 5ns with a large damping constant of  $\alpha = 0.3$ . The magnetization dynamics is then computed about this equilibrium state. The excitation modes of the skyrmion are determined from the transient response of the system to a time-varying but spatially uniform field applied in the perpendicular z direction. The amplitude of the excitation field is 0.5 mT.

### A.3.2 Dynamic response to driving perpendicular fields

An example of the calculated power spectrum of excitation is shown in figure A.4 for an intermediate value of the DMI,  $|D| = 3$  mJ/m<sup>2</sup>.

Three distinct modes are observed in the frequency range considered. To highlight the distinct features associated with the presence of the skyrmion, the power spectrum for a dot with no skyrmion is shown in the same figure. In this case, the magnetization

is uniformly magnetized in the  $+z$  direction at the center of the dot, but it tilts at the edges as a result of the boundary conditions related to the DMI [49, 175]. Because of these tilts,  $\chi_{zz}$  is finite even for this case and three modes can be seen in the same frequency range. The lowest mode corresponds to the uniform precession mode and all three modes exhibit a linear field dependence, which is expected for spin waves in this geometry. The appearance of a low-frequency excitation, such as the branch below 10 GHz, is suggested as a strong signature of the presence of a confined skyrmion in a dot and a measure of the DMI.

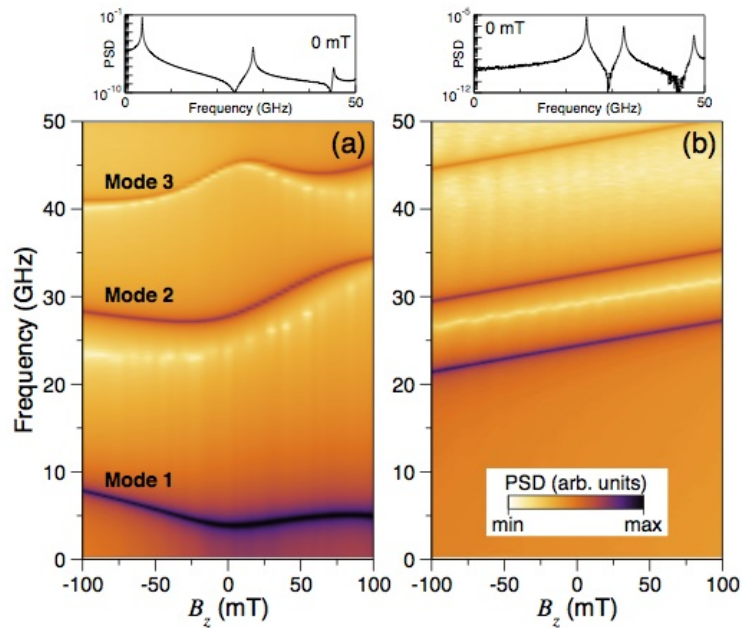


Figure A.4: Map of the power spectra density (PSD) of excitations as function of perpendicular applied field  $B_z$  for  $|D| = 3 \text{ mJ/m}^2$ . (a) Single isolated skyrmion in ground state. (b) Nominally uniform ground state. The insets at the top show the corresponding PSD at zero field.

# Bibliography

- [1] W. Heisenberg. *Z. Phys.*, 1928.
- [2] I. Dzyaloshinskii. *J. Phys. Chem. Solids*, 1958.
- [3] T. Moriya. *Phys. Rev. Lett.*, 1960.
- [4] A. Fert P.M. Levy. *Phys. Rev. Lett.*, 44:1538, 1980.
- [5] A. Fert et al. *Nat. Nanotech.*, 8:152–156, 2013.
- [6] S. Emori et al. *Nat. Mat.*, 12:611–616, 2013.
- [7] A. Hrabec et al. *Phys. Rev. B*, 90:020402, 2014.
- [8] A. Thiaville et al. *Europhys. Lett.*, 100:57002, 2012.
- [9] S. Blundell. *Magnetism in condensed matter*. Oxford University Press, 2009.
- [10] Louis Néel. *C. R. Acad. Sci., Paris*, 237:1468–1470, 1953.
- [11] P. Bruno. *J. Magn. Soc. Jpn.*, 5, 1991.
- [12] P. Bruno et al. *J. Appl. Phys.*, 64:3153, 1988.
- [13] F. J. A. den Broeder et al. *Phys. Rev. Lett.*, 60:2769, 1988.
- [14] S. T. Purcell et al. *J. Magn. Magn. Mater.*, 113:257, 1992.
- [15] P.J.H. Bloemen et al. *J. Magn. Magn. Mater.*, 93:105, 1991.
- [16] D. Atkinson et al. *Nat. Mater.*, 42, 2003.
- [17] N. Vernier et al. *arXiv: 1609.0304549*, 2016.
- [18] L.K. Bogart et al. *Phys. Rev. B*, 79, 2009.
- [19] R.C. O’Handley. *Modern Magnetic Materials: Principles and Applications*. John Wiley, 1999.
- [20] T. Koyama et al. *App. Phys. Lett.*, 98:192509, 2011.

- 
- [21] N.L. Schryer and L.R. Walker. *J. Appl. Phys.*, 45:5406, 1974.
- [22] O.A. Tretiakov and A. Abanov. *Phys. Rev. Lett.*, 105:157201, 2010.
- [23] L. Berger. *J. Appl. Phys.*, 49:2156, 1978.
- [24] P. Gambardella and I.M. Miron. *Phil. Trans. R. Soc.*, 369:3175, 2011.
- [25] I.M. Miron et al. *Nature*, 476, 2011.
- [26] X. Zhang et al. *Sci. Rep.*, 6, 2016.
- [27] L. Liu et al. *Phys. Rev. Lett.*, 109, 2012.
- [28] K. Garello et al. *Nat. Nanotech.*, 8, 2013.
- [29] C.O. Avci et al. *App. Phys. Lett.*, 100:212404, 2012.
- [30] L.Q. Liu et al. *Science*, 336, 2012.
- [31] J. Kim et al. *Nat. Mater.*, 12, 2013.
- [32] H. Hayashi et al. *Phys. Rev. B.*, 89:144425, 2014.
- [33] C. Zhang et al. *App. Phys. Lett.*, 103, 2013.
- [34] C.F. Pai et al. *App. Phys. Lett.*, 101, 2012.
- [35] X. Fan et al. *Nat. Comm.*, 4, 2013.
- [36] T. Schulz et al. *App. Phys. Lett.*, 107, 2015.
- [37] P.P.J. Haazen et al. *Nat. Mater.*, 12, 2013.
- [38] M. Jamali et al. *Phys. Rev. Lett.*, 111, 2013.
- [39] I. Miron et al. *Nat. Mat.*, 9:230, 2010.
- [40] U.H. Pi et al. *Appl. Phys. Lett.*, 97:162507, 2010.
- [41] S.-G. Je et al. *Phys. Rev. B.*, 88, 2013.
- [42] R. Lavrijsen et al. *Phys. Rev. B.*, 91, 2015.
- [43] M. Vaňatka et al. *J. Phys. Condes. Matter.*, 27, 2015.
- [44] A. Bogdanov and A. Hubert. *J. Magn. Magn. Mat.*, 138, 1994.
- [45] N. Romming et al. *Phys. Rev. Lett.*, 114:177203, 2015.
- [46] T.H.R. Skyrme. *A non-linear field theory*. Proceedings of the Royal Society of London. Series A. Mathematical and Physical Sciences, 1961.

- 
- [47] N. Nagaosa and Y. Tokura. *Nat. Nanotech.*, 243:899–911, 2013.
- [48] N.D. Mermin. *Rev. Mod. Phys.*, 51, 1979.
- [49] S. Rohart and A. Thiaville. *Phys. Rev. B*, 88:184422, 2013.
- [50] J. Sampaio et al. *Nat. Nanotech.*, 8:839–844, 2013.
- [51] A.N. Bogdanov and D.A. Yablonskii. *Sov. Phys. JETP*, 68, 1989.
- [52] U.K. Rö ßler, A.N. Bogdanov, and C. Pfleiderer. *Nature*, 442:797–801, 2006.
- [53] S. Mühlbauer et al. *Science*, 323:915–919, 2009.
- [54] C. Pappas et al. *Phys. Rev. Lett.*, 102:197202, 2009.
- [55] C. Pfleiderer et al. *J. Phys. Condens. Matter*, 22:164207, 2010.
- [56] T. Adams et al. *Phys. Rev. Lett.*, 107:217206, 2011.
- [57] A. Tonomura et al. *Nano Lett.*, 12:5438–5442, 2012.
- [58] W. Munzer et al. *Phys. Rev. B*, 81:041203(R), 2010.
- [59] X.Z. Yu et al. *Nature*, 465:901–904, 2010.
- [60] D. Morikawa et al. *Phys. Rev. B*, 88:020101(R), 2013.
- [61] P. Milde et al. *Science*, 340:1076–1080, 2013.
- [62] K. Shibata et al. *Nat. Nanotech.*, 8:723–728, 2013.
- [63] S.V. Grigoriev et al. *Phys. Rev. Lett.*, 110:207201, 2013.
- [64] S. Seki et al. *Science*, 336:198–201, 2012.
- [65] S. Seki et al. *Phys. Rev. B*, 85:220406 (R), 2012.
- [66] S. Seki et al. *Phys. Rev. B*, 86:060403 (R), 2012.
- [67] T. Adams et al. *Phys. Rev. Lett.*, 108:237204, 2012.
- [68] P. Bak and M.H. Jensen. *J. Phy. C*, 13, 1980.
- [69] K. Kadowaki, K. Okuda, and M. Date. *J. Phys. Soc. Jpn.*, 51, 1982.
- [70] M. Date, K. Okuda, and K. Kadowaki. *J. Phys. Soc. Jpn.*, 42, 1977.
- [71] S. Kusaka et al. *Solid State Commun.*, 20, 1976.
- [72] Neubauer et al. *Phys. Rev. Lett.*, 102:186602, 2009.
- [73] M. Uchida et al. *Science*, 311:359–361, 2006.

- 
- [74] X.Z. Yu et al. *Nat. Mater.*, 10:106–109, 2011.
- [75] A.B. Butenko et al. *Phys. Rev. B*, 82:052403, 2010.
- [76] A.N. Bogdanov et al. *Phys. Rev. B*, 66:214410, 2002.
- [77] A.B. Butenko et al. *J. Phys. Conf. Ser.*, 200, 2009.
- [78] N. Kanazawa et al. *Phys. Rev. Lett.*, 106:156603, 2011.
- [79] S. Heinze et al. *Nat. Phys.*, 7:713–718, 2011.
- [80] N. Romming et al. *Science*, 341:636–639, 2013.
- [81] A.H. Eschenfelder. *Magnetic Bubble Technology*. Springer, 1980.
- [82] A.P. Malozemoff and J.C. Slonczewski. *Magnetic Domain Walls in Bubble Materials*. Academic, New York, 1979.
- [83] S. Heinze et al. *Science*, 288:1805–1808, 2000.
- [84] C. Pfeleiderer et al. *Phys. Rev. B*, 55, 1997.
- [85] B. Binz and A. Vishwanath. *Physica B.*, 402, 2008.
- [86] N. Kanazawa et al. *Phys. Rev. B*, 86:134425, 2012.
- [87] P. Sinha et al. *Phys. Rev. B*, 89, 2014.
- [88] N.A. Porter et al. *Phys. Rev. B*, 90, 2014.
- [89] C. Ritz et al. *Nature*, 497, 2013.
- [90] Y. Machida et al. *Nature*, 463, 2010.
- [91] C. Pfeleiderer et al. *Science*, 316:5833, 2007.
- [92] X.Z. Yu et al. *Proc. Natl. Acad. Sci. U.S.A.*, 109:8793–8794, 2012.
- [93] J. Zang et al. *Phys. Rev. Lett.*, 107:136804, 2011.
- [94] T. Schulz et al. *Nat. Phys.*, 8:8856–8860, 2012.
- [95] A. Thiaville et al. *Europhys. Lett.*, 69:990–996, 2005.
- [96] K. Everschor et al. *Phys. Rev. B*, 86:054432, 2012.
- [97] J. Iwasaki et al. *Nat. Comm.*, 4:2442, 2013.
- [98] A. Rosch. *Nat. Nanotech.*, 8:899, 2013.
- [99] J. Iwasaki et al. *Nat. Nanotech.*, 8:742–747, 2013.

- 
- [100] Y.-H. Liu and Y.-Q. Li. *J. Phys. Condens. Matter*, 25, 2013.
- [101] H. Draaisma et al. *J. Magn. Magn. Mater.*, 66, 1987.
- [102] W. Zhang et al. *Nat. Phys.*, 11, 2015.
- [103] J.A. King. *Appl. Phys. Lett.*, 66, 2014.
- [104] C. Vieu et al. *J. Appl. Phys.*, 91, 2002.
- [105] J. Geissler et al. *Phys. Rev. B*, 65, 2001.
- [106] T.P.A. Hase et al. *Phys. Rev. B*, 90, 2014.
- [107] H. Yang et al. *Phys. Rev. Lett.*, 115:267210, 2015.
- [108] B. Dupé et al. *Nat. Comm.*, 5, 2014.
- [109] W. Jiang et al. *Science*, 349:283, 2015.
- [110] B. Dupé et al. *Nat. Comm.*, 7, 2016.
- [111] A. Belabbes et al. *Arxiv : 1609.04004v1*, 2016.
- [112] P.J. Flanders. *J. Appl. Phys.*, 63:3940, 1988.
- [113] J. Stöhr and H.C. Siegmann. *Magnetism*. Springer, Berlin, 2006.
- [114] C. Moreau-Luchaire et al. *Nat. Nanotech*, 11:444–448, 2016.
- [115] B.T. Thole et al. *Phys. Rev. Lett.*, 68, 1992.
- [116] P. Carra et al. *Phys. Rev. Lett.*, 70, 1993.
- [117] C.T. Chen et al. *Phys. Rev. Lett.*, 75, 1995.
- [118] J. Kirz and H. Rarback. *Rev. sci. Instrum.*, 56, 1985.
- [119] A.L.D. Kilcoyne et al. *Synchrotron Radiat.*, 10, 2003.
- [120] E. Beaurepaire, H. Bulou, F. Scheurer, and J.P. Kappler. *Magnetism and Synchrotron Radiation*. Springer, 2010.
- [121] M. Rowen et al. *Nucl. Instrum. Methods Phys. Res. A*, 467, 2001.
- [122] J.H. Dunn et al. *J. Magn. Magn. Mater.*, 316, 2007.
- [123] A. Hubert and R. Schäfer. *Quantum Magnetism*. Springer Netherland, 2000.
- [124] V. Baltz et al. *Phys. Rev. B*, 75, 2007.
- [125] O. Boulle et al. *Nat. Nanotech.*, 11:449, 2016.

- 
- [126] C. Kittel. *Introduction to Solid State Physics*. Wiley, New York, 1996.
- [127] A. Aharoni. *Introduction to the Theory of Ferromagnetism*. Oxford University Press, Oxford, 2000.
- [128] C. Eyrieh et al. *Phys. Rev. B*, 90:235408, 2015.
- [129] N.S. Kiselev et al. *J. Phys. D*, 44:392001, 2011.
- [130] C. Moutafis et al. *Phys. Rev. B*, 79:224429, 2009.
- [131] C. Moutafis et al. *Phys. Rev. B*, 76:104426, 2007.
- [132] F. Büttner et al. *Nat. Phys.*, 11:225–228, 2015.
- [133] T. Liu et al. *Journal of Physics D: App. Physics*, 49, 2016.
- [134] G. Chen et al. *Appl. Phys. Lett.*, 106:242404, 2015.
- [135] S. Woo et al. *Nat. Mat*, 15:501, 2016.
- [136] A. Soumyanarayanan et al. *arXiv : 1606.06034*12016, 2016.
- [137] M. Baćani et al. *arXiv : 1609.01615*, 2016.
- [138] K. Everschor. *Current-Induced Dynamics of Chiral Magnetic Structures*. PhD thesis, University of Köln, Germany, 2012.
- [139] A. Hrabec et al. *Arxiv:1611.00647*, 2016.
- [140] A. Vansteenkiste et al. *AIP Advances* 4, 4:107133, 2014.
- [141] S. Pizzini et al. *Phys. Rev. Lett.*, 113:047203, 2014.
- [142] M. Belmeguenai et al. *Phys. Rev. B*, 91:180405(R), 2015.
- [143] K. Di et al. *App. Phys. Lett.*, 106:052403, 2015.
- [144] A.M. Clagston et al. *Phys.Rev.*, 125, 1962.
- [145] J. Crangle. *Phil. Mag.*, 5, 1960.
- [146] Y. Sakamoto et al. *Phys. Rev. B*, 83, 2011.
- [147] M. Zuckermann. *Solid State Commun.*, 12, 1973.
- [148] B.N. Cox et al. *Phys. Rev. B*, 20, 1979.
- [149] R. Wienke et al. *J. Appl. Phys.*, 69, 1991.
- [150] H. Akai. *Hyperfine Interact.*, 43, 1988.

- [151] K.S. Ryu et al. *Nat. Commun.*, 5:3910, 2014.
- [152] F. Wilhelm et al. *Phys. Rev. Lett.*, 85, 2000.
- [153] W. Lim et al. *Appl. Phys. Lett.*, 102:162404, 2013.
- [154] S.Y. Huang et al. *Phys. Rev. Lett.*, 109:107204, 2012.
- [155] S. Geprags et al. *Appl. Phys. Lett.*, 101:261407, 2012.
- [156] S. Ferrer et al. *Phys. Rev. Lett.*, 77, 1996.
- [157] W.B. Zeper et al. *J. Appl. Phys.*, 65, 1989.
- [158] P. He et al. *J. Appl. Phys.*, 69, 1991.
- [159] Q.L. Lv et al. *J. Magn. Magn. Mater.*, 323, 2011.
- [160] T. Ueno et al. *Sci. Rep.*, 5:12534, 2015.
- [161] G. Schütz et al. *Phys. Rev. Lett.*, 58, 1987.
- [162] G. Schütz et al. *J. Appl. Phys.*, 67, 1990.
- [163] S. Rüegg et al. *J. Appl. Phys.*, 69, 1991.
- [164] G. Schütz et al. *J. Appl. Phys.*, 73, 1993.
- [165] M. Abes et al. *Phys. Rev. B.*, 82:094444, 2010.
- [166] G. Schütz et al. *Z. Phys. B : Condens. Matter*, 75, 1989.
- [167] W.E. Bailey et al. *Phys. Rev. B*, 86:144403, 2012.
- [168] F. Wilhelm et al. *Phys. Rev. Lett.*, 87:017002, 2001.
- [169] H.T.Nembach et al. *Nat. Phys.*, 11:189–193, 2015.
- [170] K.S. Ryu et al. *Nat. Nanotech.*, 8:527–533, 2013.
- [171] H. Nakayama et al. *Phys. Rev. Lett.*, 110, 2013.
- [172] B.T. Thole et al. *Phys. Rev. Lett.*, 70, 1993.
- [173] A.I. Figueroa et al. *Phys. Rev. B*, 90, 2014.
- [174] W. Grange et al. *Phys. Rev. B*, 58, 1998.
- [175] F. Garcia-Sanchez et al. *Phys. Rev. B*, 89, 2014.
- [176] I. Purnama et al. *Sci. Rep.*, 5:10620, 2015.
- [177] X. Zhang et al. *Nat. Comm.*, 7:10636, 2016.

- 
- [178] Y. Onose et al. *Phys. Rev. Lett.*, 81, 2012.
- [179] B. Barbara, Y. Imry, G. Sawatzky, and R. C. E. Stamp. *Quantum Magnetism*. Springer Netherland, 2006.
- [180] B. D. Cullity and C. D. Graham. *Introduction to Magnetic Materials*. John Wiley, 2005.
- [181] J. Xiao et al. *Phys. Rev. B*, 73:054428, 2006.
- [182] A. Yamaguchi et al. *Phys. Rev. Lett.*, 92:077205, 2004.
- [183] S. Zhang et al. *Phys. Rev. Lett.*, 93:156804, 2004.
- [184] E.A. Giess. *Science*, 208, 1980.
- [185] Y.S. Lin et al. *Phys. Lett.*, 23, 1973.
- [186] T. Garel and S. Doniach. *Phys. Rev. B*, 26, 1982.
- [187] T. Suzuki. *J. Magn. Magn. Mater.*, 31-34, 1983.
- [188] A Correspondent. *Nature*, 240, 1972.
- [189] N. Nagaosa et al. *Phil. Trans. R. Soc. A*, 370:5794–5805, 2012.
- [190] X.Z.Yu et al. *Nat. Comm.*, 5, 2014.
- [191] M. Onada et al. *J. Phys. Soc. Jpn.*, 73:2624–2627, 2004.
- [192] F. Wilhem et al. *Phys. Rev. Lett.*, 87, 2001.
- [193] S. Konishi. *IEEE Trans. Magn.*, 19, 1983.
- [194] H. Nakatani. *IEEE Trans. Magn*, 29, 1993.
- [195] A. Thiaville et al. *Phys. Rev. B*, 67, 2003.
- [196] M. Sparks. *Ferromagnetic-relaxation Theory*. Mc Graw-Hill, New York, 1964.
- [197] K.W. Moon et al. *Phys. Rev. B*, 89, 2013.
- [198] E.C. Stoner. *Proc. R. Soc. London, Ser. A*, 165, 1938.
- [199] J. Zang et al. *Phys. Rev. Lett.*, 107, 2011.
- [200] J. Barker et al. *Phys. Rev. Lett.*, 116:147203, 2016.
- [201] X. Zhang et al. *arXiv : 1601.03896*, 2016.
- [202] L. Herrera Diez et al. *App. Phys. Lett.*, 107, 2015.
- [203] J.F. Pulecio et al. *Arxiv:1611.06869*, 2016.

# Résumé

Au cours des dernières années, les appareils électroniques tels que les processeurs et la mémoire sont devenus plus rapides et plus petits. Cependant, la vitesse d'amélioration de ces dispositifs ne semble pas aussi importantes qu'il y a une dizaine d'années. Les dispositifs électroniques à base de silicium ont presque atteint leur limite physique. L'échelle de ces appareils est un problème lorsque la taille est inférieure à 10 nm, en raison d'un effet quantique difficile à contrôler. Trouver une nouvelle voie pour construire des dispositifs de nouvelle génération devient une nécessité. Il existe plusieurs candidats pour ces dispositifs de nouvelle génération, tels que les jonctions magnétiques à effet tunnel, les mémoires race-track, les unités de calcul à base de nanotubes de carbone ou l'informatique quantique. Notre but ici est de trouver une nouvelle technologie capable de surmonter l'étranglement actuel dans ce domaine.

En parallèle, le concept de topologie a suscité un intérêt considérable pour la science de la matière condensée. Les nouvelles propriétés quantiques utilisent le concept de topologie et le guidage de la théorie. Le célèbre exemple de différentes topologies est la différence entre un donut et une sphère : deux objets qui ne peuvent pas être transformés en continu l'un vers l'autre, à cause du trou au centre du donut, créant une singularité topologique. En chimie, la topologie est connue dans le contexte de la latéralité des molécules chirales. Le phénomène de chiralité a récemment été trouvé dans les systèmes de la matière condensée, dans les matériaux magnétiques avec des structures non centrosymétriques et à la surface des isolants topologiques. Les Skyrmions sont des configurations magnétiques topologiquement non triviales, dans l'espace réel, des nanostructures magnétiques s'apparentant à une vis. Par analogie avec l'exemple de l'espace réel d'un anneau et d'une bande de Möbius, deux états quantiques topologiques différents ne peuvent pas être transformés l'un vers l'autre et coexisteront.

Dans cette thèse, nous étudions un candidat très prometteur pour les dispositifs de nouvelle génération: des skyrmions magnétiques isolés dans des multicouches à base de ferromagnétiques ultra-minces avec un alignement hors-plan préféré des moments magnétiques. Historiquement, les domaines ferromagnétiques sont le support le plus important pour le stockage de données numériques, et les bulles magnétiques (avec un nombre topologique de 0) jouent un rôle majeur dans la recherche sur la statique et la dynamique des domaines ferromagnétiques et dans le développement de nouveaux

dispositifs. Du côté de l'application, les bulles ont été utilisées avec succès dans les dispositifs de stockage à semi-conducteurs, dans lesquels les informations (les bulles) sont déplacées dans le matériau au lieu que la tête de lecture ou d'écriture passe à la position du bit d'information. Malheureusement, les mémoires à bulles ont montré leurs limites: leur taille (diamètre  $\sim 1\mu\text{m}$ , et la manière de les déplacer (par champ tournant) inadaptée aux appareils d'application ... De nos jours, on utilise encore des disques magnétiques rotatifs, et la recherche de nouveaux concepts pour les dispositifs magnétiques à l'état solide est plus vive que jamais. Un concept qui présente un intérêt particulier dans ce contexte est la mémoire race-track, un fil magnétique dans lequel les parois de domaine sont déplacées par des courants de spin. Récemment, on a découvert que les skyrmions chiraux peuvent être déplacés avec des densités de courant environ un million de fois plus petites que celles de parois de domaines. afin de promouvoir leur application dans des dispositifs réels, il est important d'étudier leur nucléation, stabilisation et propagation dans un système technologiquement pertinent et à température ambiante.

Au début de ma thèse, l'objectif principal était d'observer à température ambiante des skyrmions magnétiques isolés stabilisés. Ce but a été atteint par l'observation par une technique synchrotron de skyrmions isolées dans des échantillons  $\{\text{Ir}|\text{Co}|\text{Pt}\}$ . Après quoi, nous avons développé deux nouvelles approches pour estimer la force moyenne DMI dans les échantillons. De plus, nous avons développé plusieurs échantillons avec différents paramètres pour changer les interfaces en jeu et ainsi essayer de régler les propriétés des skyrmions magnétiques observables dans ces échantillons (comme leur taille, densité et stabilité sous champ magnétique) et améliorer l'interaction qui aide à stabiliser les skyrmions, l'interaction Dzyaloshinskii-Moriya (DMI). Enfin, nous avons conçu des dispositifs pour commencer l'étude du mouvement des petits skyrmions isolés dans les race-track.

Cette thèse est structurée comme suit.

- Chapitre 1 Dans le chapitre 1, nous rappelons les principales énergies micromagnétiques impliquées dans les échantillons étudiés au cours de ce travail, y compris l'interaction Dzyaloshinskii-Moriya (DMI) qui aide à stabiliser les skyrmions dans notre cas. Nous avons également un aperçu du sujet des murs de domaine (DW), d'autres candidats aux appareils de prochaine génération, en raison de sa grande quantité de similitudes avec les skyrmions.
- Chapitre 2 Dans ce chapitre, nous expliquons le concept de topologie (en particulier des skyrmions dans le magnétisme), suivi d'une revue de l'histoire de l'observation des skyrmions magnétiques dans différents types de structures, y compris dans les structures d'interfaces comme dans les ultra-minces multicouches comme ceux que nous avons étudiés.
- Chapitre 3 La conception de ces systèmes multicouches ultraminces est présentée au chapitre 3, où sont présentés les détails de la croissance, les méthodes de caractérisation et les méthodes d'observation.

Chapitre 4 Ce rapport technique est suivi de l'observation à la température ambiante de skyrmions magnétiques isolés, ce qui était notre premier objectif principal. Ces observations ont été faites avec une technique de synchrotron (STXM) et une technique de laboratoire (MFM), et une comparaison entre les deux techniques a été faite. Nous comparons également le comportement magnétique de deux échantillons différents:  $\{\text{Co|Pt}\}$  et  $\{\text{Ir|Co|Pt}\}$  multicouches pour montrer l'effet de différentes amplitudes DMI. Nous montrons également quelques résultats préliminaires sur le mouvement des skyrmions magnétiques isolés dans les race-track. Dans ce chapitre, nous présentons les premières images de skyrmions magnétiques à température ambiante dans des multicouches ultraminces. Nous avons pu observer différentes structures magnétiques, y compris des skyrmions, et cette étude a été réalisée sur deux échantillons différents: une multicouche asymétrique avec du Cobalt:  $\text{Pt}_{10}|\text{Co}_{0.6}|\text{Pt}_1|\{\text{Ir}_1|\text{Co}_{0.6}|\text{Pt}_1\}_{10}|\text{Pt}_3$  et une multicouche symétrique avec du Cobalt également :  $\text{Pt}_{10}|\text{Co}_{0.6}|\text{Pt}_1|\{\text{Co}_{0.6}|\text{Pt}_1\}_{10}|\text{Pt}_3$ . Le concept d'avoir deux échantillons différents est que, parce que les deux interfaces sont les mêmes dans l'échantillon  $\{\text{Co|Pt}\}$ , on s'attend à ce que les deux composantes de DMI s'annihilent alors que, comme vu avec la prédiction des calculs *ab initio* dans le chapitre précédent [108, 109, 110], les amplitudes DMI aux interfaces de l'échantillon  $\{\text{Ir|Co|Pt}\}$  devraient s'ajouter l'une à l'autre. De plus, ces échantillons ont été imagés par deux techniques différentes: une technique synchrotron (STXM) et une technique de laboratoire (MFM), toutes deux expliquées dans le chapitre précédent. Nous avons choisi de travailler avec deux techniques différentes qui ont leurs propres avantages et inconvénients et de comparer les résultats.

Chapitre 5 Après la réalisation de ce premier objectif, nous avons développé deux techniques indépendantes pour estimer la force DMI dans nos systèmes. Nous présentons ici ces techniques et les appliquons aux observations faites par STXM et MFM. Nous concluons sur la possibilité d'estimer l'amplitude DMI avec les techniques STXM ou MFM, et sur la grande valeur trouvée pour l'échantillon  $\{\text{Ir|Co|Pt}\}$ . Nous présentons également quelques analyses quantitatives du mouvement des skyrmions isolés dans les hippodromes présentés dans le chapitre précédent. Les principaux résultats de cette étude sont:

- L'observation des domaines à la rémanence et l'évolution de la taille des skyrmions avec un champ magnétique hors-plan appliqué permettent d'estimer l'amplitude moyenne de la DMI,
- Une très grande amplitude DMI a été trouvée dans l'échantillon  $\{\text{Ir|Co|Pt}\}$ , de  $1,9 \text{ mJ} / \text{m}^3$  - en bon accord avec des échantillons similaires mesurés par d'autres groupes,
- Une amplitude DMI très faible, même si non nulle, a été trouvée pour l'échantillon  $\{\text{Co|Pt}\}$  de  $0.2 \text{ mJ} / \text{m}^3$ ,
- Les deux expériences STXM et MFM permettent d'estimer l'amplitude DMI, et la valeur trouvée est exactement la même pour les deux observations,

- L'aimantation induite par effet de proximité a été trouvée à la fois dans le Pt et dans l'Ir par XMCD estimé dans nos structures,
- L'effet de proximité diminue la valeur estimée du DMI dans les échantillons d'environ 20 %.

Chapitre 6 Enfin, nous avons effectué au chapitre 6 une étude systématique par MFM de différents échantillons, en faisant varier plusieurs paramètres. Nous montrons que nous sommes en mesure de régler les propriétés des skyrmions (telles que leur taille, leur densité et leur stabilité sous un champ magnétique appliqué hors-plan) et d'améliorer l'amplitude DMI. Nous avons pu tirer plusieurs conclusions en considérant l'amplitude DMI:

- Le nombre de répétitions de la tricoche principale ne modifie pas l'amplitude DMI dans nos échantillons {Ir|Co|Pt}
- L'augmentation de l'épaisseur de Co conduit à une diminution de l'amplitude moyenne de DMI
- La variation de l'épaisseur Ir ne modifie pas l'amplitude DMI bien que la rugosité aux interfaces conduise à une estimation de l'amplitude DMI moins précise que dans les autres mesures
- La variation de l'épaisseur de Pt ne semble pas changer l'amplitude de DMI, bien qu'une épaisseur de Pt plus fine puisse aider à l'améliorer. Cependant, plus de mesures doivent être effectuées avec une gamme plus large d'épaisseurs de Pt pour confirmer ou infirmer cette possibilité.
- Des mesures sur des échantillons avec remplacement de Ir par W ou AlOx ont été effectuées. L'échantillon W conduit à une amplitude DMI moins importante que Ir, bien que de belles images de skyrmion unique au centre de nanodisques aient été observées à température ambiante par MFM. L'échantillon AlOx conduit à une amélioration de la force DMI dans l'échantillon, comme observé par d'autres groupes.

**Title :** Étude et contrôle des propriétés interfaciales de multicouches magnétiques pour l'observation de skyrmions à température ambiante

**Mots clefs :** Skyrmions, Dzyaloshinskii-Moriya, Température ambiante, multicouches

**Résumé :** Dans cette thèse, nous montrons que nous avons réussi à observer des skyrmions isolés sub-100nm dans des échantillons Ir|Co|Pt. Ces observations ont été faites via deux techniques différentes : le STXM (technique synchrotron qui permet d'imager l'aimantation hors du plan de l'échantillon) et le MFM (technique de laboratoire qui permet d'imager le gradient de l'aimantation). Nous avons également montré que nous les avons observés à la fois dans les films étendus ainsi que dans des nanostructures (nanodisques de diamètre entre 200 nm et 1  $\mu$  m, ainsi que les bandes dont la largeur varie de 400 nm à 1  $\mu$  m ).

Nous avons également développé deux approches différentes pour estimer l'amplitude DMI dans les échantillons. La première est basée sur la périodicité des domaines dans les échantillons après désaimantation. La

deuxième technique est basée sur l'évolution de la taille des skyrmions avec un champ magnétique appliqué hors-plan. Pour la nécessité des simulations micromagnétiques, nous avons également essayé de déterminer l'échange de nos échantillons. Avec cette valeur, le DMI trouvé dans nos échantillons est d'environ 2 mJ/m<sup>2</sup>.

Nous avons effectué une étude systématique sur des échantillons avec variation de différents paramètres: nombre de répétitions de la tricoche principale, épaisseur du Co, épaisseur du Pt, épaisseur de l'Ir, composition des couches d'Ir avec W ou AlOx. Nous avons montré que pour tous les systèmes, nous avons pu observer des skyrmions stabilisés à température ambiante grâce au MFM. Nous avons également observé que la densité des skyrmions diminue avec l'augmentation de l'anisotropie effective.

**Title :** Tailoring the interfacial properties of magnetic multilayers for the observation of skyrmions at room temperature

**Keywords :** skyrmions, Dzyaloshinskii-Moriya, multilayers, room temperature

**Abstract :** We have been able to successfully observe isolated sub-100nm skyrmions in Ir|Co|Pt samples. Moreover, we have been able to observe them with two different techniques : STXM - a synchrotron technique that maps the out-of-plane magnetization of a sample, and MFM - a laboratory technique that images the gradient of the magnetization. We have also shown that we have stabilized them in extended films as well as in nanostructures (nanodisks with diameter from 200 nm to 1  $\mu$ m, as well as stripes with width from 400 nm to 1 $\mu$ m).

Secondly, we have developed two different approaches to estimate the DMI amplitude in samples. The first one is based on the mean domain periodicity in samples after

demagnetization. The second technique is based on the size evolution of skyrmions with applied out-of-plane magnetic field. For the need of the micromagnetic simulations, we have also tried to determine the exchange stiffness of our samples. With this value, the DMI amplitude found in our samples is about 2 mJ/m<sup>2</sup>.

We have performed a systematic study on samples with variation of different parameters : number of repetitions of the main trilayers, Co thickness, Pt thickness, Ir thickness, composition of the buffer layers, and switching Ir with W or AlOx. We also observed that the density of skyrmions is decreasing with increasing effective anisotropy.

